Design and Fabrication of the Catalyst Systems for the Control of Sintering of Metal Nanoparticles during the Growth of Carbon Nanotubes and ZnO nanorods

A thesis submitted for the partial fulfilment of the requirements for the degree

of

Doctor of Philosophy in Chemistry

By

Nei-Jin Ke

The University of Canterbury

2015

I would like to thank God for the good health, wisdom and wellbeing necessary to complete this thesis.

Acknowledgements

Finishing writing this Ph.D thesis has been one of the most challenging tasks in my life. In full gratitude I would like to acknowledge the following individuals who encouraged, inspired, supported, assisted, and sacrificed their time to help in my pursuit of this Ph.D degree. First of all, I wish to express my sincere thanks to my supervisor Dr. Vladimir Golovko and my co-supervisor Prof. Alison Downard. Thank you very much for all the mentoring, advice and patience, without your support and encouragement I would never have been able to finish this task.

Many thanks also go to Downard's and Golovko's groups for all kinds of support, fun and help. Thanks Brad for showing me all the details of preparing the citrate-capped Au nanocolloids with good quality. Also, Baira and Daniil enthusiastically shared their knowledge and experience of synthesising Au nanoparticles. I would like to thank Prof. Simon Brown and his Ph.D student Domagoj Belić at the Physics and Astronomy Department for the knowledge of ultra-high vacuum deposition. Many thanks to Assoc. Prof. Martin Allen and his Ph.D student Max Lynam from the Electrical and Computer Engineering Department for using my samples to grow ZnO in their pulsed laser deposition. I would like to extend my appreciation to Domagoj Belić and Yu-Ming Chen (from Material Science and Engineering, National Cheng Kung University, Taiwan) for all of the technical assistance as well as the TEM images. It was a great pleasure to work with all of you and learn so many different instrumentation techniques. Special thanks to all the staff at the Chemistry Department especially Danny Leonard, Nick Oliver, Robert McGregor and Steven Graham for the making of special devices, glassware and keeping everything going. Also, many thanks to the following people for all other technical training and assistance: Helen Devereux at the nanofabrication laboratory for the training of AFM, Mike Flaw at the Mechanical

Engineering Department for the training of SEM and TEM, and Dr. Eric Le Ru from Raman laboratory in Victoria University of Wellington for the training of Raman Spectroscopy. Finally, I am indebted to the MacDiarmid Institute for its financial support.

Thanks to my beloved family, especially my grandparents and my parents, Dean and Lina who put their unwavering faith in my ability, always encouraging and supporting me during some difficult times. Thanks for my lovely friend Shaun and his family who have supported me throughout this long time. It has been wonderful to have you during this precious journey which will continue on for the future life journey as well. Thanks for my friends, Helen, Lawrence, Peter, Ruth and Kirsty for helping me to adapt and enjoy the NZ life.

Jin

Table of contents

Abstract

This thesis reports two distinct approaches towards controlled fabrication of catalyst systems for carbon nanotube (CNT) and ZnO nanorod growth.

For CNT growth, a shallow porous anodic alumina (PAA) membrane was utilised to prevent the sintering of Co metal catalyst nanoparticles (NPs) during the growth of CNTs by chemical vapour deposition (CVD). This part of the work involved optimisation of PAA membrane fabrication (several key process parameters, such as pre-treatment, anodization and chemical etching), development of a new strategy for electrodeposition of Co (*via* control over voltage pulse sequence, pH and atmosphere) as well as optimisation of the CVD conditions (temperature used during the catalyst reduction and growth stage). Dense CNTs with diameters smaller than the PAA pores were successfully grown using optimised catalyst system under optimal growth conditions.

For ZnO nanorod growth, the optimal catalyst system was fabricated by forming a sub-monolayer of Au nanocolloids adsorbed onto an APTMS-modified sapphire substrate. In order to optimize catalyst fabrication effects of various key catalyst fabrication parameters (drop- *vs*. dip-coating *vs*. sputtering, effect of the type of sapphire substrate surface, tether modification of substrate, colloid loading *etc*.) had been explored in the interactive fashion. Pulsed laser deposition (PLD) was utilised for the subsequent ZnO nanorod growth and effects of various key process parameters (use of eclipse configuration, oxidizing *in situ* during heating up stage, laser pulse frequency *etc*.) were explored in detail. By using the optimised catalyst system and the optimised PLD conditions which have been developed in this thesis, dense arrays of ZnO nanorods with highly uniform size and nanorods tip diameter similar to the diameter of the Au colloids used as catalysts were successfully fabricated.

Abbreviations

AC	Alternating current
AFM	Atomic force microscopy
APTMS	3-aminopropyltrimethoxysilane
CNT	Carbon nanotube
CVD	Chemical vapour deposition
CVTC	Chemical vapour transport and condensation
CNF	Carbon nanofiber
DC	Direct current
E-beam	Electron beam
EDS	Energy dispersive spectroscopy
EDX	Energy dispersive X-ray spectroscopy
EtOH	Ethanol
FIB	Focused ion beam
HER	Hydrogen evolution reaction
MeOH	Methanol
MBE	Molecular beam epitaxy
MWCNT	Multi-walled carbon nanotube
NP	Nanoparticle
NW	Nanowire
PAA	Porous anodic alumina
PLA	Pulsed laser ablation
PLD	Pulsed laser deposition
PS	Polystyrene

SEM	Scanning electron microscopy
SWCNT	Single walled carbon nanotube
TEM	Transmission electron microscopy
TPR	Temperature programmed reduction
UV-vis	Ultraviolet-visible
UHV	Ultra-high vacuum
VLS	Vapour-liquid-solid

Chapter 1. Introduction

1.1 Background and motivation

Since the Haber-Bosch process was invented in early 20th century, a method of directly synthesising ammonia from hydrogen and nitrogen using a metal catalyst, heterogeneous catalysis has been developed and widely used in the chemical industry. Heterogeneous reactions take place with two or more phases present, for instance, solids and liquids or gases and solids and these reactions are often understood using concepts of surface science and nanoscience.[1] However, even since the development of the first major industrial catalytic process, the Haber-Bosch process, the nanostructured materials have been contributing to the improving quality of our daily life.[2] Due to the further development of microscopies, nanoscience as well as nanotechnology has become an active subject for current science.[3]

Fabricating inorganic nanostructures of materials such as metals, carbons and semiconductors often rely on the use of catalysts and is one of the important themes in nanoscience. Using metal nanoparticles (NPs) as the catalyst for synthesising nanostructures such as carbon nanotubes (CNTs) and metal oxide (semiconductor) nanowires (NWs) is one of the classic examples which combines heterogeneous catalysis and nanoscience[4,5,6] The role of metal NPs in growth of such nanostructures clearly defines them as catalysts in a sense that without metal NPs no growth would typically occur. Yet, in contrast to classical heterogeneous catalysts, metal NPs used in catalytic nanofabrication are rarely separated from the products for the purpose of catalyst recycling. Since vapour deposition methods and instrumentation have been highly developed, they have been widely utilised for synthesis of

CNTs and metal oxide NWs. The process of fabricating CNTs or NWs is usually divided into three stages:

1. Fabrication of the catalyst system which involves depositing metal catalyst onto a substrate and the formation of the metal NPs.

2. Reducing the metal NPs to the metallic state which is assumed to enable their catalytic activity.

3. Growth of CNTs or metal oxide NWs by the reaction between vapour phase of the feedstock and the metal NPs.

For the first stage, there are many methods that can be used for deposition as well as the formation of metal NPs on a substrate. For chemical methods, the metal NPs can be pre-synthesised in solution with control over their size and composition by utilising inverse micelles, capping agent or dendrimers,[7,8,9] The solution can be coated onto a substrate surface as a sub-monolayer or monolayer by dip coating or spin coating.[10,11] For physical methods, metal NPs can be formed by sputtering, soft landing of nanoclusters, or electrodeposition.[12,13,14] One of the most common physical methods of catalyst fabrication replies on deposition of a thin metal film onto a substrate followed by annealing to break the film into small particles (also known as dewetting).[15,16,17] The size and the morphology of metal NPs are often related to the thickness of the metal film and the conditions of annealing process.[17,18]

The second stage is often accompanied by the third, reductive stage. Some catalyst metals (*e.g.* Fe, Ni and Co) are very easily oxidised in the ambient atmosphere and lose their catalyst activity. In order to reduce the oxidised NPs to the metallic state, heating the catalyst

system at a high temperature in the presence of $H_{2(g)}$ prior to the growth of CNTs or metal oxide NWs is often required.[19]

The second stage and the third stage are often carried out sequentually in the same instrument which allows the processes of heating, gas purging and delivery of the nanostructure precursor *via* the vapour phase. In the case of using thermal chemical vapour deposition (CVD) and pulsed laser deposition (PLD), the growth of the CNTs or NWs is through a chemical vapour deposition and physical vapour deposition respectively. During these two methods, the catalyst system is usually heated up to a high temperature and the catalyst metal NPs react with the nanostructure building blocks delivered to the catalyst *via* gas phase, based on the vapour-liquid-solid (VLS) growth mechanism.[20] The VLS growth mechanism will be introduced in the next section. During the elevation of temperature, the aggregation of metal NPs can occur and form a larger particle which can negatively affect CNT and NW growths.[21] For growing CNTs in thermal CVD, the unwanted large metal catalyst particles could result in the formation graphitic particles (carbon nano-onions) or defective MWCNTs.[22] Also, because the diameter of the metal NP determines the size of CNT and metal oxide NW, for the purpose of fabricating a uniform array of CNTs or NWs, controlling the size of catalyst metal NPs prior to the CNT or metal oxide NW growth has become a challenging issue.

It should be noted that the fabrication of CNTs or metal oxide NWs often involves the deposition of metal catalyst onto a substrate (*i.e.* Si, sapphire, glass *etc.*), followed by the steps including dewetting, reduction and deposition of the nanostructure which sometimes can all take place in the same instrument. This is sometimes the case for growth methods such as CVD, PLD, and molecular beam epitaxy (MBE).[23,24,25]

Many strategies for controlling the size of catalyst metal NPs have been reported. Table 1.1, summarises different approaches towards control of the catalyst for growth of well-defined NTs and NWs reported in the literature. Among these methods, electrodepositing metal into a highly ordered porous anodic alumina membrane has been widely used for fabricating catalyst systems for CNT growth. However, due to a limited conductivity of this type of substrate, growing highly ordered CNTs with controllable diameters is the main challenge of this option.[14]

Table 1.1. Methods of fabricating metal nanoparticles on a substrate.

Methodologies	**Fabrication process**	**Range of metal size**
Electron-beam lithography	Similar technique to photolithography but use a focused electron beam as the exposure source which creates a nanoscale pattern on the substrate. [26,26-27]	100 - 250 nm
Soft-landing	Using ultra-high vacuum (UHV) deposition methods to deposit metal clusters onto a substrate with sample coverage less than 3 %.[13]	3 - 10 nm
Polystyrene (PS) bead layer as a porous template	Utilising a substrate modified with a monolayer of spherical PS beads. Metal is deposited through the gaps of the PS beads onto the substrate. After etching the PS, a very small amount of metal remains on the substrate. Dewetting is used to form the metal NPs. The dewetting conditions determine the size of metal NP. [28]	50 - 150 nm
Dewetting metal thin film on a dimpled substrate	Coating a thin metal film onto a substrate with dimple structure. Dewetting the template so the metal NPs will form in the bottom of the dimples. The thickness of the deposited metal thin film and the dewetting conditions determine the size of metal NPs.[29]	5 - 15 nm
Depositing metal NPs into a porous structure	Utilising a highly ordered porous anodic alumina membrane as a substrate to trap a certain amount of metal NPs in each pore. Metal NPs can be deposited into the pore by electrodeposition or dip coating.[14,30]	60 – 90 nm depends on the diameter of the pore.

In this thesis, two catalyst systems which can effectively prevent the aggregation of catalyst metal nanoparticles will be demonstrated. One catalyst system was developed utilising porous alumina membranes as a substrate and electrodepositing Co within the pores. CNTs were grown using this catalyst system. Another catalyst system was fabricated by depositing a sub-monolayer of Au nanocolloids on a sapphire substrate under optimised coating conditions. ZnO nanorods were grown on this catalyst system.

More detailed information related to the fabrication of the catalyst systems for CNT growth and ZnO NW growth will be presented in Chapters 3, 4, and 5. The following section will focus on the VLS growth mechanism which is an important growth mechanism for CNT and ZnO NW growth. Also CNT and ZnO NW will be briefly introduced in the following sections.

1.2 VLS growth mechanism

To introduce the VLS mechanism, it is worth to briefly mention its history. The VLS mechanism was first proposed by Wagner *et al.* in 1964 who successfully grew silicon whiskers with a micro scale dimension using Au droplets as the catalyst (Fig. 1.1).[31] However, successful nanowire growth was first demonstrated in 1998 by Morales *et al.* who used pulsed laser ablation (PLA) to generate Si vapour which reacted with Fe catalyst *via* the VLS growth mechanism to form nanowires.[24] Fig. 1.2 illustrates the principles of the VLS mechanism.[32] In this example, Au NPs are heated to a high temperature which is near the melting point of Au and above the eutectic temperature of the metal/semiconductor eutectic system (363 ºC in the case of Au/Si). Si vapour is then introduced when the temperature nearly reached the selected temperature, resulting in the formation of the eutectic alloy (Au/Si). The Si vapour is continuously supplied and reacts with the eutectic alloy creating a

vapour/liquid phase supersaturated with respect to Si in the eutectic alloy, eventually the nucleation and precipitation of Si occurs. The liquid/solid phase interface is formed once the precipitation of Si starts. As a result, the nanowire growth is carried out by transferring Si vapour through the vapour/liquid interface into the eutectic alloy and followed by the continuous nucleation and precipitation through the liquid/solid interface.[31,32]

It should be noticed that CNT grown from metal NPs in CVD is also based on the VLS growth mechanism. Hence, for CNT or metal oxide NW growth using methods based on VLS, the diameter of CNT or metal oxide NW is determined by the diameter of the catalyst metal NP.

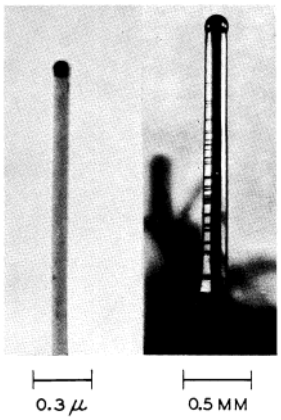

Fig. 1.1. TEM image of Si microwires grown using an Au droplet on a Si substrate. Figure adapted from reference 31.

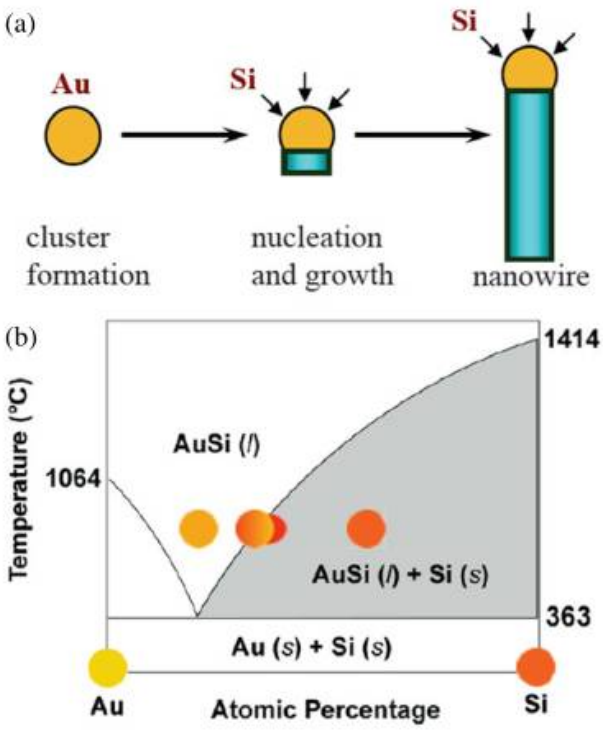

Fig. 1.2. Schematic of VLS growth of Si nanowires using Au NPs as the catalyst. (a) A liquid alloy droplet of AuSi is first formed above the eutectic temperature (363 °C) of Au and Si. Continuously feeding of Si in the vapour phase into the liquid alloy causes supersaturation, resulting in nucleation and directional nanowire growth. (b) Binary phase diagram for Au/Si system. Figure adapted from reference 32.

1.3 Carbon nanotubes

The first technical record of the synthesis of fibrous carbon was probably a patent published by Hughes and Cambers in 1889.[33] However, the first TEM image which revealed the hollow core structure of the multi walled carbon nanotubes (MWCNTs) was published by two Russian scientists Raduskevich and Lukyanovich in 1952 in The Journal of Physical Chemistry (Fig. 1.3).[34] Dr. John Abrahamson from the Chemical and Process Engineering Department, University of Canterbury reported a series of studies related to graphite and CNTs. Those papers, published during 1973 -1984, have been acknowledged as some early fundamental studies of CNTs.[35,36,37,38] However, it should be noted that the term "nanotube"

was first used in 1990s. Before then, CNTs were often named as (carbon) fibres. In the early 1990s, three important papers were published which verified the synthesis of CNTs as well as reported details of their structural characterisation. The first paper in *Nature* was reported by Iijima working at the NEC, Japan in 1991. The author observed (using HRTEM) the tubular structure of MWCNTs which contained different number of graphene sheets within their walls as illustrated in Fig. 1.4.[39] In 1993, the synthesis of single walled carbon nanotubes (SWCNT) was reported by the Iijima and his research group, while only two months later, another study focused on synthesis of SWCNTs was reported by Bethune *et al.* from IBM, USA.[40,41] Subsequent research reports also indicated beneficial properties of CNTs including unique stiffness (high strength, elasticity and tenacity), high electrical and thermal conductivity, and chemical stability. These properties can find applications in many fields.[5] For example, CNTs were used in scanning probe microscopy (*e.g.* CNTs as AFM tips)[42], micro- and nano-electronics (field emission displays)[43] and biosensors (glucose biosensors).[44] In summary, CNTs have been widely investigated and proposed to become an important constituent of many technologies.[39]

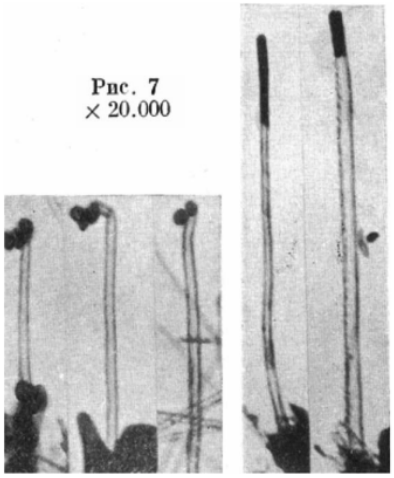

Fig. 1.3. TEM image of MWCNTs formed by the thermal decomposition of carbon monoxide on iron. Figure reproduced from 33.

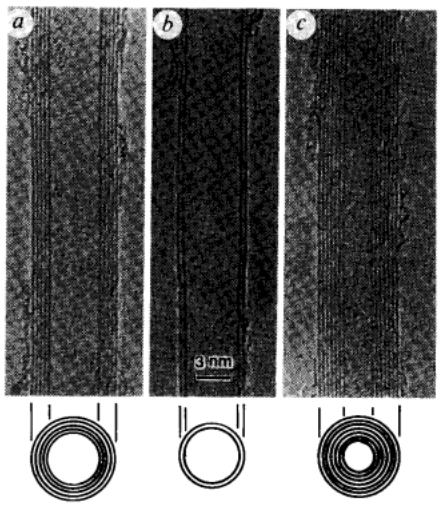

Fig. 1.4. TEM images of MWCNTs with different numbers of graphite layers and the illustration of the cross-section for each tube. Figure adopted from reference 39.

The structure of SWCNTs can be considered as a sheet of graphite (also called graphene) rolled up like a tube. The way of rolling graphene along the honeycomb structure determines the chirality of the SWCNT. Saito *et al.* proposed an indexing system for differentiating SWCNTs which has been widely used.[45] Fig. 1.5 (A) shows the index system based on vector $\vec{C}$ which results from the two vectors $\overrightarrow{a_1}$ and $\overrightarrow{a_2}$ according to the equation of $\vec{C} = n\overrightarrow{a_1} + m\overrightarrow{a_2}$ where the *n* and *m* are integers as illustrated in Fig. 1.5 (A). The types of SWCNT morphology can be determined by the integers (*n,m*) as the numbers shown in Fig. 1.5 (B). SWCNTs with zigzag morphology are formed when the graphene sheet rolling direction is defined by (*n,0*). The name of this type of SWNT refers to the zigzag arrangement of carbon atoms at the tip of SWNT. When the rolling direction is followed by *n = m (n,n)*, the type of SWCNT is armchair. The name of this type of SWNTs refers to the armchair arrangement of carbon atoms at the tip of SWNT (in analogy to armchair conformation of cyclohexane *etc.*). And the type of SWNT morphology which is chiral is formed when the rolling direction is followed by $n > m > 0$. The name of this type of SWNTs

refers to the chirality due to spiral arrangement of carbon atoms along the length of SWNT (in analogy to chirality of DNA helices *etc*.).

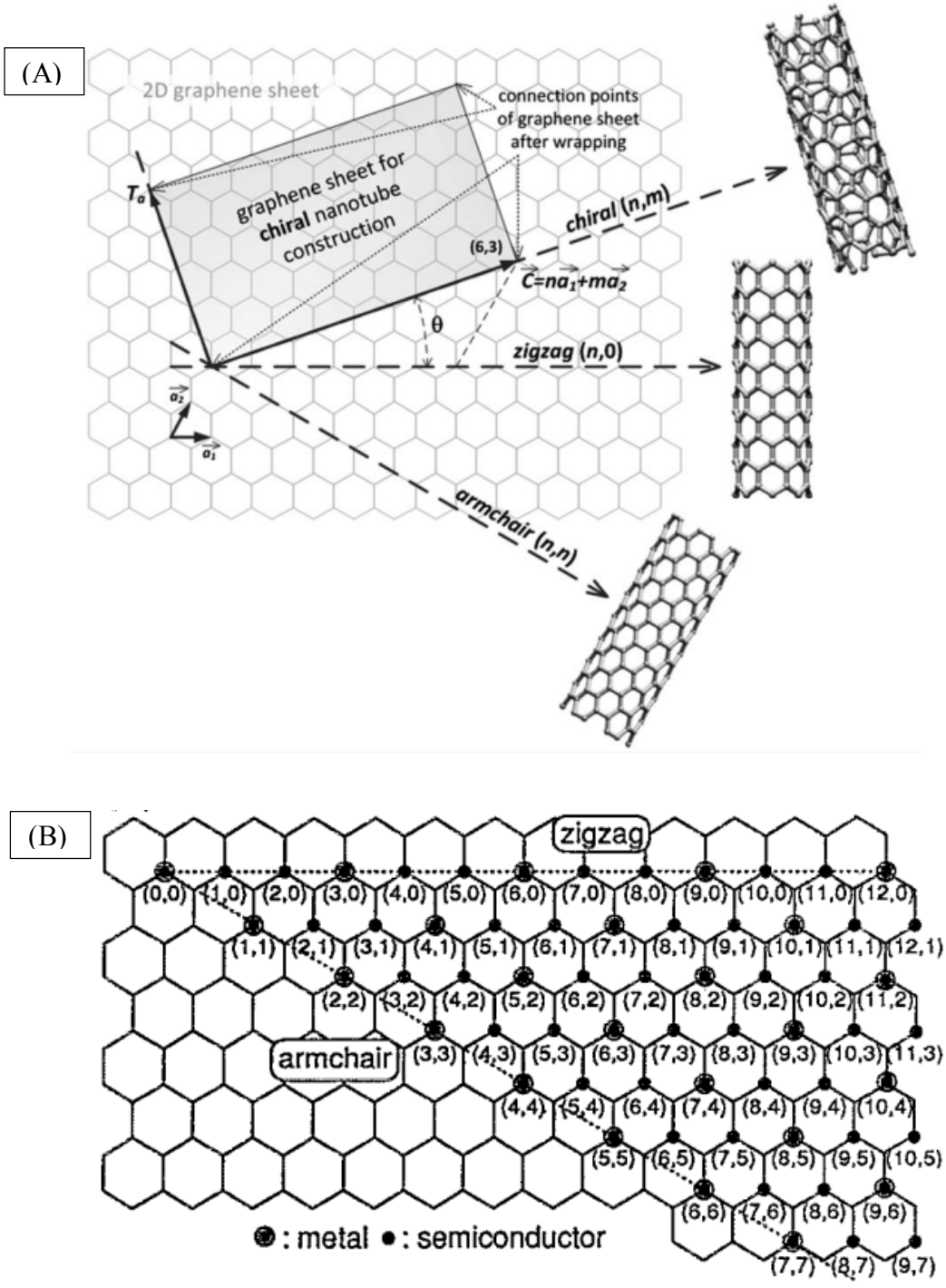

Fig. 1.5. (A) The principle of CNT construction from graphene sheet along the chiral vector $\vec{C}$. (B) Possible vectors for chiral fibres. The dots with circles and the small solid dots denote metallic and semiconducting behaviour respectively for each fibber. Figures adopted from reference 23 and 45.

CNTs can be constructed as SWCNTs and MWCNTs. MWCNT are composed of several concentric graphene tubes which fit one inside the other as shown in Fig. 1.6 (A). Another carbon nanostructure is known as carbon nanofiber (CNF) which is constructed by stacked-cup graphene layers as shown in Fig. 1.6 (B). All these carbon structures are likely to form bundles *via* intermolecular interaction between their high surface areas.[46]

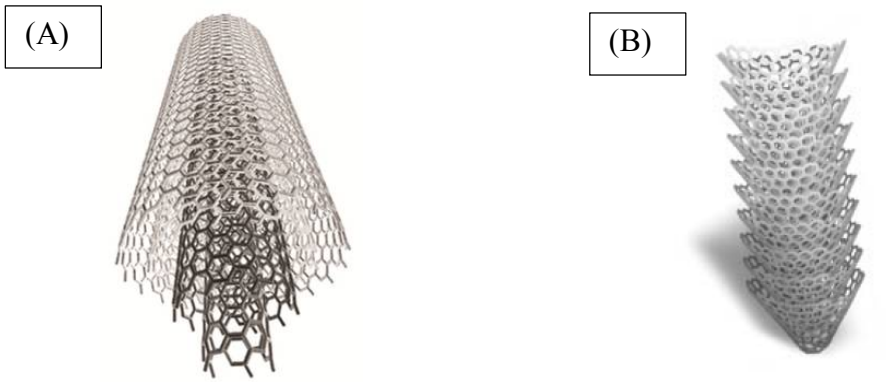

Fig. 1.6. Schematic diagrams of (A) MWCNT and (B) carbon nanofiber. Figures adapted from references 47 and 48 respectively.

The mechanism of CNT growth during the CVD process has been reported by several research groups most of which point out that the mechanism depends on the specific catalyst system and the reaction conditions.[22,49,50] It is well known that some transition metals, such as Fe, Co and Ni, have high catalytic activity for CNT growth. The general hypothesis which has been widely accepted is as follows: when hydrocarbon vapour (carbon feedstock) contacts with the metal NP at high temperature (normally 450 – 700 °C which is below the melting point of the bulk metal), the hydrocarbon decomposes into hydrogen and carbon. Hydrogen is removed by the flow of a carrier gas and the carbon dissolves into the metal. After reaching the carbon solubility limit at the high temperature, the carbon starts to precipitate at the metal surface forming graphitized structures such as graphite, carbon

filaments or CNTs depending on the particle size of catalyst and morphology of catalyst particle.[22,51] Fig. 1.7 illustrates two types of growth mechanism of CNTs that result from the process: tip growth and base growth. During the decomposition of the hydrocarbon, carbon diffuses through the catalyst. When the interaction between the catalyst particle and substrate is weak meaning that the contact angle between two substances is larger, it is easier for carbon to diffuse down to the base of the catalyst particle, and hence the precipitation can occur across the metal base. In the subsequent precipitation, the catalyst particle will be lifted up giving the "tip growth mechanism" (Fig. 1.7 (A)). When the interaction between the catalyst particle and substrate is strong and the contact angle between two substances is small, the precipitation across the metal base is not able to lift the catalyst particle up. However, the precipitation continuously occurs on the catalyst surface and the CNT emerges out from the top of the catalyst particle. A hemispherical dome will form first and then extend up as a graphitic carbon cylinder (Fig. 1.7 (B)). This is called the "base growth mechanism".[22]

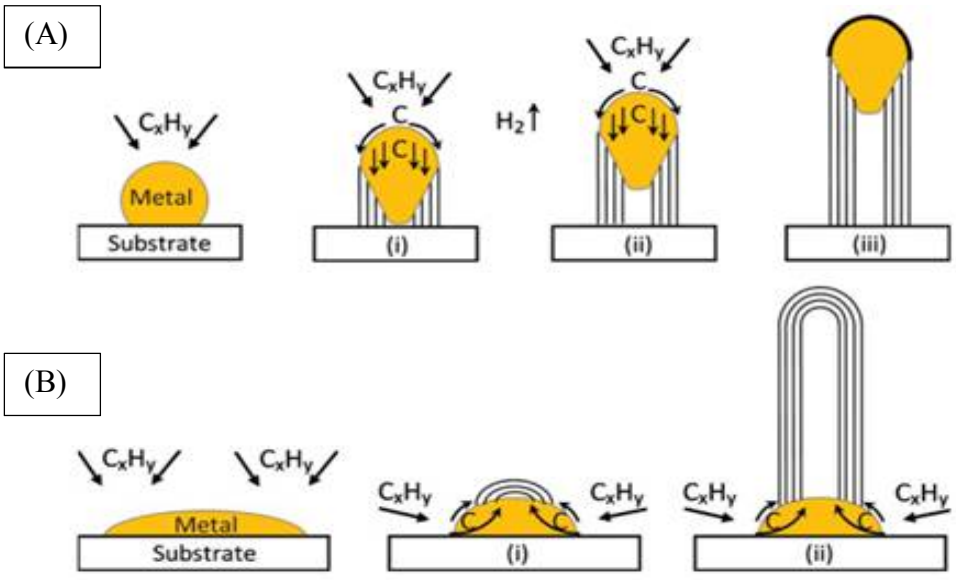

Fig. 1.7. An illustration of (A) tip growth mechanism and (B) base growth mechanism of CNT growth. Figure reproduced from reference 22 .

In a recent review, Kumar *et al.* indicated that SWCNTs preferentailly form on small metal NPs (diameter in a range between 1 and 2 nm) which has also been proven by Li *et al.* who successfully grew SWCNTs on the Fe NPs within this range of diameters.[22,52] However, SWCNTs are known to form on the larger metal NPs too (see later discussion of HiPco method). MWCNTs typically form on bigger metal NPs with diameter in a range between 5 and 20 nm).[22] Finally, the use metal NPs with diameters between 50 and 200 nm often results in formation of CNFs instead of CNTs.[53]

Raty *et al.* studied the early stages of SWCNT growth by using *ab initio* molecular dynamic simulations.[54] According to the explanation by Raty *et al.,* the surface of a small Fe NP (1 - 2 nm) is more curved than a bigger metal NP. When C atoms diffuse to the catalyst surface, they start to form sp^2 graphene sheets which consist of pentagons and hexagons of C. The surface curvature of such small Fe NPs makes it easier for the sp^2 graphene sheet to follow the shape of the top of the Fe NP and form a cap structure, and to continue the SWCNT growth (Fig. 1.8).

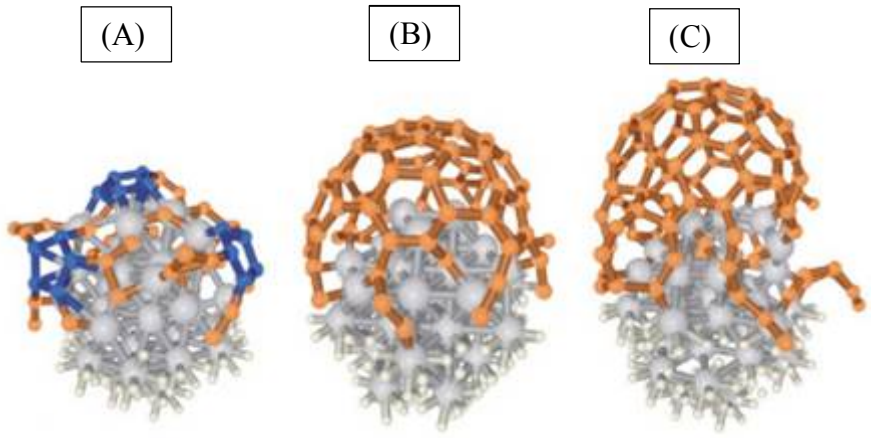

Fig. 1.8. Snapshots from *ab initio* simulations of early stages of SWCNT growth on 1 nm Fe catalyst. Fe atoms are represented in grey, carbon atoms in orange and blue, and hydrogen atoms in white. (A) After diffusion of C atoms on the metallic surface and formation of C-C bonds, pentagons and hexagons of C appear on the surface (highlighted in blue). (B) Formation of a *sp2* graphene sheet floating on the catalyst surface which results in the subsequent SWCNT growth (C). Figure reproduced from reference 54.

Another method which can be used to synthesize SWCNT using relatively large metal NPs (15-30 nm) is the high pressure carbon monoxide (CO) method (also known as the HiPco method).[55] This method is carried out by flowing $CO_{(g)}$ mixed with a small amount of powder containing a catalyst compound (*i.e.* $Fe(CO)_5$ or Ni acetylacetonate) through a heated tube furnace. A high pressure (30 – 50 atm) and a high temperature (900 – 1216 ºC) are required for disproportionation of CO (eq. 1), so that the C vapour can be generated. The precipitation rate of C is the key parameter which determines the formation of either carbon onions (spherical structures that cover the metal NPs) or SWCNTs.[56,57] However, the reason why SWCNTs can grow on such large metal NPs using this strategy is still unclear.[55] The drawbacks of this method include the inability of forming arrays of ordered CNTs on a substrate and the high cost of the process coming from the high reaction temperature.[56,57]

$$CO_{(g)} + CO_{(g)} \rightarrow C_{(vapour)} + CO_{2(g)} \quad \text{(eq. 1)}$$

For the case of MWCNT growth on a bigger metal NP (5- 20 nm), Hofmann *et al.* observed the MWCNT growth by using *in-situ* TEM.[58] They also proposed that the metal NP becomes "liquid-like" and the shape is elongated at a high temperature (700 ºC in the case of MWCNT growth on Ni NP) as shown in Fig. 1.9 (A).[58] The sharpness of the boundary (carbon and metallic metal surface) decreases as more atomic steps are formed which results in the formation of multi layers of graphene on each atomic step as shown Fig. 1.9 (B) and (C). Kumar *et al.* also mentioned that CNTs cannot grow on a too big metal NP (*viz* 100 nm) because the boundary will become almost spherical at a high temperature with nearly no existence of stair-like atomic steps as shown in Fig. 1.9 (C).[22]

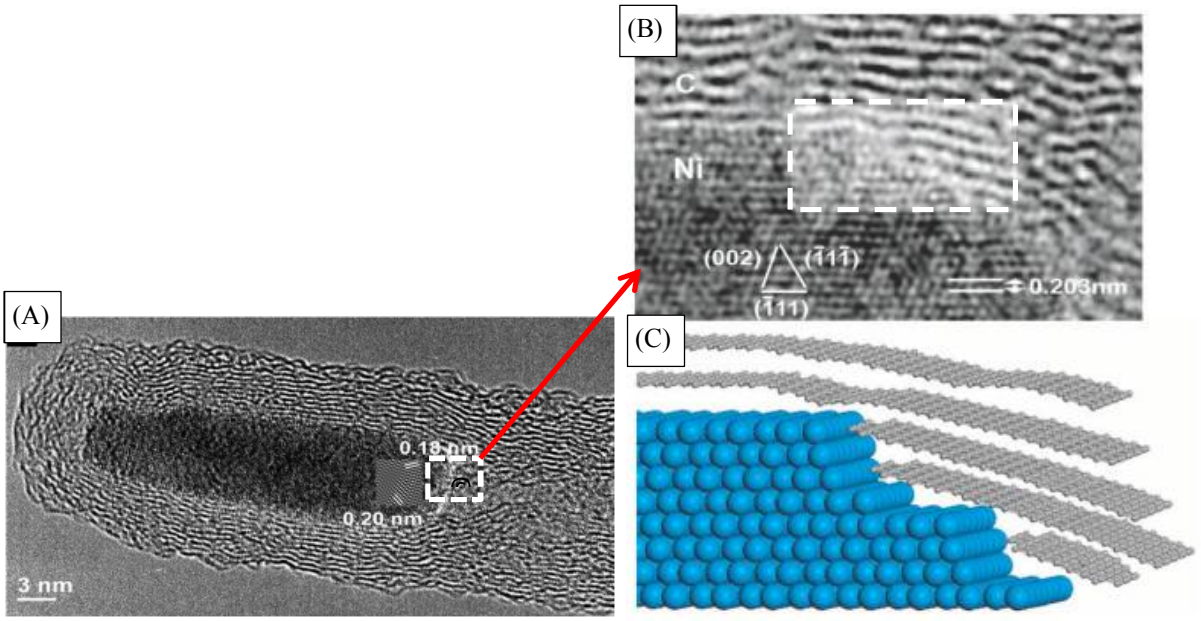

Fig. 1.9. (A) TEM image of the tip region of a Ni-catalyzed MWCNT. The face-centered cubic (fcc) Ni particle is imaged in the [110] projection. The inset shows a Fourier-filtered image of the lattice. (B) TEM image of Ni - C interface (as the area highlighted in (A)) at the tip of a MWCNT and (C) Schematic ball-and-stick model of area highlighted in (B). Figure reproduced from reference 58.

Many synthesis methods such as arc discharge, laser ablation and chemical vapour deposition can be used for the synthesis of CNTs.[23,22] The metal catalyst-mediated CVD method is a convenient and popular technique where a carbon feedstock is supplied to the catalyst in a controlled fashion *via* the gas phase.[59,22] The CVD methodology offers excellent flexibility and control over nanotube fabrication conditions *via* temperature programming, process duration, combinations and flow rates of various gases (carbon source *e.g.* C_2H_2, CH_4 *etc.*; etching agent, *e.g.* H_2, H_2O, NH_3 *etc.*; carrier gas, *e.g.* N_2, Ar, He) and choice of a catalyst system.[59,22]

1.4 ZnO nanorods and nanowires

ZnO has a hexagonal wurtzite structure (Fig. 1.10) with a lattice constant "a" in the basal plane (0.325 nm) and a unit vector "c" along the [0001] direction (0.5201 nm) as shown in Fig. 1.11.[60,61] Each Zn^{2+} ion bonds with four O^{2-} ions forming a tetrahedron representing a structure which can be described as a number of alternating planes of Zn and O ions stacking along the [0001] direction (Fig. 1.10).[60] For the purpose of growing vertically aligned ZnO NWs on a substrate, it is important to choose a substrate which has a similar lattice structure with that of ZnO enabling epitaxial growth (*e.g.* deposition of a crystalline structure overlay onto another crystalline substrate in an ordered manner).[62] More details related to the type of substrate for ZnO NW growth will be discussed in Chapter 5.

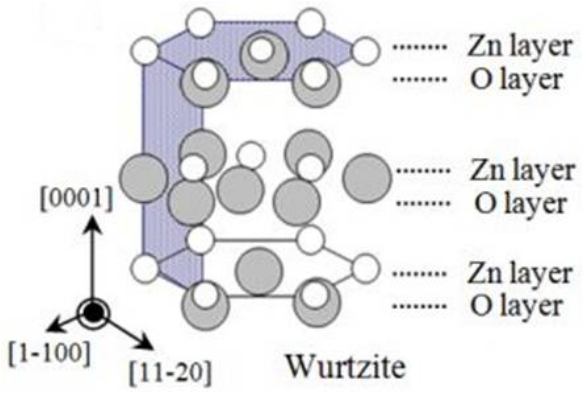

Fig. 1.10. Schematic structure of ZnO with a stacking sequence of Zn (white circles) and O layers (grey circles). Figure reproduced from reference 60.

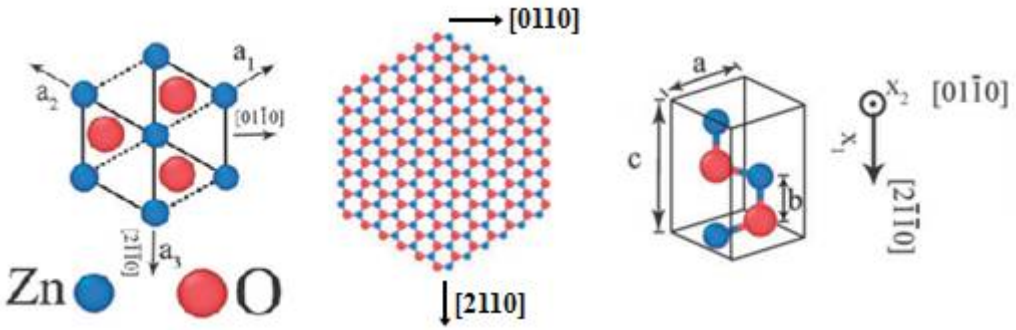

Fig. 1.11. Crystal structure and geometry of 1D ZnO nanostructures. Figure reproduced from reference 61.

Since Thomas reported the exciton spectrum of ZnO crystals in 1960 demonstrating a high exciton binding energy (60 meV) and a direct band gap (3.37 eV) defining ZnO as a semiconductor material.[63] This report revealed the potential utilization of its excitonic effect at room temperature. The direct band gap means that an electron can shift between the lowest-energy state in the conduction band and the highest-energy state in the valence band without changing in crystal momentum (Fig. 1.12).[64] In 1997, Zu *et al*. first observed the spontaneous and stimulated UV emission from ZnO thin films which raised interest in studying the optoelectronic properties of ZnO.[65]

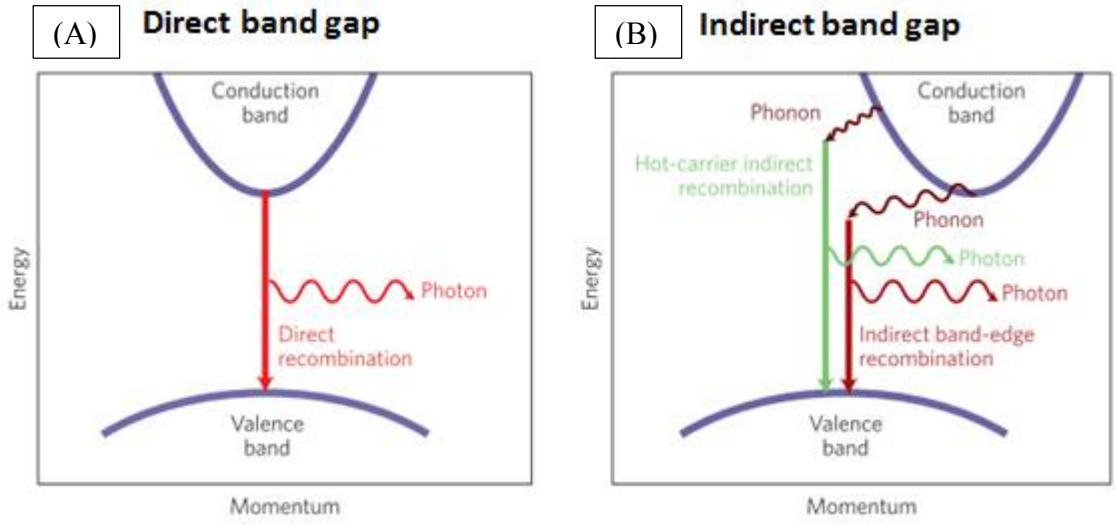

Fig. 1.12. (A) Direct band gap and (B) indirect band gap. Figures reproduced from reference 64.

With the increased attention to the fabrication of nanostructured semiconducting materials, including ZnO, various fabrication methods for ZnO nanorods and NWs have been widely studied, for example, solution phase synthesis, electrochemical synthesis and vapour phase synthesis.[66,67,68] A well-known hydrothermal method is usually carried out by coating ZnO NPs onto a substrate and reacting with a mixture solution containing a base (*i.e.* NaOH or hexamethylenetetramine) and Zn^{2+} salt (*i.e.* $Zn(NO_3)_2$ or $ZnCl_2$) at a temperature around 200 ºC.[66] The advantages of using solution phase synthesis include low cost, low temperature, scalability and ease of handling.[66] However, for the needs of fabricating a highly ordered array of ZnO NWs, electrochemical synthesis or vapour phase synthesis are the better options.[67,68] Li *et al*. demonstrated an electrochemical method by utilising a free-standing PAA membrane with a layer of Au on one side as a template. The fabrication of ZnO nanorods was carried out by electrodepositing Zn into the PAA template and reoxidising the deposited Zn NWs.[67] Growth of ZnO NWs *via* vapour phase synthesis is normally carried out in a closed chamber with a gaseous enviroment.[66]

In vapour phase synthesis, vapour can be generated by thermal evaporation, chemical reduction and laser ablation.[69,70,71] Thermal evaporation has been carried out by heating high purity Zn powder to a high temperature (750 ºC) to generate Zn vapour. Zn vapour is oxidised by purging into $O_{2(g)}$ and ZnO is condensed on a substrate while the furnace is cooled down. A typical chemical method involves heating a mixture of ZnO and graphite powder at a high temperature (900 ºC - 1200 ºC) to reduce ZnO to Zn vapour (equations 2 and 3).[72]

$$ZnO_{(s)} + C_{(s)} \rightarrow Zn_{(vapour)} + CO_{(g)} \qquad \text{(eq. 2)}$$

$$ZnO_{(s)} + C_{(s)} \rightarrow Zn_{(vapour)} + CO_{2(g)} \qquad \text{(eq. 3)}$$

Zn vapour is oxidised by purging into $O_{2(g)}$ and condensed to give ZnO.[70] In the case of growing ZnO nanowires *via* the VLS mechanism, metal NPs immobilised on a substrate act as the catalyst. Zn or ZnO vapour is delivered onto the substrate and react with the catalyst metal NPs following the VLS mechanism. The whole process including generating Zn or ZnO vapour and growth of ZnO nanowire can be carried out by using many techniques such as CVD, molecular beam epitaxy (MBE) and PLD.[73,74 ,75]In this thesis, PLD was used for generating ZnO vapour and a catalyst system was fabricated by controlled deposition of Au colloids with known size onto atomically well-defined sapphire substrates. This work is discussed in Chapter 5.

1.5 Thesis aims and organization

The aim of this thesis work is to fabricate catalyst systems with size controllable catalyst metal NPs using different strategies. The strategies were designed to prevent the aggregation of metal NPs at high temperature prior to the growth of CNTs and ZnO NWs. Ultimately, the diameter of CNTs and ZnO NWs can be controlled *via* control over the size of the catalyst metal NPs. The thesis is organised as follows.

Chapter 1: Introduction.

Chapter 2: General experimental; general description of the materials, chemicals and equipment relevant to the work presented in this thesis.

Chapter 3: Design and fabrication of porous anodic alumina (PAA) templates: describes the optimisation of fabrication of PAA templates which can improve the efficiency of electrodepositing Co NP within the pores of the template for subsequent CNT growth by CVD.

Chapter 4: Optimisation of the procedures and conditions of the electrodeposition of Co within pores of PAA template: the optimisation of the electrodeposition of Co to improved the coverage and uniformity of Co NPs is reflected in the quality of CNT growth. Moreover, this chapter also demonstrates that the diameters of CNTs can be controlled by adjusting the Co electrodeposition time. This work has been published in RSC Advances (Ke, N. J.; Downard, A. J.; Golovko, V. B., Carbon nanotube diameter control via catalytic Co nanoparticles electrodeposited in porous alumina membranes. *RSC Advances* **2015,** *5* (33), 25747-25754).

Chapter 5: Growth of ZnO nanorods catalysed by gold colloids using pulsed laser deposition: develop a unique strategy for chemically fabricating a catalyst system for growing ZnO nanorods using PLD. This work was a collaboration with Dr. Martin Allen and his student Max Lynam from Electric and Computer Engineering Department, University of Canterbury.

1.6 References

1. Kolasinski, K. K., *Surface Science: Foundations of Catalysis and Nanoscience*. John Wiley & Sons: Hoboken, 2012.
2. Polshettiwar, V.; Basset, J. M.; Astruc, D., Nanoscience Makes Catalysis Greener. *Chemsuschem* **2012,** *5* (1), 6-8.
3. Van Hove, M. A., From surface science to nanotechnology. *Catalysis Today* **2006,** *113* (3–4), 133-140.
4. Baughman, R. H.; Zakhidov, A. A.; de Heer, W. A., Carbon nanotubes - the route toward applications. *Science* **2002,** *297* (5582), 787-792.
5. Chapter 1 Carbon Nanotubes. In *Nanotubes and Nanowires (2)*, The Royal Society of Chemistry: 2011; pp 1-242.
6. Chapter 2 Inorganic Nanotubes. In *Nanotubes and Nanowires (2)*, The Royal Society of Chemistry: 2011; pp 243-342.
7. Wilcoxon, J. P.; Williamson, R. L.; Baughman, R., Optical properties of gold colloids formed in inverse micelles. *J. Chem. Phys.* **1993,** *98* (12), 9933-9950.
8. Steigerwald, M. L.; Brus, L. E., Semiconductor Crystallites - a class of large molecules. *Acc. Chem. Res.* **1990,** *23* (6), 183-188.
9. Niu, Y. H.; Crooks, R. M., Preparation of dendrimer-encapsulated metal nanoparticles using organic solvents. *Chem. Mater.* **2003,** *15* (18), 3463-3467.
10. Grabar, K. C.; Freeman, R. G.; Hommer, M. B.; Natan, M. J., Preparation and charaterization of Au colloid monolayers. *Anal. Chem.* **1995,** *67* (4), 735-743.
11. Huh, Y.; Green, M. L. H.; Kim, Y. H.; Lee, J. Y.; Lee, C. J., Control of carbon nanotube growth using cobalt nanoparticles as catalyst. *Appl. Surf. Sci.* **2005,** *249* (1–4), 145-150.
12. Henley, S. J.; Carey, J. D.; Silva, S. R. P., Pulsed-laser-induced nanoscale island formation in thin metal-on-oxide films. *Phys. Rev. B* **2005,** *72* (19), 10.
13. Belic, D.; Chantry, R. L.; Li, Z. Y.; Brown, S. A., Ag-Au nanoclusters: Structure and phase segregation. *Appl. Phys. Lett.* **2011,** *99* (17), 3.
14. Jeong, S.-H.; Hwang, H.-Y.; Hwang, S.-K.; Lee, K.-H., Carbon nanotubes based on anodic aluminum oxide nano-template. *Carbon* **2004,** *42* (10), 2073-2080.
15. Cheng, H. P.; Landman, U., Controlled deposition, soft landing, and glass-formation in nanocluster-surface collisions. *Science* **1993,** *260* (5112), 1304-1307.
16. Sun, M.; Zangari, G.; Shamsuzzoha, M.; Metzger, R. M., Electrodeposition of highly uniform magnetic nanoparticle arrays in ordered alumite. *Appl. Phys. Lett.* **2001,** *78* (19), 2964-2966.
17. Wei, Y. Y.; Eres, G.; Merkulov, V. I.; Lowndes, D. H., Effect of catalyst film thickness on carbon nanotube growth by selective area chemical vapor deposition. *Appl. Phys. Lett.* **2001,** *78* (10), 1394-1396.
18. Dalal, S. H.; Baptista, D. L.; Teo, K. B. K.; Lacerda, R. G.; Jefferson, D. A.; Milne, W. I., Controllable growth of vertically aligned zinc oxide nanowires using vapour deposition. *Nanotechnology* **2006,** *17* (19), 4811-4818.
19. Cao, A.; Lu, R.; Veser, G., Stabilizing metal nanoparticles for heterogeneous catalysis. *PCCP* **2010,** *12* (41), 13499-13510.
20. Swihart, M. T., Vapor-phase synthesis of nanoparticles. *Curr. Opin. Colloid Interface Sci.* **2003,** *8* (1), 127-133.
21. Dai, H., Carbon nanotubes: opportunities and challenges. *Surf. Sci.* **2002,** *500* (1–3), 218-241.

22. Kumar, M.; Ando, Y., Chemical vapor deposition of carbon nanotubes: a review on growth mechanism and mass production. *J. Nanosci. Nanotechnol.* **2010,** *10* (6), 3739-3758.
23. Prasek, J.; Drbohlavova, J.; Chomoucka, J.; Hubalek, J.; Jasek, O.; Adam, V.; Kizek, R., Methods for carbon nanotubes synthesis-review. *J. Mater. Chem.* **2011,** *21* (40), 15872-15884.
24. Morales, A. M.; Lieber, C. M., A laser ablation method for the synthesis of crystalline semiconductor nanowires. *Science* **1998,** *279* (5348), 208-211.
25. Han, C.; Xiang, D.; Zheng, M. R.; Lin, J. D.; Zhong, J. Q.; Sow, C. H.; Chen, W., Tuning the electronic properties of ZnO nanowire field effect transistors via surface functionalization. *Nanotechnology* **2015,** *26* (9), 6.
26. Haynes, C. L.; McFarland, A. D.; Zhao, L.; Van Duyne, R. P.; Schatz, G. C.; Gunnarsson, L.; Prikulis, J.; Kasemo, B.; Käll, M., Nanoparticle Optics: The Importance of Radiative Dipole Coupling in Two-Dimensional Nanoparticle Arrays†. *J. Phys. Chem. B* **2003,** *107* (30), 7337-7342.
27. Hicks, E. M.; Zou, S. L.; Schatz, G. C.; Spears, K. G.; Van Duyne, R. P.; Gunnarsson, L.; Rindzevicius, T.; Kasemo, B.; Kall, M., Controlling plasmon line shapes through diffractive coupling in linear arrays of cylindrical nanoparticles fabricated by electron beam lithography. *Nano Lett.* **2005,** *5* (6), 1065-1070.
28. Wang, X. D.; Summers, C. J.; Wang, Z. L., Large-scale hexagonal-patterned growth of aligned ZnO nanorods for nano-optoelectronics and nanosensor arrays. *Nano Lett.* **2004,** *4* (3), 423-426.
29. Oh, Y. J.; Ross, C. A.; Jung, Y. S.; Wang, Y.; Thompson, C. V., Cobalt Nanoparticle Arrays made by Templated Solid-State Dewetting. *Small* **2009,** *5* (7), 860-865.
30. Rana, K.; Kucukayan-Dogu, G.; Bengu, E., Growth of vertically aligned carbon nanotubes over self-ordered nano-porous alumina films and their surface properties. *Appl. Surf. Sci.* **2012,** *258* (18), 7112-7117.
31. Wagner, R. S.; Ellis, W. C., Vapor-Liquid-Solid mechanism of single crystal growth. *Appl. Phys. Lett.* **1964,** *4* (5), 89-90.
32. Lu, W.; Lieber, C. M., Semiconductor nanowires. *J. Phys. D-Appl. Phys.* **2006,** *39* (21), R387-R406.
33. Monthioux, M.; Kuznetsov, V. L., Who should be given the credit for the discovery of carbon nanotubes? *Carbon* **2006,** *44* (9), 1621-1623.
34. Radushkevich, L. V.; Lukyanovich, V. M., About the structure of carbon formed by thermal decomposition of carbon monoxide on iron substrate. *Zurn Fis Chim* **1952,** *26*, 88-95.
35. Abrahamson, J., The surface energies of graphite. *Carbon* **1973,** *11* (4), 337-362.
36. Abrahamson, J., Graphite sublimation temperatures, carbon arcs and crystallite erosion. *Carbon* **1974,** *12* (2), 111-141.
37. Wiles, P. G.; Abrahamson, J., Carbon fibre layers on arc electrodes—I: Their properties and cool-down behaviour. *Carbon* **1978,** *16* (5), 341-349.
38. Abrahamson, J.; Maclagan, R. G. A. R., Theoretical studies of interstitials in graphite. *Carbon* **1984,** *22* (3), 291-295.
39. Iijima, S., Helical microtubules of graphitic carbon. *Nature* **1991,** *354* (6348), 56-58.
40. Iijima, S.; Ichihashi, T., Single-shell carbon nanotubes of 1 nm diameter. *Nature* **1993,** *363* (6430), 603-605.
41. Bethune, D. S.; Kiang, C. H.; Devries, M. S.; Gorman, G.; Savoy, R.; Vazquez, J.; Beyers, R., Cobalt-Catalyzed growth of carbon nanotubes with single-atomic-layerwalls. *Nature* **1993,** *363* (6430), 605-607.
42. Cheung, C. L.; Hafner, J. H.; Lieber, C. M., Carbon nanotube atomic force microscopy tips: Direct growth by chemical vapor deposition and application to high-resolution imaging. *Proc. Natl. Acad. Sci. U. S. A.* **2000,** *97* (8), 3809-3813.

43. Choi, W. B.; Chung, D. S.; Kang, J. H.; Kim, H. Y.; Jin, Y. W.; Han, I. T.; Lee, Y. H.; Jung, J. E.; Lee, N. S.; Park, G. S.; Kim, J. M., Fully sealed, high-brightness carbon-nanotube field-emission display. *Appl. Phys. Lett.* **1999,** *75* (20), 3129-3131.
44. Chen, Y. S.; Huang, J. H.; Chuang, C. C., Glucose biosensor based on multiwalled carbon nanotubes grown directly on Si. *Carbon* **2009,** *47* (13), 3106-3112.
45. Saito, R.; Fujita, M.; Dresselhaus, G.; Dresselhaus, M. S., Electronic-structure of chiral graphene tubules. *Appl. Phys. Lett.* **1992,** *60* (18), 2204-2206.
46. Serp, P.; Corrias, M.; Kalck, P., Carbon nanotubes and nanofibers in catalysis. *Appl. Catal., A* **2003,** *253* (2), 337-358.
47. Choudhary, V.; Gupta, A., *Polymer/Carbon Nanotube Nanocomposites*. 2011.
48. Sato, Y.; Shibata, K.-i.; Kataoka, H.; Ogino, S.-i.; Bunshi, F.; Yokoyama, A.; Tamura, K.; Akasaka, T.; Uo, M.; Motomiya, K.; Jeyadevan, B.; Hatakeyama, R.; Watari, F.; Tohji, K., Strict preparation and evaluation of water-soluble hat-stacked carbon nanofibers for biomedical application and their high biocompatibility: influence of nanofiber-surface functional groups on cytotoxicity. *Mol. Biosyst.* **2005,** *1* (2), 142-145.
49. Zaretskiy, S. N.; Hong, Y. K.; Ha, D. H.; Yoon, J. H.; Cheon, J.; Koo, J. Y., Growth of carbon nanotubes from Co nanoparticles and C2H2 by thermal chemical vapor deposition. *Chem. Phys. Lett.* **2003,** *372* (1-2), 300-305.
50. Brukh, R.; Mitra, S., Mechanism of carbon nanotube growth by CVD. *Chem. Phys. Lett.* **2006,** *424* (1–3), 126-132.
51. Esconjauregui, S.; Whelan, C. M.; Maex, K., The reasons why metals catalyze the nucleation and growth of carbon nanotubes and other carbon nanomorphologies. *Carbon* **2009,** *47* (3), 659-669.
52. Li, Y. M.; Kim, W.; Zhang, Y. G.; Rolandi, M.; Wang, D. W.; Dai, H. J., Growth of single-walled carbon nanotubes from discrete catalytic nanoparticles of various sizes. *J. Phys. Chem. B* **2001,** *105* (46), 11424-11431.
53. Kim, Y.-A.; Hayashi, T.; Naokawa, S.; Yanagisawa, T.; Endo, M., Comparative study of herringbone and stacked-cup carbon nanofibers. *Carbon* **2005,** *43* (14), 3005-3008.
54. Raty, J. Y.; Gygi, F.; Galli, G., Growth of carbon nanotubes on metal nanoparticles: A microscopic mechanism from ab initio molecular dynamics simulations. *Phys. Rev. Lett.* **2005,** *95* (9), 4.
55. Moisala, A.; Nasibulin, A. G.; Kauppinen, E. I., The role of metal nanoparticles in the catalytic production of single-walled carbon nanotubes - a review. *J. Phys.-Condes. Matter* **2003,** *15* (42), S3011-S3035.
56. Nasibulin, A. G.; Moisala, A.; Brown, D. P.; Kauppinen, E. I., Carbon nanotubes and onions from carbon monoxide using Ni(acac)2 and Cu(acac)2 as catalyst precursors. *Carbon* **2003,** *41* (14), 2711-2724.
57. Nikolaev, P., Gas-phase production of single-walled carbon nanotubes from carbon monoxide: A review of the HiPco process. *J. Nanosci. Nanotechnol.* **2004,** *4* (4), 307-316.
58. Hofmann, S.; Sharma, R.; Ducati, C.; Du, G.; Mattevi, C.; Cepek, C.; Cantoro, M.; Pisana, S.; Parvez, A.; Cervantes-Sodi, F.; Ferrari, A. C.; Dunin-Borkowski, R.; Lizzit, S.; Petaccia, L.; Goldoni, A.; Robertson, J., In situ observations of catalyst dynamics during surface-bound carbon nanotube nucleation. *Nano Lett.* **2007,** *7* (3), 602-608.
59. Terranova, M. L.; Sessa, V.; Rossi, M., The world of carbon nanotubes: An overview of CVD growth methodologies. *Chem. Vapor Depos.* **2006,** *12* (6), 315-325.
60. Matsui, H.; Tabata, H., *Lateral Surface Nanowires and Quantum Structures Based on ZnO*. 2010.
61. Momeni, K.; Attariani, H., Electromechanical properties of 1D ZnO nanostructures: nanopiezotronics building blocks, surface and size-scale effects. *PCCP* **2014,** *16* (10), 4522-4527.

62. Triboulet, R.; Perriere, J., Epitaxial growth of ZnO films. *Prog. Cryst. Growth Charact. Mater.* **2003,** *47* (2-3), 65-138.
63. Thomas, D. G., The exciton spectrum of zinc oxide. *J. Phys. Chem. Solids* **1960,** *15* (1–2), 86-96.
64. Fujita, M., Silicon photonics: Nanocavity brightens silicon. *Nat Photon* **2013,** *7* (4), 264-265.
65. Zu, P.; Tang, Z. K.; Wong, G. K. L.; Kawasaki, M.; Ohtomo, A.; Koinuma, H.; Segawa, Y., Ultraviolet spontaneous and stimulated emissions from ZnO microcrystallite thin films at room temperature. *Solid State Commun.* **1997,** *103* (8), 459-463.
66. Zhang, Y. Y.; Ram, M. K.; Stefanakos, E. K.; Goswami, D. Y., Synthesis, Characterization, and Applications of ZnO Nanowires. *J. Nanomater.* **2012**, 22.
67. Li, Y.; Cheng, G. S.; Zhang, L. D., Fabrication of highly ordered ZnO nanowire arrays in anodic alumina membranes. *J. Mater. Res.* **2000,** *15* (11), 2305-2308.
68. Amarilio-Burshtein, I.; Tamir, S.; Lifshitz, Y., Growth modes of ZnO nanostructures from laser ablation. *Appl. Phys. Lett.* **2010,** *96* (10), 3.
69. Liu, P.; Li, Y. B.; Guo, Y. Q.; Zhang, Z. H., Growth of catalyst-free high-quality ZnO nanowires by thermal evaporation under air ambient. *Nanoscale Res. Lett.* **2012,** *7*, 3.
70. Zhou, Z. H.; Zhan, C. H.; Wang, Y. Y.; Su, Y. J.; Yang, Z.; Zhang, Y. F., Rapid mass production of ZnO nanowires by a modified carbothermal reduction method. *Mater. Lett.* **2011,** *65* (5), 832-835.
71. Weigand, C.; Tveit, J.; Ladam, C.; Holmestad, R.; Grepstad, J.; Weman, H., Epitaxial relationships of ZnO nanostructures grown by Au-assisted pulsed laser deposition on c- and a-plane sapphire. *J. Cryst. Growth* **2012,** *355* (1), 52-58.
72. Burshtein, G.; Lumelsky, V.; Lifshitz, Y., ZnO nanowires growth via reduction of ZnO powder by H-2. *Nanotechnology* **2015,** *26* (12), 8.
73. Zhang, Z.; Wang, S. J.; Yu, T.; Wu, T., Controlling the growth mechanism of ZnO nanowires by selecting catalysts. *J. Phys. Chem. C* **2007,** *111* (47), 17500-17505.
74. Heo, Y. W.; Varadarajan, V.; Kaufman, M.; Kim, K.; Norton, D. P.; Ren, F.; Fleming, P. H., Site-specific growth of Zno nanorods using catalysis-driven molecular-beam epitaxy. *Appl. Phys. Lett.* **2002,** *81* (16), 3046-3048.
75. Cao, B. Q.; Lorenz, M.; Rahm, A.; von Wenckstern, H.; Czekalla, C.; Lenzner, J.; Benndorf, G.; Grundmann, M., Phosphorus acceptor doped ZnO nanowires prepared by pulsed-laser deposition. *Nanotechnology* **2007,** *18* (45), 5.

Chapter 2. General Experimental

This chapter provides the *general* description of the materials, chemicals and equipment relevant to the work presented in this thesis. The description of the details of the specific experimental procedures *etc*. will be provided in the following chapters.

2.1 General synthesis and reagents

2.1.1 Reagents, gases and substrates

The reagents, gases and substrates which have been used in this thesis and not described elsewhere are listed here in alphabetical order. The chemical formulae, purity or grade (if known) and manufacturer are included in the brackets for each compound.

Reagents: acetone ($(CH_3)_2CO$, AR grade, BDH), 3-aminopropyltrimethoxysilane ($H_2N(CH_2)_3Si(OCH_3)_3$, 97 %, Sigma-Aldrich), aluminium nitrate ($Al(NO_3)_3{\cdot}9H_2O$, CP, BDH), chromium trioxide (CrO_3, CR, BDH), boric acid (H_3BO_3, CP, BDH), cobalt sulfate heptahydrate ($CoSO_4{\cdot}7H_2O$, CP, BDH), cupric dichloride ($CuCl_2{\cdot}2H_2O$, AR, BDH), ethanol (C_2H_5OH, AR, BDH), gold(III) chloride trihydrate ($HAuCl_4{\cdot}3H_2O$, ≥ 99.9 % trace metals basis, Sigma-Aldrich), methanol (CH_3OH, AR, BDH) oxalic acid ($H_2C_2O_4$, AR, BDH), hydrochloric acid (HCl, Riedel-de Haen AG Seelze-Hannover), perchloric acid ($HClO_4$, , 65 wt.% in H_2O, BDH), phosphoric acid (H_3PO_4, 90 wt. % in H_2O, AR, BDH), sodium borohydride ($NaBH_4$, Fischer Scientific), sodium hydroxide (NaOH, AR, BDH), trichloroethylene (C_2HCl_3, AR, BDH).

Deionised (Milli-Q) water was used in all the experiments for making solutions.

Gases: acetylene gas (instrumental grade, BOC), argon gas (instrumental grade, BOC), hydrogen gas (instrumental grade, BOC).

Substrates: Al (99.9995 %, 0.5 mm thick, 100 mm × 100 mm, Alfa Aesar) and sapphire (>99.99 %, 1 mm thick, double-side polished, A, C, M and R planes, MTI corporation). The Al substrate was firstly cut into many discs with a diameter of 2 cm using a punch press (this cutting was performed by Danny Leonard from mechanical workshop, Department of Chemistry, UC). After cutting, the substrates were stored in a clean container. The sapphire substrate was spin coated with a layer of photoresist (AZ1518, MicroChemicals GmbH) using 3000 rpm of spin rate for 1 min in order to protect the surface during the cutting. Then, the sapphire substrate was cut into *ca*. 1 cm × 1 cm wafers with the size of using a diamond saw. Water was sprayed during the cutting process in order to reduce the frictional heat and capture the dust. Cutting was performed by Rob McGregor, glassblower of the Department of Chemistry, UC. After cutting, the sapphire substrates were cleaned by using acetone in order to wash off the photoresist and then dried under a flow of $N_{2(g)}$. Sapphire substrates were stored in a clean container.

2.2 Electrochemistry apparatus

2.2.1 Anodization cell setup

Porous Al_2O_3 membrane was fabricated by anodizing an Al foil disc. A 2 electrode cell was used for anodization as shown in Fig. 2.1 (A). Two electrodes (Teflon electrode assembly holding Al foil and a bulk graphite electrode) and a thermometer were fitted into a Teflon cap and placed on a 400 mL beaker which normally contained 200 mL of 0.4 M oxalic acid (pH 1.0) and a magnetic stirring bar in the bottom of the beaker. This beaker with two

electrode set-up was placed in another larger glass container (crystallization dish) which contained water and was used as thermal sink. The temperature of oxalic acid solution was controlled at 16 ± 1 ºC by constantly adding ice into the outer glass container (Fig. 2.1 (B)). The components of the Teflon assembly electrode are shown in Fig. 2.2. An Al disc was mounted in the centre of the holders (Fig 2.2) and contacted at the back by a graphite disc which is a graphite rod leading to the external contact. In order to prevent leakage of the electrolyte solution into inner space of the electrode assembly, two O-rings were installed in the front Teflon plate which is on the side facing toward to the Al disc and the Teflon electrode assembly was tightly sealed by using three nylon screws. A rubber band was attached between the top of Teflon holder and a brass screw at the end of the graphite rod (Fig. 2.2), to apply pressure and ensure contact between the graphite rod and the graphite disc. The two electrodes were connected to a power supply so that the graphite electrode was the cathode and the Teflon electrode assembly with Al foil was the anode. The Teflon cell cap and electrodes were made by Danny Leonard, mechanical workshop, Department of Chemistry, University of Canterbury. Specific details of the anodization process parameters are given in Chapter 3, p. 59.

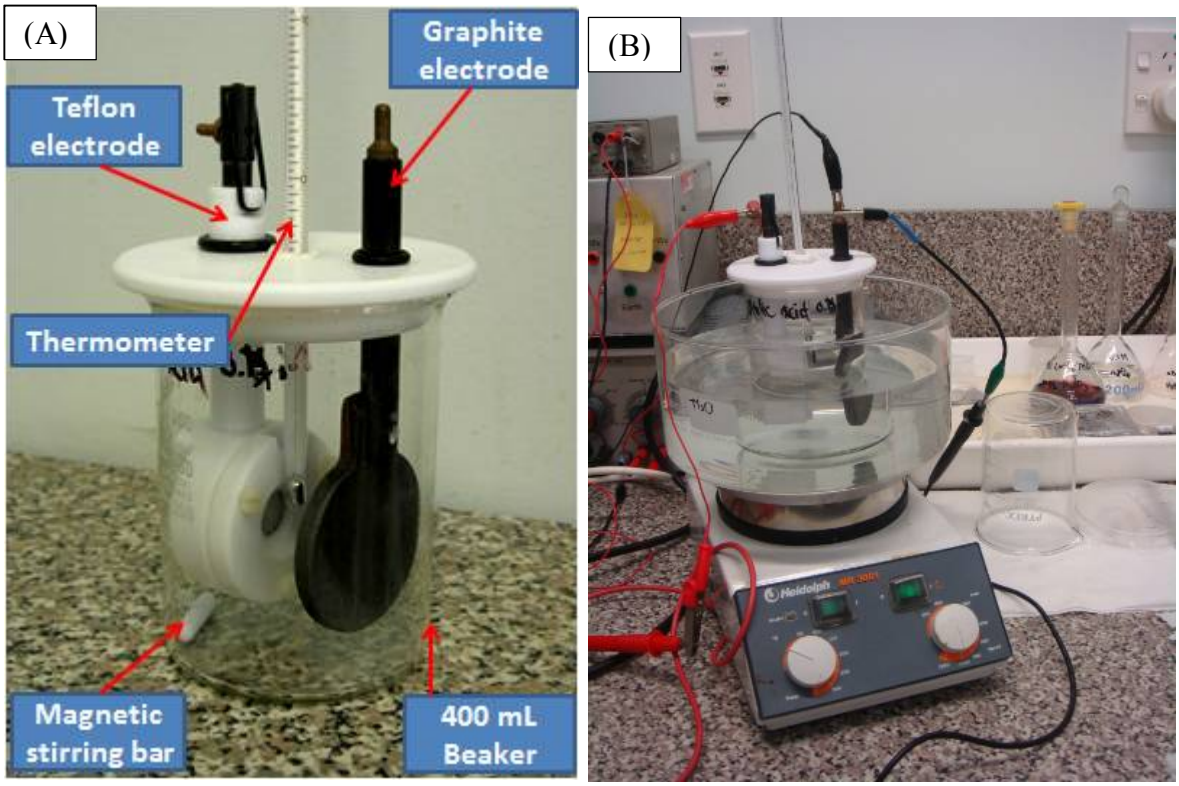

Fig. 2.1. (A) The anodization cell setup and (B) The final setup for anodization process.

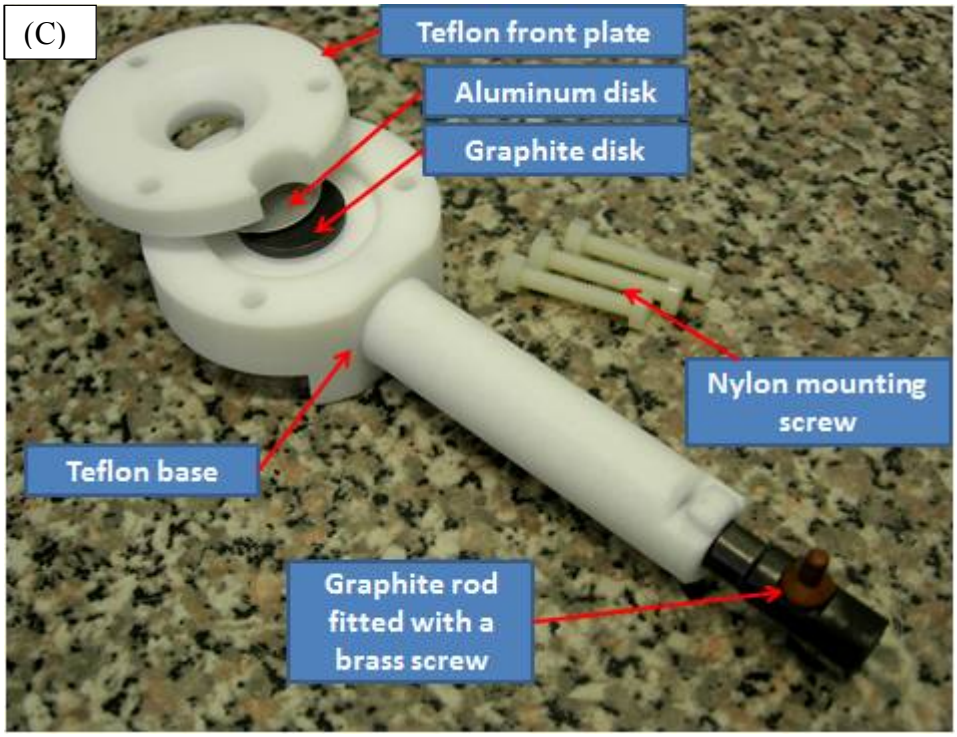

Fig. 2.2. Photo of the Teflon electrode assembly showing individual components.

2.2.2 Electrodeposition cell setup

Electrodeposition of Co NPs within pores of the PAA membrane was carried out in a 2 electrode pear-shaped glass cell as shown in Fig. 2.3. The cell with a hole of approximately 3 mm diameter at the bottom was placed on top of a PAA membrane (Fig. 2.3 (A)) and fastened to the base using springs. The PAA membrane (on quarter of a PAA disc) was positioned on top of a piece of Cu foil which was supported by a ceramic disc (Fig. 2.3 (B)). A viton O-ring formed the seal between the PAA mambrane and the cell. The ceramic disc provides a hard flat surface and was needed to prevent the deformation of the PAA sample during the cell assembly and electrodeposition. The Cu foil connection between the working electrode (PAA) and the external electrodeposition apparatus as shown in the following section. A Pt mesh electrode was inserted in the glass cell and used as the counter electrode.

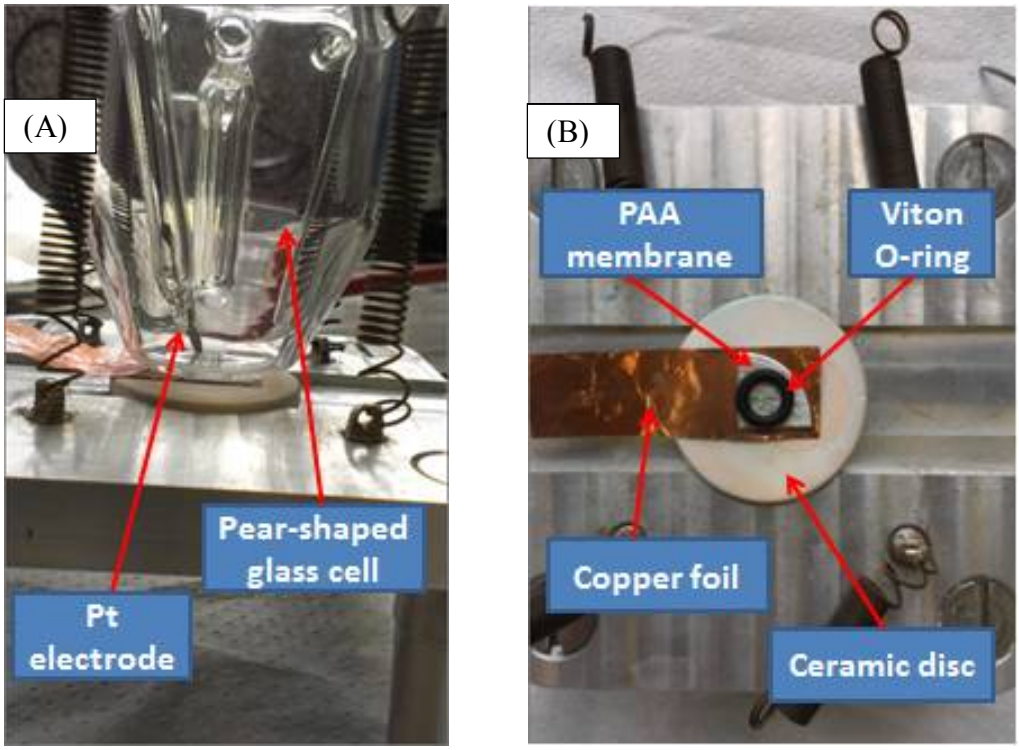

Fig. 2.3. Cell setup for electrodeposition of Co NPs within PAA membrane.

2.2.3 Electrodeposition apparatus

The programmable pulse generator (Fig. 2.4) was made by Steven Graham from the Electronics Workshop, Department of Chemistry, University of Canterbury. This pulse generator can generate a sequence of 10 ms (5 ms/5ms) pulses with adjustable amplitude (± 1.00 to 20.01 V) and the duration of either positive or negative sine wave is constant set up for 5 ms. The electrodeposition time can be adjusted from 10 ms to 30 min.

Fig. 2.4. The programmable pulse generator.

2.3 Vapour deposition apparatus

2.4.1 Chemical vapour deposition (CVD)

For CNT growth, a tube furnace (MTI OTF-1200X) with multi-channel gas flow ratio/pressure controller (MKS Type 647C) was used in this work (Fig. 2.5). The dual zone split furnace allows easy loading of the working tube when the furnace is open as well as precise to 1℃ dual zone temperature programming in the range of temperatures from the room temperature to 1100 ºC (note: the thermocouples are located within each hot zone, but

outside the quartz tube containing samples). The heating rate, the period of heating at a constant temperature and the cooling were programmed using the digital control panel on the tube furnace. Fig. 2.6 illustrates the inside of the tube furnace. Four heating coils are inside the furnace. The samples were put on a quartz boat (sample holder) and inserted into a quartz tube. The quartz tube was placed inside the open furnace so that the boats were placed at the positions corresponding to the location of the heating coils. The tube was sealed using flanges connected to the gas supply/exhaust lines ensuring tightness of fit via two O-rings at each side. The gas flow rates were controlled by the multi-channel gas flow ratio/pressure controller unit connected to a set of digital MKS flow controllers which ensured that known amounts of gas passed through the quartz tube. The flow controllers can control flow rates for H_2 in the range from 0 to 100 sccm, for C_2H_2 in the range from 0 to 500 sccm and for Ar in the range from 0 to 200 sccm.

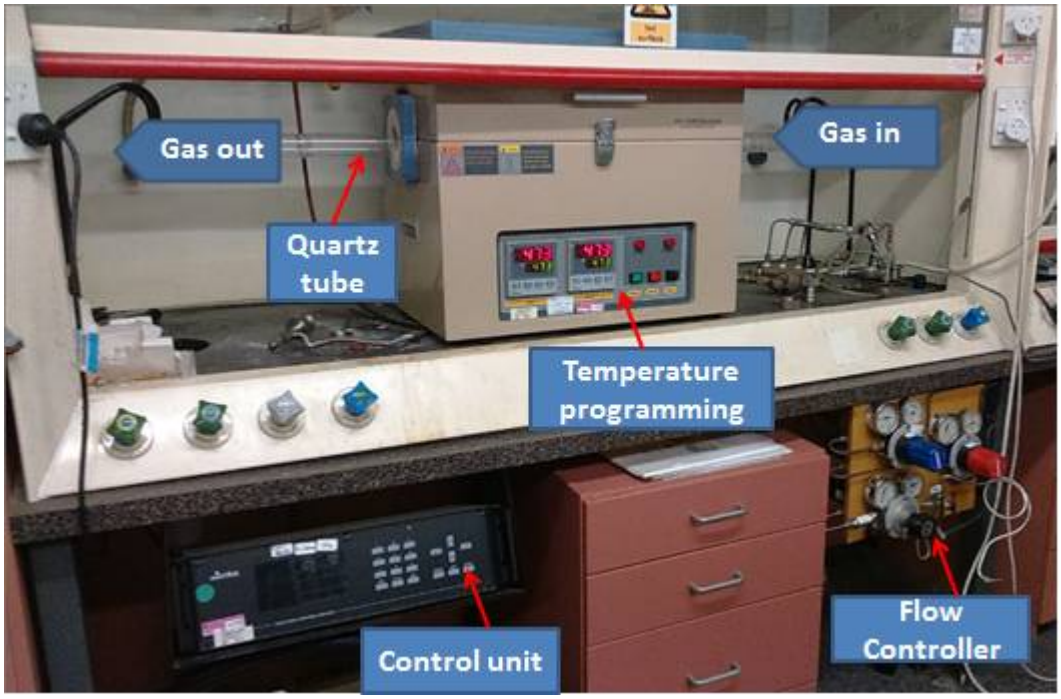

Fig. 2.5. Photograph of the thermal CVD system used in this work showing individual hardware components.

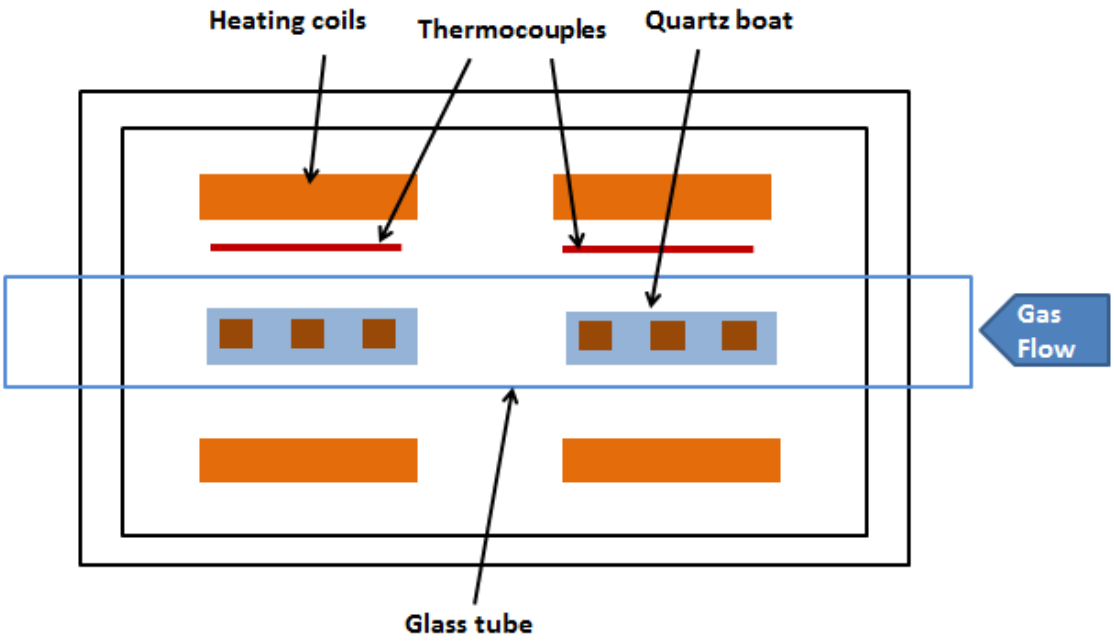

Fig. 2.6. Schematic diagram of the interior of the tube furnace.

2.4.2 Pulsed Laser Deposition (PLD) system

All PLD experiments were performed by PhD student Max Lynam supervised by Dr. Martin Allen (Department of Electrical and Computer Engineering, University of Canterbury). For ZnO nanorod growth, an excimer laser (Lamda physik, COMPex 205) with KrF radiation was used (the wavelength is 248 nm) to generate a pulsed flux of high energy photons (Fig. 2.7). The laser fluence was controlled by using a focusing lens with f = 750 nm to procedure a "spot" of *ca*. 2.5 mm^2. The incident energy focusing on a rotating ceramic ZnO target (ZnO 99.9 % purity from Kurt J Lesker Company) was 100 mJ/pulse. The ZnO target and samples are placed in the PLD chamber as shown in (Fig. 2.8).

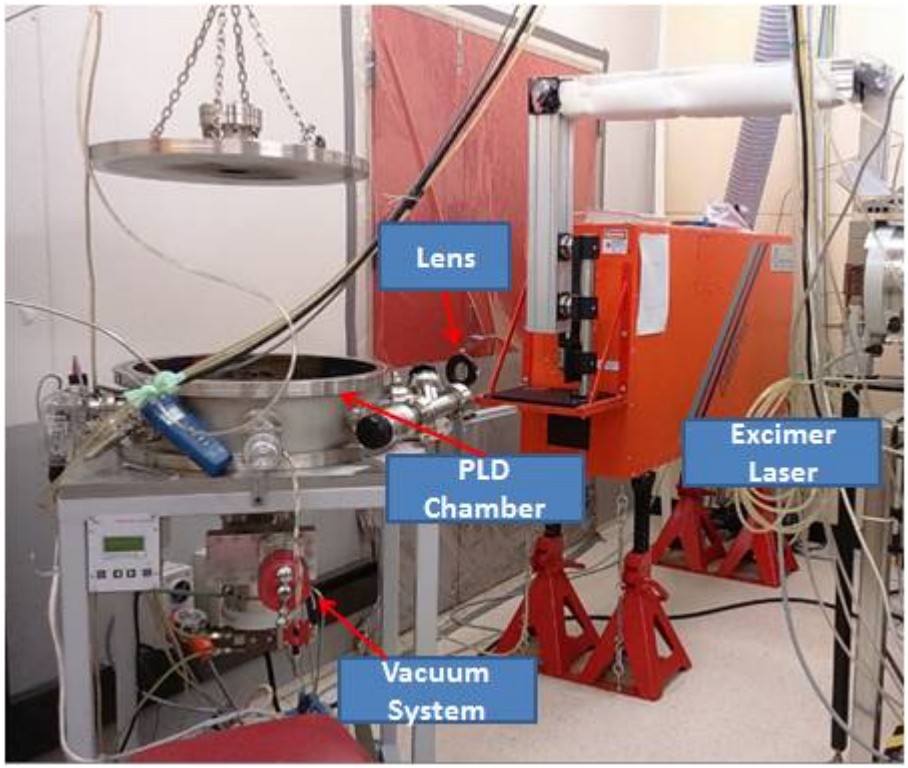

Fig. 2.7. The PLD system used for ZnO nanorod growth.

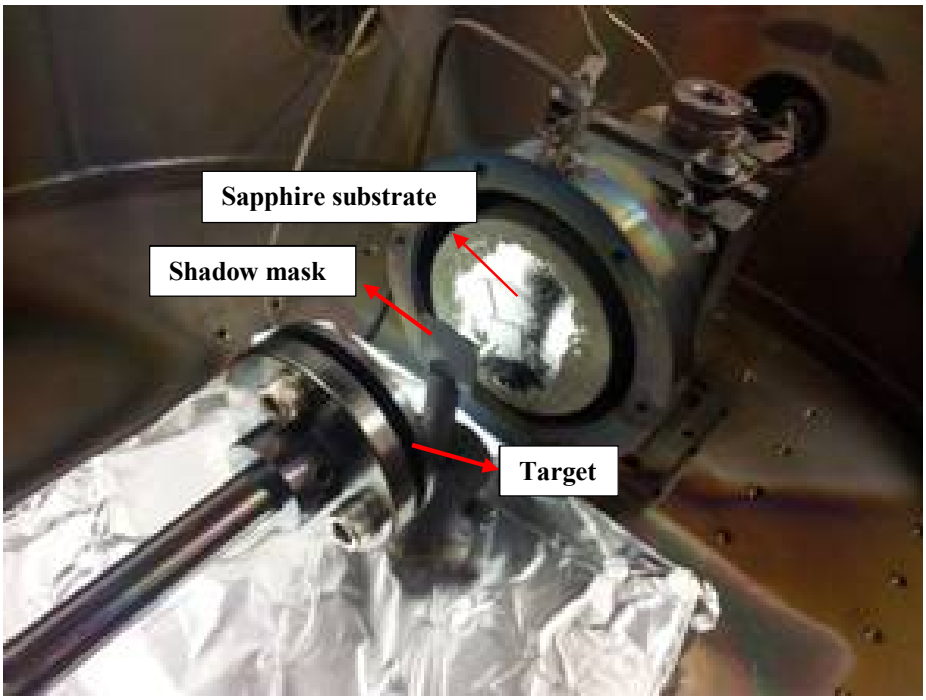

Fig. 2.8. Photo of the set-up inside of the PLD chamber.

2.4 Apparatus used for characterization of the samples

2.4.1 Atomic force microscope (AFM)

AFM images were obtained in air with a Dimension 3100 AFM and Nanoscope IIIa controller (Digital Instruments, Vecco). The AFM was used exclusively in tapping mode using silicon cantilevers (TAP300A1-G series, Innovative Solutions Ltd) which have resonant frequencies close to 3 kHz. The 500 × 500 nm scans were recorded at resolution 512 × 512 pixels at a scan rate of 1.001 Hz. The amplitude set point and gains were optimised for each sample.

2.4.2 Scanning (SEM) and transmission (TEM) electron microscopes

Most of the SEM images were taken using a JEOL 7000 HRSEM. Some of the SEM images (reported in Chapter 5) were taken using Raith150 electron beam lithography system. The Raith150 electron beam lithography system was operated by Max Lynam from the Department of Electrical and Computer Engineering University of Canterbury. The accelerating voltage was optimised for each sample. TEM images were taken using a Phillips CM200 or JEOL JEM-1230 microscopes operating at 200 and 120 kV respectively. The microscope was operated by Domagoj Belic from the Physics and Astronomy Department, University of Canterbury and the JEOL JEM-1230 was operated by Yu-Ming Chen from the Department of Material Science and Engineering National Chang Kung University, Taiwan.

2.4.3 Raman spectroscopy

Raman spectroscopy was used in this thesis work for identifying the presence and the nature of CNTs. Raman spectra were recorded in the backscattering mode using a 633 nm He – Ne laser (5 mW) focused on the sample by means of a 100× objective of 1 numerical aperture. The CCD detector was coupled to a high resolution monochromator (Jovin Yvon, T-64000). Dr. Eric Le Ru, School of Chemical and Physical Sciences provided assistance with Raman measurements.

2.4.4 UV-vis spectroscopy

UV-vis spectroscopy was used in this thesis work to study Au nanocolloids in the liquid phase. Au colloidal solution was diluted from 17 nM to 3.4 nM for analysis. UV-vis spectra were obtained with a Cary 4040 Spectrometer, fitted with a transmission mode cuvette. Spectra were recorded for the Au colloidal solution from 300 to 600 nm in absorbance mode, at a rate of 500 nm/min with a slit width of 2 nm.

Chapter 3. Design and fabrication of porous anodic alumina (PAA) templates

3.1 Introduction

Porous anodic alumina (PAA) membrane (Fig. 3.1) is a typical self-ordered nanoporous material that has been widely utilized as a template in the fabrication of highly ordered nanostructures. One of the most remarkable features of the PAA template is that pores form a high density hexagonal pattern when viewed from the top. In the cross-section of the membrane, the pores are vertically aligned and have a high aspect ratio (ratio of their length to diameter). Importantly, the morphology of PAA membranes is highly controllable *via* careful choice of the key parameters in the well-established fabrication method (anodization). Hence, it is not surprising that alumina (Al_2O_3) films have received intense interest for a variety of applications such as photonic crystals,[1] light emitting diodes,[2] super-capacitors,[3] humidity sensors[4] and tactile sensors.[5]

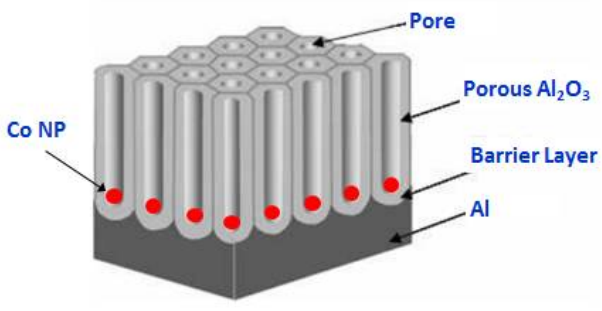

Fig. 3.1. A schematic drawing of an ideal porous Al_2O_3 membrane with Co nanoparticles at the bottom of the pores. Figure reproduced from reference 6.

The goal of this project is to grow CNTs using electrodeposited metal nanoparticle (NP) catalysts that are confined within the pores of PAA membranes. In this arrangement, the NPs cannot aggregate at the elevated temperatures needed for CNT growth. This chapter discusses the preparation of optimised PAA template for this application.

In this chapter, firstly, the fabrication of shallow PAA membranes with satisfactory uniformity will be discussed. The use of shallow membranes containing pores (sub-1 micron in depth) would facilitate of diffusion of Co^{2+} ions during electrodeposition and mass transfer of hydrocarbon gas during CNT growth in CVD. Secondly, the results which were obtained during optimisation of the chemical etching procedure used to thin the barrier layer of Al_2O_3 at the bottom of the pores will be presented. It was hypothesised that the uniformity of the electrodeposition of metal NPs would be significantly improved if a uniformly thin and conductive barrier layer could be obtained in this way.

3.1.1 The mechanism of pore formation in PAA membranes

In general, two types of Al_2O_3 layers can be formed during anodization of Al depending on the properties of the electrolyte used.[7] The first type is a thin, compact and nonporous layer of Al_2O_3 also called barrier type film that normally forms in a near-neutral electrolyte (*e.g.* citric acid, maleic acid or a mixture of boric acid and sodium borate).[8] The second porous layer which has been widely studied is formed during anodization in acidic electrolytes such as sulfuric acid, oxalic acid and phosphoric acid. This porous layer has a distinct morphology which strongly depends on the anodizing conditions including the specific chemical nature of the electrolyte, temperature, time, pH and potential applied during the anodization. In 1953, Keller *et al*. published the first study which focused on the structure

of porous Al_2O_3 and proposed a mechanism for the growth process.[9] The authors proposed that a homogeneous oxide barrier film is formed at the very beginning of the anodization process and the further dissolution of the oxide barrier layer is caused by the flowing current. The current flow increases the local temperature of the electrolyte and facilitates the dissolution of the oxide barrier layer which occurs at specific individual "points" on the oxide layers which are often associated with various defect sites or grain boundaries. The possible reactions involved in this process include the dissolution of the oxide barrier layer which reduces its thickness at those points, and subsequently repair of the damage by oxidation of Al metal. Since Keller's original report, the mechanism for the PAA membrane formation has been under vigorous discussion with several key contributions explaining the role of the anodization conditions in terms of mild anodization and hard anodization. Table 3.1 shows the comparison of the conditions for mild anodization and hard anodization.

Table 3.1. Mild and hard anodization conditions for preparation and self-ordering of PAA membranes. Table adapted from reference 10.

Mild Anodization				Hard anodization			
Electrolyte concentration (M)	**Temperature (°C)**	**Range of Potential (V)**	**Self-ordering regime (V)**	**Electrolyte concentration (M)**	**Temperature (°C)**	**Range of potential (V)**	**Self-ordering regime (V)**
0.3 H_2SO_4	10	10-25	25	1.8 H_2SO_4	0	40-70	70
2.4 H_2SO_4	1	15-25	25	-	-	-	-
6.0 H_2SO_4	20	-	18	-	-	-	-
0.3$H_2C_2O_4$	1-5	30-100	40	0.03-0.06 $H_2C_2O_4$	3	100-160	160
	15-20	20-40	40	0.3 $H_2C_2O_4$	1	110-150	120-150
0.2-0.3 H_3PO_4	0-5	160-195	195	0.1 H_3PO_4	0	195-235	235
H_3PO_4-CH_3OH-H_2O (1:10:89)	-4	-	195	H_3PO_4-CH_3OH-H_2O (1:20:79)	-10 to 0	195	195

Mild and hard anodization refers to anodization conditions that give slow or fast formation of a porous structure respectively. Anodization rate depends on the particular choice of the electrolyte and its concentration, temperature as well as the voltage used. In

general, the voltage which is used for mild anodization is lower than that used for hard anodization.[10] Typically, the range of the voltage used for mild anodization is between 10 and 100 V depending on the electrolyte and the anodization temperature, although higher voltages could be necessary in some cases (Table 3.1). This also means the porous Al_2O_3 layer is normally formed under lower current density conditions in the case of mild anodization. The growth rate of the porous Al_2O_3 layer is typically 1500 to 3500 times slower and the uniformity is normally better for mild anodization compared with hard anodization.[11] However, in recent years, the hard anodization process has been optimised and successfully applied for fabrication of self-ordered porous Al_2O_3 membranes.[11,12] Therefore hard anodization is often used for fabrication of the thick porous Al_2O_3 layers.

The natural tendency of spherical distribution of voltage and current fields about the erosion point (pore) is presumed to be the reason for the hexagonal pore arrangement in Al_2O_3 membranes. The closed-packed hexagonal arrangement of oxide porous structure is formed due to the steric factors during the pore self-alignment stage of film growth (discussed in detail later).

The theory of forming a porous anodic Al_2O_3 structure has been widely discussed. Fig. 3.2 (A) shows a simple model of this formation. According to the milestone works by Thompson *et al.*[13], Shingubara[14] and O'Sullivan[15], the formation of the porous Al_2O_3 layer during the anodization includes: (1) the growth of Al_2O_3 at the interface between oxide layer and Al (the O/A interface shown in Fig. 3.2 (B)) and (2) the dissolution of Al_2O_3 at the interface between electrolyte and Al_2O_3 (the E/O interface shown in Fig. 3.2 (B)).

It is well known that Al is very easy to be oxidised, so a layer of Al_2O_3 is naturally formed on Al foil exposed to the atmosphere. During anodization, Al is oxidised and the dissolution of Al_2O_3 occurs at the same time (eq. 1). Then Al^{3+} ions diffuse through the O/A

interface to the Al_2O_3 layer (Fig. 3.2 (B)). Under the influence of the electric field, O^{2-} and OH^- ions migrate from the E/O interface and go through the Al_2O_3 layer to react with Al^{3+} at the O/A interface forming Al_2O_3 (eq. 2 and 3). The growth of pores is controlled by the balance between Al_2O_3 formation and dissolution rates, with at least formation rate being dependent on the diffusion. The reactions for forming O^{2-} and OH^- are not well-understood as the ratio of O^{2-} and OH^- has not been determined or their origin traced.[10,16,17] They could be formed by the water splitting-reaction (eq. 4) or the interaction between water and electrolyte anions at the E/O interface (as shown schematically in Fig. 3.3).[10] Meanwhile, the Al_2O_3 also slowly dissolves and reduces the thickness of the oxide layer at the side exposed to electrolyte (eq. 5) while the oxidation of Al at the O/A interface (eq. 1) consumes Al. The dissolution rate will affect the structure of Al_2O_3 layer based on the choice of electrolyte. Generally, in a near-neutral electrolyte such as H_3BO_4 or $(NH_4)_2B_4O_7$, the dissolution rate will be much slower than the growth rate (forming Al_2O_3) which results in a thick and non-porous Al_2O_3 layer.[8] Conversely, in an acidic electrolyte (*e.g.* $H_2C_2O_4$, H_2SO_4 and H_3PO_4) the dissolution rate is faster and the balance between growth rate and dissolution rate keeps a constant thickness of barrier layer during anodization.[10,16,17,18]

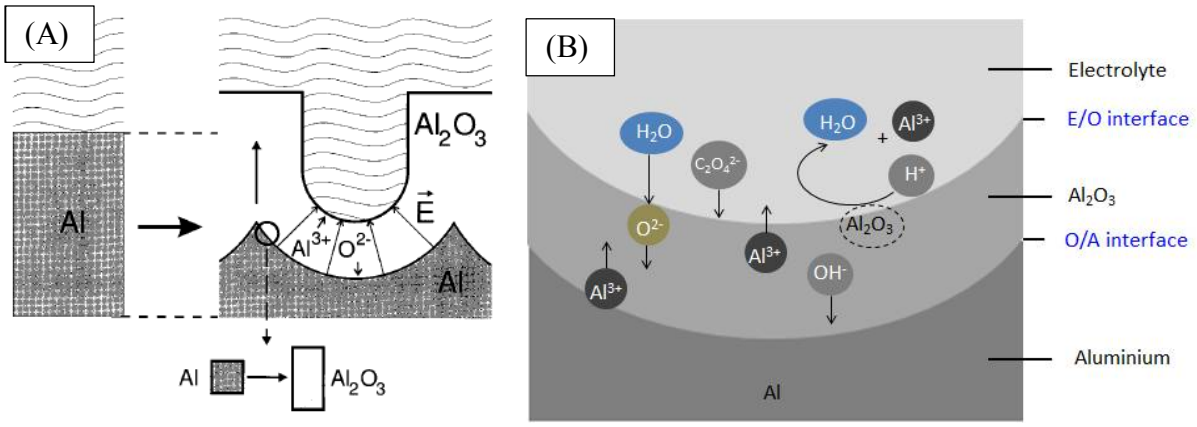

Fig. 3.2. (A) Model of porous Al_2O_3 structure formation. (B) Key ion processes occurring during anodization in sulfuric acid: oxidation of aluminium, diffusion of ions and dissolution of Al_2O_3. Figure (A) adopted from reference 16 and figure (B) reproduced from 10.

(1) Formation of aluminium oxide

$$Al_{(s)} \rightarrow Al^{3+}_{(s)} + 3e^- \quad \text{(eq. 1)}$$

$$2Al^{3+}_{(s)} + 3O^{2-}_{(s)} \rightarrow Al_2O_{3(s)} \quad \text{(eq. 2)}$$

$$2Al^{3+}_{(s)} + 3OH^-_{(s)} \rightarrow Al_2O_{3(s)} + 3H^+ \quad \text{(eq. 3)}$$

$$3H_2O_{(l)} \rightarrow 6H^+_{(aq)} + 3O^{2-}_{(s)} \text{ (water-splitting reaction)} \quad \text{(eq. 4)}$$

(2) Dissolution of aluminium oxide

$$Al_2O_{3(s)} + 6H^+_{(aq)} \rightarrow 2Al^{3+}_{(aq)} + 3H_2O \quad \text{(eq. 5)}$$

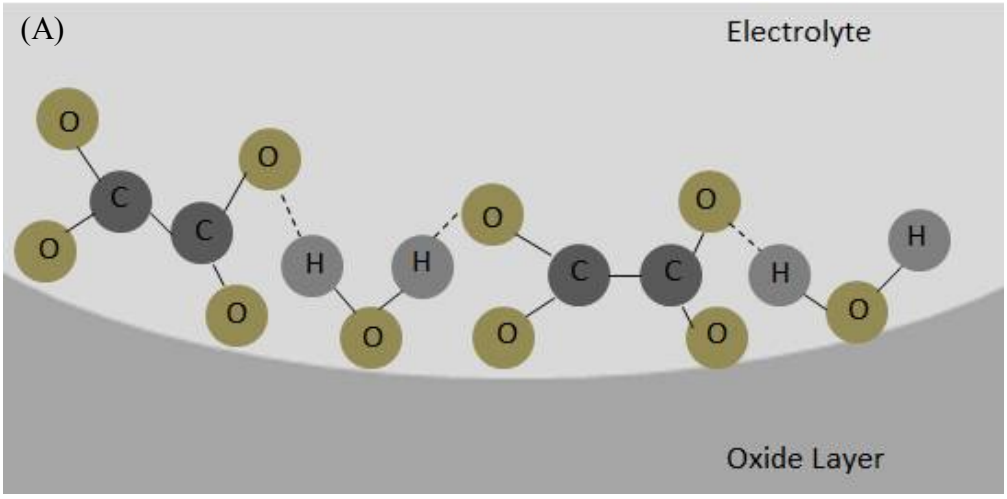

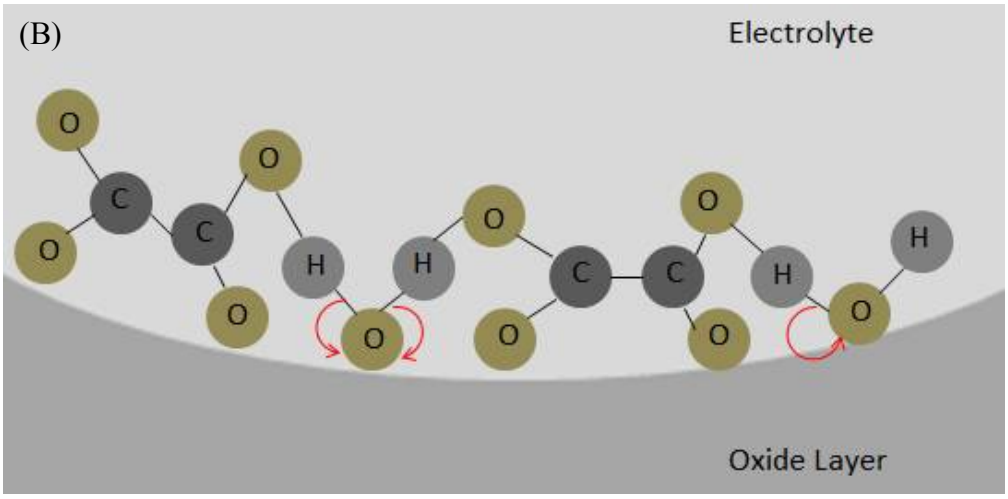

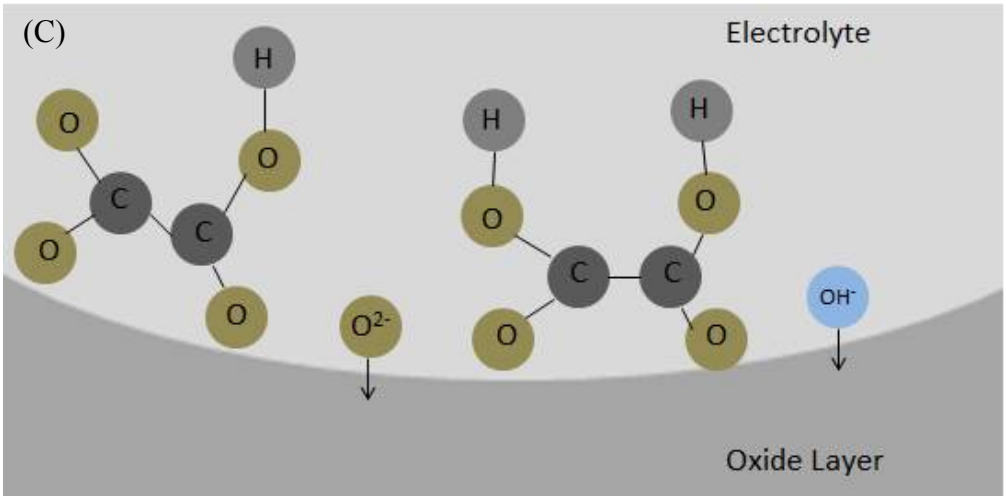

Fig. 3.3. Schematic representation of O^{2-} and OH^- ions formation at the interface between the electrolyte and oxide layer from water interaction with adsorbed $C_2O_4^{2-}$ anions. Figure reproduced from reference 10.

Su *et al.* used eq. 6 to explain the relationship between the dissolution rate of Al_2O_3 at the E/O interface and the morphology of the Al_2O_3 layer when the anodization in near-neutral or acidic electrolyte E is the electric field strength, U is the applied voltage to an oxide layer and d is the thickness of the oxide layer.[18]

$$E=U/d \qquad \text{(eq. 6)}$$

In a near-neutral electrolyte, the dissolution rate of Al_2O_3 at the side exposed to electrolyte is much slower than the formation rate of Al_2O_3 at the O/A interface. As a result, the thickness of oxide layer (d) keeps increasing and the electric field strength (E) decreasing.[18] Eventually, the oxidation process will stop when the electric field strength is too weak to drive the anions through the oxide layer to react with Al^{3+} and form Al_2O_3. At this stage, the electric field strength has been experimentally determined to be 0.7 Vnm^{-1}.[8]

Conversely, in an acidic electrolyte, the dissolution of Al_2O_3 is fast.[18] The equilibrium between the rates of oxidation of Al and dissolution of Al_2O_3 results in a constant thickness of oxide layer which is typically smaller than that of the film obtained during anodization in a

near-neutral electrolyte. Therefore, the anodization process in acidic electrolyte can be continued indefinitely using an experimentally accessible voltage.[18]

In practice, during anodization, the dissolution rate of Al_2O_3 at the surface of the Al foil is uneven because of the presence of various defects in the Al foil such as impurities, dislocations and grain boundaries.[10] These defects result in non-uniform current distribution and a local thinning of the film occurs.[10] Fig. 3.4 (A) shows the initial oxide formation at an Al foil with defects. Fig. 3.4 (B) shows that the initial defects develop penetrating paths which result from the local field strength. When the development of penetrating paths is more advanced, the local field strength is increased and dissolution through the paths occurs (Fig. 3.4 (C-D)).[20] Therefore the uneven dissolution rate of the Al_2O_3 layer leads to the natural generation of pores (Fig. 3.4 (C-D)).[18] Moreover, the pore growth is directed predominantly downward instead of sideways due to alignment with the electric field and the steric restrictions arising from the presence of a high density of neighbouring pores which equalises the strength of the field within the whole area. The hemispherical shape at the bottom of the pores is the only morphology which allows the strength to be equalised and maintains a uniform thickness.[18]

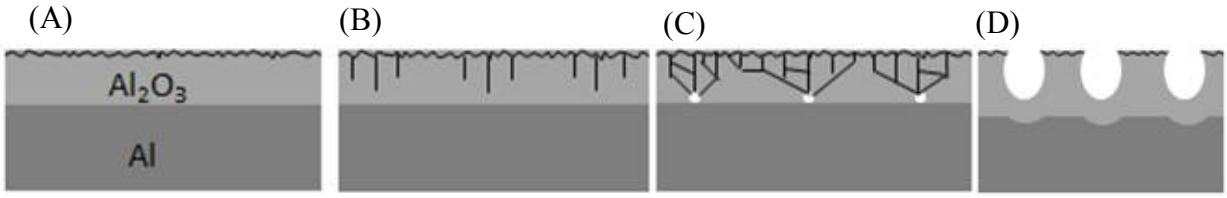

Fig. 3.4. Schematic diagram illustrating the development of penetration paths and the precursors to pores during anodization. Figure reproduced from reference 10.

3.1.2 The kinetics of pore formation

An ordered porous structure is typically formed by anodizing Al at a constant current density or constant anodizing potential in acidic electrolyte. The current density *vs.* anodizing time behaviour can provide another piece of evidence that the pore formation occurs in several stages. As shown in Fig. 3.5, at the beginning of the anodization process the current density is high due to the higher conductivity of pure Al metal.

The current density then decreases rapidly from "A" to "B" due to the formation of an Al_2O_3 barrier layer on the Al metal decreasing the conductivity. Simultaneously, the initial pores start to form during a short period of non-steady state. Subsequently the thickness of the barrier layer becomes thinner resulting in the increase in pore depth and a small increase in current density from "B" to "C". When anodization reaches steady state, the rate of dissolution of Al and the rate of formation the oxide layer are in equilibrium. The rate of formation of the oxide layer can be continuously grown as long as a constant voltage applied. The importance of specific parameters on the anodization process is discussed in 3.1.4). Obtaining a highly ordered porous structure needs a very long anodization time for self-adjustment of the porous structure as the initial pores are developed from an uneven surface of the oxide layer. Alternatively, a multi-step anodization process can achieve the formation of a highly ordered porous structure which will be discussed in the next section.

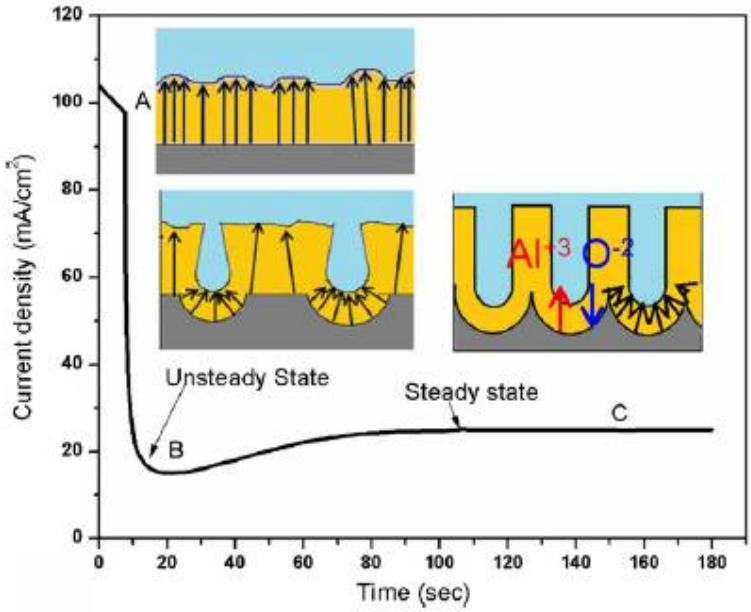

Fig. 3.5. A typical current density-anodizing time curve for anodization at a constant voltage of mode 40 V in 3 wt% oxalic acid electrolyte at 15 °C. Figure adapted from reference 21.

3.1.3 The self-ordering of pore growth and multi-steps anodization

The porous Al_2O_3 structure can be fabricated on a commercial Al foil or on a layer of Al film sputtered onto another conductive substrate (*e.g.* Si wafer with a layer of sputtered Nb).[22] However, regardless of the specific nature of the starting Al film, all have the same problem that the initial pore arrangement is disordered. This occurs because the pores are not aligned at the beginning of the anodization. Although there are methods that can be used to flatten the Al surface before the first anodization process (*e.g.* annealing the Al substrate at high temperature[23] and electropolishing[24]), a protracted anodization time is still required to develop an ordered PAA. An alternative approach is to use a 2-step procedure in which the porous Al_2O_3 layer is removed after the first anodization process leaving a dimpled structure that facilitates the formation of an ordered and vertical porous structure during a second anodization process.[25] Mazuda *et al.* developed a 2-step anodization process in 1995 and

successfully fabricated a highly ordered pore arrangement over a large area, This 2-step anodization process has been widely utilized for making PAA templates in numerous follow-up studies as it offers significant improvement in quality of PAA membranes compared to a single-step anodization process.[26,27,25] There are fewer reports of porous Al_2O_3 structures fabricated using multi-step (i.e. more than 2-steps) anodization processes.

Fig. 3.6, which is reproduced from the study of Yuan *et al.*, compares the trends in the current density *vs.* anodization time during repeats of the anodization process.[28] In the 2nd anodization, the time to reach steady state is shorter than in the 1st anodization. The origin of this phenomenon is the pore pre-patterning (dimple structure remaining on the Al surface after removal of the PAA membrane formed during the 1st anodization). In the 1st anodization, only a simple planar Al_2O_3 layer is formed before the nucleation of the pore structure. Hence resistance is higher and the current density is lower at the beginning of pore formation in the 1st anodization than the 2nd and a longer time is required to reach steady state in the 1st anodization. In addition, since the porous structure has been self-organising during the 1st anodization, the remaining dimple structure on the Al surface is highly uniform. It helps the formation of a highly ordered porous structure from the start of the 2nd anodization. Hence a 2-step anodization process is commonly used to fabricate a uniform PAA structure.

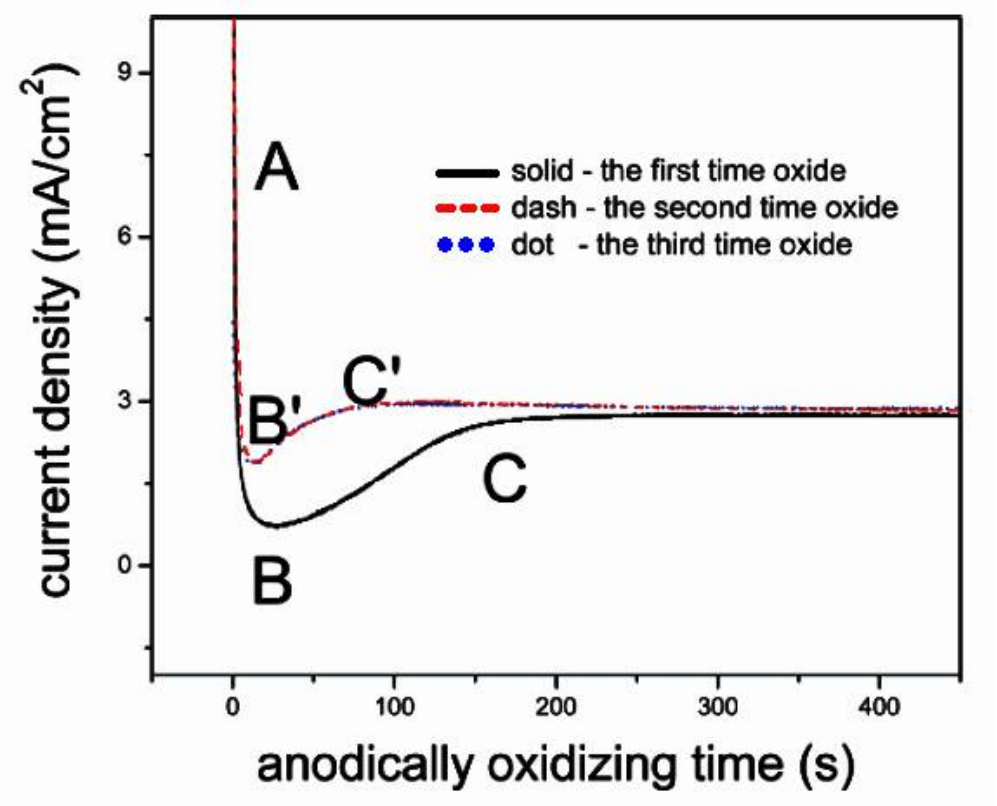

Fig. 3.6. Current density-anodizing time curve during 1, 2 and 3 anodization processes at 30 V in a 0.5 M oxalic acid electrolyte at 15 °C. Figure reproduced from reference 28.

The data in Fig. 3.6 suggests that more than 2 anodization steps should lead to negligible changes in membrane structure. However other studies show that in some conditions at least, additional steps do improve the membrane quality. Hwang *et al.* discussed the porous structures obtained after doing 1, 2, 3 and 4-step anodization processes (anodization conditions: 40 V in a 0.3 M oxalic acid at 15 °C and the anodization times were 5, 4, 3 and 5 min for each anodization process) with removal of the oxide layer after anodization steps 1, 2 and 3.[22] A series of SEM images in Fig. 3.7 show the top view and cross section of the pores after each step. The insert images in each of the top view SEM images shown in Fig. 3.7 give fast Fourier transform (FFT) image corresponding to each of the SEM image. Analysis of the FFT images has been used for assessment of the uniformity of the pore arrangement. For a reasonable pore arrangement, a round circle with a ring

surrounding it would appear as shown in Fig. 3.7 (B)-(D). The level of symmetry of both the inner circle and the ring correlate with the uniformity of the pore arrangement, with highly symmetrical FFT images corresponding to highly uniform PAA membranes.[46] Based on such FFT analysis (Fig. 3.7), the authors concluded that the pores become more ordered and uniform with each additional anodization. In their research, the substrate was a layer of high purity Al (99.999%) sputtered onto a layer of Nb on a Si wafer.[22] Similarly, Chen *et al.* showed that the current density reaches a steady state more quickly when the anodization process is repeated more than four times (Fig. 3.8 (A)).[29] The anodization conditions they used for 5-step anodization process were: 120 V in a 10 wt. % phosphoric acid at 3 °C for 30 min (Fig. 3.8 (B)). It is worth noting that short anodization times were used in the studies by Hwang *et al.* and Chen *et al*. Instead of a 2 h 1st anodization process as is typically used, they used a 5 or 30 min anodization and repeated this process for four or five times. According to the studies by Hwang *et al.* and Chen *et al*., a multi-step anodization process (more than 2-steps) with a short period of anodization is an alternative strategy for fabricating a highly ordered PAA membrane.[22,29]

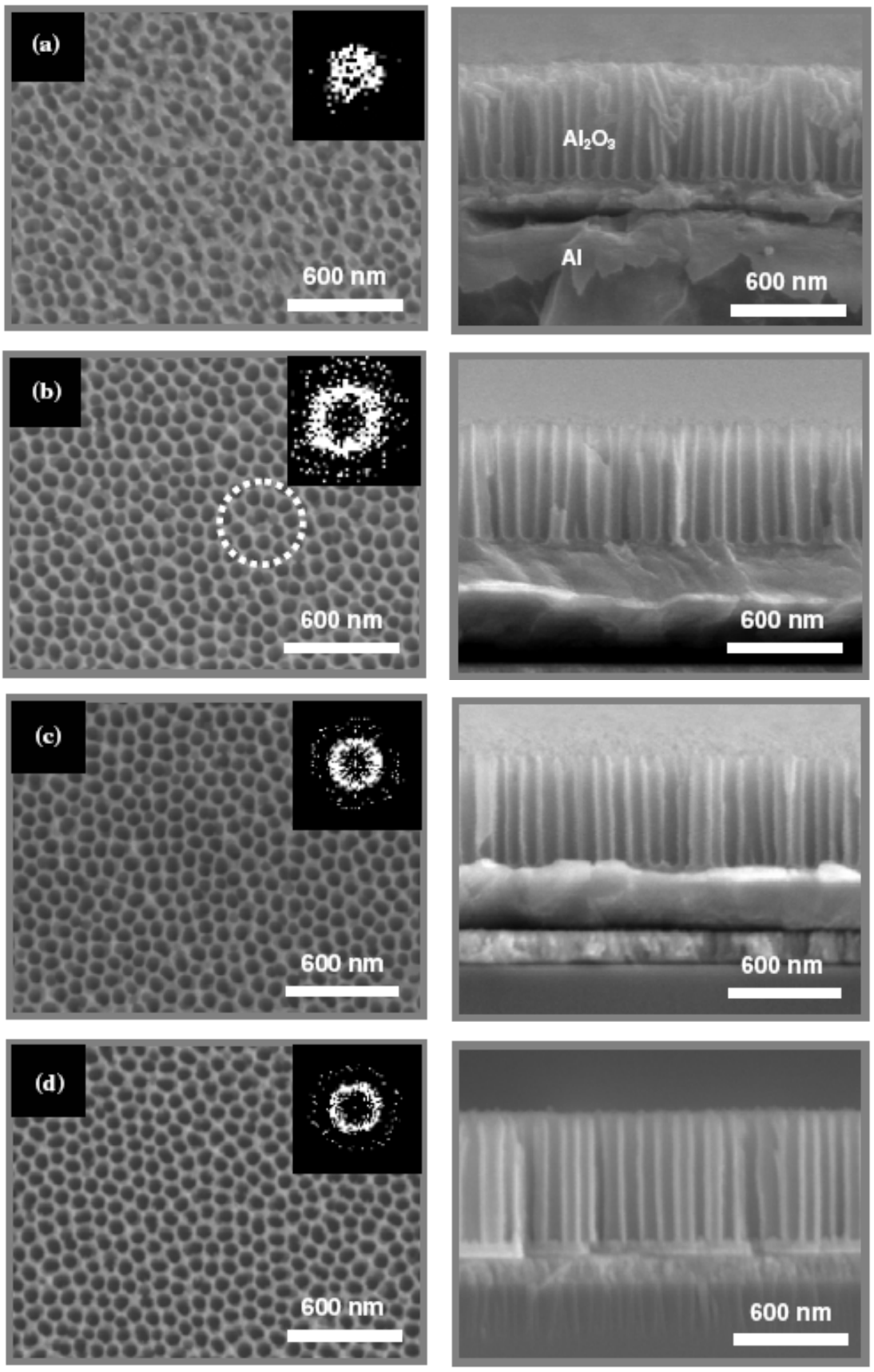

Fig. 3.7. Step wise progress in formation of PAA membrane during anodization in oxalic acid. (a) After 1st anodization; (b) after 2nd anodization; (c) after 3rd anodization and (d) after 4th anodization. (The original thickness of the evaporated Al layer was 1.6 µm. Anodization conditions: 40 V in a 0.3 M oxalic acid

solution at 15 °C. The insets are the results of Fourier transform (FT) analysis. Figure reproduced from reference 22.

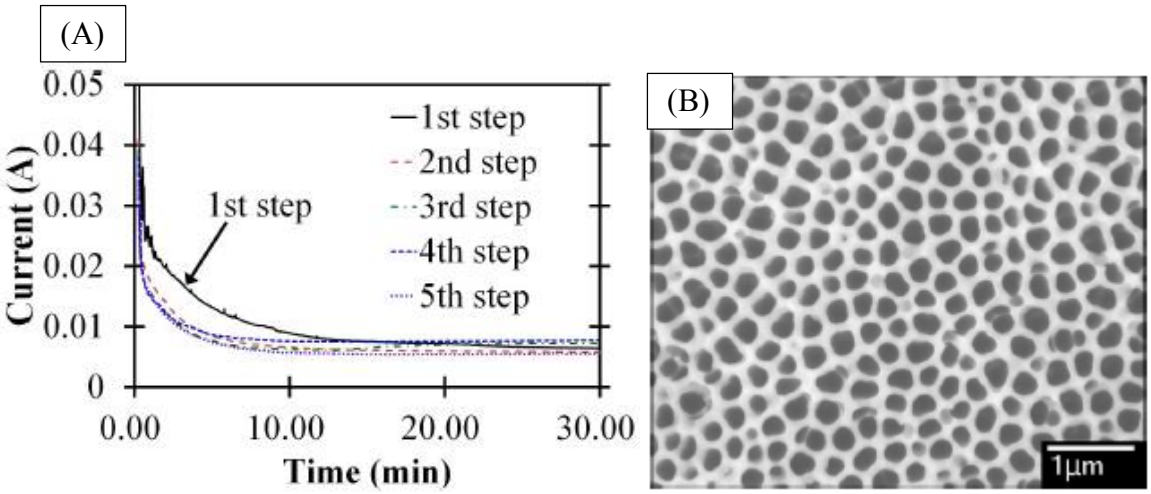

Fig. 3.8. (A) Current-time curve of first to fifth-step anodization process and (B) SEM image of PAA membrane after 5-step anodization. Anodization conditions: 120 V in a 10 wt. % phosphoric acid solution at 3 °C. Figure adopted from reference 29.

3.1.4 The effects of the anodization parameters on self-ordering

The pore characteristics including the pore diameter, interpore distance and the thickness of a PAA membrane are controlled by the key anodizing parameters: the type of electrolyte and its concentration, the anodizing voltage, the temperature and the duration of the anodization process. Each electrolyte has a specific range of anodizing potentials at which the process can be carried out. Different voltages give rise to differences in the interpore distance (termed "cell diameter" by the author) as shown in Fig. 3.9.

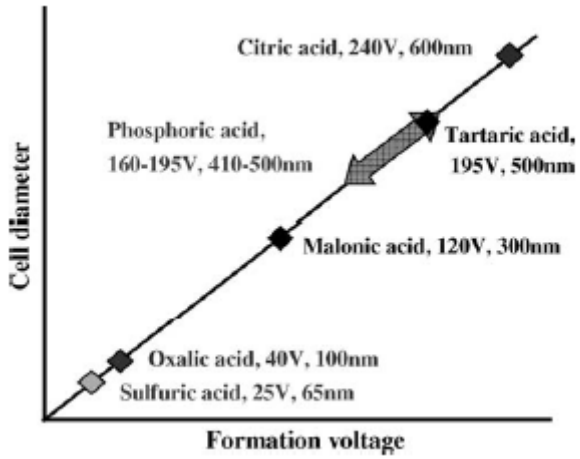

Fig. 3.9. The linear relationship between the cell diameter (interpore distance) and the applied voltage for various acids. Figure adopted from reference 30.

Hwang *et al.* compared the morphologies of PAA membranes obtained using sulfuric, oxalic and phosphoric acid solutions under potentials of 25 V, 40 V and 180 V respectively. These experiments utilised a 4-step anodization process and the substrate was prepared by depositing high purity Al onto a layer of Nb on a Si wafer (Table 3.2).[22] Mild anodization was used with sulfuric and oxalic acids and hard anodization with phosphoric acid.

Table 3.2. Experimental conditions for preparation of PAA templates. Table adopted from reference 22.

Processing condition			Oxalic acid	Sulfuric acid	Phosphoric acid
Anodizing condition	Potential (V)		40	25	180
	Concentration (M)		0.3	0.1	0.1
	Temperature (°C)		15	0	0
	1st anodizing time (min)	5	20	10	9
	2nd anodizing time (min)	4	10	10	6
	3rd anodizing time (min)	3	10	10	6
	Final anodizing time (min)	5	86	10	20

Analysis by SEM (oxalic acid: Fig. 3.7 (d); sulfuric acid: Fig. 3.10 (a); and phosphoric acid: Fig. 3.10 (b)) show that the size and shape of pores are more uniform when oxalic acid

and sulfuric acid are used as the electrolyte. In addition, the Fourier transform (FT) analysis (shown in the insets in each figure) of these images could be used to access the ordering level and confirmed that. The pore arrangement is better when these two electrolytes were used.[22] However, according to many reports sulfuric is not as popular a choice for anodization as oxalic acid due to the low operating temperature (0 °C) required and much lower anodization rate.[10, 22,27]

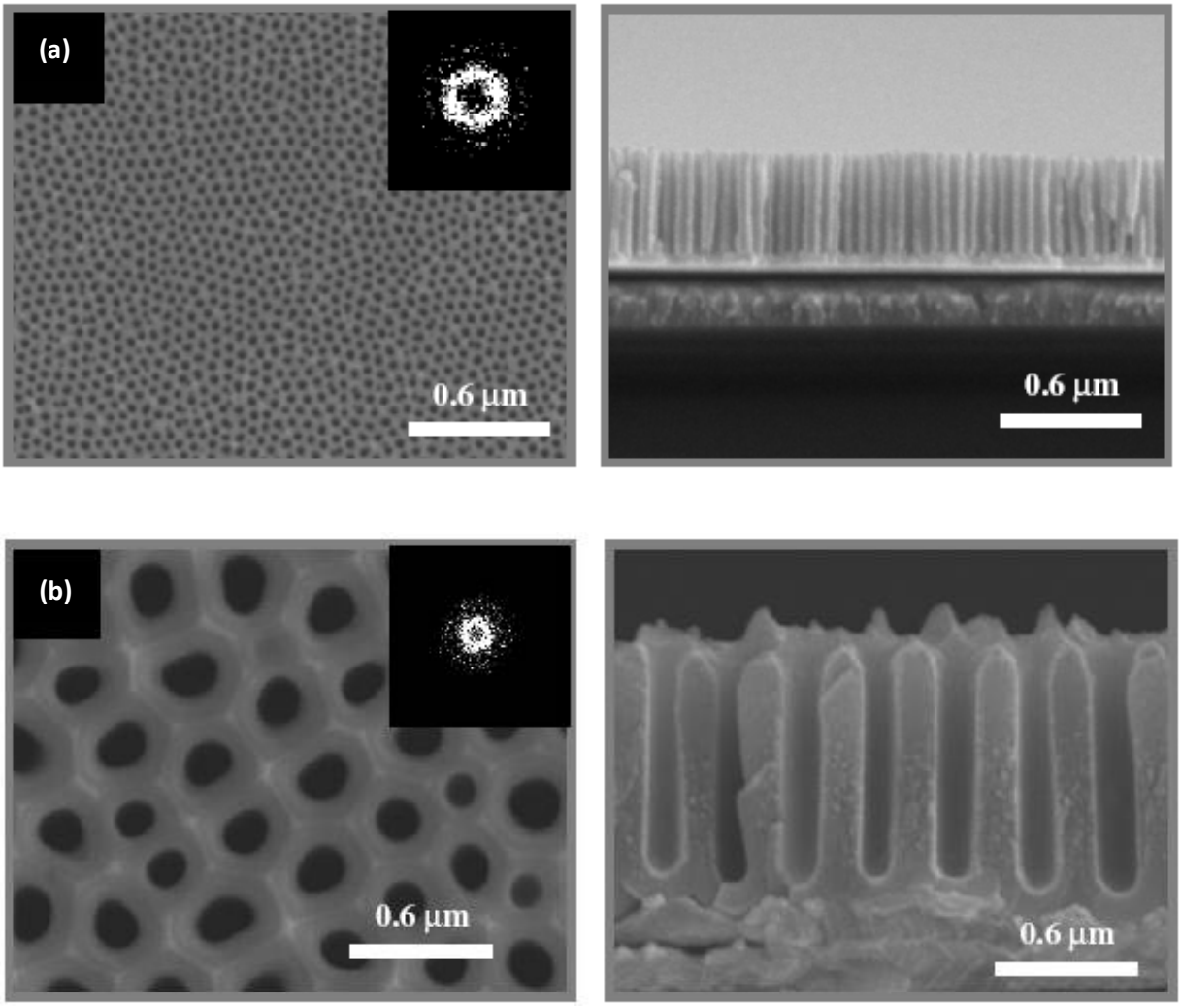

Fig. 3.10. The progression of pores in the PAA membrane after 4-step anodization process in (a) sulfuric acid and (b) phosphoric. The insets show the results of the Fourier transformation (FT) analysis of corresponding SEM images. Figure reproduced from reference 22.

3.1.5 Thinning barrier layer by electrochemical method and chemical etching

The conductivity of the barrier layer is very low as it is made up of aluminium oxide. Lillo *et al.* reported the resistance of PAA membrane decreased significantly (from 5000 MΩ to 50 MΩ) after widening the pores by 10 nm as well as thinning the barrier layer at the pore bottoms.[48] Hence, it is important to decrease the thickness of the barrier layer when using PAA membrane as a template and electrodepositing metal catalyst at the bottom of the pores. Two thinning processes have been widely used: an electrochemical thinning method and a chemical etching method.

The electrochemical method to thin the barrier layer generally involved dropping the voltage at the end of the final anodization process. During the voltage drop, a branched structure of cracks is created in the barrier layer which creates paths for current flow in the subsequent electrodeposition of metal catalyst. Cheng *et al.* depicted the formation of this branched structure as shown in Fig. 3.11 (A).[31] Fig. 3.11 (B) is a TEM image of a cross section of PAA membrane with a branched structure at the bottom of the pores, Au is deposited into pores in order to increase the contrast when observing the detailed structure in TEM.

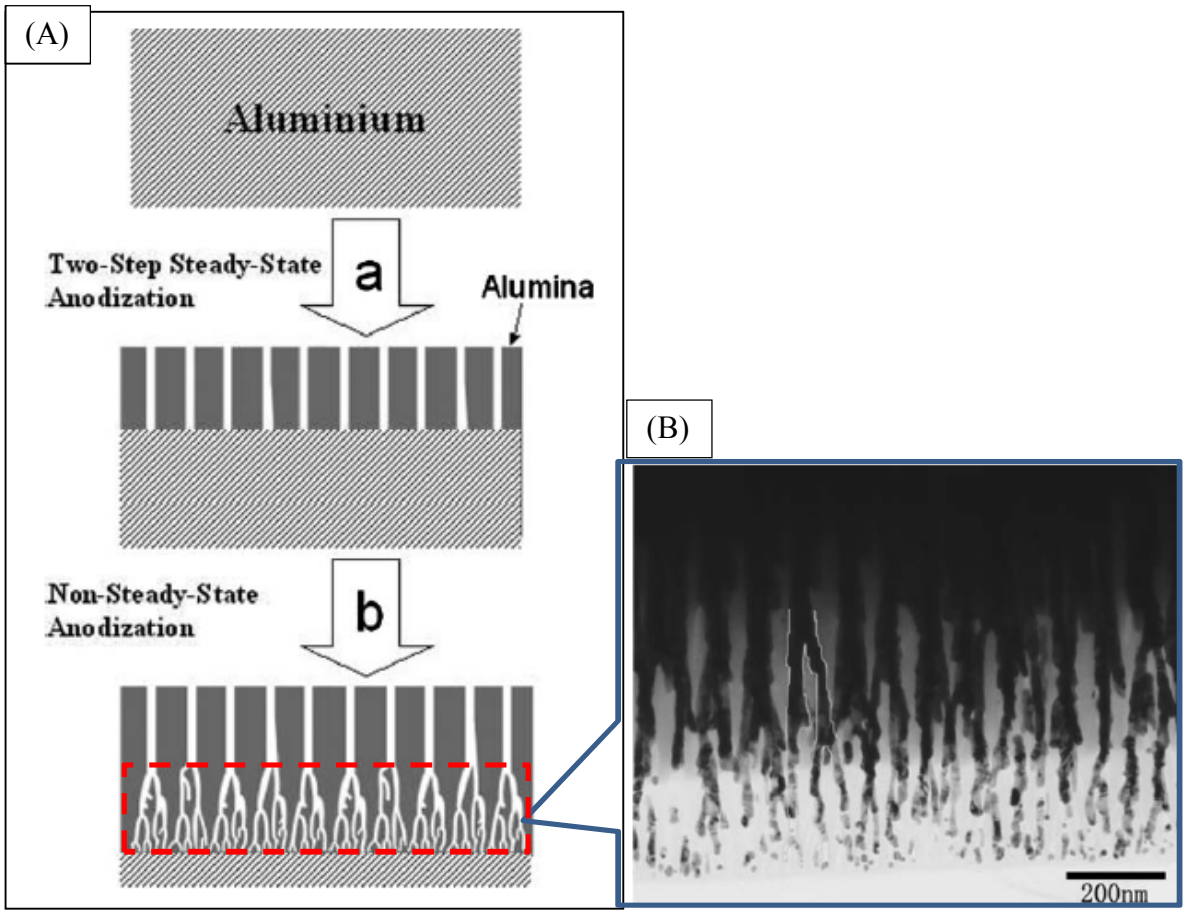

Fig. 3.11. (A) Schematic diagram illustrating the electrochemical fabrication of branched structure at the bottom of the pores and (B) TEM image of cross-section microtomed gold impregnated nanoporous Al_2O_3 film. The PAA membrane was made by 2-step anodization at 40 V in a 0.3 M oxalic acid electrolyte at 3 and 4 ° C in each anodization process. Figures reproduced from 31.

To create the branched pore structure shown in Fig. 3.11 (B), the voltage was dropped from the original anodizing voltage (40 V) to the final voltage (5 V). The ratio of the dropping voltage is based on (eq. 7), where U is the anodizing potential, U_0 is the initial potential, t is the time and τ is exponential time constant (mean life time or scaling time).[31]

$$U=U_0 \times e^{-t/\tau} \quad \text{(eq. 7)}$$

Fig. 3.12 (A) and (B) show the potential-time and current-time behaviour respectively during the voltage drop.[31] The authors explained the current-time behaviour during voltage dropping as follows. It is known that the thickness of barrier layer is constant when a steady-

state anodizing potential is applied. When the voltage suddenly drops, the current drops dramatically (as shown in the insert figure in Fig. 3.12 (B)). Simultaneously, the number of Al^{3+} ions generated at the O/A interface is decreased as the rate of the oxidation is decreased as well. However, the chemical microenvironment at the E/O interface of the barrier layer is unchanged. Therefore, the dissolution rate of Al_2O_3 is faster than the formation rate of Al_2O_3. In this case, the barrier layer is thinned leading to an increasing current. This increasing current also results in the increasing generation of Al^{3+} ions which leads to restore the balance between formation of Al_2O_3 and the dissolution of Al_2O_3. However, the next voltage drop is applied before the balance is achieved which results in the toothed current-time curve with repeated voltage drops.[31] Although, the reason for formation of the branched structure during the non-steady state anodization process is still unclear, this morphology is beneficial for electrodeposition of metal NPs or NWs within the pores.[27]

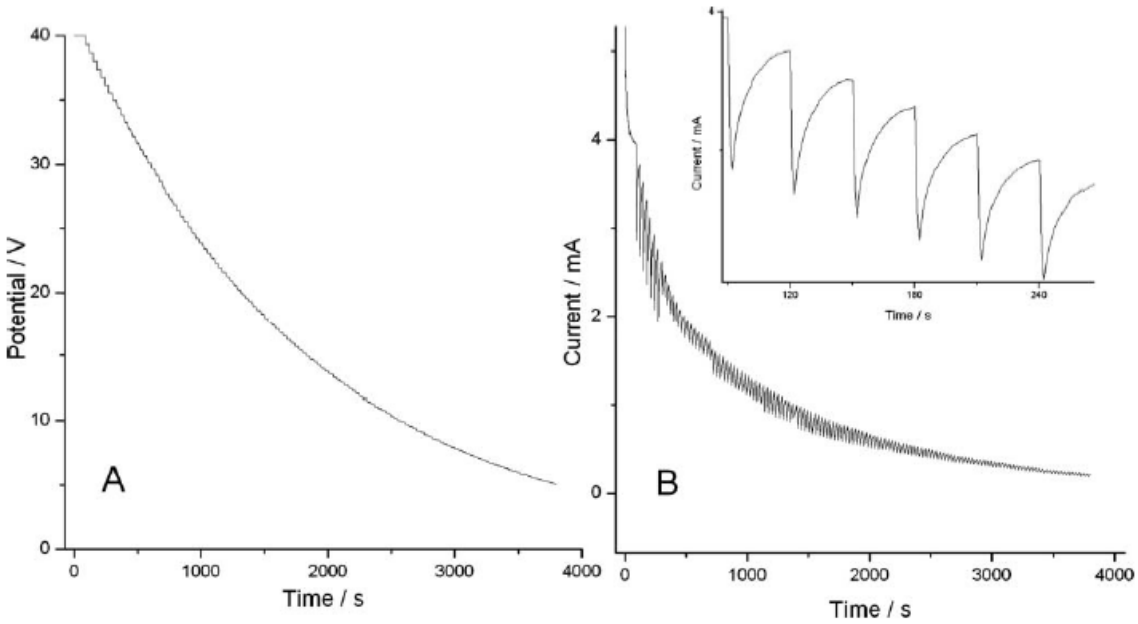

Fig. 3.12. (A) Potential–time and (B) current–time curves recorded in non-steady-state anodization. Inset of (B) is a magnified view of the partial current curve. Figures adopted from 31.

The electrochemical barrier layer thinning in this work is based on the method of Gerein *et al.* which was also used in the previous study by Xu.[32,33] Gerein *et al.* prepared the PAA membrane using a 2-step anodization at 40 V in 0.3 M oxalic acid at 3 °C. Apart from the temperature, the same conditions were used to prepare PAA membrane in this work. Gerein *et al.* used a voltage drop rate of 1 V/min and although the authors did not provide detailed TEM images of the branched thinned barrier layer structure. The authors were able to electrodeposit Co NWs in the pores which was confirmed by SEM images (top view) allowing estimate of pore filling efficiency (Fig. 4.2). The success of their electrodeposition experiment provides convincing evidence that such barrier layer thinning procedure results in a barrier layer structure conductive enough for the purpose of electrodeposition of Co.[32]

Chemical etching is another method for widening the pores as well as thinning the barrier layer. It is often used after the electrochemical thinning process. The branched crack structure is formed by the electrochemical thinning process makes it easier to thin or potentially break through the barrier layer during the chemical etching process. The chemical etching process used in this work is based the previous study by Xu which involved immersing the PAA membrane in a 0.1 M H_3PO_4 solution at 30 °C for 1 h after the multi-steps anodization and the electrochemical thinning process. Under these mild conditions, the pores would be widened from 35 nm to 50 nm. However, in this work, extended etching times were also examined in order to thin the barrier layer as much as possible and improve the uniformity of Co NP electrodeposition. This part of the study will be discussed in 3.3.4.

3.1.6 Aims for this chapter

The aim of work detailed in his chapter is to produce PAA membranes that can be used for the electrodeposition of Co nanoparticles (NPs) into the pores, and subsequent growth of CNTs from the NP catalysts. In this arrangement, the NPs cannot aggregate at the elevated temperatures needed for CNT growth. This chapter discusses the preparation of optimised PAA templates for this application. It was expected that membranes with shallow pores would be most effective. It was also anticipated that a thin and uniform barrier layer would promote the uniform deposition of Co NPs at the bottom of the pores. The optimisation of a chemical etching procedure for the barrier layer was also investigated.

Fig. 3.13 shows graphical schematic illustration of the strategy followed in the work discussed in this and the following chapters.

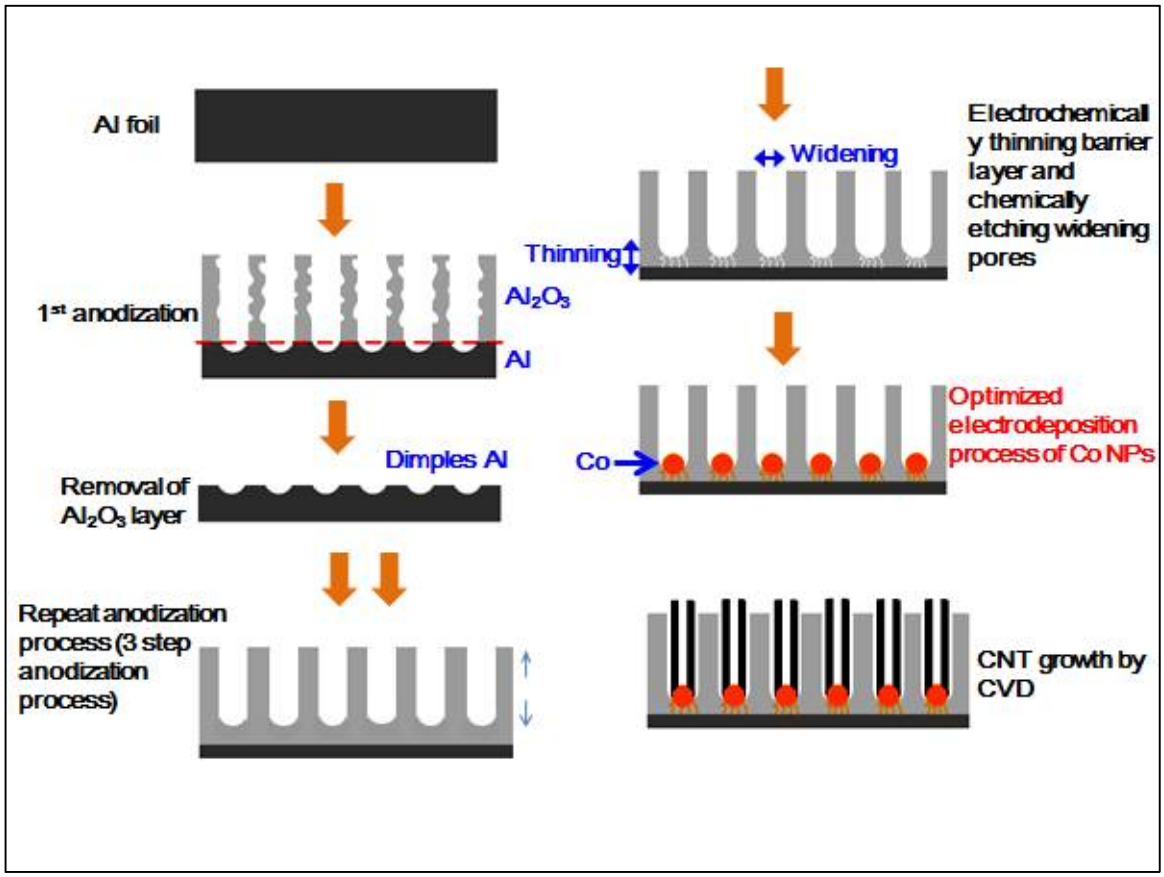

Fig. 3.13. The schematic flow-chart of the fabrication of PAA template, deposition of Co nanoparticles and CNT growth.

3.2 Experimental section

3.2.1 Pre-treatments of Al foil

Pre-treatments were sometime applied to high purity Al foil (99.9995 %). A circular (*ca.* 2 cm in diameter) piece of Al foil (99.9995 %) with thickness of 0.5 mm was used in a typical preparation. Before anodization, Al sample were either: (i) degreased by immersing Al foil in acetone and sonicating for 10 min, (ii) annealed and then degreased or (iii) annealed, degreased and electropolished. Degreasing was carried out by 30 min sonicating in acetone.

When an Al sample was pre-treated by annealing, the pre-cut pieces of Al foil were heated in a tube furnace (chapter 2) at 500 ºC for 1 h in an $Ar_{(g)}$ atmosphere. The quartz tube containing Al foil samples supported in a quartz boat was purged with $Ar_{(g)}$ prior to heating and its flow (200 sccm) was maintained through the tube for the annealing and cooling process . This purge ensured that there is no $O_{2(g)}$ in the quartz tube during the annealing process.

When samples were pre-treated by electropolishing, the procedure followed that of Ono *et al*.[30] Specifically, after degreasing the Al foil, the sample was electropolished in a solution containing $HClO_4$ (60%) and ethanol (1:4 v/v) at 10 ºC and 20 V for 10 s using the anodization cell described in chapter 2. After electropolishing, the samples were rinsed thoroughly with Milli-Q water and then dried under $N_{2(g)}$.

3.2.2 The multi-step anodization process

A 2-step anodization process was used to fabricate PAA templates. The first anodization step was carried out at 30 V for 2 h in a 0.4 M oxalic acid solution at 16 ± 1 ºC with a stirring rate of 1000 rpm. Then the Al_2O_3 layer was removed in a mixture of 10 mL of 0.8 M H_3PO_4 and 10 mL of 0.2 M H_2CrO_4 maintained at approximately 70 ± 1 ºC by immersing the sample for 40-60 min. The second anodization step was carried out under identical conditions to the first anodization but for 1 hr. To improve the uniformity of the porous structure, the Al_2O_3 layer was removed after the second anodization, and a third anodization step was carried out during a short period (30 s). Due to the hardware limitations current densities during anodization were not measured

3.2.3 Thinning the barrier layer

At the end of anodization process, the barrier layer was thinned by gradually dropping voltage at the end of anodization. The anodizing voltage was gradually dropped from 30 V to 10 V (1 V/min), and then was kept at 10 V for 3 min in order to achieve equilibrium at the barrier layer.[32,34]

3.2.4 Chemical etching process

The chemical etching process was carried out by immersing the PAA sample in 0.1 M H_3PO_4 at approximately 30 °C for 60 min[35], 65 min or 70 min. The pores were widened to approximately 50 nm and the barrier layer at the bottom of the pores was expected to be similarly thinned by this chemical etching procedure.

3.3 Results and discussion

3.3.1 Pre-treatments of Al foil before the anodization process Annealing and electropolishing

In the early stage of this project, two pre-treatments (annealing and electropolishing) were tested with an aim of improving the uniformity of the subsequently prepared PAA membrane. The purpose of the electropolishing was to reduce the roughness of the surface of

the Al foil as previously reported.[30] Annealing has been reported to lead to reduce deformation of the foil during anodization.[23, 36] It has been suggested by Jensen *et al.* that the origin of this effect is the recrystallization of Al which takes place during annealing which may reduce the grain boundaries as well as reduce the number of defects.[37] Annealing has been often used in the case of an Al foil of low purity (*i.e.* lower than 99.995%) and involves heating the foil at 500 °C under $Ar_{(g)}$ for 1 or 2 h.[23, 36] Several literature reports describe a combination of annealing and electropolishing and claim that such an approach leads to a better quality Al surface than annealing or electropolishing alone.[29, 36] The commercially purchased Al foil which was used during this project had been annealed by the manufacturer. Experiments were undertaken to see if additional pre-treatments could improve the uniformity of the final porous structure.

The first attempt to pre-treat Al foil was made in the following way. Al foil (99.995 %) was first annealed to 500 °C under the conditions described in section 3.2.1. After annealing, the surface of the pre-cut Al foil disc appeared unchanged by visual inspection. The discs were then electropolished as described in section 3.2.1. Unexpectedly, this was found to increase the roughness of the surface (Fig. 3.14 (B)). This result was obtained reproducibly for several samples before a decision was made not to use this approach any further. Importantly, it should be noted that formation of pin-holes penetrating through the whole thickness of the Al foil occurred occasionally during the electropolishing.

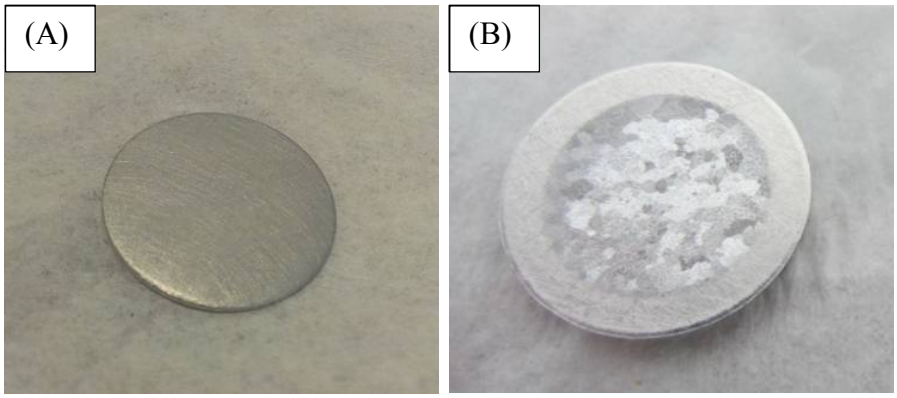

Fig. 3.14. Photographs of Al foil (A) before annealing and (B) after pre-treatment by annealing and electropolishing.

At this stage it was not clear if the high surface roughness in the case of annealing followed by electropolishing resulted from the annealing step. When a non-annealed sample was electropolished, the surface roughness appeared the same as that in the presence of pre-annealing. Hence annealing was not the main factor. The above results clearly contradict the literature which claims that combination of pre-treatments improves the flatness of Al surfaces.[23,38] However, Schoone *et al.* have reported perforation of Al foil during electropolishing.[39] The authors actually utilised this phenomenon and developed a technique for fabrication of metal specimens for TEM imaging because the thinning rate in the centre of the Al foil is higher than in the edge.

The use of pre-treated, but not perforated Al foil samples for anodization was examined (details of anodization experiments are discussed in the following section). Samples pre-treated using the combination approach (annealing followed by electropolishing), electropolishing alone and annealing alone in most cases developed severe, macroscopic perforations (Fig. 3.15 (A)) during the anodization process. The same damage occurred regardless of which pre-treatment had been used before anodization.

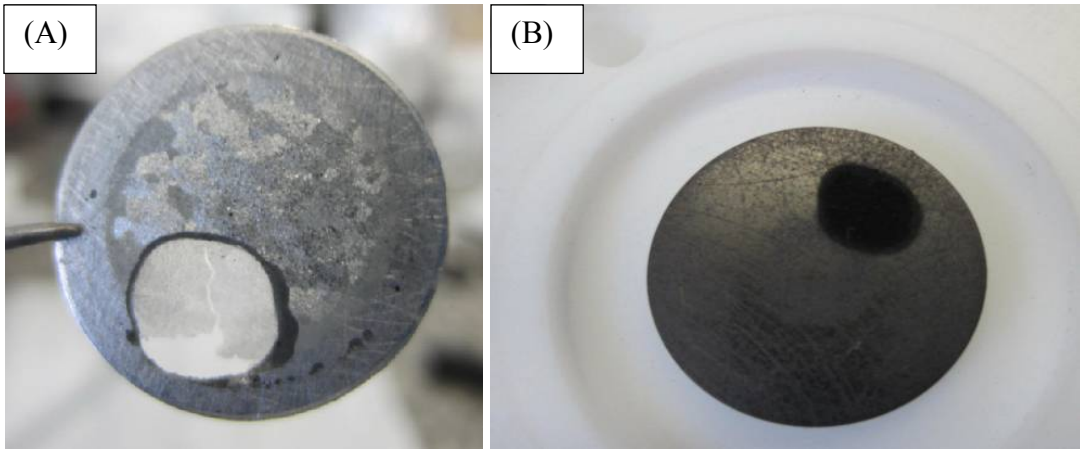

Fig. 3.15. Photographs of the PAA template with a hole formed during anodization (A) and (B) graphite electrode was damaged during the anodization.

In most cases when the samples were pre-treated, the temperature of the electrolyte solution dramatically increased (by up to 10 °C from a typical value of 16 °C) within the first few minutes of the anodization process. This contrasts with anodization of foil that had not been pre-treated where the temperature change was typically 0.5 °C in 10-15 min. The rapid rise in temperature for pre-treated foils suggests that very rapid anodization occurs at a localised area. When perforation occurred and the anodization was not stopped in time, the underlying graphite electrode was etched (Fig. 3.15 (B)). The reason for the perforation is assumed to be localised changes in characteristics of the Al foil as a result of annealing and electropolishing. Al foil undergoes re-crystallization during annealing process and is noticeably softer after annealing. This re-crystallization, if non-uniform across the sample could lead to the localised increase in the dissolution rate of the Al and non-uniform electropolishing could have a same effect.

Clearly these results are different to those in the literature that claim an improvement in PAA structure after the foil pre-treatment. Considering possible reasons for this, the tube furnace used in this work for annealing does not have a vacuum system to pump the air out.

Hence, traces of $O_{2(g)}$ may be present despite the long $Ar_{(g)}$ purge time. Also, the level of the $O_{2(g)}$ in the $Ar_{(g)}$ used was 0.0005 % and it is possible that traces of $O_{2(g)}$ cause the problems. The possible importance of trace $O_{2(g)}$ is unknown as no relevant details considering annealing conditions could be found in the literature.

Due to the lack of evidence that pre-treatment at Al foil could improve the quality of PAA membranes, in subsequent experiments the Al foils were simply degreased prior to anodization.

3.3.2 Comparison of 2 and 3-step anodization processes

To design a shallow Al_2O_3 membrane as a substrate for Co NP deposition, the uniformity of pore shape, pore size, barrier layer thickness and structure are very important. The thickness of the aluminium oxide wall separating two adjacent pores is approximately equal to the thickness of barrier layer (see Fig. 3.16. b, right-hand side SEM image of PAA cross-section for example). Hence, measurements of the wall thickness performed based on the top-view SEM images can be used as estimates of the thickness of the barrier layer.[18] Therefore, the uniformity of the barrier layer structure can be evaluated by observing the top view of the porous membrane. The depth of pores is controlled by the duration of the anodization process. The pores self-order during the anodization process which means a minimum duration of anodization is essential in order to form a uniform pore structure. In the previous study by Xu, good uniformity of pores with the average pore depth of 4 μm was achieved after a 2- step anodization process at 30 V in 0.4 M oxalic acid at 16 ± 1 °C.[33] The duration of the 2nd anodization was 1 h.

For the present work, a shallow membrane is required. So, in initial experiments, the duration of 2nd anodization was shortened to 90 s while maintaining other conditions of Xu's anodization procedure constant. The choice of this anodization time is based on results reported by Yuan *et al.* who demonstrated that the current density could reach steady state in 90-100 s during the 2nd anodization under very similar conditions (Fig. 3.6).[28] Table 3.3 compares the anodizing conditions used by Yuan *et al., by* Xu and this work.[28,33]

Table 3.3. The comparison of three anodization conditions.

	Yuan. *et. al.*[28]	Xu[33]	This work
Purity of Al foil	99.99 %	99.995 %	99.9995%
Concentration of oxalic acid	0.5 M	0.4 M	0.4 M
Applied voltage	30 V	30 V	30 V
1st anodization time	1h	2h	2h
2nd anodization time	1h	1h	90s
Temperature	15 °C	16 ± 1 °C	16 ± 1 °C

The morphology of the pores formed during the 2nd anodization which was carried out for 90 s was not uniform. Fig. 3.17 (A) and (B) show the top view and the cross section of the PAA membrane respectively. The shape of pore openings is variable and there is a wide range of pore size (Fig. 3.17 (A)). Fig. 3.17 (B) shows that the depth of the pores is approximately 500 nm. Note that this value has considerable uncertainty because to image pore depth, the sample was bent to crack the PAA membrane. Hence the tilt angle of the sample in the image is unknown. Nevertheless, it is clear that a shallow membrane has been generated. On the other hand, the non-uniform pores suggested that the underlying barrier layer is likely to have variable thickness and irregular arrangement of dimples.

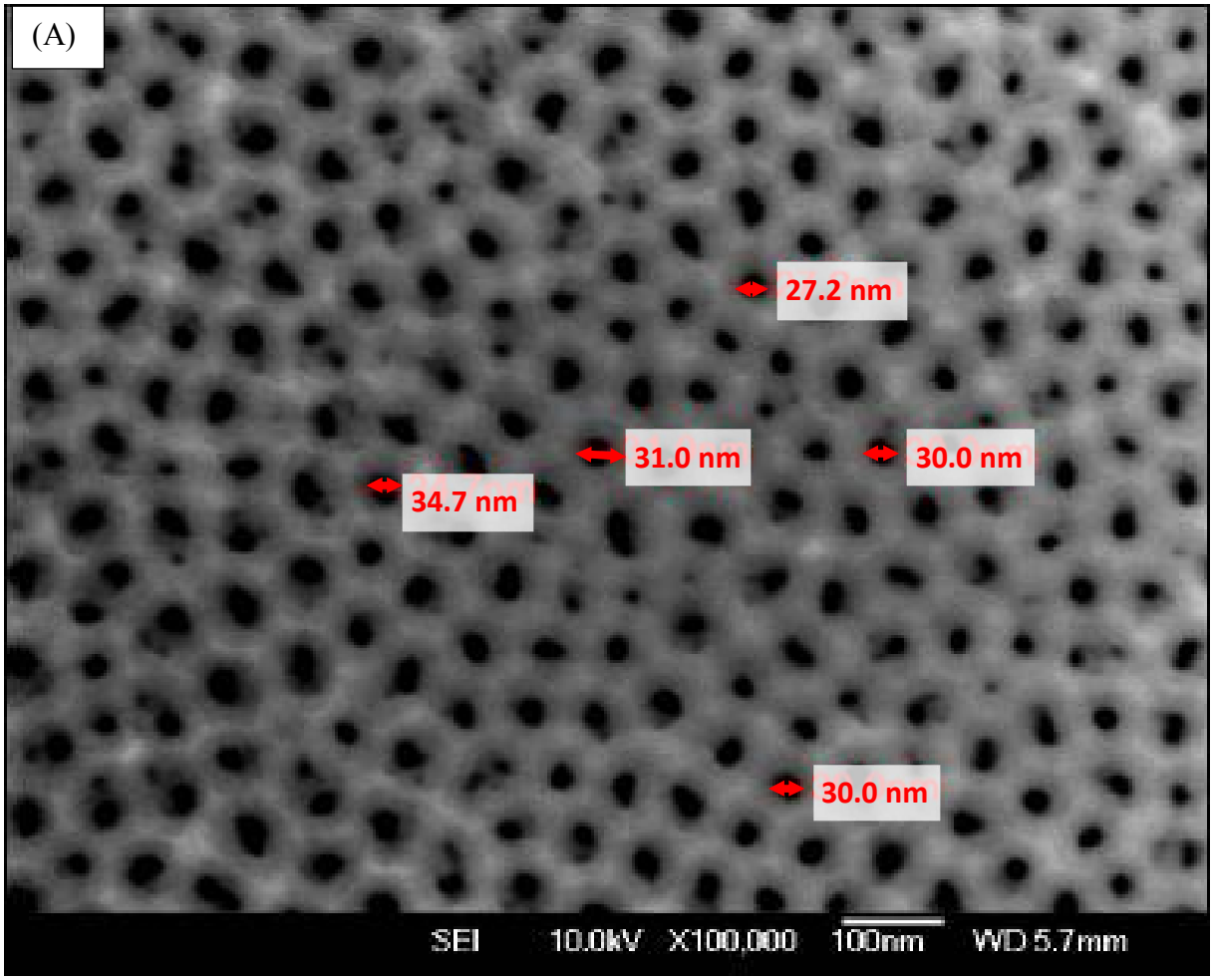
(A)
27.2 nm
31.0 nm
30.0 nm
34.7 nm
30.0 nm
SEI 10.0kV X100,000 100nm WD 5.7mm

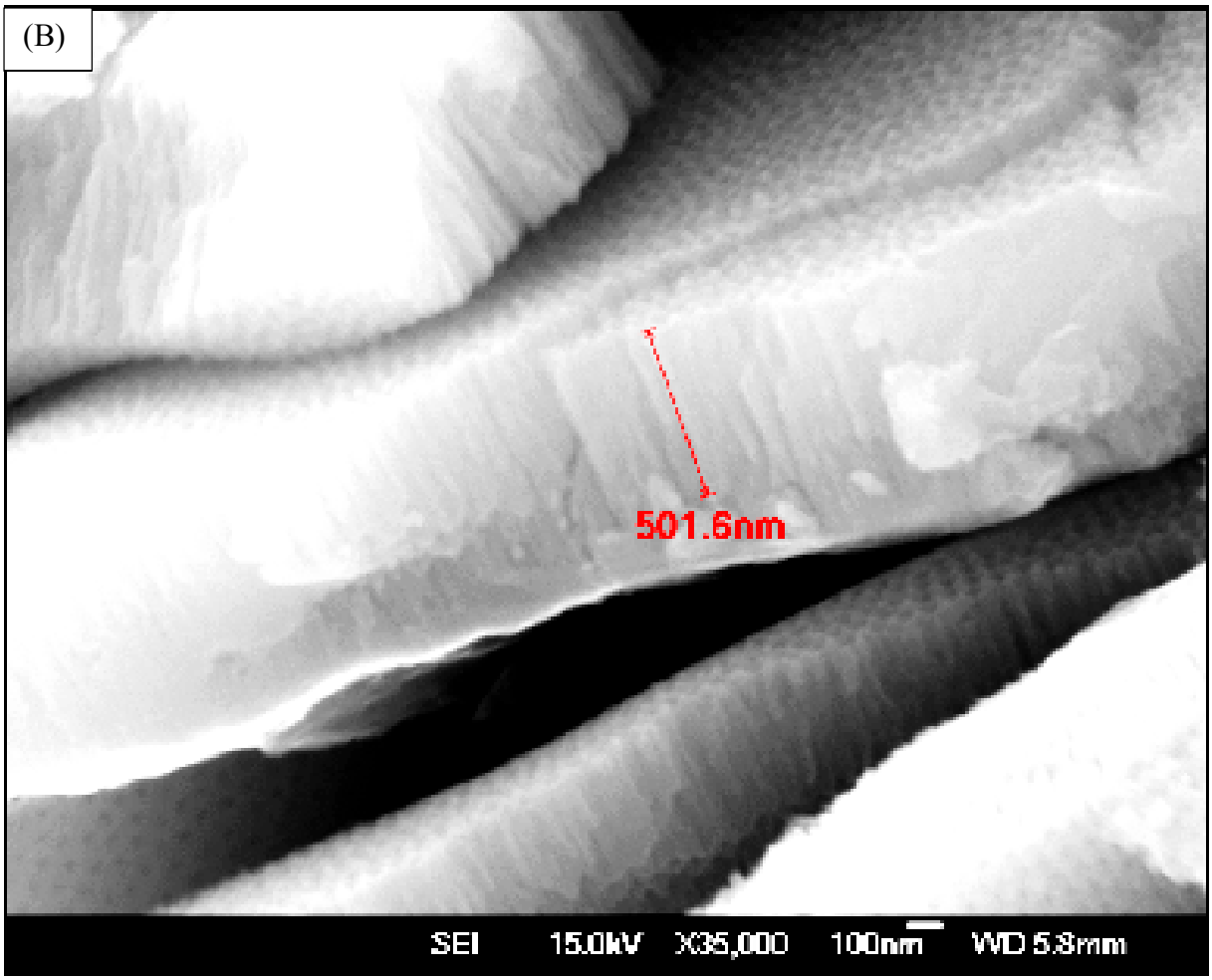

Fig. 3.17. SEM image of PAA membrane which was made by 2-step anodization process: (A) top view and (B) cross section. The duration of the 2nd anodization was 90 s.

There are two possible reasons for the observed non-uniformity. Firstly, during the very brief 2nd anodization process, the current may not have reached steady state. Secondly, it possible that the dimpled structure formed by removing the porous Al_2O_3 layer fabricated during the 1st anodization process is not sufficiently ordered to form an ordered shallow porous Al_2O_3 membrane after a short 2nd anodization time. Based on the studies of multi anodization steps of Hwang *et al.*[22] and Chen *et al.*[29] discussed in the introduction, it was decided to investigate to use of an additional anodization step as a means of generating a

more uniform structure. The aim of this work is to obtain a *shallow* ordered PAA membrane and hence the 3-step anodization process involved two "long" anodization steps (with removal of the Al_2O_3 after each step), and a final short anodization to give a shallow membrane.

The optimum procedures for obtaining a PAA membrane with the ordered characteristic involved a 1st anodization for 2 h, a second for 1 h and a third for 30s. Fig. 3.18 (A) shows the morphology of pores after the 3rd anodization for 30 s and Fig. 3.18 (B) shows the cross section of this membrane. Fig. 3.19 shows a histogram of the pore diameters; the average diameter is 29 nm ± 3 nm. The depth of the pores is estimated to be close to 300 nm but as explained earlier, difficulties in imaging prevent a quantitative analysis. The pores are clearly much more uniform than the ones formed using 2-step anodization.

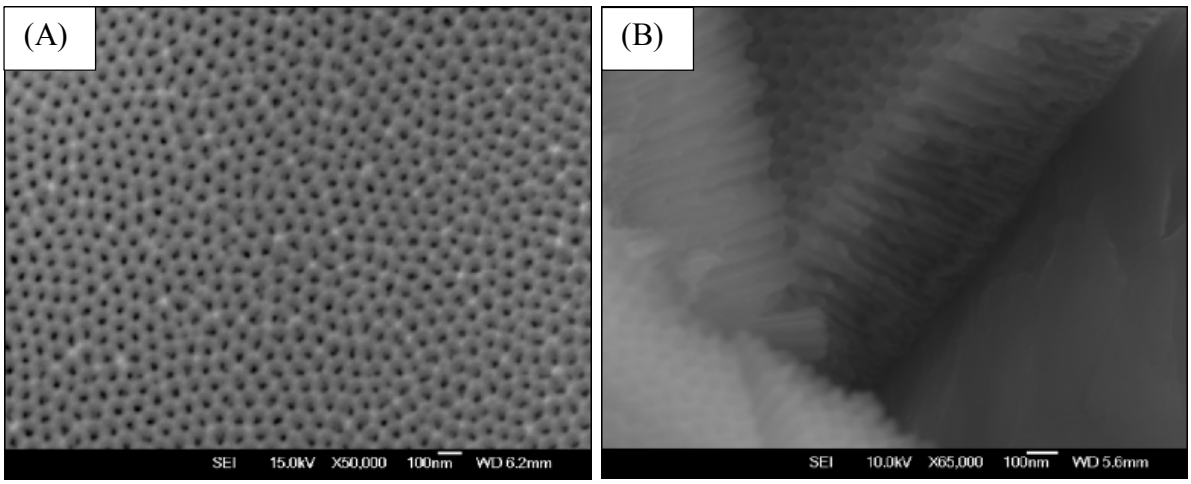

Fig. 3.18. SEM image of a PAA membrane which was made by 3-step anodization process: (A) top view and (B) cross section. The duration of the 1st anodization was 1hr, 2nd anodization was 1 hr and 3rd anodization process was 30s.

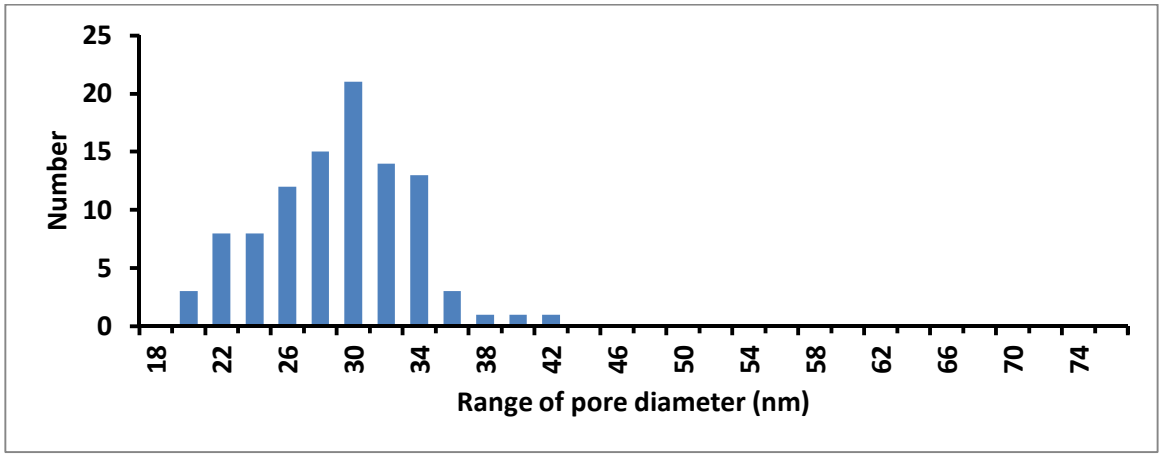

Fig. 3.19. The distributions of diameters of pores on PAA template after 3-step anodization

It was expected that growth of CNTs in the PAA membrane would be facilitated by minimising the pore depth and hence a shorter 3rd anodization time was investigated. Pores formed in a 10 s anodization were found to be disordered with widely variable pore size (Fig. 3.20 (A) and (B)). It is likely that the current density did not reach steady state in this case as would be expected considering the current density *vs.* time curve shown in Fig. 3.6.

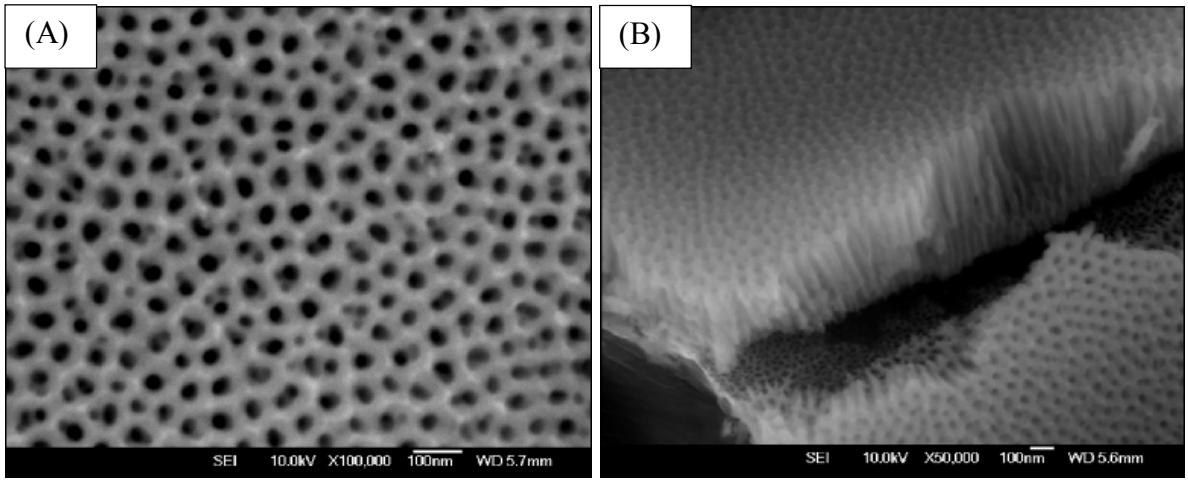

Fig. 3.20. SEM images of PAA membrane which was made by 3-step anodization process. The duration of the 3rd anodization process was 10 s (A) top view and (B) cross section.

3.3.3 Chemical Etching

For use of the membrane as a template for electrodeposition of Co NPs at the bottom of the pores, the thickness of barrier layer and the wall thickness will strongly affect the electrodeposition. Reducing the thickness of the barrier layer should improve its conductivity and improve the uniformity of electrodeposition of Co NPs. Moreover, widening the pores will ensure that diffusion of the Co^{2+} ions towards barrier layer is not hindered. The following chemical reaction takes place during etching:

$$6H^{+} + Al_2O_3 \rightarrow 2Al^{3+} + 3H_2O$$

Commonly used conditions for thinning the barrier layer include use of 0.1-0.6 M H_3PO_4, at approximately 30 °C for 12-90 min.[40,41] However, these conditions have been applied to significantly thicker membranes than those prepared in this work.[40,41] The conditions used by Xu to etch his 4 μm thick PAA membrane (0.1 M H_3PO_4 at 30 ± 1°C for 1 h) were initially examined to etch the shallow membranes generated in this work.[33] The SEM images of Fig. 3.21 (A) and (B) show the pores before and after chemical etching for 1 h. Etching reduces the wall thickness by approximately 20 nm.

According to Han *et al*., the rate of barrier layer is etching much faster than that of the pore due to the lower density of the barrier layer.[42] The lower density is attributed to a mixed structure which incorporates oxalate anions (Ox) in addition to O^{2-} giving a composite of $Al_2(Ox)_3$ and Al_2O_3.[42] Han *et al.* demonstrated that the barrier layer can be completely removed by chemical etching in 5 % H_3PO_4 (approximately 0.5 M) solution for 40 min.[42] Hence, further experiments were undertaken to establish the maximum etching time in 0.1 M H_3PO_4 that could be used without decreasing the uniformity of the pores. It was assumed that

these conditions would give the minimum barrier thickness while maintaining an ordered pore structure.

In this systematic study, chemical etching times of 60, 65 and 70 min were used and results were compared to the non-etched membrane. The four SEM images in Fig. 3.21 compare the morphologies of pores before and after the chemical etching process. Histograms of pore diameter distributions are also provided in

Fig. 3.22. Image J software was used to count the area of individual pores openings and convert the measurements to the diameters of pores, assuming circular pores. As expected, the diameter of pore increased with etching time. After chemical etching for 65 min, the average diameter of pores is approximately 60 nm. Although a few defects can be observed on the membrane, the distribution of diameters is acceptable (Fig. 3.22 (C)). Etching for 70 min gave a broad distribution of pore diameters (Fig. 3.22 (D)). Hemce, 65 min was adopted as the stabdard etching time.

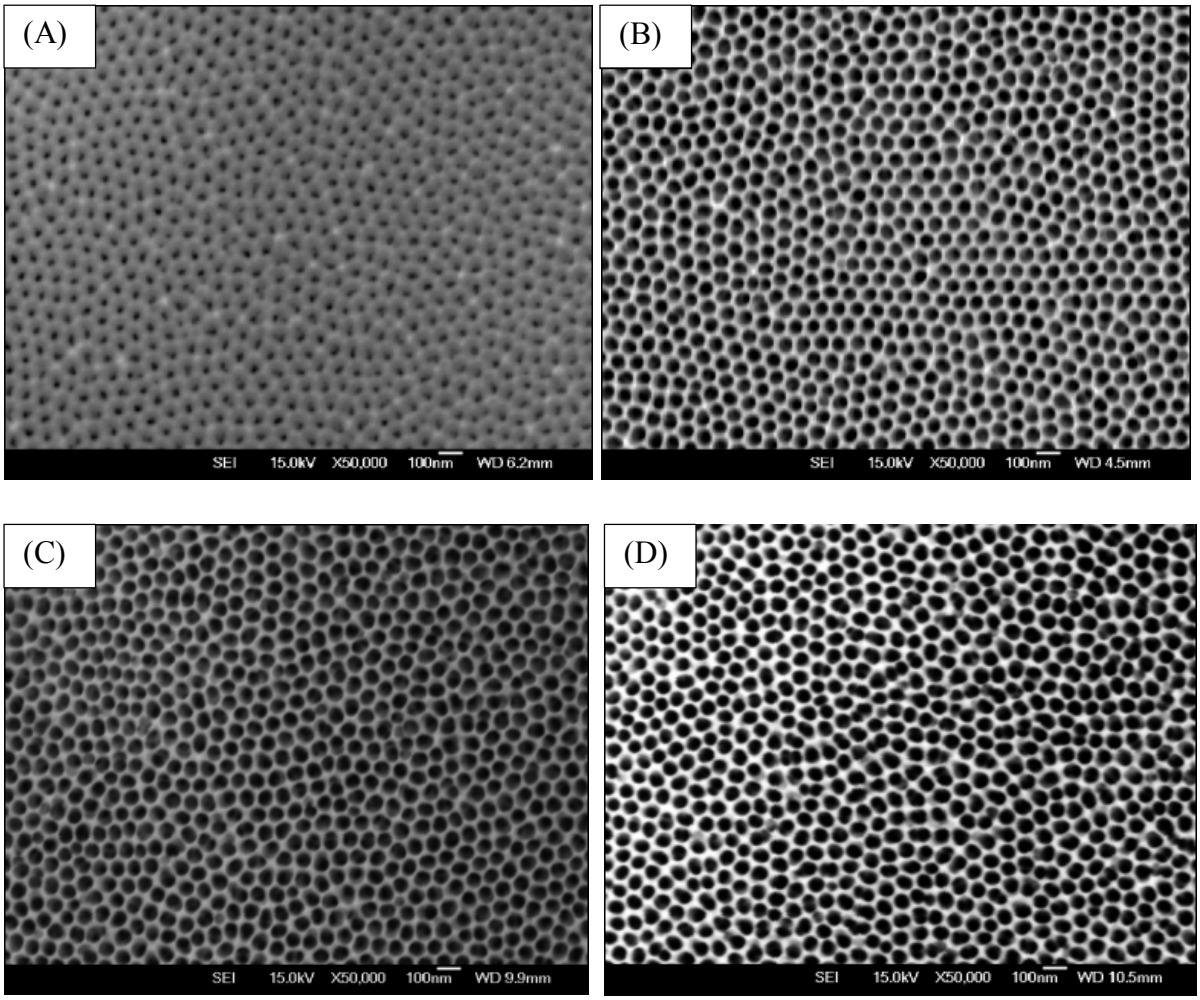

Fig. 3.21. SEM images of pores of PAA membranes which have been chemically etched for (A) 0 min, (B) 60 min, (C) 65 min and (D) 70 min in 0.1 M H_3PO_4 at 30 ± 1 °C.

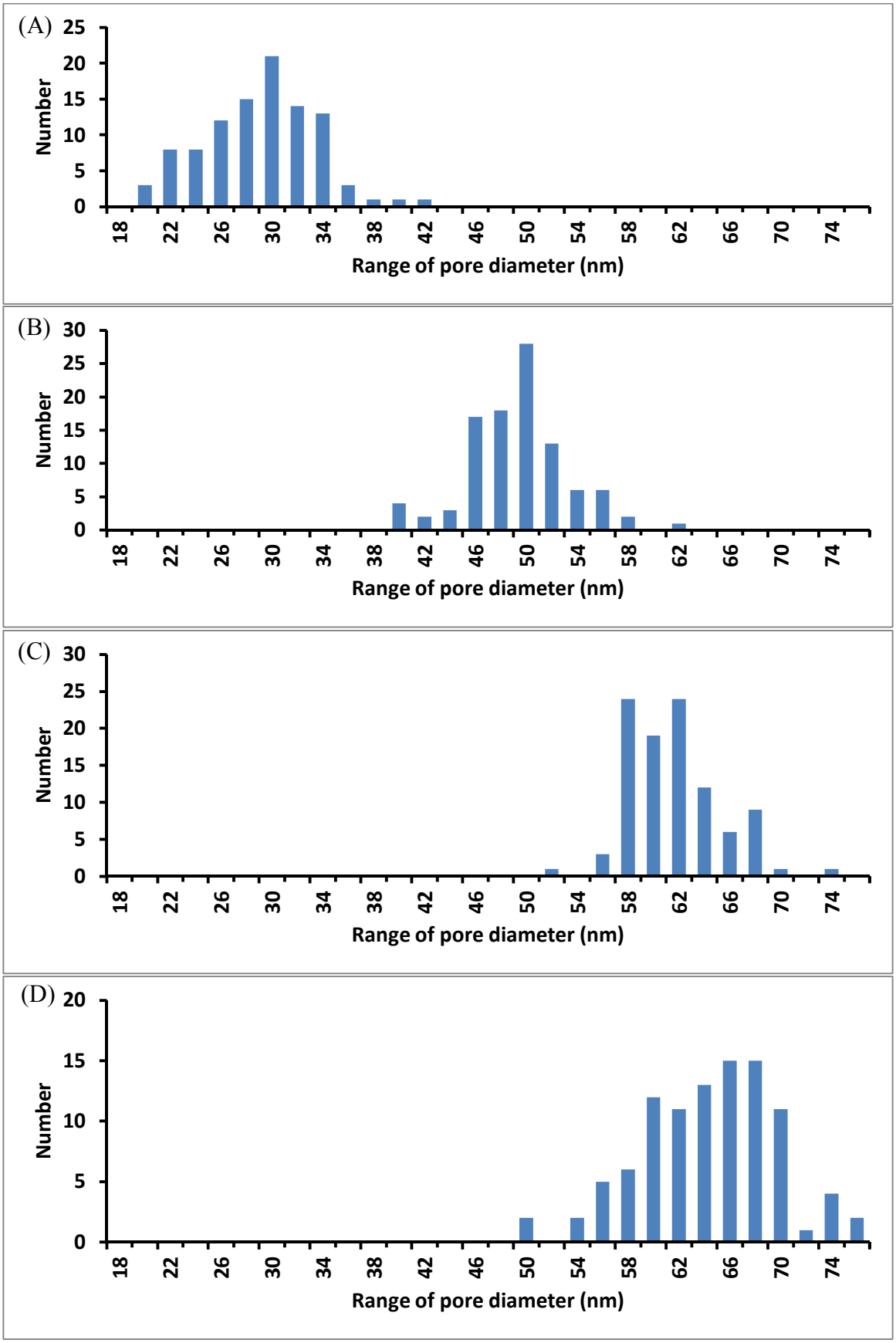

Fig. 3.22. The distributions of diameters of pores on PAA template which have been chemical etched for (A) 0 min (re-showed here for convenience), (B) 60 min, (C) 65 min and (D) 70 min.

3.3.4 Fabrication of dimpled Al_2O_3 membrane

A very thin dimpled Al_2O_3 layer is naturally formed after removing the porous Al_2O_3 layer formed by anodization. This dimpled structure can be observed by AFM (Fig. 3.23 and Fig. 3.24) and SEM (Fig. 3.25). Fig. 3.23 (A) shows a top view AFM image of the dimpled Al_2O_3 layer after removing the porous structure which was made by the first anodization step. Although the structure appears uniform on the three-dimensional image (Fig. 3.23 (B)), the depth of these dimples is variable ranging between 13-26 nm (Fig. 3.23 (C)). In fact, deeper dimples may be present but are unable to be accessed by the AFM tip.

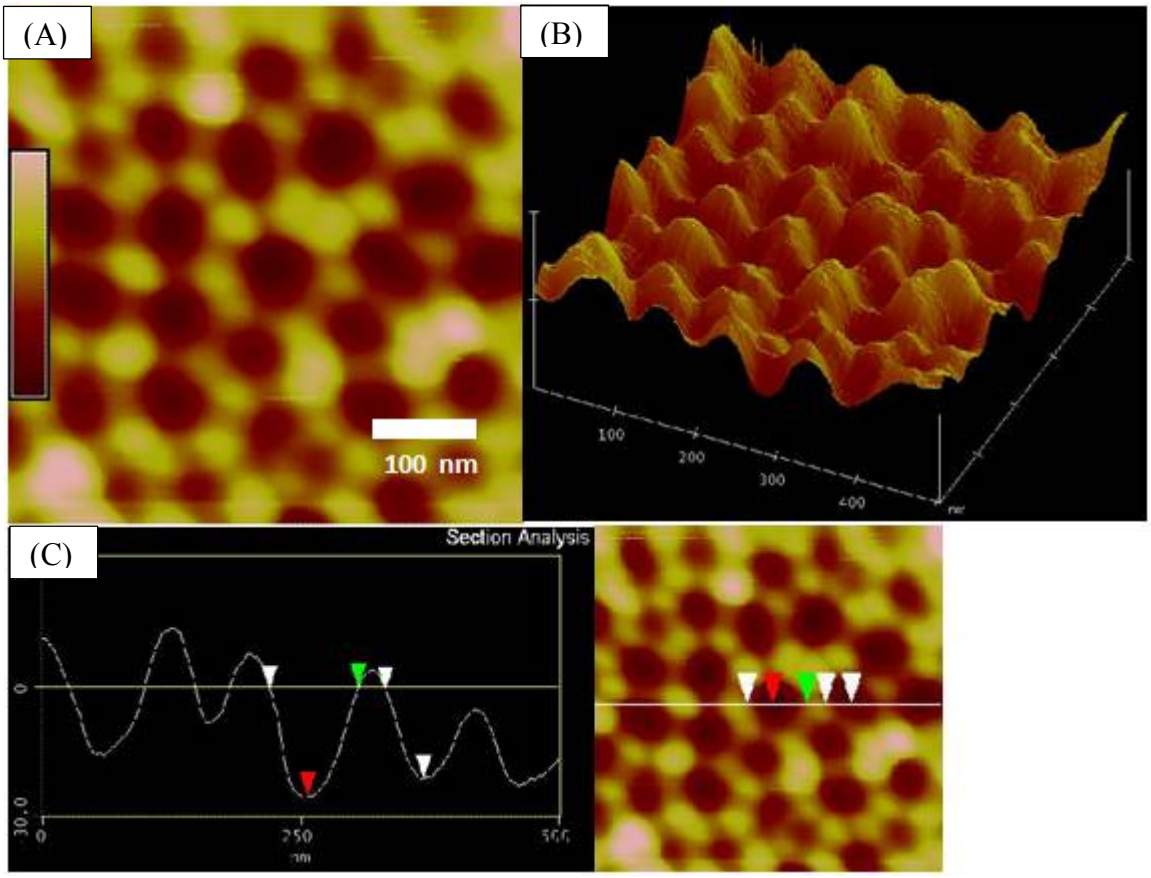

Fig. 3.23. The AFM images of dimple Al_2O_3 template after removing the oxidised layer which was formed in the 1st anodization process.

Fig. 3.24 (A) shows a top view AFM image of the dimpled step Al_2O_3 layer after removing the porous structure which was made by a second anodization step. A more ordered dimpled structure is indicated by the appearance of the more extended hexagonal structure. The diameter of the dimple at the surface and the depth and spacing of the dimples are more uniform than after the first anodization (Fig. 3.24 (B)). Fig. 3.24 (C) shows the depth of the dimples is 13-17 nm and the diameters of the dimple are approximately 60 nm. The SEM image in Fig. 3.25 provides an alternative measurement of the diameter of the dimples.

The significant improvement in the uniformity of the dimpled substrate after two long anodization steps accounts for the significant improvement of the shallow membrane formed by 3 rather than 2 anodization steps.

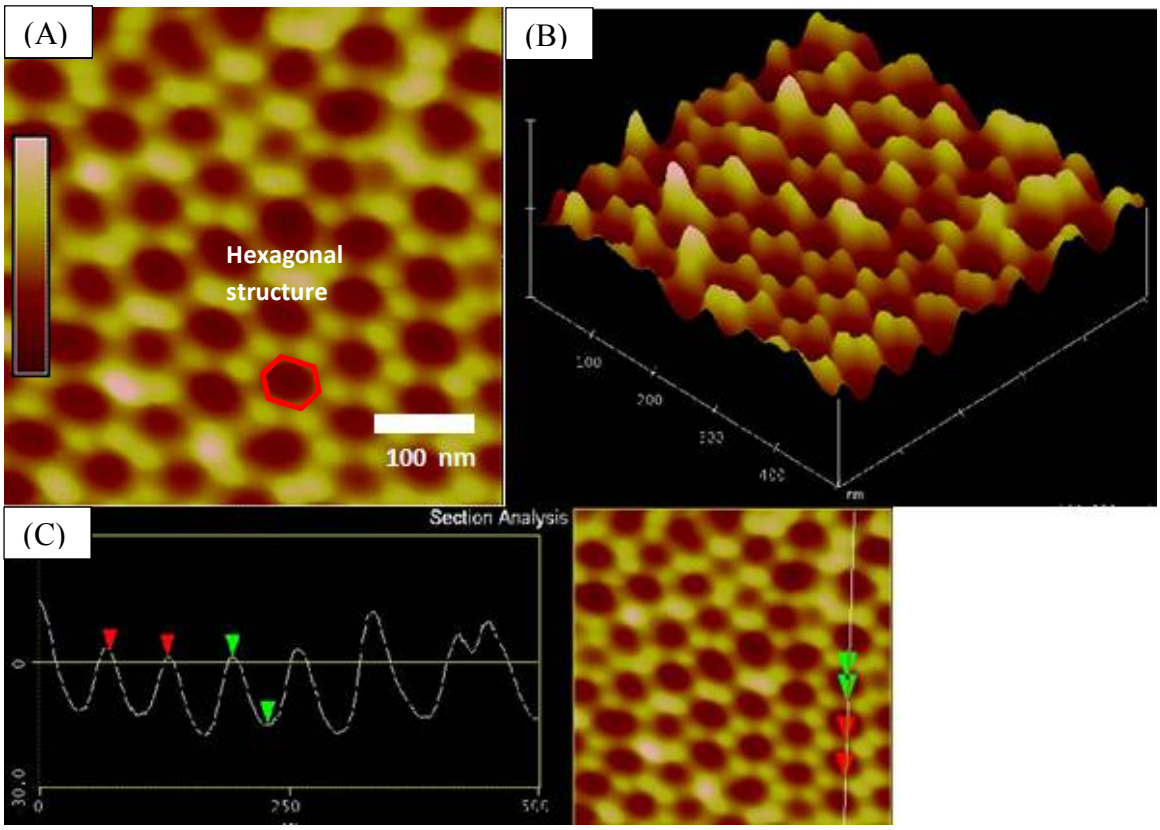

Fig. 3.24. The AFM image of dimple Al_2O_3 template after removing the oxidised layer which was formed in the 2nd anodization process. The hexagonal structure is highlighted in (A).

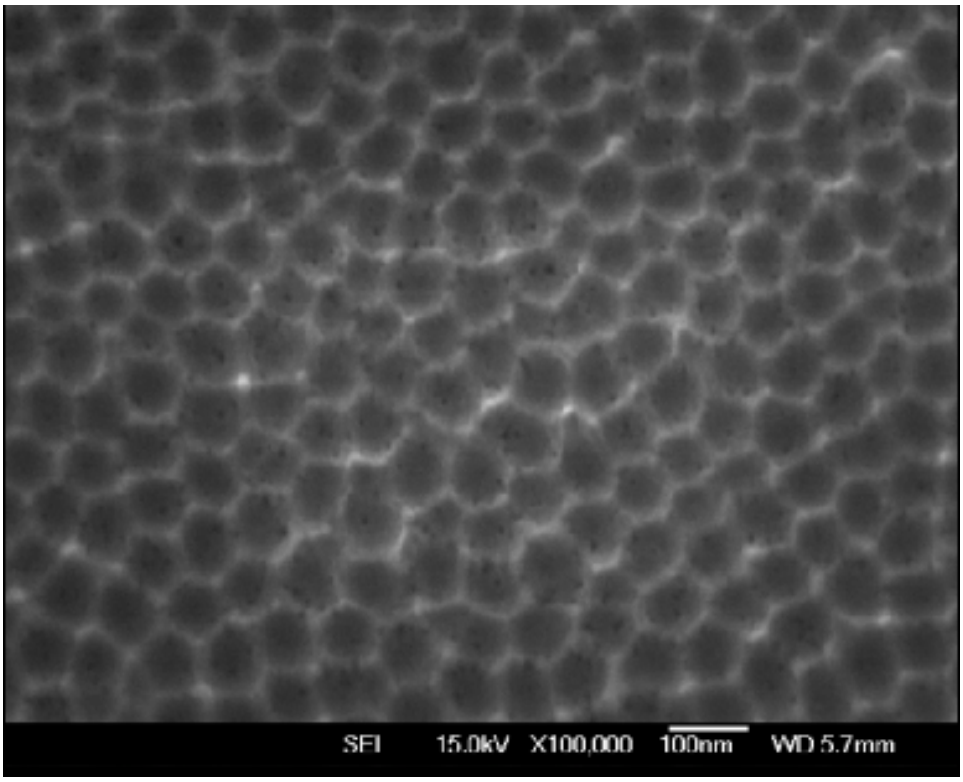

Fig. 3.25. The SEM image of dimpled Al_2O_3 template after removing the oxidised layer which was formed in the 2nd anodization process.

3.3.5 Fabrication the PAA template with opened inner pore ends

An alternative fabrication strategy was attempted with the aim of avoiding complications arising from Co NP deposition at a barrier layer of poor uniformity. This strategy was adapted from one used successfully with much thicker PAA membranes.[43] The strategy is presented in Fig. 3.26. A layer of Au is sputtered onto the top of the PAA template. This Au layer could be thick enough to act as a mechanical support for the porous Al_2O_3 structure yet without completely filling up the pores. Then the PAA template is turned upside down and placed in the PTFE holder shown in the bottom left corner of Fig. 3.26. The Al at the base of the PAA membrane (now on the top side) could be selectively dissolved within the two small areas defined by O-rings by carefully placing a few drops of solution

containing 0.51 g of $CuCl_2$, 25 mL of distilled water and 5 mL of HCl (38 %). After Al is removed (eq. 8 and 9 show the reaction), the barrier layer could be removed by a short chemical etching in H_3PO_4 solution leaving the remaining PAA membrane intact, but with open pores.[44]

$$2Al_{(s)} + 6H^{+}_{(aq)} \rightarrow 2\ Al^{3+}_{(aq)} + 3H_{2(g)} \qquad \text{(eq. 8)}$$

$$3CuCl_{2(s)} + 2Al_{(s)} \rightarrow 3Cu_{(s)} + 2AlCl_{3(s)} \qquad \text{(eq. 9)}$$

To make sure that the strategy would work as described above, an initial and simplified experiment was performed. The layer of sputtered Au was replaced with nail polish which was brush-coated on the top of the PAA template after anodization. Nail polish is a convenient and cheap material, which has been previously used for fixing and supporting porous Al_2O_3 structures when removing Al from underneath the PAA template.[45] Under optimized conditions (*i.e.* when the Al layer is successfully removed), Lillo *et al*. observed the bottom of the barrier layer using SEM as is illustrated by the image in the top right corner of Fig. 3.24. Success of this preliminary trial using the nail polish coating would indicate that the experiment using a sputtered Au layer is achievable, without damaging the remaining porous Al_2O_3 structure.

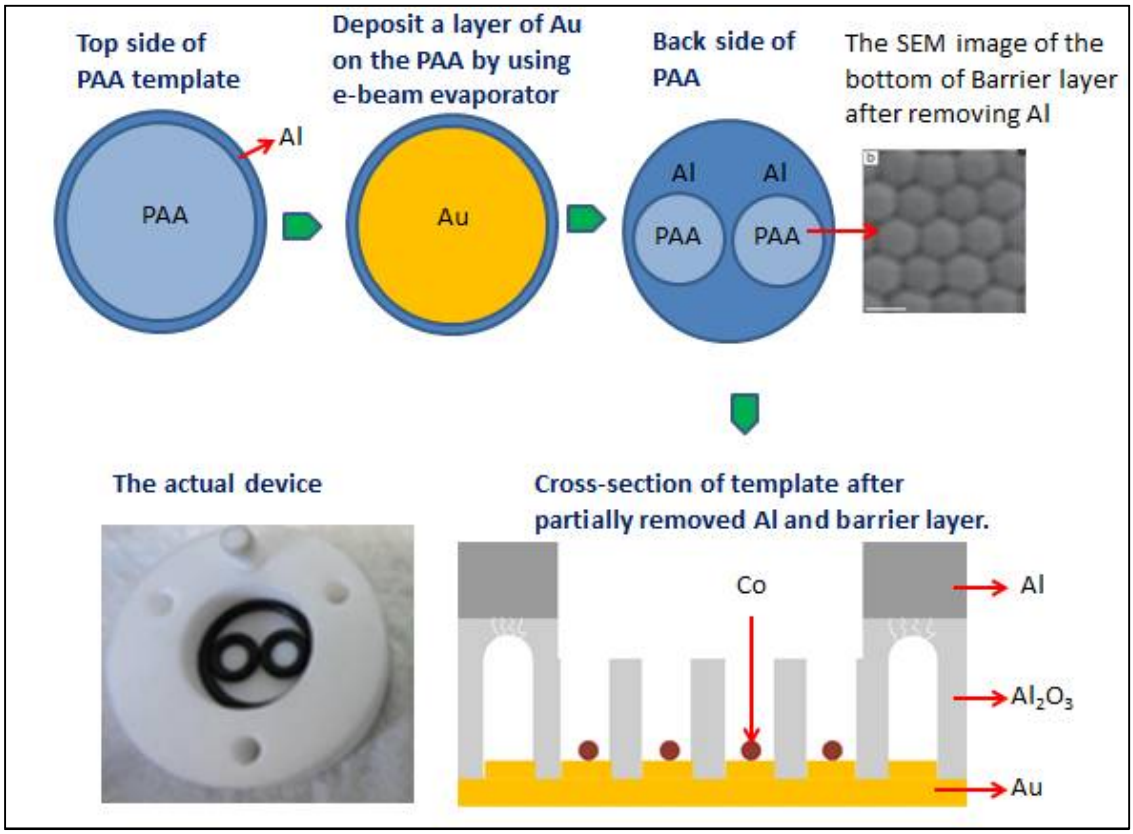

Fig. 3.26. The scheme of the fabrication of the PAA template with opened pore ends and deposition of Co nanoparticles.

The nail polish was coated in 3 layers on the top of the PAA template which was made using a 3-step anodization and barrier layer thinning process as was discussed earlier. After air drying the nail polish, the PAA template was placed in the PTFE device (shown in Fig. 3.26) and removal of the Al layer attempted. Although the Al layer can be dissolved effectively (as evidenced by vigorous bubbling and formation of flakes of metallic Cu), it is very difficult to estimate by visual inspection the exact moment when the Al has been removed completely. In all cases, the whole porous Al_2O_3 structure were removed or alternatively the Al was not removed completely (Fig. 3.27). A further problem was that metallic copper deposition during the etching reaction could not be removed by washing.

Fig. 3.27 (A) shows the back side of an Al_2O_3 membrane after application of $CuCl_2$ solution in two areas. The dark colour is metallic copper. In the left hand circular area, there

is a hole through the membrane, as shown in the front-side image of Fig. 3.27 (B). Closer examination of the damaged area by SEM (Fig. 3.27 (C)) shows the spiky brush-like copper deposition and residual porous Al_2O_3 structure. SEM analysis of the second area in Fig. 3.27 which has a continuous copper layer did not show any Al_2O_3 areas (Fig. 3.27 (E) and (F)). Hence, it is assumed that Al remains of the surface.

Therefore, this study was not continued (deposition of Au in place of nail polish was not attempted) because it proved to be impossible to avoid damaging the thin and fragile PAA film. The next chapter describes electrodeposition of Co NPs using PAA membrane with thinned barrier layers.

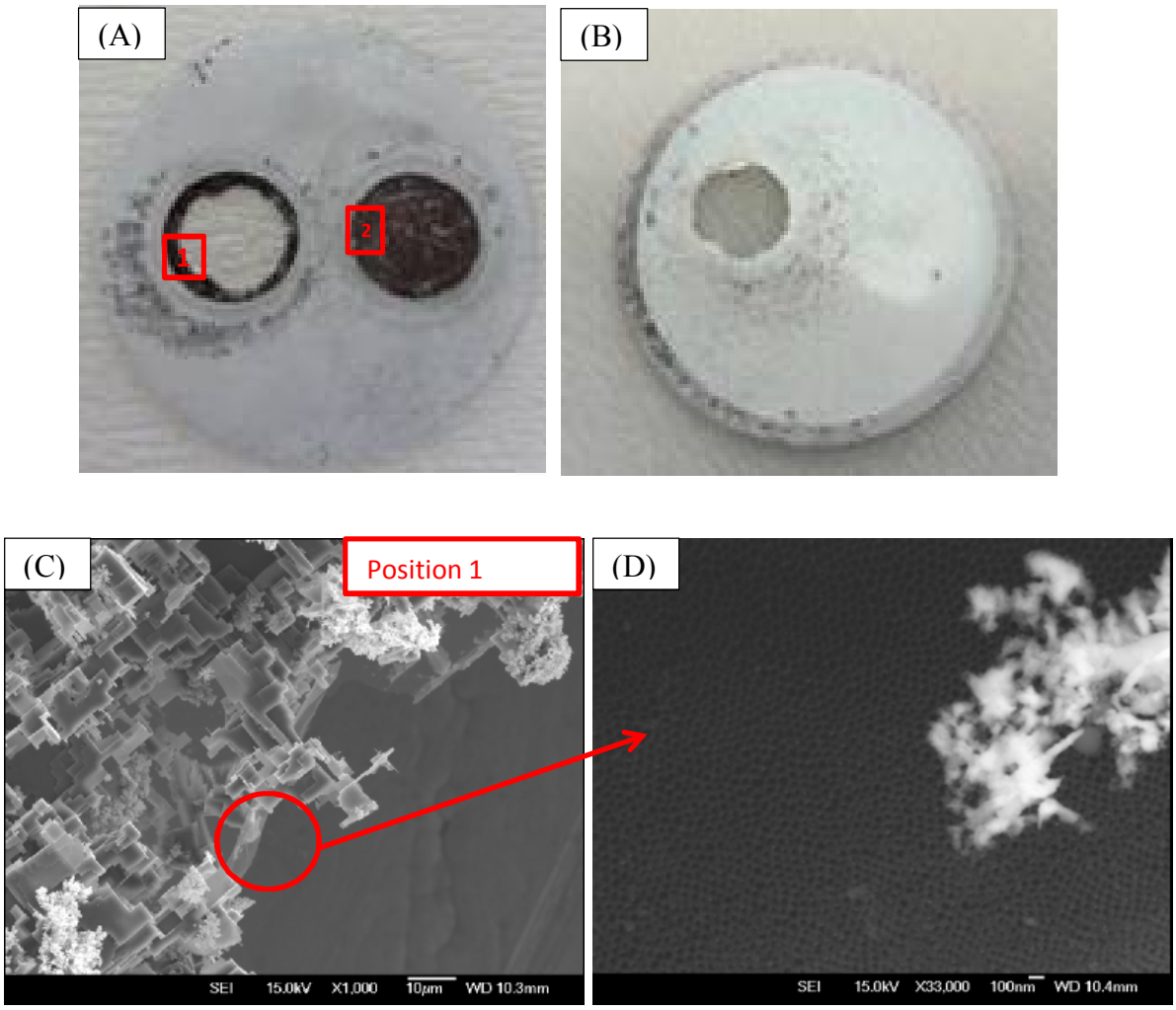

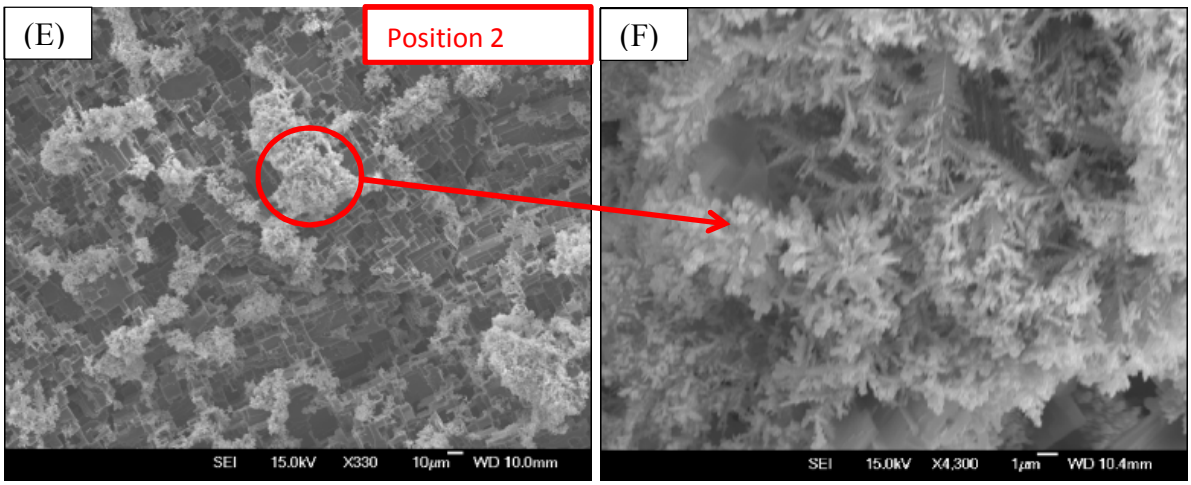

Fig. 3.27. The images of an opened PAA template after partially removing Al in two small circular areas. (A) is the back side of the PAA template; (B) is the top side of the PAA template; (C) refers to positions on (A); (D) high magnification of SEM image of the circular area in (C); (E) refers to position 2 in (A) and (F) high magnification SEM image of the circular area in (E).

3.4 Conclusions

The optimised fabrication of PAA membranes aimed to improve the subsequent uniformity of Co NP electrodeposition and to facilitate the mass transfer for gases during CNT growth by CVD. Therefore, fabricating a shallow PAA membrane with the depth of pore in a range between 100-600 nm was a goal for the catalyst system which is a template for CNT growth. Annealing and electrochemical polish were tried in this work as many reports suggest that the amount of impurities and grain boundaries of the Al foil can be reduced by using these strategies. However, annealing and electrochemical polishing led to damage of the Al foil during the anodization process. Alternatively, a 3-step anodization process was utilised in order to fabricate a highly ordered porous structure for a shallow membrane. Anodization time of 10 s for the 3rd anodization was too short to form a uniform pore structure. Ultimately, the shallow porous membrane was prepared using a 30 s 3rd

anodization. The depth of the pore is 300 nm and the average diameter of the pore is 30-35 nm according to the measurements from SEM image.

After 3-step anodization, electrochemical thinning of the barrier layer, and chemical etching was also applied, chemical etching for 65 min gives the largest diameter of pore (*ca.* 60 nm) while maintaining an ordered structure.

The study of the dimpled Al_2O_3 membrane by AFM shows the dimple base on Al foil (after removal of the porous Al_2O_3 structure) is more uniform after the 2nd anodization than after the 1st anodization. This is also supported by the observation of a highly uniform porous Al_2O_3 structure after a 3-step anodization process. This dimpled Al_2O_3 substrate has potential for other application due to its special texture. For example, a template for forming the order metal NPs by depositing a thin layer of metal on it and annealing the template which cause agglomeration at the bottom of the dimples.

Finally, an alternative fabrication of a PAA template with opened inner pore ends was attempted. However, this strategy was not successful in this work due to the unoptimised etching process. The spiky brush-like Cu structures were formed on the porous Al_2O_3 structure which cannot be removed. Additionally, the shallow PAA membrane proved to be too fragile to survive manipulations during this experiment.

3.5 References

1. Mizeikis, V.; Mikulskas, I.; Tomasiunas, R.; Juodkazis, S.; Matsuo, S.; Misawa, H., Optical characteristics of two-dimensional photonic crystals in anodic aluminum oxide films. *Jpn. J. Appl. Phys. Part 1 - Regul. Pap. Short Notes Rev. Pap.* **2004,** *43* (6A), 3643-3647.
2. Wang, Y. D.; Zang, K. Y.; Chua, S. J.; Tripathy, S.; Chen, P.; Fonstad, C. G., Nanoair-bridged lateral overgrowth of GaN on ordered nanoporous GaN template. *Appl. Phys. Lett.* **2005,** *87* (25).
3. Shelimov, K. B.; Davydov, D. N.; Moskovits, M., Template-grown high-density nanocapacitor arrays. *Appl. Phys. Lett.* **2000,** *77* (11), 1722-1724.
4. Nahar, R. K., Study of the performance degradation of thin film aluminum oxide sensor at high humidity. *Sens. Actuator B-Chem.* **2000,** *63* (1-2), 49-54.
5. Yilmazoglu, O.; Popp, A.; Pavlidis, D.; Schneider, J. J.; Garth, D.; Schuttler, F.; Battenberg, G., Vertically aligned multiwalled carbon nanotubes for pressure, tactile and vibration sensing. *Nanotechnology* **2012,** *23* (8), 085501.
6. Report on self-ordered porous alumina template technology. *N2T2 european framwork 6 grant.*
[On line] https://wiki.bath.ac.uk/display/N2T2/Research+Output accessed on 01.03.2014.
7. Li, D. D.; Jiang, C. H.; Ren, X.; Long, M. C.; Jiang, J. H., Fabrication of porous anodic alumina membranes with ultrathick barrier layer. *Mater. Lett.* **2008,** *62* (17-18), 3228-3231.
8. Diggle, J. W.; Downie, T. C.; Goulding, C. W., Anodic oxide films on aluminium. *Chem. Rev.* **1969,** *69* (3), 365-405.
9. Keller, F.; Hunter, M. S.; Robinson, D. L., Structural features of oxide coatings on aluminium. *J. Electrochem. Soc.* **1953,** *100* (9), 411-419.
10. Eftekhari, A., Nanostructured materials in electrochemistry. *Wiley-VCH: Weinheim*, **2008**.
11. Lee, W.; Ji, R.; Gosele, U.; Nielsch, K., Fast fabrication of long-range ordered porous alumina membranes by hard anodization. *Nat. Mater.* **2006,** *5* (9), 741-747.
12. Chu, S. Z.; Wada, K.; Inoue, S.; Isogai, M.; Yasumori, A., Fabrication of ideally ordered nanoporous alumina films and integrated alumina nanotubule arrays by high-field anodization. *Adv. Mater.* **2005,** *17* (17), 2115-2119.
13. Thompson, G. E.; Furneaux, R. C.; Wood, G. C.; Richardson, J. A.; Goode, J. S., Nucleation and growth of porous anodic films on aluminium. *Nature* **1978,** *272* (5652), 433-435.
14. Shingubara, S., Fabrication of nanomaterials using porous alumina templates. *J. Nanopart. Res.* **2003,** *5* (1-2), 17-30.
15. Osulliva.Jp; Wood, G. C., Morphology and mechanism of formation of porous anodic films on aluminium. *Proc. R. Soc. London, Ser. A* **1970,** *317* (1531), 511-543.
16. Jessensky, O.; Muller, F.; Gosele, U., Self-organized formation of hexagonal pore arrays in anodic alumina. *Appl. Phys. Lett.* **1998,** *72* (10), 1173-1175.
17. Wu, Z.; Richter, C.; Menon, L., A study of anodization process during pore formation in nanoporous alumina templates. *J. Electrochem. Soc.* **2007,** *154* (1), E8-E12.
18. Su, Z. X.; Zhou, W. Z., Formation mechanism of porous anodic aluminium and titanium oxides. *Adv. Mater.* **2008,** *20* (19), 3663-3667.

19. Chung, C. K.; Liao, M. W.; Lee, C. T.; Chang, H. C., Anodization of nanoporous alumina on impurity-induced hemisphere curved surface of aluminum at room temperature. *Nanoscale Res. Lett.* **2011,** *6*, 596.
20. Thompson, G. E., Porous anodic alumina: Fabrication, characterization and applications. *Thin Solid Films* **1997,** *297* (1-2), 192-201.
21. Rana, K.; Kucukayan-Dogu, G.; Bengu, E., Growth of vertically aligned carbon nanotubes over self-ordered nano-porous alumina films and their surface properties. *Appl. Surf. Sci.* **2012,** *258* (18), 7112-7117.
22. Hwang, S. K.; Lee, J.; Jeong, S. H.; Lee, P. S.; Lee, K. H., Fabrication of carbon nanotube emitters in an anodic aluminium oxide nanotemplate on a Si wafer by multi-step anodization. *Nanotechnology* **2005,** *16* (6), 850-858.
23. Du, Y.; Cai, W. L.; Mo, C. M.; Chen, J.; Zhang, L. D.; Zhu, X. G., Preparation and photoluminescence of alumina membranes with ordered pore arrays. *Appl. Phys. Lett.* **1999,** *74* (20), 2951-2953.
24. Rauf, A.; Mehmood, M.; Rasheed, M. A.; Aslam, M., The effects of electropolishing on the nanochannel ordering of the porous anodic alumina prepared in oxalic acid. *J. Solid State Electrochem.* **2009,** *13* (2), 321-332.
25. Li, F. Y.; Zhang, L.; Metzger, R. M., On the growth of highly ordered pores in anodized aluminum oxide. *Chem. Mater.* **1998,** *10* (9), 2470-2480.
26. Masuda, H.; Fukuda, K., Ordered metal nanohole arrays made by a two-dtep replication of honeycomb dtructures of anodic alumina. *Science* **1995,** *268* (5216), 1466-1468.
27. Nielsch, K.; Muller, F.; Li, A. P.; Gosele, U., Uniform nickel deposition into ordered alumina pores by pulsed electrodeposition. *Adv. Mater.* **2000,** *12* (8), 582-586.
28. Yuan, J. H.; He, F. Y.; Sun, D. C.; Xia, X. H., A simple method for preparation of through-hole porous anodic alumina membrane. *Chem. Mater.* **2004,** *16* (10), 1841-1844.
29. Chen, C. K.; Chen, S. H., Multi-electrolyte-step anodic aluminum oxide method for the fabrication of self-organized nanochannel arrays. *Nanoscale Res. Lett.* **2012,** *7*, 122.
30. Ono, S.; Saito, M.; Asoh, H., Self-ordering of anodic porous alumina formed in organic acid electrolytes. *Electrochim. Acta* **2005,** *51* (5), 827-833.
31. Cheng, W. L.; Steinhart, M.; Gosele, U.; Wehrspohn, R. B., Tree-like alumina nanopores generated in a non-steady-state anodization. *J. Mater. Chem.* **2007,** *17* (33), 3493-3495.
32. Gerein, N. J.; Haber, J. A., Effect of ac electrodeposition conditions on the growth of high aspect ratio copper nanowires in porous aluminum oxide templates. *J. Phys. Chem. B* **2005,** *109* (37), 17372-17385.
33. Xu, R., Preparation and Characterisation of Vertically aligned carbon nanotubes. *MSc thesis of University of Canterbury. Chemistry* **2010**.
34. Sharma, G.; Pishko, M. V.; Grimes, C. A., Fabrication of metallic nanowire arrays by electrodeposition into nanoporous alumina membranes: effect of barrier layer. *J. Mater. Sci.* **2007,** *42* (13), 4738-4744.
35. Li, J.; Moskovits, M.; Haslett, T. L., Nanoscale electroless metal deposition in aligned carbon nanotubes. *Chem. Mater.* **1998,** *10* (7), 1963-1967.
36. Bocchetta, P.; Sunseri, C.; Masi, R.; Piazza, S.; Di Quarto, F., Influence of initial treatments of aluminium on the morphological features of electrochemically formed alumina membranes. *Mater. Sci. Eng. C-Biomimetic Supramol. Syst.* **2003,** *23* (6-8), 1021-1026.
37. Jensen, D. J.; Hansen, N.; Humphreys, F. J., Texture development during recrystallization of aluminium containing large particles. *Acta Metall.* **1985,** *33* (12), 2155-2162.

38. Rahimi, M. H.; Tabaian, S. H.; Marashi, S. P. H.; Saramad, S.; Arab, M.; Hemasian, A., Heat treatment of aluminum in preparing porous anodic alumina templates. *Micro Nano Lett.* **2012,** *7* (2), 125-129.
39. Schoone, R. D.; Fischion.Ea, Automic unit for thinning transmission electron microscopy specimens of metals. *Rev. Sci. Instrum.* **1966,** *37* (10), 1351-&.
40. Jeong, S. H.; Lee, O. J.; Lee, K. H.; Oh, S. H.; Park, C. G., Preparation of aligned carbon nanotubes with prescribed dimensions: template synthesis and sonication cutting approach. *Chem. Mater.* **2002,** *14* (4), 1859-1862.
41. Jeong, S.-H.; Hwang, H.-Y.; Hwang, S.-K.; Lee, K.-H., Carbon nanotubes based on anodic aluminum oxide nano-template. *Carbon* **2004,** *42* (10), 2073-2080.
42. Han, C. Y.; Willing, G. A.; Xiao, Z. L.; Wang, H. H., Control of the anodic aluminum oxide barrier layer opening process by wet chemical etching. *Langmuir* **2007,** *23* (3), 1564-1568.
43. Byun, J.; Lee, J. I.; Kwon, S.; Jeon, G.; Kim, J. K., Highly Ordered nanoporous alumina on conducting substrates with adhesion enhanced by surface modification: universal templates for ultrahigh-density arrays of nanorods. *Adv. Mater.* **2009,** *22* (18), 2028-2032.
44. Lillo, M.; Losic, D., Pore opening detection for controlled dissolution of barrier oxide layer and fabrication of nanoporous alumina with through-hole morphology. *J. Membr. Sci.* **2009,** *327* (1-2), 11-17.
45. Xu, T. T.; Piner, R. D.; Ruoff, R. S., An improved method to strip aluminum from porous anodic alumina films. *Langmuir* **2003,** *19* (4), 1443-1445.
46. Stepniowski, W. J.; Nowak-Stepniowska, A.; Bojar, Z., Quantitative arrangement analysis of anodic alumina formed by short anodizations in oxalic acid. *Mater. Charact.* **2013,** *78*, 79-86.
47. Lillo, M.; Losic, D., Pore opening detection for controlled dissolution of barrier oxide layer and fabrication of nanoporous alumina with through-hole morphology. *J. Membr. Sci.* **2009,** *327* (1-2), 11-17.

Chapter 4. Optimisation of the procedures and conditions of the electrodeposition of Co within pores of PAA template

4.1 Introduction

Using PAA membrane with an oxide barrier layer as a substrate for Co electrodeposition is very different from using a flat and conductive substrate such as Si wafer. The following issues make a uniform electrodeposition very challenging. The porous structure slows down the diffusion of the Co^{2+} ions from bulk of electrolyte solution to the bottom of the pores which leads to the competition from hydrogen evolution reaction (HER) when most of the Co^{2+} ions are consumed. The base oxide barrier layer has low conductivity and because of this a high voltage (10 - 20 V) is normally required for tunnelling the electrons through the barrier layer.[1] Electrodeposition by direct current (DC) results in a partial removal of barrier layer and damage in the form of pin holes in the PAA membrane leading to non-uniform local deposition.[2] Considering the difficulties, it is not surprising that electrodeposition of metal by DC within PAA membrane is more often utilized with detached PAA membranes with the ends of pores opened and in contact with a conductive metal substrate.[3,4]

As Wada *et al.* described in a literature review on electrolytic colouring of Al with a PAA membrane, Caboni firstly tried to colour porous alumina by electrodepositing metals from a solution containing copper, nickel or silver salt and utilising an alternating current (AC).[5,6] Since then, electrodeposition by AC has been widely utilised for depositing metal NPs and NWs within PAA membranes.

A difficulty with electrodeposition of metal within PAA membranes is lack of uniformity of the deposit caused by the poor conductivity of the oxide barrier layer. Hence, some research reports have described the fabrication of the barrier layer with branched cracks as was discussed earlier in Chapter 3. The branched cracks create an Al/Al_2O_3/deposited metal junction that has a rectifying contact which allows cathodic but not anodic current to flow. As a consequence, metal ions are reduced during the negative voltage pulse but the deposited metal is not electrooxided during the positive pulse.[2,7,8] Although the thickness of the oxide barrier layer and type of anodization process used (hard or soft) would affect the conductivity, the proper thinning process by electrochemical and chemical methods can significantly reduce the effects of the of barrier layer.[8]

4.1.1 Previous studies of the waveform and pulse polarity for AC electrodeposition

Gerein *et al.* reported a systematic study of electrodeposition of Cu NWs within a PAA membrane.[8] Various electrodeposition conditions including pulsed-waveforms (sine and square waveform) and order of pulse polarity (reductive/oxidative and oxidative/reductive) were investigated in their study.[8] Two types of PAA membranes which were made by anodization in different electrolytes (oxalic acid and sulfuric acid at 40 and 25 V respectively) were used in their research in order to compare the effect of the specific type of porous structures.[8] Fig. 4.1 illustrates the electrodeposition conditions which were used in their experiment. Because the PAA membranes used in this thesis were made by anodization in oxalic acid at 30 V, the following discussion will be focused on the results of Gerein *et al*. for PAA membrane made using oxalic acid as electrolyte.[8] The authors concluded that the square waveform with the reductive/oxidative pulse order results in the best uniformity of pore

filling during the electrodeposition (Fig. 4.2).[8] They explained that with a very short effective width of the sine wave (< 2.5 ms) at the voltage needed for electrodeposition (*i.e.* the very tip of the sine wave), the amount of Cu^{2+} ions which can be reduced and electrodeposited at the bottom of the pores is very small and unstable.[8] However, they did not give a clear explanation of why they chose the reductive/oxidative polarity pulse order. Other research reports about electrodeposition within PAA membrane have mainly used a square waveform with the reductive/oxidative pulse order as this was found to be optimal for reducing the effect of the HER.[2,7]

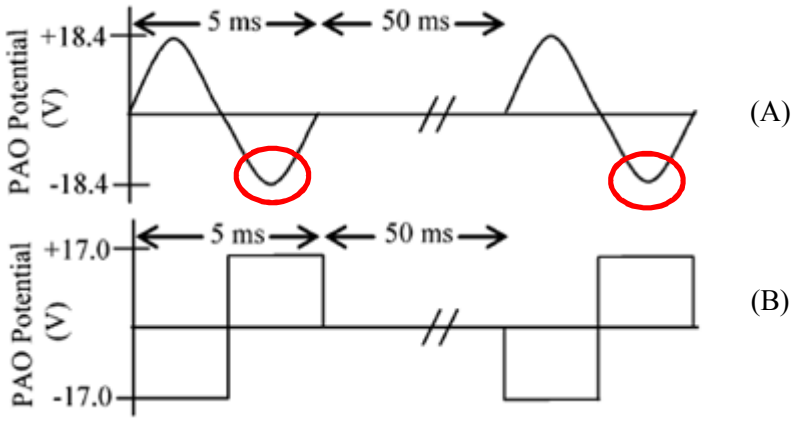

Fig. 4.1. Schematics of two of the waveforms and pulse polarities employed by Gerein *et al.* for electrodeposition of Cu in PAA membrane: (A) pulsed sine wave with and (B) pulsed square wave. Figure reproduced from reference 8.

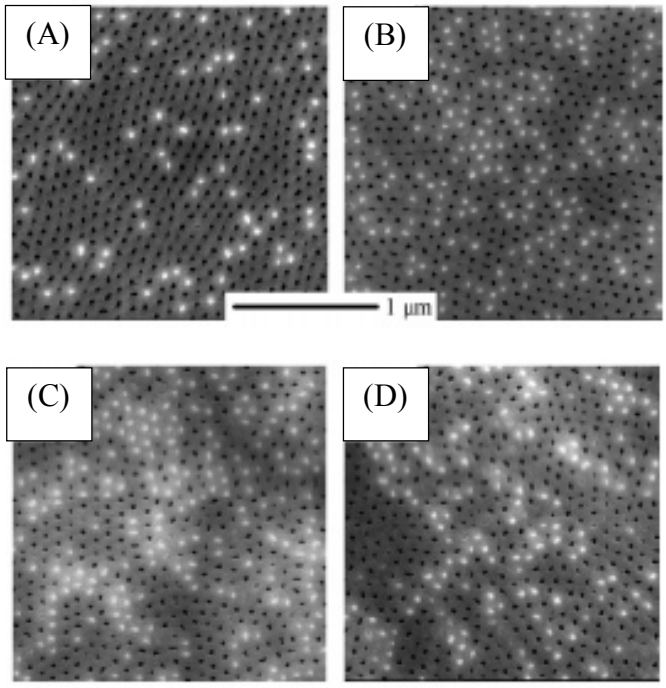

Fig. 4.2. SEM images of 24 µm deep oxalic acid anodised pores with Cu deposited using sine waves (A) and (B); and square waves (C) and (D). The (A) and (C) are electrodeposited using the reductive/oxidative pulsed order, and (B) and (D) are electrodeposited using the oxidative/reductive pulsed order. Samples have been ion-milled to 5 µm below the original surface. Figure reproduced from reference 8.

4.1.2 The mechanism of HER and strategies for preventing HER

An important issue which leads to non-uniform electrodeposition of metal in PAA membranes is the HER. During the electrodeposition, the metal ions in the pores can be exhausted if the consumption of metal ions is faster than the diffusion rate of metal ions. The diffusion of metal ions into the pores takes time as it involves movement of ions from the bulk electrolyte solution to the bottom of the pores. Therefore, competitive water electrolysis and reduction of H^+ take place yielding $H_{2(g)}$ (eq. 1 and eq. 2). The following discussion will be focused on the mechanisms of the HER and the reported strategies for preventing it.[9,10]

$$2H_2O + 2e^- \rightarrow H_{2(g)} + 2OH^- \qquad \text{(eq. 1)}$$

$2H^+ + 2e^- \rightarrow H_{2(g)}$ (eq. 2)

The generation of $H_{2(g)}$ during the electrodeposition of metals is a side reaction that affects the coverage and uniformity of the metal electrodeposition.[9,10] In general, water electrolysis tends to occur in a near neutral solution and the reduction of H^+ ions tends to occur in acidic solution.[10] Many studies related to the HER have used flat conductive electrodes for electrodeposition and the studies focussed on the effect of HER on hydrogen embrittlement or on the fabrication of nanoporous metal structures.[11,12] However, for the work in this thesis, generation of $H_{2(g)}$ bubbles in PAA membranes is the critical issue. Therefore, the following discussion will focus on some studies which relate to metal electrodeposition within PAA membranes and the HER. In some early research during 2000-2005, many reports claimed that the reduction of metal ions (*e.g.* Co^{2+}, Ni^{2+} and Cu^{2+}) is the main reaction during the electrodeposition.[8,13,14] Most of the work used an acidic electrolyte solution for electrodeposition with pH 3.3-3.8. For example, the pH of a commonly used Co^{2+} electrolyte solution which contains 0.85 M $CoSO_4$ and 0.64 M H_3BO_3 is pH 3.7-3.8.[15] The H_3BO_3 is added as a buffer to prevent a local pH rise near the surface of the electrode which results from water electrolysis (eq. 2).[16,17]

However, as the briefly described in the beginning of this chapter, the porous membrane structure slows down the diffusion of metal ions from the bulk electrolyte solution to the bottom of the pores (the depth of pores is typically more than 5 μm). Depletion of metal ions occurs during electrodeposition and subsequently, water electrolysis takes place generating $H_{2(g)}$. These $H_{2(g)}$ bubbles can block the pores and terminate the electrodeposition of metal. From the study by Gerein *et al.*, this phenomenon can be observed in their SEM results.[8] The authors electrodeposited Cu NWs in a PAA membrane with 24 μm pore depth. In order to observe the progress of the electrodeposition, the samples were then ion-milled to

expose a surface 5, 10 and 15 µm below the original surface. The series of SEM images in Fig. 4.3 shows that the uniformity of Cu electrodeposition deteriorated as electrodeposition time increased. This illustrates the consequence of depleting Cu^{2+} ions and generating $H_{2(g)}$ during the electrodeposition.

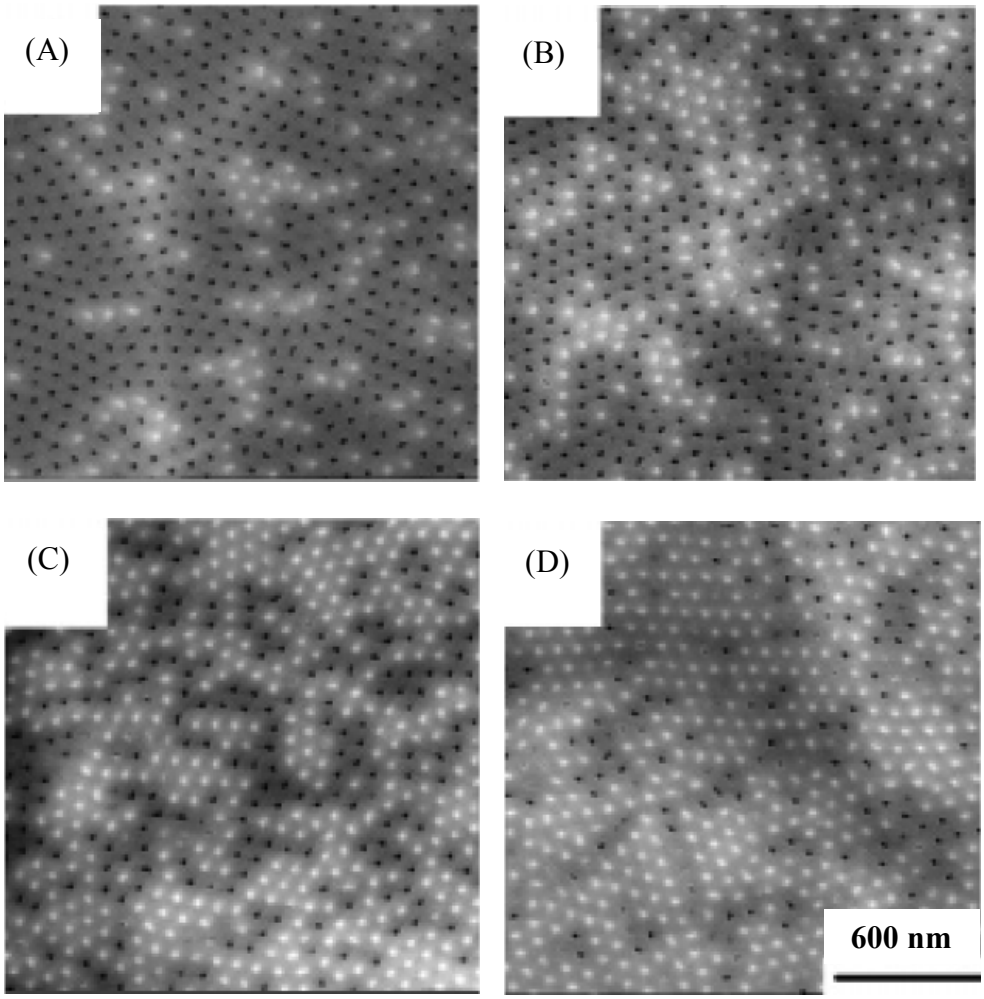

Fig. 4.3. SEM images of 24 µm deep oxalic acid anodised pores with Cu deposited using square waves with the reductive/oxidative pulsed polarity. Samples (B) – (D) have been ion-milled to expose the membrane, 5, 10 and 15 µm below the original surface respectively showing the progression of pore-filling as a function of depth. Figure reproduced from reference 8.

In 2000, Nielsch *et al.* was the first research group to mention using a pH 4.5 Ni^{2+} electrolyte (300 g/L $NiSO_4 \cdot 6H_2O$, 45 g/L $NiCl_2 \cdot 6H_2O$ and 45 g/L H_3BO_3) for electrodepositing Ni NWs within a PAA membrane.[2] The researchers also introduced the strategy of leaving rest periods between current pulses as shown in Fig. 4.4. The rest periods

between pulses allow sufficient time for recovery of the metal ions concentration in the pores after each electrodeposition pulse which results in decreased competition from the HER. Using the higher pH electrolyte for electrodeposition and rest periods, a high pore filling ratio was achieved.[2] The pore filling ratio is the ratio of (number of pores filled with metal) : (total number of pores). Since 2009, electrolytes with pH between 4.50-5.50 have been more commonly used in order to increase the pore filling ratio of electrodeposited of metal NWs.[18,15] One significant result is reported by Ghaddar *et al.* who illustrated the progress of electrodeposition of Co NWs within PAA membrane by observing the change of current density *vs.* electrodeposition time.[15] The authors compared the current density *vs.* time curves for electrodeposition at pH 3.5 and 5.5 Co electrolyte solutions respectively (Fig. 4.5).[15] The Co^{2+} electrolyte solution which was used in their research contained 0.43 M $CoSO_4$ and 0.48 H_3BO_3 and the pH was adjusted by addition of NaOH. As shown in Fig. 4.5, at pH 5.5, the current density increased then decreased rapidly over the first few seconds due to the initial nucleation and electrodeposition process at the bottom of the pores. Then, from 5-35 s, the current density maintained a stable value corresponding to the process of pore filling by Co NW. After 35 s electrodeposition time, the current density increased dramatically because most of the pores had been filled completely and consequentially the Co was electrodeposited on the top of the PAA membrane. In contrast, at pH 3.5, the current density after 10 s maintains a stable value. According to the interpretation of the authors, complete pore filling was not observed at pH 3.5 which may result from blockage of pores by $H_{2(g)}$ bubbles. Although the authors did explain how HER affects the uniformity of electrodeposition at a lower pH, the hypothesis is that the effect of the HER is less when electrodeposition is carried out at a higher pH due to a lower concentration of H^+ ions in the solution. The concentration of H^+ ions in pH 3.8 Co^{2+} electrolyte solution is 6.3 times the concentration of H^+ ions at pH 4.6.

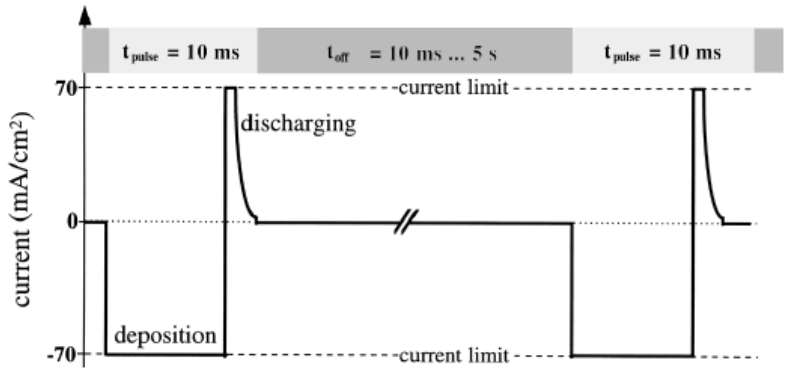

Fig. 4.4. Schematic of electrodeposition sequence used by Nielsch *et al*. Figure reproduced from reference 2.

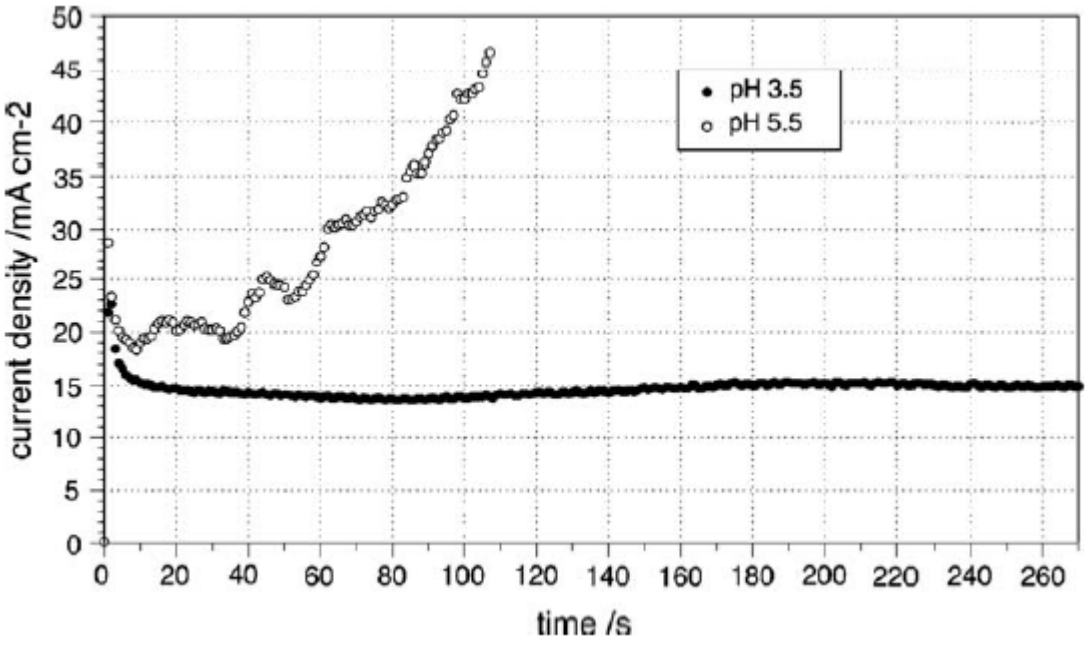

Fig. 4.5. A Current density *vs.* electrodeposition time curves for Co electrodeposition in PAA membrane. Electrodeposition conditions: 0.43 M $CoSO_4$ + 0.48 H_3BO_3 (pH 3.5 or 5.5). ± 15 V, 50 Hz, square waveform; pH of electrolyte was adjusted by adding NaOH. Figure adopted from reference 15.

4.1.3 Other factors which may result in reduced uniformity of Co electrodeposition

Apart from the poor conductivity of the barrier layer and the HER, there are some other factors which interfere with uniformity of electrodeposition: oxidative dissolution of deposited NPs and non-optimal experimental procedures. In 1990, Jiang *et al.* compared the morphology of Co layers obtained by applying a galvanostatic current density of 20 mA/cm^2 for electrodeposition in 0.25 M $CoCl_2$ solution at 25 °C under different gases: $O_{2(g)}$, $N_{2(g)}$ and air.[19] According to the SEM image shown in Fig. 4.6 (A), when electrodeposition was performed under air, large cuboid-like structures of Co were individually formed in the initial electrodeposition stage.[19] After a longer electrodeposition time, these structures became smaller and denser (Fig. 4.6 (B)). This morphology is similar to the sample which was electrodeposited with $O_{2(g)}$ purging (Fig. 4.6 (D)), although the structure in Fig.4.6 (D) is more needle-like. The authors accounted for these morphologies by proposing that the deposited material was a combination of Co and cobalt oxides such as Co(O)OH, Co_3O_4 and CoO which form due to the presence of O_2 during the electrodeposition. As the Co oxides are more soluble than Co in the acidic electrolyte solution, the large cuboid-like structures gradually dissolve during longer electrodeposition time. This effect is more obvious when electrodepositing with $O_{2(g)}$ purging (Fig. 4.6 (D)). However, when solutions were purged with $N_{2(g)}$ during the electrodeposition, only a dense and thin metallic Co layer was formed as illustrated by Fig. 4.6 (C).[19]

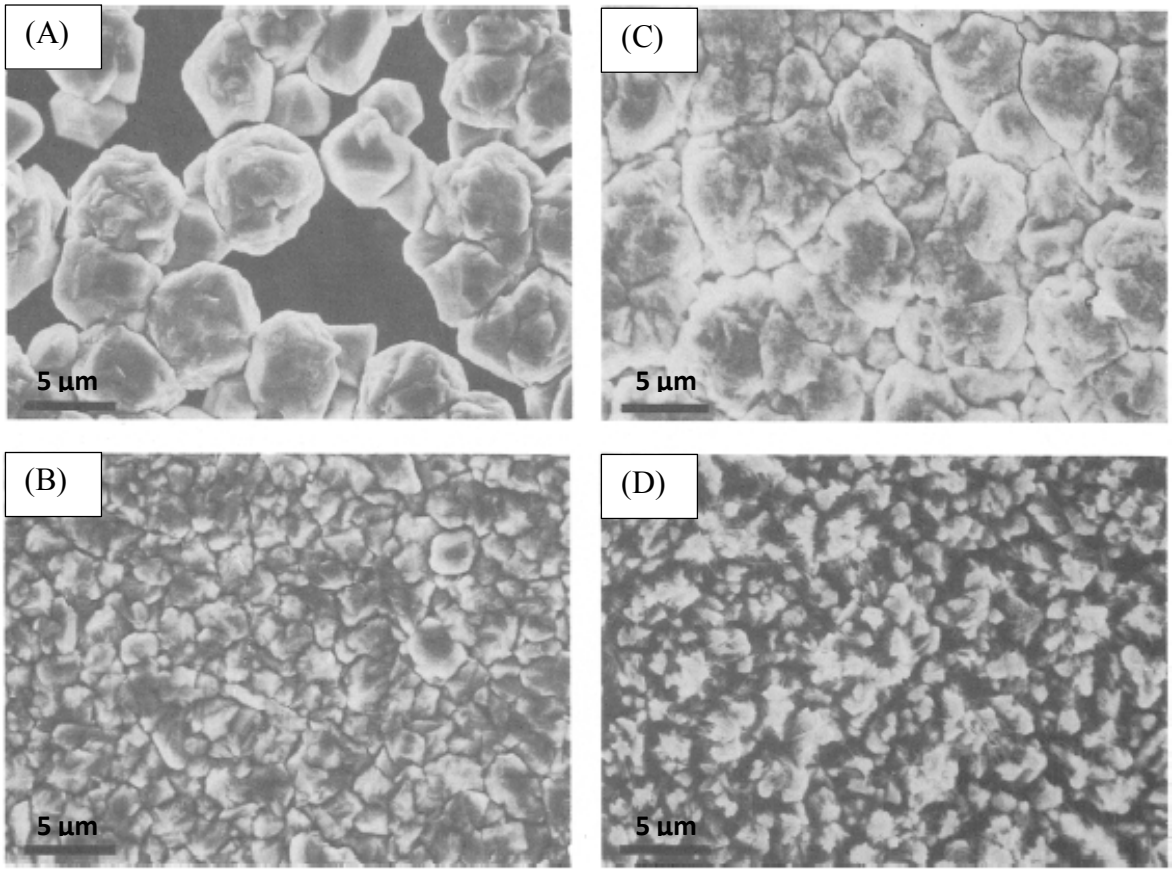

Fig. 4.6. SEM images of Co electrodeposition at 2 mA/cm^2 in 0.42 M $CoCl_2$ and in the presence of bubbling gases. (A) electrodepositing for 1 h in the solution without purging any gases; (B) electrodepositing for 2 h under the same condition with (A); (C) electrodepositing for 2 h in the solution with bubbling $N_{2(g)}$ and (D) electrodepositing for 2 h in the solution with bubbling $O_{2(g)}$. Figure reproduced from reference 19.

Although these results show that purging with $N_{2(g)}$ during electrodeposition prevents the formation and dissolution of Co oxides, this strategy has not been applied to metal deposition in the pores of PAA membranes. Hence, deposition and dissolution of Co oxides may contribute to the reported nonuniform deposition of NPs and NWs in PAA membranes.

4.1.4 Approaches to monitoring of the uniformity of the electrodeposition

The uniformity of the electrodeposited metal in PAA membranes can be estimated by observation of the cross-section of a cut PAA membrane or the top view of filled pores using

SEM.[2,7,8] Observing the pore filling from the top view in SEM is experimentally easier and does not involve destruction of the sample. However, for typical pore depth (more than 5 μm), it is not possible to directly observe deposited NPs by top view using SEM.[2,7,8] As mentioned earlier Gerein *et al.* used ion-milling to physically etch the top of a PAA membrane with Cu NWs deposited inside. The etching depth is controllable. By SEM imaging of samples which had been etched to different depths, the pore filling ratio was found to progressively increase with increase in etching depth from 0 to 15 μm below the surface. This indicates significant variability in the lengths of metal NWs (Fig. 4.3). Even in the case of the deepest etching 15 μm, it is evident that some of the pores remain empty implying that the electrodeposition process used by the authors was not optimal.

Observing small NPs at the bottom of the pores of PAA membranes is particularly difficult. The common method involves observing the cross-section image of the cut PAA template by SEM or TEM. For sample preparation, techniques, such as focused ion beam (FIB) micro- and nano-machining or chemical etching, have been used to cut or partially remove the PAA membrane.[14,20,21] Alternatively PAA membrane can be mechanically bent or cracked to expose the PAA cross-section close to the pore base.[21] However, using destructive sample preparation such as chemical etching or mechanical bending may result in loss some of the electrodeposited metal NPs. FIB appears to be the most promising method for cutting the PAA membrane prior to imaging deposited metal NPs (Fig. 4.7).[14]

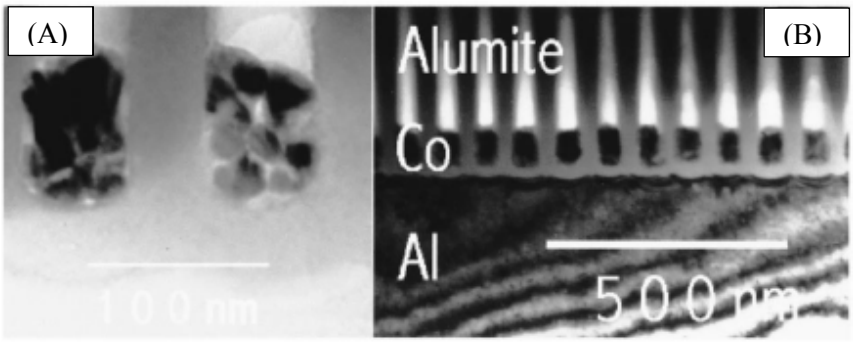

Fig. 4.7. Cross-section TEM images of Co particles in ordered PAA membrane (alumite is alumina). (A) details of microstructure of electrodeposited Co NPs and (B) overview of electrodeposited Co NPs. Figure reproduced from 14.

An alternative to direct observation of metal NPs in PAA membranes is to use the NPs to catalyse growth of CNTs. The uniformity of CNT growth may provide indirect evidence for the uniformity of metal deposition in the PAA membrane. Importantly, this strategy has to be based on the premise that the CVD conditions are optimised, so that the coverage of CNTs can be an indicator of the pore filling ratio of the deposited metal NPs and the variation of the CNT diameters corresponds to the variability in the amount of metal that has been electrodeposited in each pore.

During 2002-2004, Jeong *et al.* reported a series of studies which related to this approach. [20,22,23,24] The authors fabricated a shallow PAA template with Co NPs for growing CNTs. In their study, the PAA membrane was fabricated in oxalic acid by 2-step anodization followed by barrier layer thinning.[24] The depth of the pore was 1 μm or 2 μm and the diameter of the pore was 80 nm.[23] The Co NPs were electrodeposited from a solution containing 5 % $CoSO_4 \cdot 7H_2O$ and 2 % H_3BO_3 by applying 18 V AC for 1 min. These conditions were chosen to electrodeposit small Co NPs.[20,24] The CVD process was carried out by reducing Co NPs at 500 °C for 1 h under $H_{2(g)}$ and $Ar_{(g)}$. Subsequently, the CNTs were grown at 650 °C under $C_2H_{2(g)}$, $H_{2(g)}$ and $Ar_{(g)}$.[20] The SEM images in Fig. 4.8 (A) and (B) show the electrodeposited Co NPs and the CNT growth respectively. From the image of Fig.

4.8 (A), the electrodeposited Co NPs are seen to fill the bottom of the pores. The authors claimed the Co NPs were electrodeposited uniformly. However, in this case, a dense CNT growth would be expected but Fig. 4.8 (B) shows many empty pores.

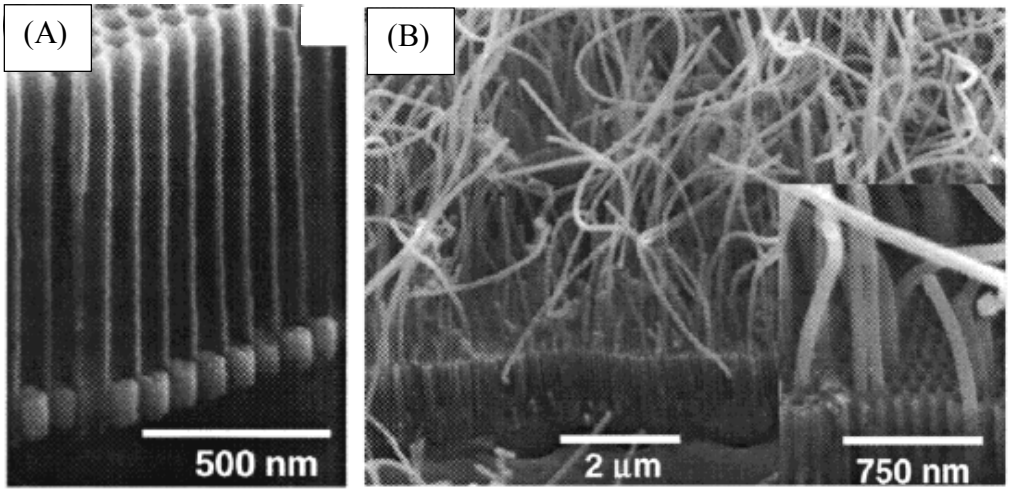

Fig. 4.8. SEM images of (A) PAA template with electrodeposited Co NPs at the bottom of the pores and (B) CNTs grown out or PAA membrane. Figures adopt from 22.

There are two possible reasons for the observed non-uniformity of CNT growth. First, some of the particle sizes may have been too big to be catalytic for CNT growth. As seen in the SEM image in Fig. 4.8 (A), the Co NPs have a length and diameter about 100 nm and 80 nm respectively. It is well-known that the size of the catalyst particles will affect the growth of CNTs and larger particles tend to be less catalytic for CNT growth.[25] The typical diameter of Co NPs which have been used to successfully grow dense MWCNTs is in the range of 4-10 nm, much smaller than the NPs shown in Fig. 4.8 (A).[26,27] However, if it is a size effect, it is not clear why some of the Co NPs are still catalytic for CNT growth.

An alternative explanation for the sparse CNT growth shown in Fig. 4.8 (B) is that the temperature used for the reduction step prior to CNT growth was too low. Co is easily oxidised and forms Co_3O_4 when exposed to air. Therefore, during the CVD process, it is important to reduce Co_3O_4 to metallic Co in order to recover the catalytic activity for CNT

growth. Lin *et al.* investigated the reduction of Co_3O_4 in the presence of $H_{2(g)}$ and inert gas (*e.g.* $Ar_{(g)}$ or $N_{2(g)}$) using a temperature programmed reduction (TPR) method.[28] The sample was prepared by mixing $Co(NO_3)\cdot 6H_2O$ and a commercially purchased silica gel in a glass vessel under stirring. This mixture was vacuum dried for 24-48 h at 120 °C and then calcined for 3 h at 600 °C.[28] (The authors did not state the particle size of Co but it can be assumed the size is in a range between 5-20 nm based on other reports which have similar sample preparation methods.[29,30] The two peaks in the TPR spectra in Fig. 4.9 correspond to the reactions give in equation 5 and 6.[28]

$$Co_3O_{4(s)} + H_{2(g)} \rightarrow 3CoO_{(s)} + H_2O_{(g)} \qquad \text{(eq. 5)}$$

$$CoO_{(s)} + H_{2(g)} \rightarrow Co_{(s)} + H_2O_{(g)} \qquad \text{(eq. 6)}$$

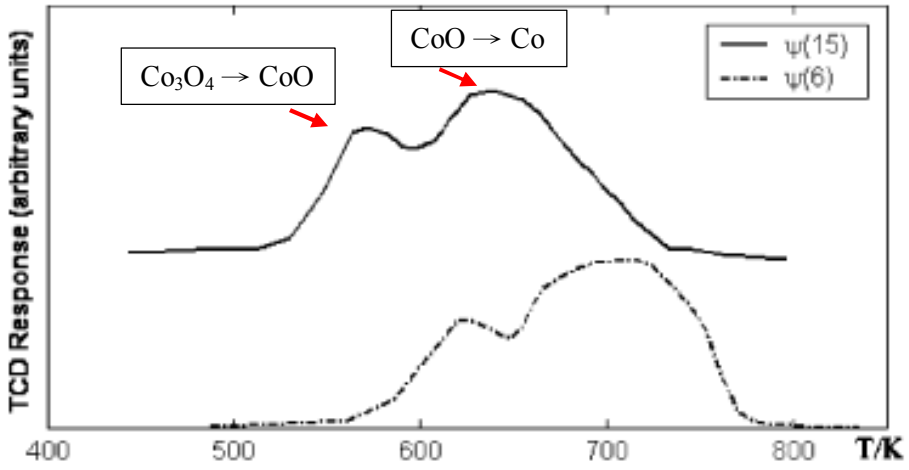

Fig. 4.9. TPR profile for reducing Co_2O_3 from different heating rates: ϕ = 6 and 15 K/min. Figure reproduced from reference 28.

It has been shown that in addition to the heating rate, temperature required for reduction depends on the particle size of Co_2O_3 and the support material.[28,31] The following section will mainly focus on Co NPs on Al_2O_3 supports.[28,31] Liu *et al.* prepared a sample of Co oxide by mixing co-precipitated $Co(OH)_2$ and the support material (*e.g.* α-Al_2O_3) with a

weight ratio of 1:8 and mechanically milling for 24 h.[31] This sample was used to examine the temperature required to completely reduce Co oxides to metallic Co. CNT growth followed the reduction to show the catalytic properties of the Co NPs. To monitor the reduction process, the authors analysed the change of the saturation magnetization (M_s) of Co NPs for reduction in the temperature range between 300-700 °C under a flow of $H_{2(g)}$ and inert gas for 1 h.[31] A rising value of M_s corresponds to an increasing percentage of metallic Co within the particles. Fig. 4.10 (A) shows that M_s was close to the theoretical value for metallic Co for reducing at 600 °C and above.[31] The size of the Co NPs was 12-13 nm after reducing under these conditions. Therefore, the authors chose 600 °C as the reduction temperature and subsequently grew CNTs using CH_4 as the feedstock. Fig. 4.10 (B). This study further confirms that the nonuniform CNT growth in the work of Jeong *et al.*(Fig. 4.8 (B)) can be at least partly due to the low reduction temperature (500 °C) which resulted in an incomplete reduction of Co NPs.[20]

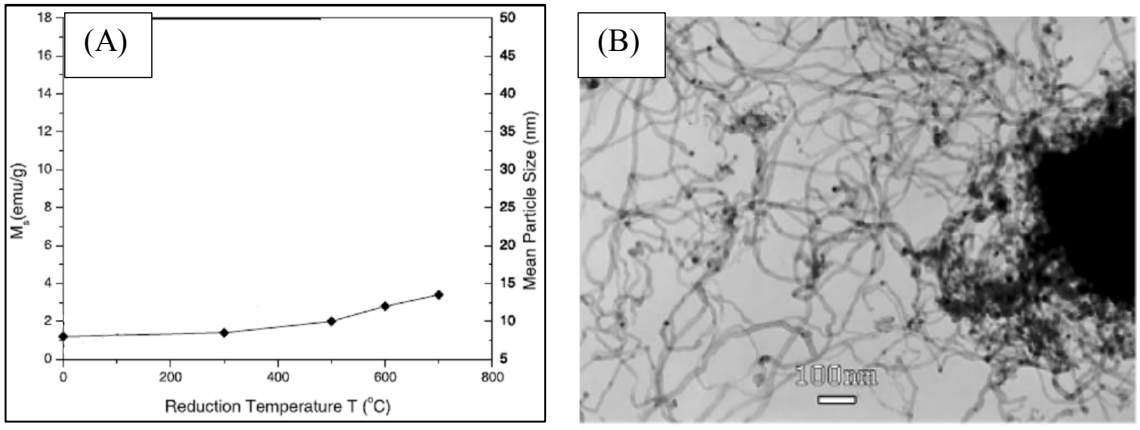

Fig. 4.10. (A) Saturation magnetization (*Ms*) as a function of reduction temperature of Co/Al_2O_3 and (B) TEM image of CNTs grown on Co/Al_2O_3 catalyst at 600 °C. Fig 4.10 (A) and (B) were reproduced and adopted from reference 31 respectively.

4.1.5 Aims for this chapter

The overall goal of work in this chapter is control the diameter of CNTs through control of the size of Co NP catalysts. Control of the size of Co NPs is achieved by depositing Co into the pores of PAA membranes. Most of the work in this chapter is aimed at optimising the electrodeposition of Co NPs. As the Co NPs are the catalyst for CNTs growth, the uniformity of the electrodeposition of Co NPs can be estimated from the uniformity of the coverage and the morphology of the produced CNTs. In addition, conditions for the reduction of Co NPs prior to CNT growth were optimised.

4.2 Experimental section

4.2.1 Preparation for the electrodeposition of Co nanoparticles

The shallow PAA membrane was fabricated following the 3-step anodization process and barrier layer thinning by chemical etching as described in Chapter 3. To ensure that the electrodeposition was not affected by residual amounts of the chemicals used during previous stages, the PAA template was cleaned by immersing in Milli-Q water and gentle shaking on an orbital shaker for at least 15 min. After cleaning, the round membrane was chopped into quarters using a sharp blade (Fig. 4.11). These four sample pieces were then rinsed using Milli-Q water and quickly blow dried under $N_{2(g)}$. In order to ensure diffusion of Co^{2+} ions into the pores of the membrane prior to the start of electrodeposition, the membranes were immersed in the Co^{2+} electrolyte solution containing 0.85 M $CoSO_4$ and 0.64 M H_3BO_3 for

15-30 min before proceeding to the electrodeposition stage. The remainder of the samples which were used for later electrodeposition experiments were stored in Milli-Q water to keep the pores filled with water. The pH of the as-prepared Co^{2+} electrolyte solution was pH 3.8. In the later stage of the optimisation of these experiments, the Co^{2+} electrolyte solution was adjusted using 0.1 M NaOH to pH 4.60-4.70 (measured using a pH meter accurate to two decimal places).[32]

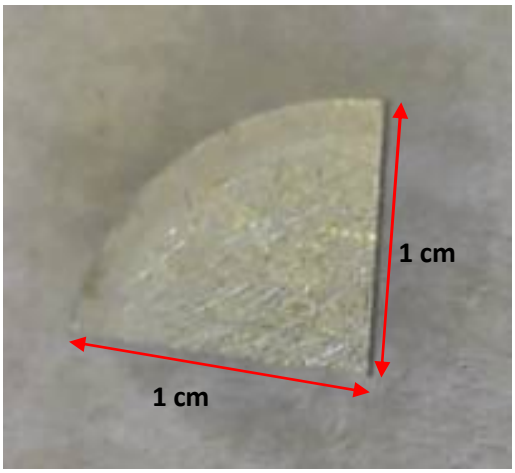

Fig. 4.11. A PAA sample typically used for electrodeposition experiments.

4.2.2 Electrodeposition conditions and procedures

After taking the sample out from the Co^{2+} electrolyte solution used to impregnate pores, a wet tissue was used to wipe the back side of the sample. The topside was then blow dried under $N_{2(g)}$ flow and mounted in an electrodeposition cell (the cell was discussed in detail in Chapter 2). Co^{2+} electrolyte solution was added to the cell.

Electrodeposition was undertaken using a sequence of 10 ms pulses with amplitude ± 10 V. The pulse sequence was initiated at -10 V and finished at +10 V. These pulses were applied for different amounts of time as specified in the Results and Discussion section. In

some experiments, the pulse sequences were periodically interrupted with a 15 min rest period at open circuit potential.

In early experiments, the samples were rinsed using Milli-Q water without purging with $N_{2(g)}$. During later stages of this work, the samples were cleaned by quickly dipping into Milli-Q water and briefly (5-10 s) shaking in water which had been purged with $N_{2(g)}$. Finally, the samples were blow dried with $N_{2(g)}$.

4.2.3 Procedure for CNT Growth

The CNT growth was carried out by CVD immediately after electrodeposition of Co NPs. The tube furnace with a digital temperature programmer and digital gas flow control system was used to ensure that the key parameters of the CVD process (temperature programme and gas flow rates) were controlled with high precision. This has been described detail in Chapter 2.

In this project, two CVD protocols schematically shown in Fig. 4.12 and Fig. 4.13 have been used. It should be noted that all gases were pre-purged before the CVD process. Firstly, $Ar_{(g)}$, $H_{2(g)}$ and $C_2H_{2(g)}$ were purged for 15 min with 90 sccm of gas flow rate. Then, $H_{2(g)}$ and $C_2H_{2(g)}$ were turned off and $Ar_{(g)}$ was purged for another 15 min with 200 sccm of gas flow rate.

The first protocol (Fig. 4.12) was carried out by heating the PAA samples with Co NPs from room temperature to 450 °C under a flow of $Ar_{(g)}$ (90 sccm). The samples were reduced in a mixture of $Ar_{(g)}$ (90 sccm) and $H_{2(g)}$ (30 sccm). After the reduction process, the temperature was raised to 650 °C with the same gas flow ratios of $Ar_{(g)}$ and $H_{2(g)}$. When the temperature reached 650 °C, $C_2H_{2(g)}$ was introduced into the quartz tube with a flow rate of

20 sccm. The flow rate of $H_{2(g)}$ was adjusted to 20 sccm. The flow rate of $Ar_{(g)}$ was kept at 90 sccm. The duration of the CNT growth was 30 min. After finishing the CNT growth, the furnace was cooled to room temperature with $Ar_{(g)}$ flow (200 sccm).

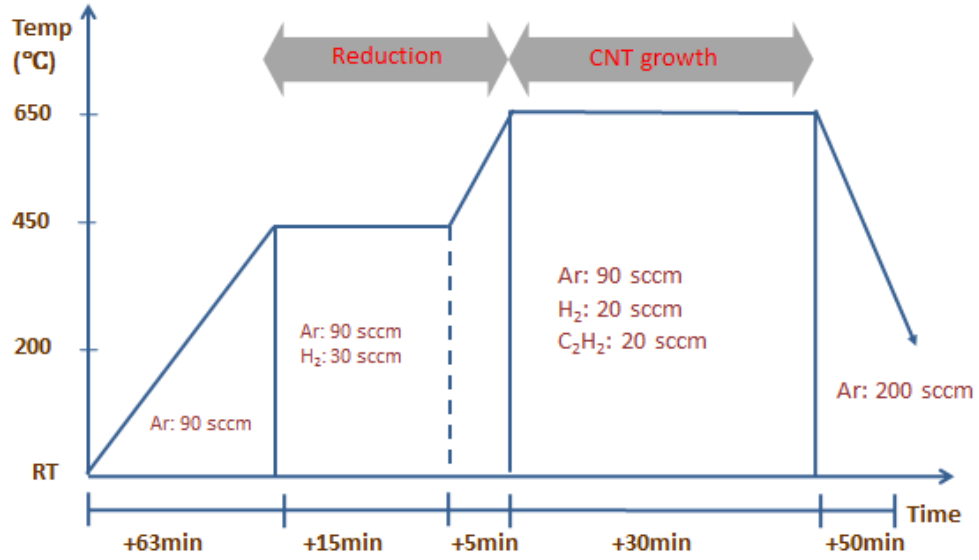

Fig. 4.12. Temperature and gas flow programme for CVD process (protocol 1)

The second protocol (Fig. 4.13) was similar to the first protocol but the temperature for the reduction stage started at 450 ºC and was ramped up to 650 ºC where it was maintained for 1 h. A gas mixture with $Ar_{(g)}$ and $H_{2(g)}$ with the same gas flow rates as for protocol 1 was used during the reduction process. CNTs were grown at 650 ºC for 23 min with the same gas mixtures and the flow rates as for protocol 1.

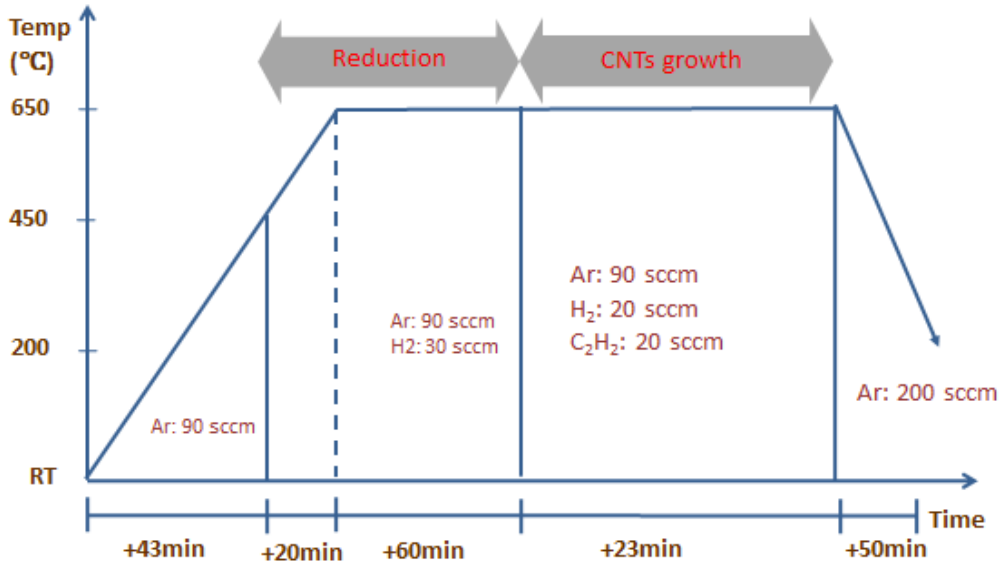

Fig. 4.13. Temperature and gas flow programme for CVD process (protocol 2)

4.2.4 TEM sample preparation

In order to observe CNTs in TEM, the sample was prepared as follows. The Al_2O_3 membrane was dissolved in 0.5 M NaOH and CNTs were released into the solution. The NaOH solution containing CNTs was collected in a centrifuge tube and then centrifuged for 5 min at 13000 rpm. After centrifuging, CNTs were at the bottom of the centrifuge tube. The NaOH solution was replaced by Milli-Q water and mixed with CNTs. The sample was centrifuged again under the same conditions. The washing process was repeated 2-3 times. After the final washing, water was carefully removed using a dropper and EtOH was added into the centrifuge tube. Subsequently, the EtOH solution of CNTs was dropped onto a holey carbon/copper TEM grid. The TEM grid was dried under vacuum overnight before use.

4.3 Results and discussion

4.3.1 Optimised procedures for electrodeposition

The conditions for electrodeposition of Co NPs and were based on previous studies by Xu.[21] Therefore, this section will be divided into two parts: 4.3.1.1 will briefly compare the experimental conditions between this work, Xu's work and selected literature reports, and 4.3.1.2 will explain the further development of the optimised procedures in this work.

4.3.1.1 Comparison of electrodeposition conditions used in this work with literature

Table 4.1 compares the conditions for electrodeposition of Co NPs by alternating current (AC) which were used in the previous study by Xu,[21] the current study and conditions used in selected relevant papers. The differences between the study by Xu and the current work have been highlighted in red. Xu's electrodeposition conditions were based on those of Nielsch *et al.*,[2] Gerein *et al.*[8] and Li *et al.*[33] In this work, most of the parameters of the electrodeposition including the concentration of the Co^{2+} electrolyte solution, the deposition voltage, frequency, waveform, temperature and the pulse polarity were chosen to be similar to parameters used by Xu.[34]

Crucially, the PAA membranes developed as a result of the reported here work have much shallower pores than ones used in Xu's study (300 nm depth in this study compared with 4 μm in the study by Xu) which was expected to improve the uniformity of electrodeposition of Co NPs.

Table 4.1 Comparison of the conditions of PAA fabrication and electrodeposition used in this work and other studies.

PAA fabrication						
Authors	Purity of Al foil	Electrolyte	Depth of the pore	Electro-chemical Etching	Chemical etching	Diameter of the pore
(1) **This Work**	99.9995%	0.4 M $H_2C_2O_4$	300 nm	Yes	Yes	55 nm ± 5nm
(2) Xu's study[21]	99.995 %	0.4 M $H_2C_2O_4$	4 μm	Yes	Yes	50 nm ± 5nm
(3) Li *et al.* [33]	99.99 %	0.3 M $H_2C_2O_4$	8 μm	-	Yes	50 nm
(4) Jeong *et al.*[22]	99.999 %	0.3 M $H_2C_2O_4$	1 μm	-	Yes	50 nm
(5) Ghaddar *et al.*[15]	-	1.8 M H_2SO_4 or 1.5 M H_3PO_4	~ 6 μm	-	-	10 nm
(6) Najafi *et al.*[18]	99.999 %	0.3 M $H_2C_2O_4$	-	Yes	NA	35 nm

Electrodeposition conditions								
Authors[a]	electrolyte	pH of the electrolyte	Deposition Voltage	Deposition Frequency	Pulse width[b]	Electrodeposition Time	Diameter of length of Co NP or NW	Purged N_2(g)
(1)	0.85 M $CoSO_4$ /0.64M H_3BO3	4.6-4.7	10 V (peak)	100 Hz	5 ms/5 ms	400 ms	5-10 nm	Yes
(2)	0.85 M $CoSO_4$ /0.64M H_3BO_3	3.8	10 V (peak)	100 Hz	5 ms/5 ms	30 s	1 μm	NA
(3)	0.85 M $CoSO_4$ /0.64M H_3BO_3	-	14 (peak)	100 Hz	-	-	100-200 nm	NA
(4)	5 % $CoSO_4$ /2 % H_3BO_3	-	15 (peak)	-	-	1 min	100 nm	NA
(5)	0.43 M $CoSO_4$ /0.48 M H_3BO_3	3.5 or 5.5	15 (peak)	50 Hz	-	20-260 s	-	NA
(6)	0.3 M $CoSO_4$ /0.75 M H_3BO_3	4.5	15 (peak)	550 Hz	1 ms/1 ms	5-120 s	1-5 μm	NA

a: The numbers refer to the numbered reports in the table above

b: The pulse is applied as a cycle of negative voltage and positive voltage with the pulse width indicated.

The following paragraphs summarize issues which became apparent as the result of the earlier research project by Xu.

According to Xu's thesis, he also reported that the H_2 bubbles can be observed in all the electrodeposition times that he had used. The range of the electrodeposition time that Xu used was between 10 s to 30 min which is sufficiently long time for generating the H_2. In his study, the electrodeposition time was controlled manually due to the limitation of the instrument using for electrodeposition. Therefore, the range of electrodeposition time was chosen from 10 s to 30 min as it is easy to manually control such durations of the electrodeposition. The colour on the PAA template in the area of Co deposition became brown after the electrodeposition of Co and the shade of brown was indicative of the amount of Co that had been deposited into the pores. Xu suggested that the optimal electrodeposition time was 30 s as the colour of the PAA membrane after electrodeposition of Co was light brown and reproducible. For an electrodeposition time less than 30 s, the colour of the Co deposit was not reproducible. Co NWs could be observed by SEM under the optimal conditions but the uniformity of the resulting NWs could not be determined. The CNTs subsequently grown using such catalysts did not fully cover the surface of the PAA template; empty pores could be easily observed by SEM. Although it is possible that the CVD conditions were not optimal in the case of study by Xu, it is also likely that Co NWs (or NP) were not deposited in all pores. The main reason for this is that $H_{2(g)}$ bubbles generated by HER blocked the pores during the electrodeposition. It should also be noted that Xu used a different furnace and the conditions of CVD for CNT growth were significantly different to those used in this work. In Xu's work, during the CVD process, gas flow rates were controlled by a set of simple ball gauges. In comparison, the CVD system used for the present work allows precise control of gas flows (using digital MKS flow control system). Another factor that may have led to sparse CNT growth in Xu's study is incomplete reduction of Co

NPs at the temperature used (500 °C). Importance of the choice of the appropriate CNT growth conditions will be discussed in 4.3.5.

4.3.1.2 Brief overview of the key steps in optimization of the electrodeposition of Co NPs within the shallow PAA membrane.

The previous study by Xu pointed out the electrodeposition time could be one of the key parameters in achieving reproducible Co deposition. The shortest deposition time Xu tested was about 3 s (manually controlled).[21] However, $H_{2(g)}$ bubbles were still observed indicating the need for an even shorter electrodeposition time. A pulse generator with digital time controller was utilised in this work allowing electrodeposition time to be precisely controlled between 10 ms and 10 min. The plan for optimisation of the electrodeposition conditions and procedures is shown in Scheme 4.1. The following description corresponds to the Scheme and briefly explains the development of the optimised procedures. The detailed results will be discussed in the following sections.

S1: The initial experiments were aimed at determining the electrodeposition time at which $H_{2(g)}$ bubbles did not form. Hence, electrodeposition times of 1 s to 400 ms were investigated. When the electrodeposition time was 1 s, H_2 bubbles were easily observed by the naked eye. When the electrodeposition time was 800 ms, only a few H_2 bubbles were observed and when the electrodeposition time was 400 ms, no H_2 bubbles could be observed by the naked eye, although bubbles could still remain in the pores. The pH of the Co^{2+} electrolyte solution was 3.8 for steps S1-S5.

S2: In order to reduce the possibility of the HER during the Co electrodeposition, the electrodeposition was carried out by dividing the total time into shorter periods with a substantial rest interval between each period. For example, if the total electrodeposition time of 400 ms was required, it was achieved with 4 × 100 ms periods of electrodeposition. The

rest period between each short electrodeposition was set to 15 min in order to allow replenishing of Co^{2+} ions within the pores by diffusion from the bulk solution and releasing of any $H_{2(g)}$ out of the pores.

S3: Since the shallow PAA membrane could be easily etched in acidic solution, the storage solution was changed from oxalic acid or Co^{2+} electrolyte solution as used by Xu to Milli-Q water.

S4: For cleaning the sample after electrodeposition, $N_{2(g)}$ was purged through the wash solution to prevent the oxidative dissolution of deposited Co NPs.

S5: The CVD conditions were optimised to improve the reduction of partially oxidized Co NPs (*e.g.* Co NPs exposed to air after electrodeposition).

S6: The pH of the Co^{2+} electrolyte solution was adjusted from pH 3.8 to pH 4.6-4.7 to further increase the influence react and thus increase the uniformity and the coverage of Co NPs.

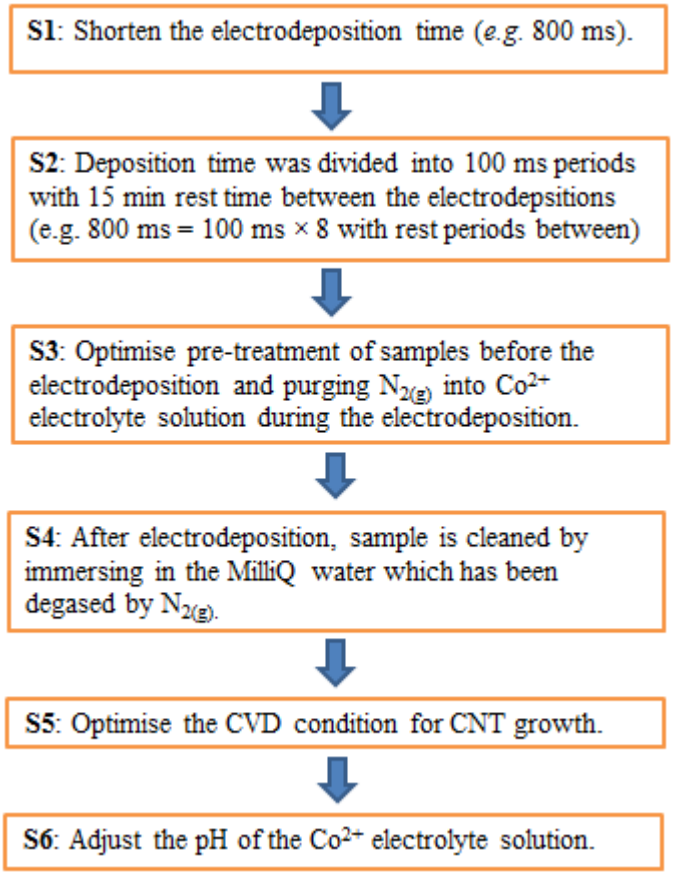

Scheme 4.1 The development of optimising procedures of the electrodeposition of Co NPs in PAA membrane.

4.3.2 Preliminary experiments focused on the effect of adding rest intervals into the electrodeposition time

Instead of continuously electrodepositing for a certain time, the total electrodeposition time was split into several intervals and the sample was left in the Co^{2+} electrolyte solution at open circuit potential for 15 min between each electrodeposition interval.

The following experiments (Series A) were aimed at finding the optimal duration of the individual electrodeposition intervals while using a total electrodeposition time of 800 ms split into shorter intervals separated by the rest periods. The electrodeposition was carried out by:

(1) Directly (non-stop) electrodepositing for 800 ms (control experiment);

(2) Electrodepositing for 400 ms × 2 (with rest period of 15 min in between);

(3) Electrodepositing for 200 ms × 4 (with rest periods of 15 min in between);

(4) Electrodepositing for 100 ms × 8 (with rest periods of 15 min in between).

As was explained in the introduction, instead of imaging the PAA template after the electrodeposition, observing the coverage of CNTs grown by CVD on the PAA template was a much easier method for gaining evidence for the existence and uniformity of Co NPs in the membrane. Several important points should be noted with respect to these experiments. Firstly, as prepared Co^{2+} electrolyte solution was used with pH 3.7-3.8. Secondly, after electrodeposition, the samples were cleaned by spraying with Milli-Q water from a wash bottle. This caused a visible decrease in the intensity of the brown colouration of the membrane suggesting cleaning could re-dissolve the Co leading to poor uniformity of the coverage of Co NPs. The effect re-dissolution of the Co will be discussed later. Thirdly, CVD protocol 1 was used and the Co NPs may not have been fully reduced at the relatively low temperature (450 °C) before CNT growth. Although the electrodeposition conditions, the cleaning procedures and the CVD growth conditions were not optimised at this preliminary stage, the experiments still provided some clues for choosing a duration of the electrodeposition interval short enough to prevent the evolution of $H_{(g)}$ bubbles.

The SEM images in Fig. 4.14 show CNTs grown in these experiments and the histograms in Fig. 4.15 show the distribution of CNT diameters which correspond to some of the images in Fig. 4.14. The coverage of the CNTs on the PAA template and uniformity of the CNT diameters are the important factors which are assumed to correspond to the coverage and uniformity of the Co NP in the PAA template respectively. The low magnification SEM images (Fig. 4.14 (A), (C), (E) and (G)) show that the coverage of the CNTs is not complete

under any of the studied conditions. This is attributed to the non-optimised parameters discussion above. Although the coverage of CNTs was variable for these four electrodeposition methods due to the non-optimised experimental conditions, the observation of high magnification SEM images (Fig. 4.14 (B), (D), (F) and (H)) was attempted to compare the uniformity of CNT diameters.

Fig. 4.14 (B) shows that electrodepositing continuously for 800 ms leads to CNTs with diameters in a range between 14 and 30 nm as shown in Fig. 4.15 (A). There was a noticeable generation of $H_{2(g)}$ bubbles during this electrodeposition experiment. When the electrodeposition was divided into two intervals (400 ms × 2), the uniformity of CNT diameters was improved as the distribution of CNT diameters was narrow down to 16 – 24 nm (Fig. 4.15 (B)). This indicates that an electrodeposition procedure with the total electrodeposition time split into several shorter intervals separated by a rest period could improve the uniformity of Co electrodeposition However, at this stage, the effect of the HER which occurred during the each electrodeposition period still resulted in a sparse CNT growth (400 ms). Therefore, shorter electrodeposition periods were examined. Fig. 4.14 (F) shows the results of dividing electrodeposition time into 4 intervals (electrodeposition time was 200 ms for each interval). This experiment was not very successful as the coverage of CNTs is very sparse and the morphology of CNTs is hard to observe in SEM. It could be hypothesised that this kind of CNTs or carbon nanofibres (CNFs) was formed because most Co NPs had been re-dissolved during the cleaning procedure. When the electrodeposition time was divided into 8 intervals (electrodeposition time was 100 ms for each interval), the coverage of the CNTs improved significantly as shown in Fig. 4.14 (G) low magnification image. The diameter of the CNTs is more uniform (Fig. 4.15 (C)). Although the coverage of the CNTs was still sparse which probably was due to other experimental parameters being not yet optimised, the reproducibility of the CNT diameters was better than in the case of all other

conditions studied in these series when this particular experiment was repeated (Fig. 4.14 (I). This also implies the deposited Co NPs are more stable when fabricated using electrodeposition split into 8 intervals of 100 ms each as HER may not cause a significant build-up of $H_{2(g)}$ during a such short electrodeposition periods . However, it is hard to explain why Co NPs produced in this way appeared more stable against dissolution during washing.

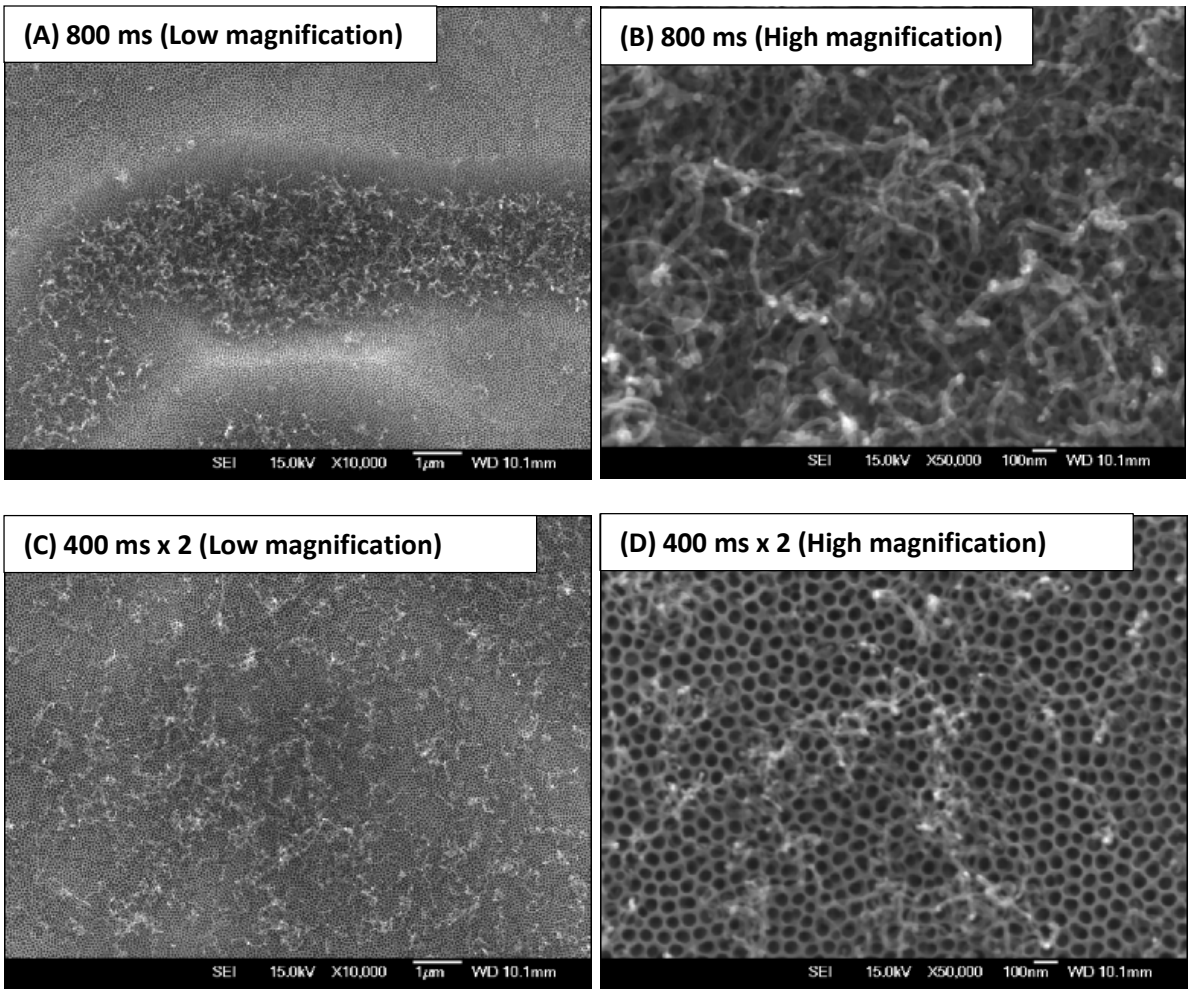

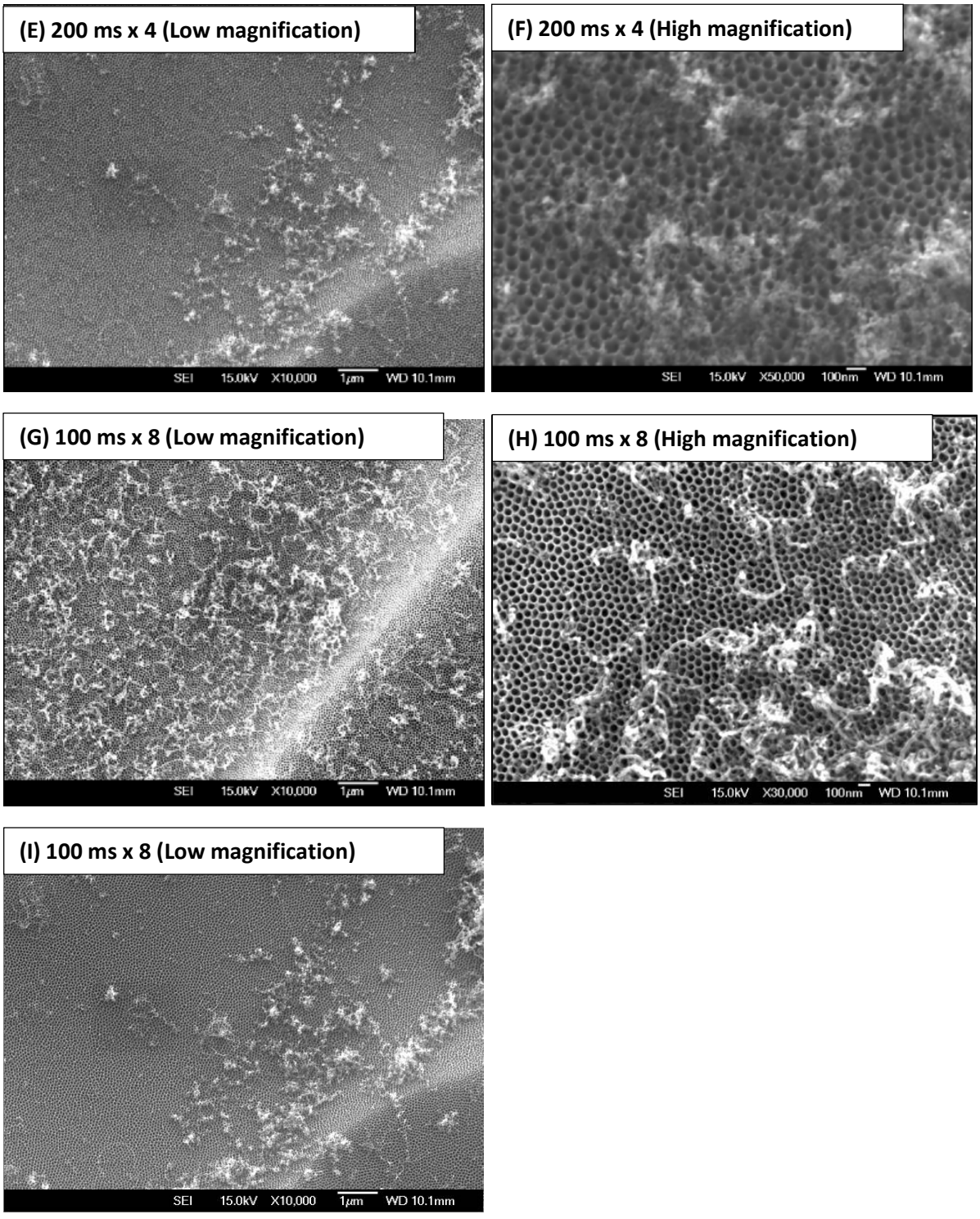

Fig. 4.14. The SEM images of top view of a PAA template with the CNTs. The total electrodeposition times and number of repeats are: (A) and (B) 800 ms directly; (C) and (D) 400 ms × 2; (E) and (F) 200 ms × 4; (G), (H) 100 × 8 ms and (I) another sample of 100 ms × 8 ms to show the reproducibility. There was 15 min rest period at open circuit potential between each repeat. The pH of the Co electrolyte is 3.8. CVD protocol 1 was used for CNT growth.

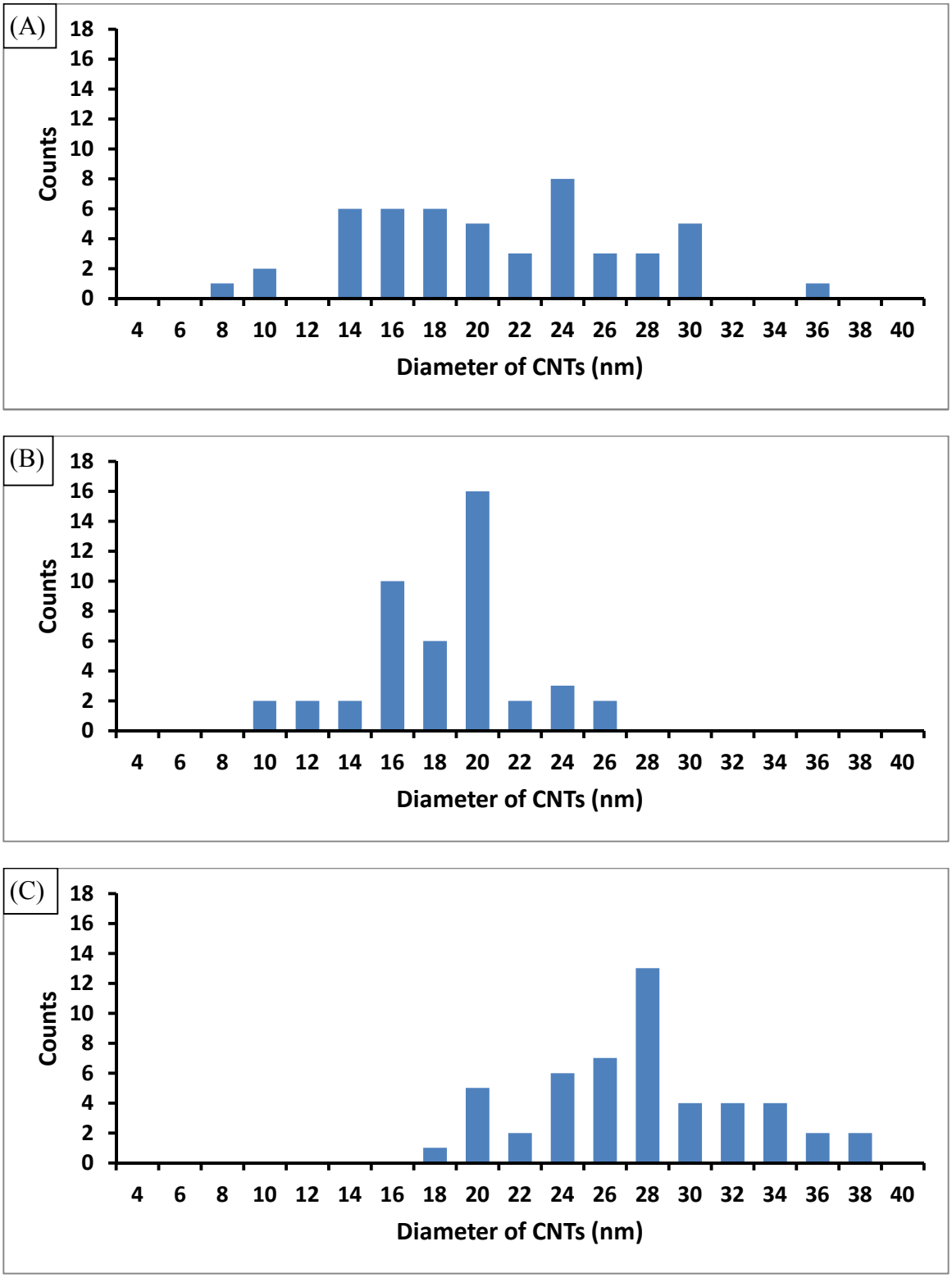

Fig. 4.15. The distributions of diameters of CNTs which were measured from SEM images shown in Fig. 4.14 (A) from image (B); (B) from image (D); (C) from image (H) in Fig. 4.14.

4.3.3 Optimisation of experimental procedures

The following sections describe optimisation of procedures relating to handling PAA membranes. This work was guided by advances in the understanding of important factors affecting the electrodeposition process.

4.3.3.1 Storage of the PAA membrane after the anodization and chemical etching processes

Preparation of PAA membrane and electrodeposition of Co NPs is a ~ 48 h process. The PAA membrane was kept moist prior to electrodeposition to prevent trapping of air bubble in the pores during re-wetting of membrane. The PAA membrane was stored by immersing in water, oxalic acid or Co electrolyte solution. In initial work, the membrane was stored in oxalic acid or Co^{2+} electrolyte solution following the method of Xu.[21] However, the ~300 nm thick PAA membrane prepared in this work is more fragile than the ~4 μm thick PAA membrane used by Xu and the thin PAA membrane was often damaged or dissolved by overnight storage in oxalic acid or Co^{2+} electrolyte solution. Damage to the membrane was not detectable by visual inspection; however, after electrodeposition of Co and CVD growth of CNTs, very disordered layers of CNFs were produced using a membrane that was stored in Co^{2+} electrolyte solution (Fig 4.16). This is attributed to breakdown of the porous structure leading to excessive electrodeposition of Co onto the PAA membrane and aggregation of Co during the CVD process. When the PAA membrane is stored in Co^{2+} electrolyte solution overnight, the porous structure could either partially removed by chemical etching or mechanically damaged during mounting into the electrode assembly for the following electrodeposition, in both cases leading to growth of CNF mixtures during CVD. Fig. 4.17 (A)

shows the SEM image of a PAA membrane after immersing in oxalic acid solution overnight. The walls in the remaining PAA structure are much thinner than after the 3-step anodization process (compare with Fig. 3.16). This finding indicates that the porous structure of PAA can be slowly etched in oxalic acid. Fig. 4.17 (B) shows the damage to a PAA membrane that was stored overnight in oxalic acid and then chemically etched for only 15 min. On the basis of these results, membranes were stored in Milli-Q water.

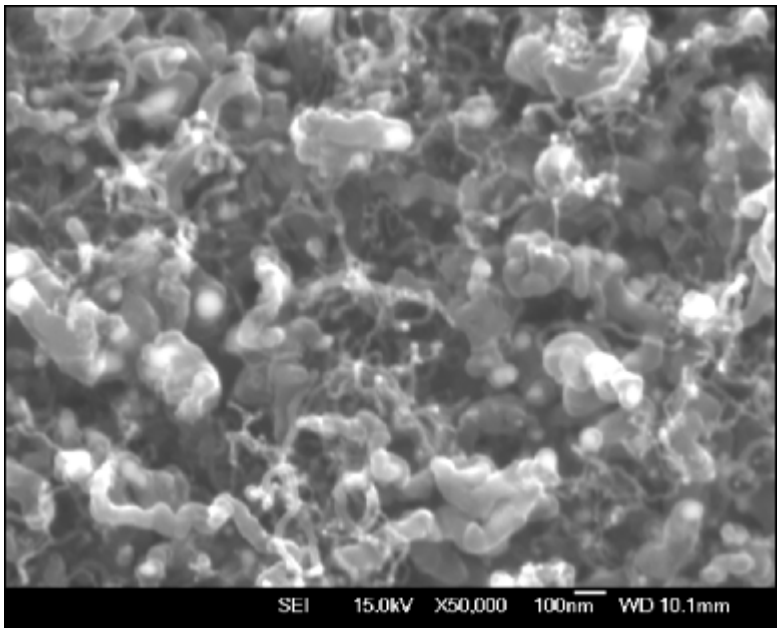

Fig. 4.15. SEM image of disordered CNTs and CNFs on a PAA template after CVD process. The CVD protocol 1 was used for this sample. The PAA template was immersed in Co electrolyte solution for overnight before the electrodeposition.

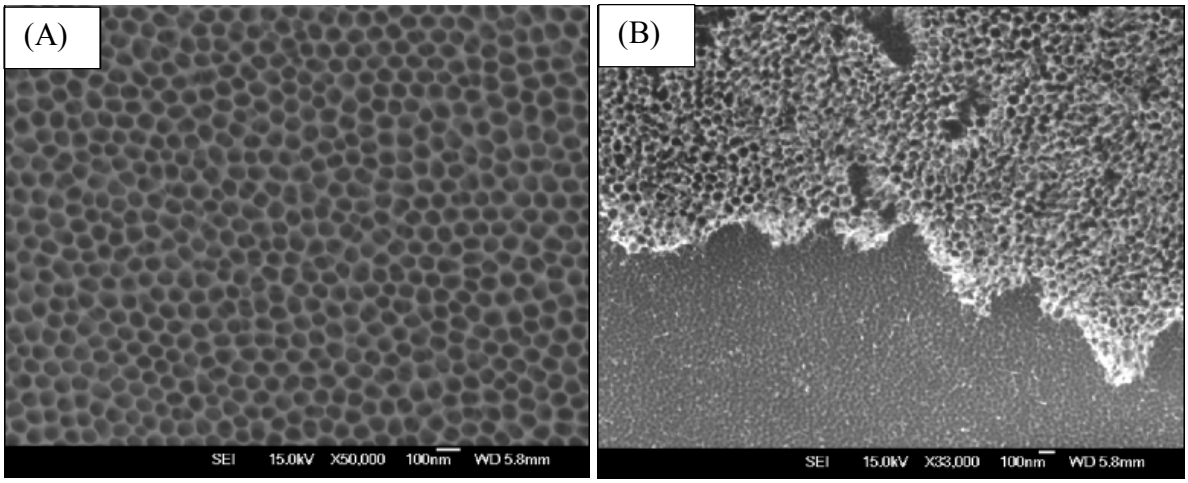

Fig. 4.16. SEM image of PAA template (A) after immersing in oxalic acid for overnight and (B) after immersing in oxalic acid for overnight and subsequently chemical etching for only 15 min on the next day.

4.3.3.2 Cleaning the PAA membrane before electrodeposition

Since Milli-Q water was used to store the PAA membrane, it was important to introduce Co^{2+} ions into the pores of PAA prior to electrodeposition. Hence, before electrodeposition, PAA membrane was immersed in Co^{2+} electrolyte solution for at least 30 min. After taking the PAA template out from the Co^{2+} electrolyte solution, the backside of the PAA template was wiped using a wet tissue and the topside was dried by gently blow drying with $N_{2(g)}$. This procedure ensured that most of the Co^{2+} electrolyte solution remained in the pores.

4.3.3.3 Preventing the Co NPs from the dissolving during and after the electrodeposition

Considering the effect of oxidative dissolution during the electrodeposition which has been explained in 4.1.3, for the optimised procedures, $N_{2(g)}$ was purged into the Co^{2+} electrolyte solution for 15 min before proceeding with electrodeposition. During electrodeposition, a gentle flow of $N_{2(g)}$ was maintained above the surface of the Co^{2+} electrolyte solution. After finishing electrodeposition, the PAA sample was quickly dipped (2 s) into Milli-Q water which had been degased by purging with $N_{2(g)}$ for at least 30 min. The sample was then blow dried under $N_{2(g)}$. Fig. 4.18 (A) shows a sparse CNT growth assumed to result from dissolution of Co when sample was cleaned by spraying with Milli-Q water from wash bottle. Fig. 4.18 (B) shows the effect of oxidative dissolution was decreased after optimising the cleaning procedure. Although the CVD protocols used in these two samples were different (protocol 1 was used for sample in Fig. 4.18 (A) and protocol 2 was used for sample in Fig. 4.18 (B)), the increase in CNT growth show in Fig. 4.18 (B) is greater than that expected from changing the CVD conditions (see section 4.3.4). Therefore, the increased coverage of CNTs in Fig. 4. 18 (B) is mainly due to the optimisation of the cleaning procedure. Other evidence to support this conclusion is the SEM image shown in Fig. 4.19 (A). The sample in Fig. 4.19 (A) was cleaned by quickly dipping into Milli-Q water not purged with $N_{2(g)}$ and CVD protocol 1 was used for CNT growth. The coverage of CNTs is better than for the sample shown in Fig. 4.18 (A), also prepared using CVD protocol 1, but washed through with water nor pre-purged with $N_{2(g)}$.

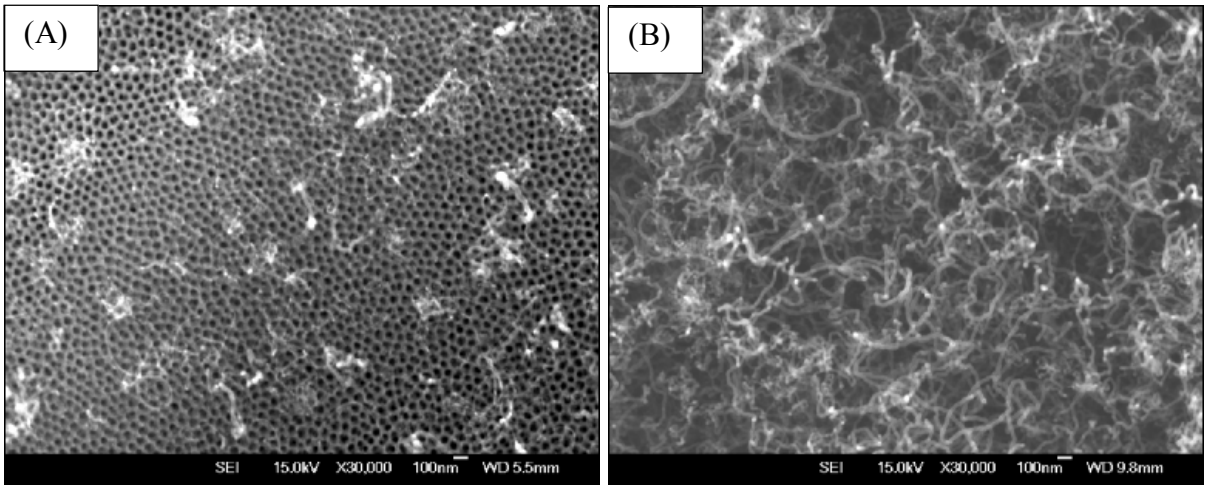

Fig. 4.17. SEM image of top view of a PAA template after growth of CNTs. Co was electrodeposited for 100 ms × 4 (pH of Co^{2+} electrolyte solution was 3.8). After electrodeposition, the sample was washed with (A) Milli-Q water from a wash bottle and (B) a quick dip into Milli-Q water pre-purged with $N_{2(g)}$. CVD protocol 1 and 2 were used for sample A and B respectively.

4.3.4 Effect of pH of the Co^{2+} electrolyte solution on the uniformity of electrodeposition

Optimisation of the procedures for handling PAA membranes (section 4.3.3) and use of CVD protocol 2 (Fig. 4.13) in place of protocol 1 (Fig. 4.12) improved the coverage of CNTs grown on PAA templates (compare Fig. 4.19 (A) and (B)). However, even with the optimised conditions, the CNT diameters were not uniform (Fig. 4.19 (B)). This indicates that the coverage of deposited Co NPs had been improved but the amount of deposited Co in the pores was not uniform. To address this problem, the pH of the Co^{2+} solution was increased from 3.8 to 4.7 with the expectation that any interference from the HER would be decreased at the higher pH. Comparison of Fig. 4.19 (B) and (C) shows a significant improvement in the uniformity of CNT diameters after adjusting the pH of the Co^{2+} electrolyte solution from 3.8 to 4.7. Fig. 4.20 (A) and (B) show the histograms of the diameter distributions for CNTs which were measured using the SEM images in Fig. 4.19 (B) and (C) respectively. The CNTs

grown from Co NPs deposited from pH 4.7 solution show a much narrower size distribution (size distribution range ~ 13 nm) compared with those grown from Co NPs deposited from pH 3.8 solution (size distribution range ~ 40 nm). These results confirm that a higher Co^{2+} solution pH improves the uniformity and coverage of Co NP and Co NW electrodeposition.

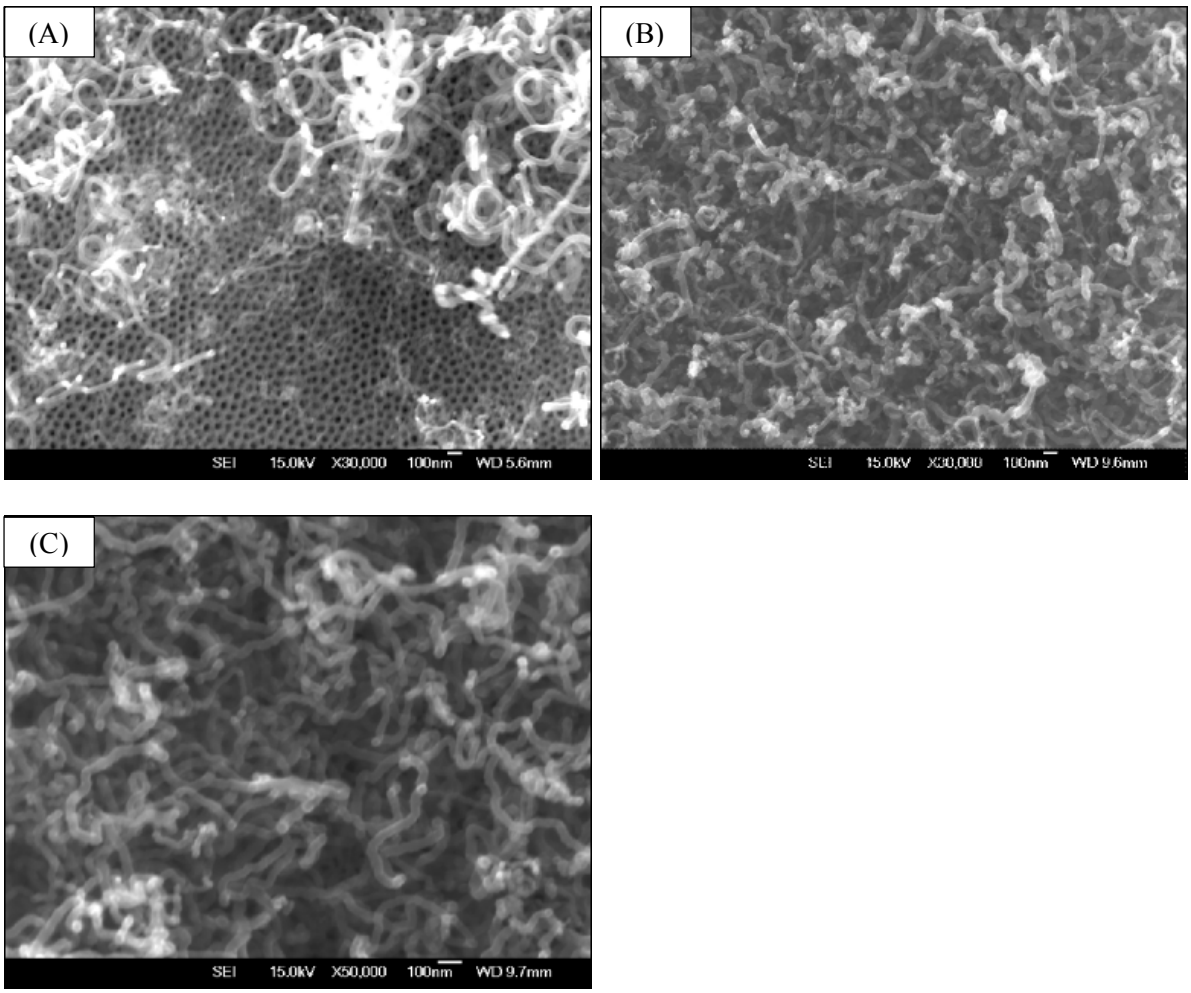

Fig. 4.18. SEM images of top view of a PAA template after growth of the CNTs. The electrodeposition times are all 400 ms (100 ms × 4). The pH of the Co electrolyte solution is (A) pH 3.8, (B) pH 3.8 and (C) pH 4.67. CVD protocol 1 was used for sample (A) and CVD protocol 2 was used for samples (B) and (C).

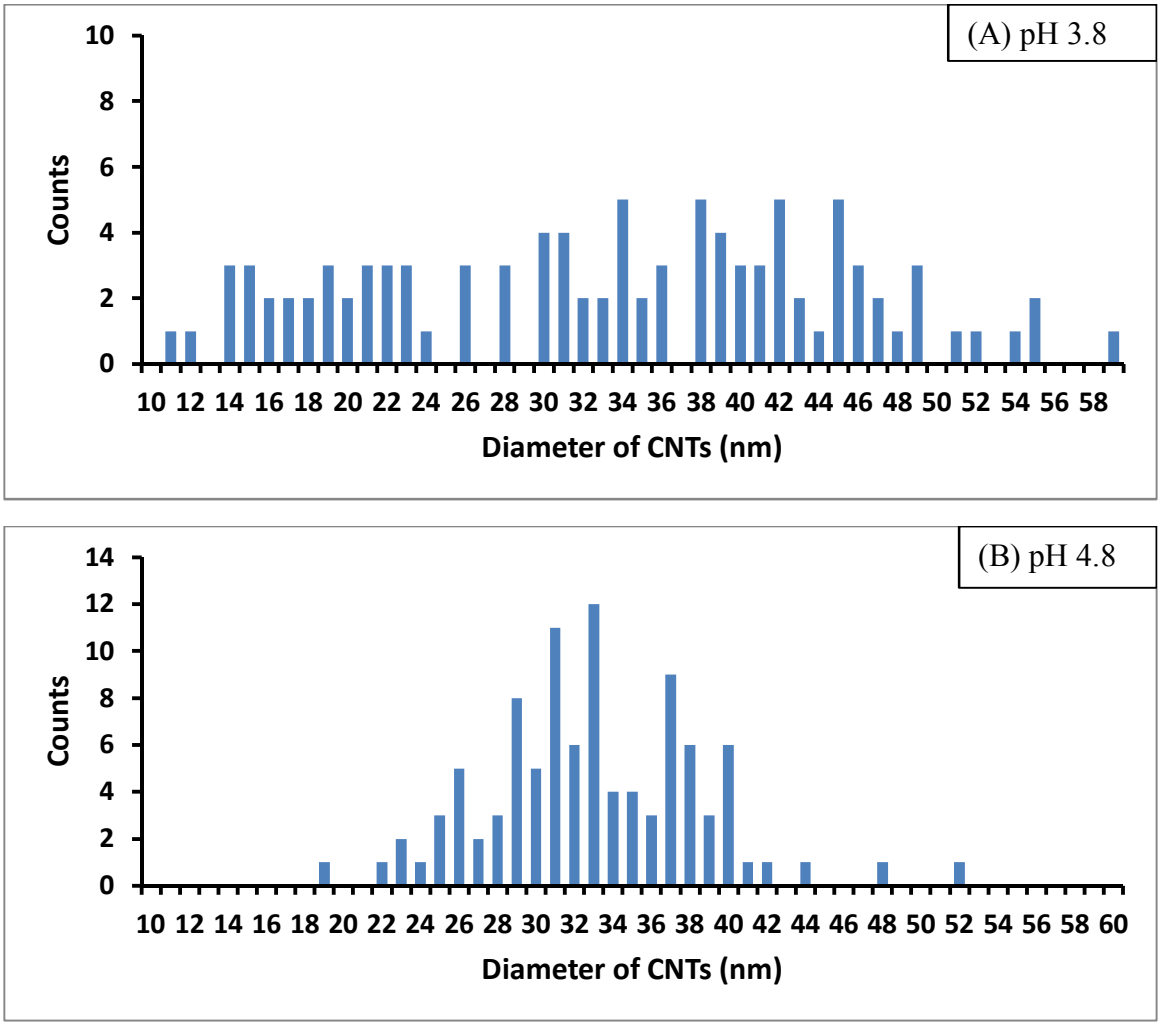

Fig. 4.20. The distributions of diameters of CNTs which were measured from SEM images (A) from image (B); (B) from image (C) in Fig. 4.18.

4.3.5 Optimisation of the CVD conditions for CNT growth

The parameters for CNT growth were based on studies in our laboratories by Knobloch[35] and Xu[21] who used Co NPs as the catalyst on different substrates with different strategies for CNT growth. Knobloch investigated Co NPs deposited on a Si wafer for CNT growth while Xu used Co NPs in a PAA membrane.[21,35] Knobloch used the same furnace as in the present work but a different furnace was employed for Xu's study. Hence, during the early stages of this study the parameters for CNT growth (protocol 1, Fig. 4.12) were based on Knobloch's experiments.[35] It should be highlighted that the reduction stage was performed

at 450 °C in this protocol. During early experiments discussed here the reduction temperature was not perceived to be a critical parameter for the uniformity of CNT growth. Indeed, some CNTs were successfully grown using this protocol and imaged using both SEM (Fig. 4.19 (A)) and TEM (Fig. 4.21). Fig. 21 (B) and (C) show high magnification images of these CNTs with about 5 graphene layers in their walls (as highlighted by the inserted measurements in Fig. 4.21 (D). Clearly, MWCNTs are produced using these conditions.

In TEM studies performed at South Taiwan University of Science with Technology by Yu-Ming Shen and at the University of Canterbury with the help of Domagoj Belic Co NPs have been observed at the base of PAA membranes after CNT grown (Fig. 4.22 (A) and (B)). Fig. 4.22 (D) shows the energy dispersive X-ray spectrum (EDS) corresponding to the sample shown in Fig. 4.22 (A). This confirms the presence of Co NPs in this sample as evidenced by K_α and K_β peaks at 6.924 and 7.057 keV.[41] However, Co NPs are not always associated with CNTs; many Co NPs were encapsulated by carbon nano-onions (Fig. 4.22 (C). This suggests that not every Co NP, partially or completely oxidized during exposure to air after electrodeposition and before CVD growth was completely reduced into metallic Co using this protocol. Based on the finding of other works discussing in the reduction, reduction of Co NPs is likely to occur mainly during the temperature increase from 450 °C to 650 °C prior to introduction of acetylene in the system $H_{2(g)}$ was continuously supplied during that period.

The optimised CVD protocol 2 (Fig. 4.13) was adopted to ensure that Co NPs were fully reduced prior to CNT growth. The use of a reduction temperature of 650 °C was based on the study of Liu *et al.* who found that the optimal temperature for complete reduction of oxidised Co was between 600-700 °C.[31] For CNT growth using Co NPs as the catalyst and a PAA membrane as a substrate, Jeong *et al.* recommended a growth temperature of 650 °C.[20]

This temperature was selected as the maximum that could be used without melting the Al foil (Al melting point is 660.32 °C).

Comparison of the SEM images in Fig. 4.19 (A) and (B) illustrates the effect of using a higher reduction temperature. Fig. 4.19 (A) shows CNTs grown using protocol 1. The sparse CNT growth is attributed to incomplete reduction of oxidised Co NPs at 450 °C. As a result of the more efficient reduction at the higher temperature (650 °C), dense CNTs were grown using protocol 2 shown in Fig. 4.19 (B).

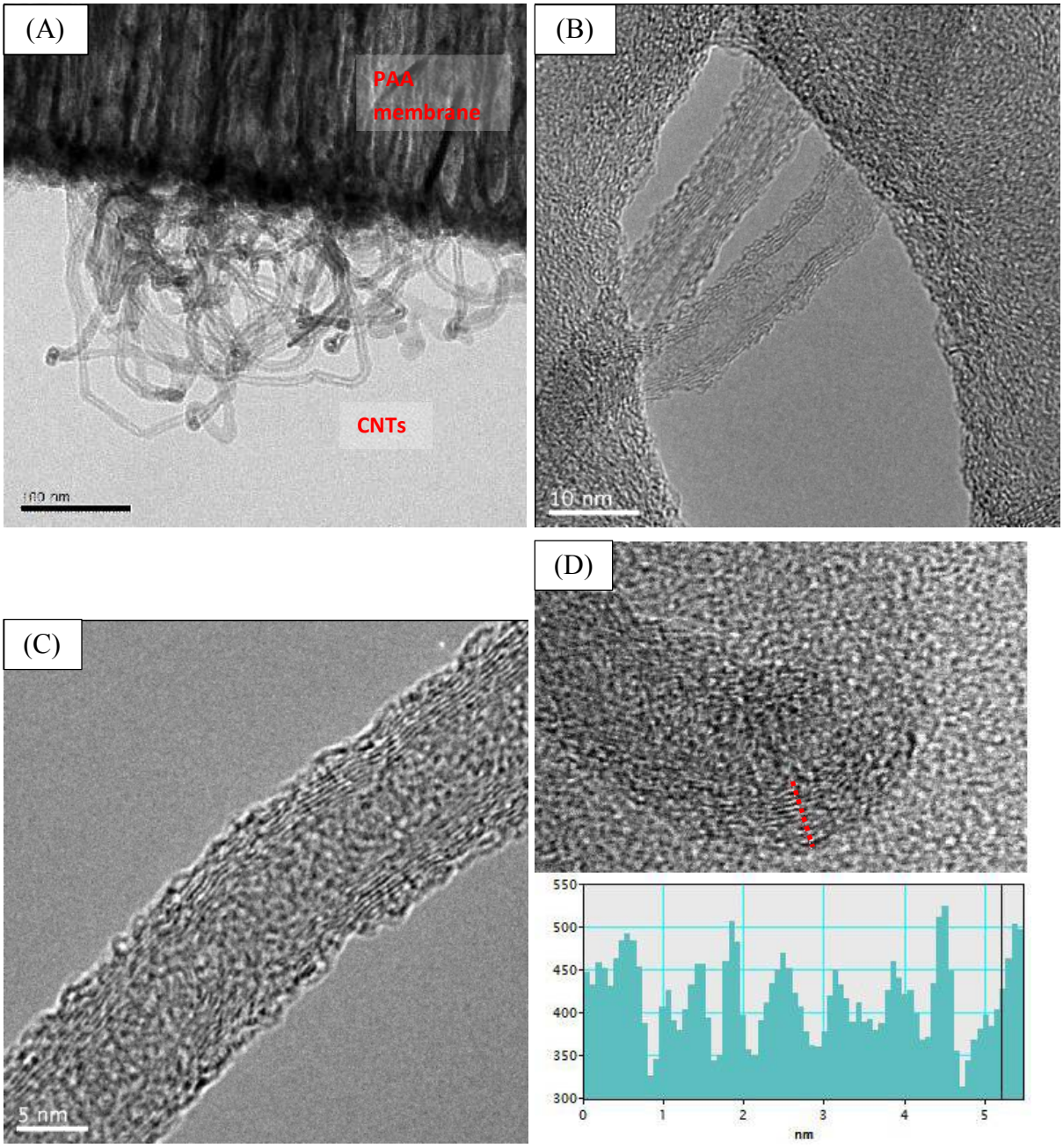

Fig. 4.19. TEM images of MWCNTs grown on a Co-PAA template. (A) Bunch of CNTs on the PAA membrane; (B), (C) and (D) are high magnification images of MWCNTs. The insert figure in (D) is the measurement of the grapheme layer of walls. The electrodeposition time was 100 ms × 4 and the pH of the Co electrolyte solution was 3.8. CVD protocol 1 was used for this sample. Images (A) and (D) were obtained by Yu-Ming Chen at the Department of Material Science and Engineering National Chang Kung University). Image (C) was obtained by Domagoj Belić from the Physics and Astronomy Department, University of Canterbury.

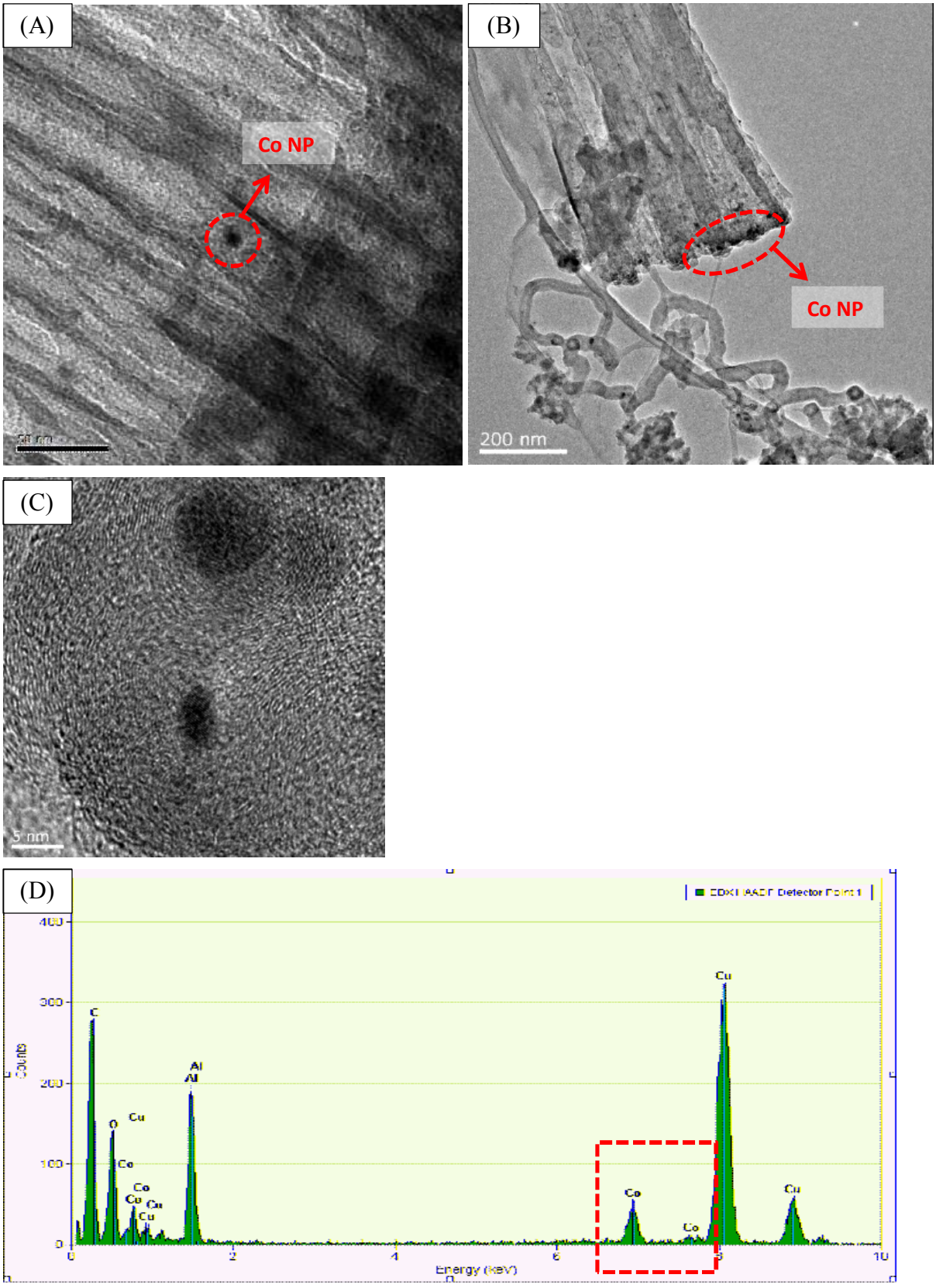

Fig. 4.20. TEM images of samples (A) and (B) showing Co NPs at the bottom of a PAA membrane. (C) is a high magnification image of Co NPs which were encapsulated by carbon. (D) The energy-dispersive X-ray spectrum for sample (A). The electrodeposition time was 100 ms × 4 and the pH of the Co electrolyte solution was 3.8. CVD protocol 1 was used for this sample. Image (A) and (D) were obtained by Yu-Ming Chen at the Department of Material Science and Engineering National Chang Kung University.

4.3.6 Control of the diameter of CNTs by controlling the size of Co NPs

This part of the experiment aimed to control the size of the Co NPs by adjusting the electrodeposition time. Attempts were made to image Co NPs at the bottom of the pores using SEM and Energy Dispersive Spectroscopy (EDS). Unfortunately, most Co NPs were too small to be observed using SEM. Fig. 4.23 shows an SEM image of a cross-section of a PAA template with Co NPs which were electrodeposited using a 2 s continuous process. After depositing, the membrane was heated in order to reduce aggregate the electrodeposited Co NPs yielding large particles, so they could be observed using SEM. The sample was bent afterwards to crack PAA layer exposing cross-section (the image shows the PAA template next to the crack). The round and small particles which two of them were highlighted in the red circles could be the aggregated Co NPs. Although these could also be remnants of PAA on Al base, as one would expect different brightness for Co NPs due to significant difference in Z (*cf*. Al and O). However, the EDS cannot provide a specific and precise measurement in this case because only a low magnification (< 3000) can be used when EDS mode is selected. In this case, the result can only confirm the existence of Co over the large area on PAA but not for a specific position corresponding to an individual Co NP.

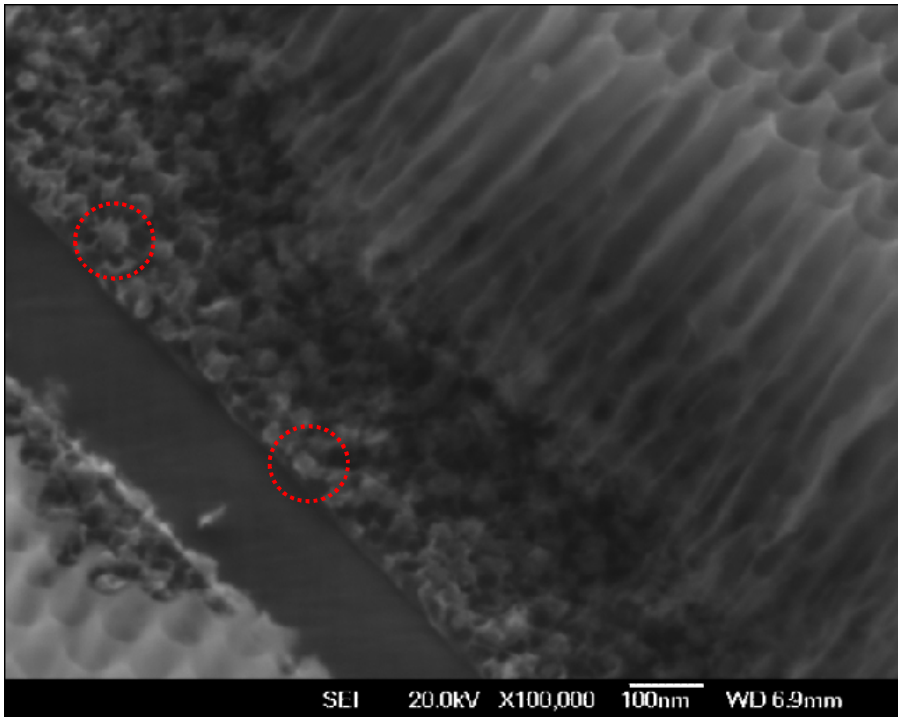

Fig. 4.21. A cross-section SEM image of PAA template with Co NPs. The electrodeposition was carried out in a pH 3.8 Co electrolyte and the electrodeposition time was 2 s. The template then was reduced at 450 °C for 1 h under $H_{2(g)}$ and $Ar_{(g)}$.

The Co NPs which were produced by electrodeposition for shorter times were not detectable using SEM. Thus, instead of direct observation of Co NPs, observations of CNT diameters after the CVD process was used to assess the uniformity of Co NPs. Fig. 4.24 (A)-(E) show CNTs which were grown using PAA templates with Co NPs which were electrodeposited using different times (100 ms × 20, 100 ms × 8, 100 ms × 4, 100 ms and 50 ms). Importantly, CVD growth was performed using optimised conditions (protocol 2). Fig. 4.25 (A)-(D) show the distributions of the CNT diameters corresponding to the samples with the electrodeposition times as shown in Fig. 4.24 (A)-(D) The sample which was electrodeposited for 50 ms had very sparse and thin CNTs (Fig. 4.26 (E) and (F). and their diameters could not be reliably measured by SEM. Nevertheless, the CNT diameters are clearly sub-20 nm as revealed by comparison of Fig. 4.22 (D) and (F). To ensure representative data was obtained, each histogram includes the measurements of CNT diameters from 5 SEM images which were taken from different areas of one sample; 20 CNT

diameter measurements were made from each SEM image. This means that for each sample, 100 CNT diameters were measured. To compare the trends based on these histograms, only parts of the histograms representative of 4 or more occurrences are considered. These diameters are highlighted in Fig. 4.25.

The distributions of the CNT diameters corresponding to the electrodeposition times of 100 ms × 20 and 100 ms × 8 are not significantly different (Fig. 4.25 (A) and (B)) with diameters varying in the range 25-35 nm. This suggests that a similar amount of Co is electrodeposited in these experiments. Examination of the voltage pulses at the electrodes during electrodeposition can account for this observation. Fig. 4.26, yellow line, shows the applied voltage waveforms at the working electrode during 4 electrodeposition steps. The blue line shows the voltage at the auxiliary electrode as the current passes though the PAA template and the Co^{2+} electrolyte. It is evident that the voltage at the auxiliary electrode gradually decreases during each electrodeposition interval indicating that the PAA template becomes less conductive with an increase in the number of electrodeposition intervals. Hence, increasing the number of deposition intervals from 8 to 20 is expected to have little effect on the amount of Co deposited.

When the electrodeposition time is 100 ms × 4, the CNT diameters show a small decrease to between 23 and 35 nm. However, all three electrodeposition times (100 ms × 20, 100 ms × 8 and 100 ms × 4) result in Co NPs which yield CNTs with a broad diameter distribution. When the electrodeposition time is 100 ms (Fig. 4.25 (D)), the range of the CNT diameter distribution is narrower from 21 to 30nm.

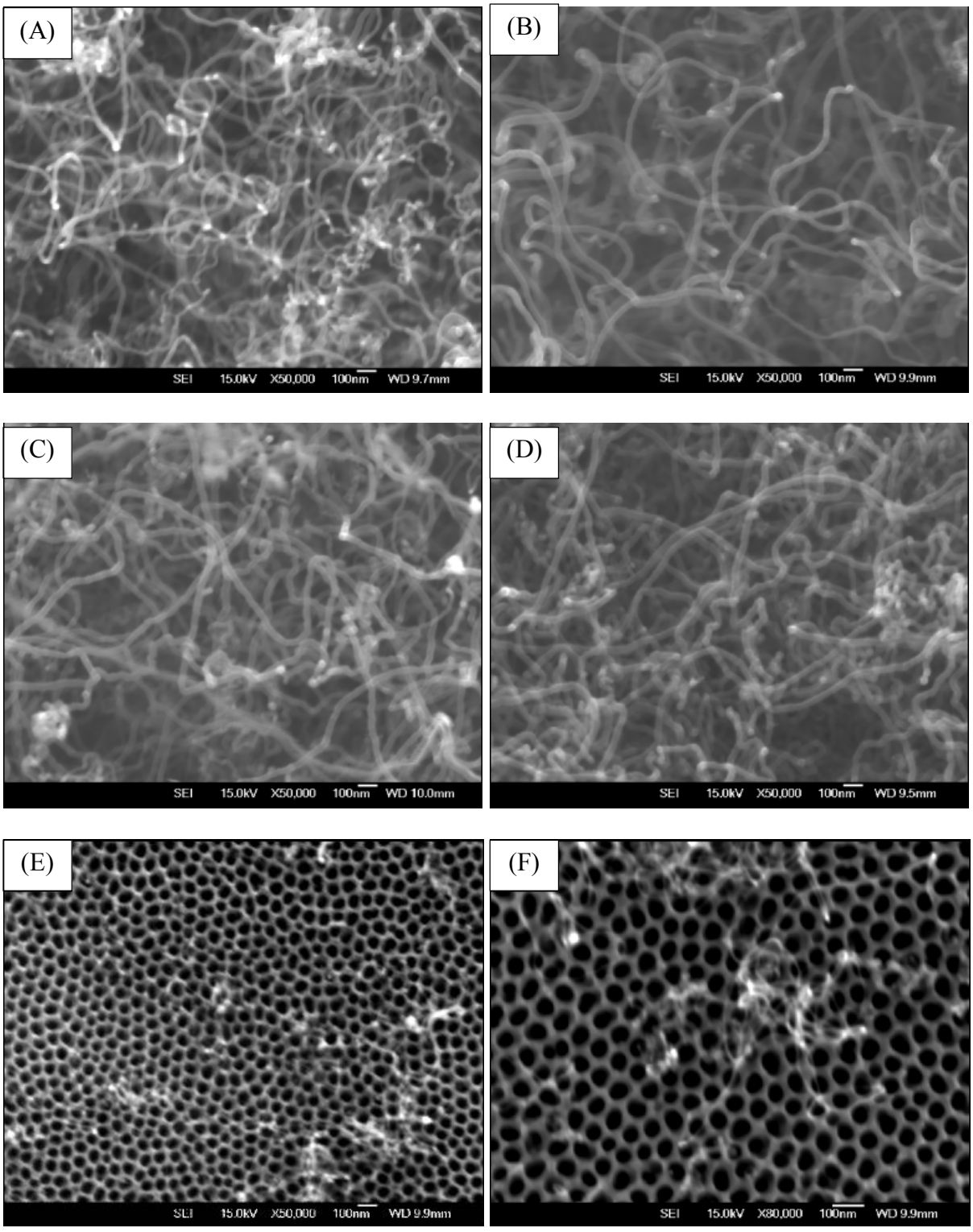

Fig. 4.22. The SEM images of top view of a PAA template with the CNTs. The electrodeposition time (A) 100 ms × 20; (B) 100 ms × 8; (C) 100 ms × 4; (D) 100 ms and (E) 50 ms. (F) high magnification image of CNTs after 50 ms electrodeposition. The pH of the Co electrolyte solution was 4.68. The CNTs were grown by using CVD process protocol 2.

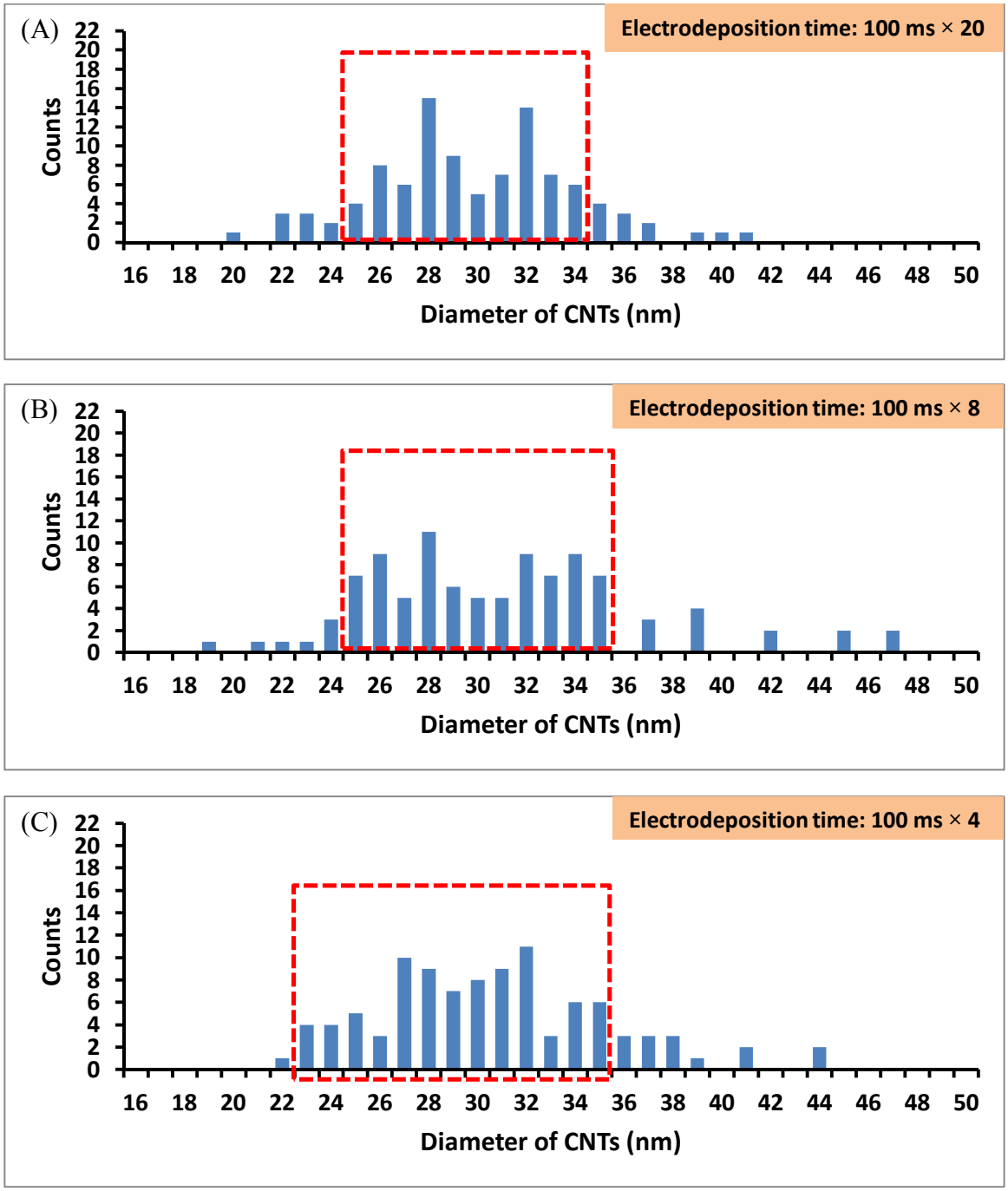
(A)
Electrodeposition time: 100 ms × 20
Counts
Diameter of CNTs (nm)
(B)
Electrodeposition time: 100 ms × 8
Counts
Diameter of CNTs (nm)
(C)
Electrodeposition time: 100 ms × 4
Counts
Diameter of CNTs (nm)

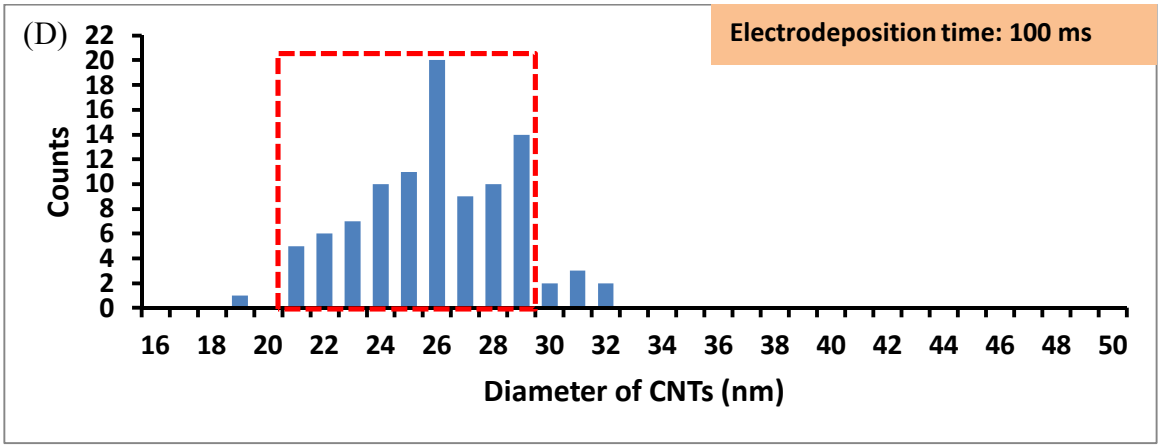

Fig. 4.23. The distributions of diameter of CNT diameters. (A) to (D) in this figure were measured from the samples (A) to (D) in Fig.4.23. The red boxes highlight diameters occurring 4 of more.

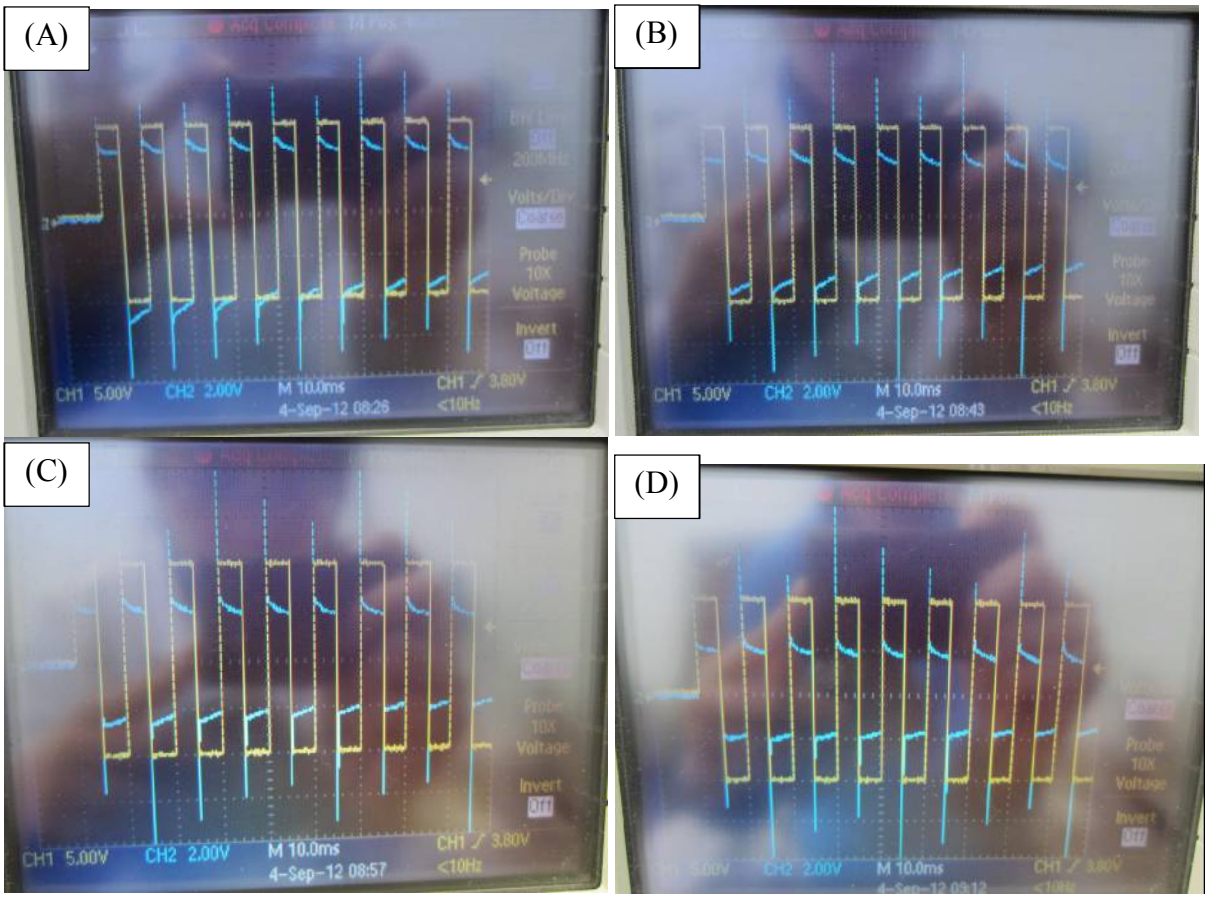

Fig. 4.24. Photos of the oscilloscope screen used for monitoring the pulsed voltage during the electrodeposition. (A) 1st electrodeposition step; (B) 2nd electrodeposition step; (C) 3rd electrodeposition step and (D) 4th electrodeposition step (electrodeposition time is 100 ms for each electrodeposition step). Yellow line shows the applied voltage and the blue line shows the voltage measured at the auxiliary electrode.

Raman spectroscopy was utilised to confirm that CNTs were grown using the shorter total electrodeposition times. Fig. 4.27 shows Raman spectra of the CNTs grown on the PAA template with Co NPs electrodeposited using 50 ms, 100 ms and 100 ms × 4 intervals. The G band, D bands and G′ band are observed; these are the typical peaks for MWCNTs in Raman spectra. According to literature reports, the G band is typically observed at 1578-1584 cm^{-1} and corresponds to vibration of the C-C bonds of sp^2 carbon. The D band normally appears at 1338-1348 cm^{-1} and corresponds to vibration of sp^3 carbon. The G' band is typically observed at 2500-2900 cm^{-1} which corresponds to well-ordered sp^2 carbons.[36,37] The Raman spectra recorded in this work show that the G band was in the range of 1581-1597 cm^{-1} and the D band was in the range of 1307-1316 cm^{-1} (Fig. 4.27). The reason for the shift of D band peaks could be a thermal effect which manifests itself in the increase of the local temperature of CNTs due to exposure to high power laser.[36,37,38] The G′ band (at around 2600 cm^{-1}) was not very obvious apart from Fig. 4.27 (A) which may result from the random analytic angle as the CNTs are twisted on the top of PAA template.[38] The relative intensity of G band to D band (I_G/I_D) corresponds to the purity and order of MWCNTs based on the double resonance theory.[38,39] The intensity of D band is considered In Fig. 4.27, The values of I_G/I_D for CNTs with three electrodeposition times are similar; (A) is 0.83, (B) is 0.81 and (C) is 0.83. These values are close to the research report by Rana *et al.* who also grew CNTs on a PAA template and provided the analysis results of Raman spectra.[39] Based on the results of Raman spectra, it is clear that MWCNTs are grown in these experiments.

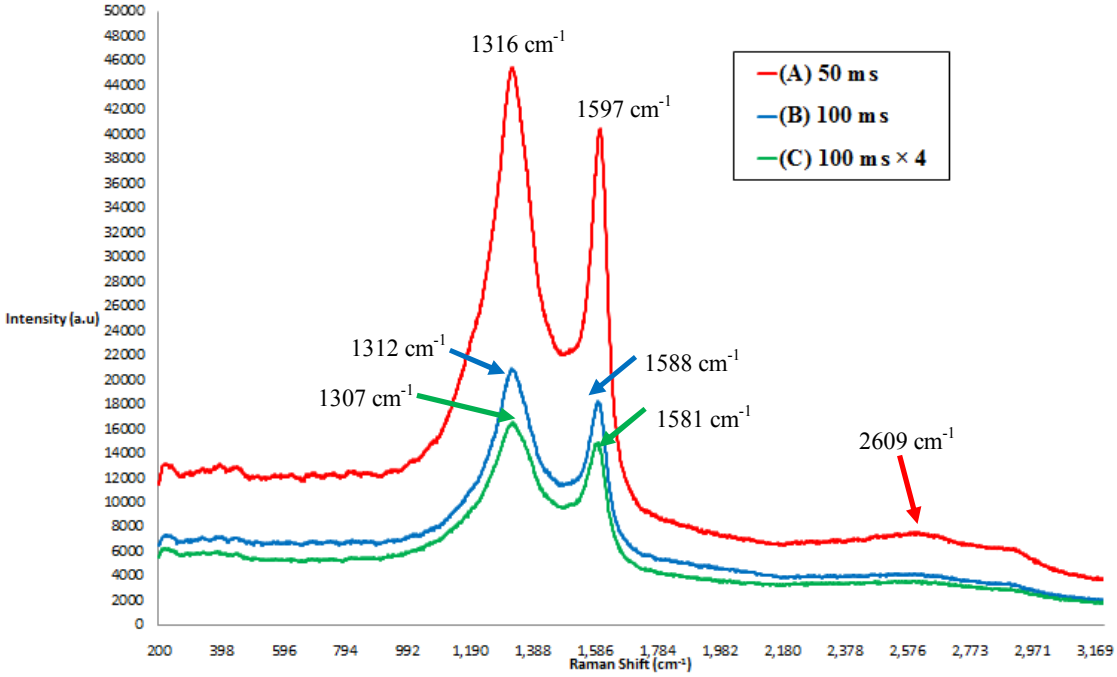

Fig. 4.25. Raman spectra of CNTs grown on PAA template. The CNTs were grown by using protocol 2 of CVD process using the Co electrodeposition times shown.

The reproducibility of CNT growth using optimized catalyst system under optimized CVD conditions was examined and the results are shown in Fig. 4.28. Two individual samples were made using same experimental conditions (electrodeposition time of 100 ms; the pH of the Co electrolyte solution was 4.7; and the CNTs were grown by using CVD process protocol 2) on the different days. The histograms in Fig. 4.28 show that these two samples have a similar distribution of CNT diameters between 20 to 30 nm. A slight variation of the CNT diameters in a range between 2 - 4 nm may result from the human erros. Each CNT diameter was measured by drawing a line across the CNT and the lenth of such line was calculated by Image J to give an estimate of the CNT diameter. Therefore, the SEM image quality such as contrast and brightness could slightly affect such measurements. However, the trend of CNT diameters should be very similar. The reproducibility of CNT growth on PAA

template based on the distribution of CNT diameters has not been reported before as such good coverage of CNTs and uniformity of CNT diameters had not been achieved before.

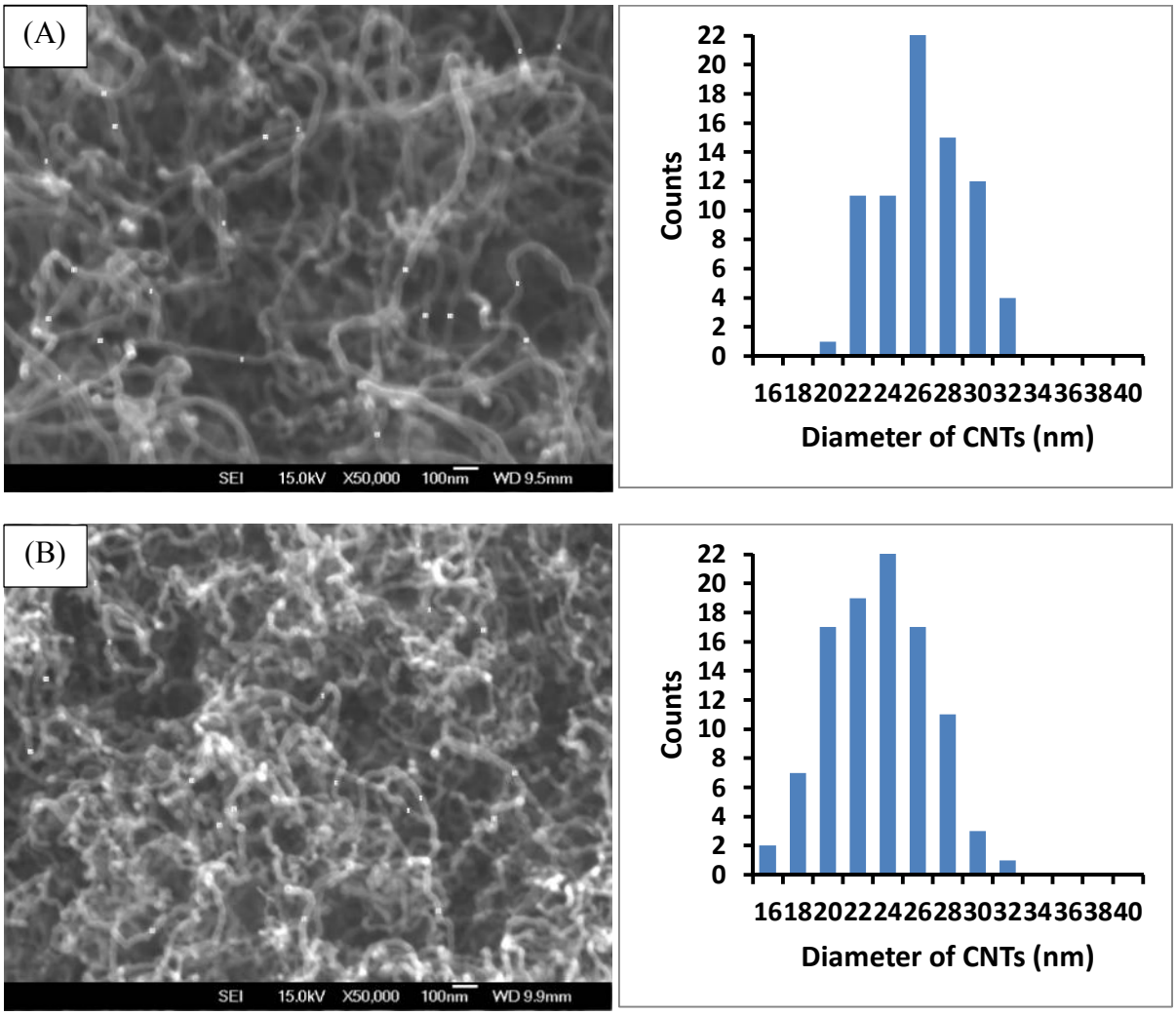

Fig. 4.26. The distributions of diameter of CNT diameters from two different samples with same electrodeposition time of 100 ms. The pH of the Co electrolyte solution was 4.7. The CNTs were grown by using CVD process protocol 2.

4.3.7 Study of the electrodeposition of Co NPs on dimpled Al_2O_3 templates

Because it was impossible to observe by SEM small Co NPs at the bottom of the pores within a shallow (300 nm deep) PAA template, use of TEM was attempted after the CNT growth. The reason for studying samples after CNT growth is that the PAA membrane must be dissolved prior to TEM imaging and it was not possible to collect Co NPs not

attached to CNTs. However, TEM (Fig. 4.21) demonstrated that even after CVD growth, the Co NPs are not always connected with CNTs.

An alternative strategy for direct SEM imaging of Co NPs was investigated. Co NPs were deposited onto a dimpled Al_2O_3 template with the expectation that this would simulate the electrodeposition of Co NPs within a PAA membrane. The fabrication of dimpled Al_2O_3 templates and their morphology has been discussed in detail in section 3.3.5 in chapter 3.

It should be noted that there is an important difference between using a shallow PAA membrane and dimpled Al_2O_3 as the substrate for electrodeposition. The dimpled Al_2O_3 template has only a very thin layer of naturally formed Al_2O_3 on top of the dimpled surface, although the bottom of the dimples could be preferred locations for electrodeposition due to a marginally thinner barrier layer of Al_2O_3.[40] Hence the whole surface of the dimpled template has higher conductivity than a PAA template. SEM observations of dimpled substrates after electrodeposition showed that the whole surface was covered by Co nanostructures. Fig. 4.29 (A) and (B) compare the morphologies of the dimpled Al_2O_3 template after electrodepositing Co for 50 ms and 100 ms respectively (note: these samples were not reduced at high temperature). After electrodepositing for 50 ms, the dimpled structure was partially filled with Co. Thin (sub-50 nm) Co NWs can be observed as they are slightly brighter than the dimpled substrate surface. In addition, Co is also deposited on the "hills" between the dimples between the dimples but the dimpled structure can still be discerned. (Fig. 4.29 (A)). After electrodepositing for 100 ms, the dimpled structure cannot be identified as the whole surface is covered by a thick deposit of Co. However, the Co layer is not a flat film as thick and long Co NWs uniformly covering the surface can be observed in SEM images.

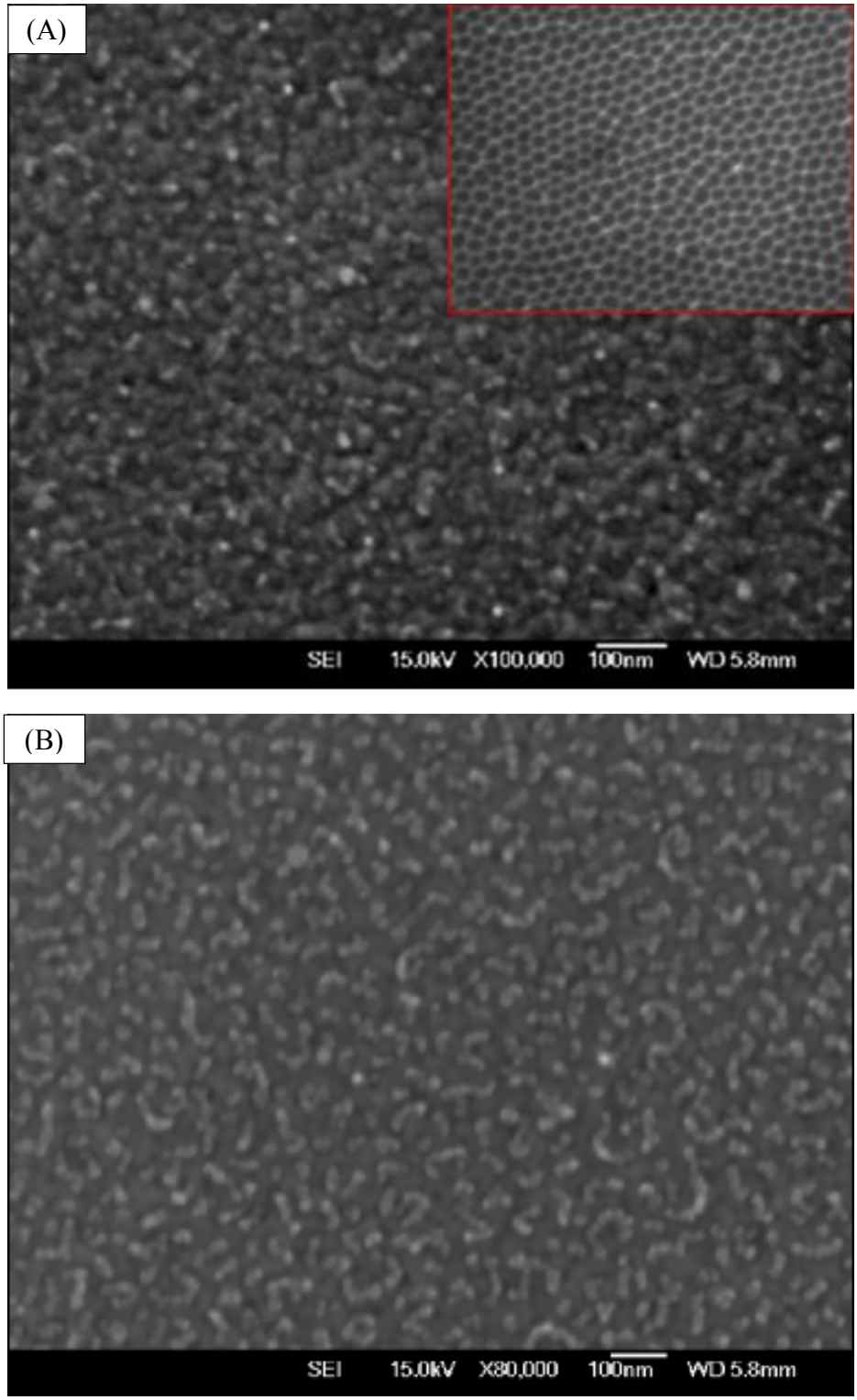

Fig. 4.29. SEM images of dimpled Al_2O_3 template after electrodeposition of Co for (A) 50 ms and (B) 100 ms. The insert image in (A) shows the surface of a dimpled Al_2O_3 membrane prior to Co electrodeposition.

In order to see how electrodeposited Co NPs aggregate in the reduction step prior to CNT growth, the dimpled Al_2O_3 templates were reduced under the same conditions as used

during the CVD process, protocol 2. After finishing the reduction process, $H_{2(g)}$ flow was stopped and the system was cooled to room temperature under $Ar_{(g)}$ flow. Fig. 4.30 (A) and (B) show SEM images of the aggregated Co NPs on the dimpled Al_2O_3 templates and Fig. 4.30 (C) shows a Co free dimpled Al_2O_3 template after the same reduction process. Notably, aggregation is directed by the dimpled structure of the substrate with large Co NPs sitting in the bottom of the dimples. Fig. 4.30 (A) shows that electrodeposition for 50 ms yields, after reduction, a sample with Co NPs varying size from 10-50 nm. This variable particle in size may be due to poor uniformity of the electrodeposition process at the early stages (similar to the early stage of PAA growth). Electrodeposition of Co for 100 ms results in better uniformity of Co NPs after reduction, with a size range of 10-20 nm. (Fig. 4.30 (B)).

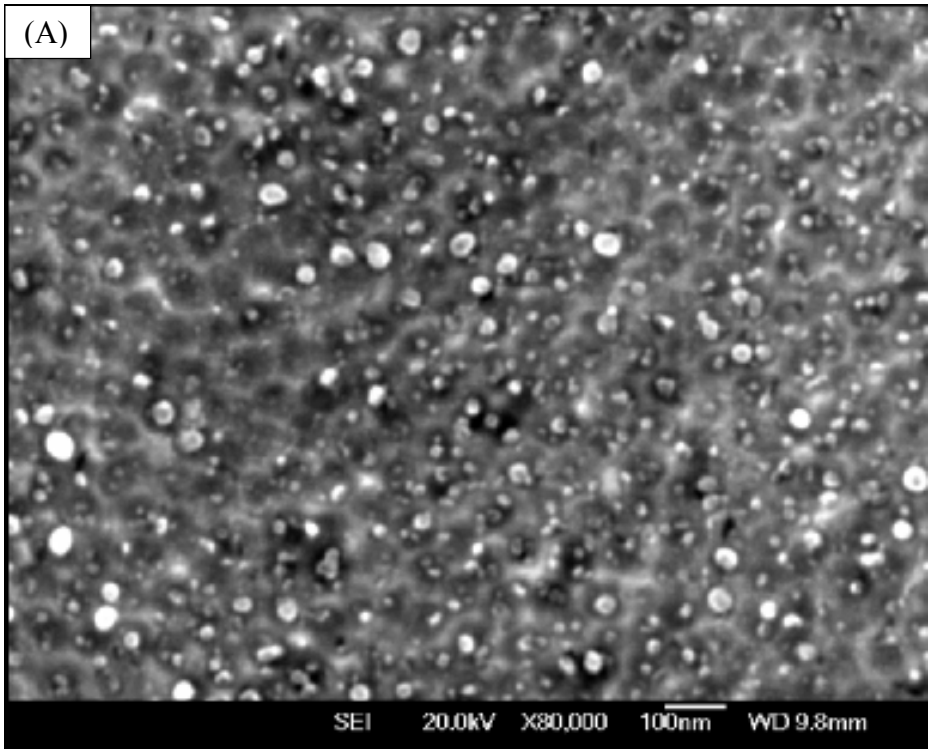

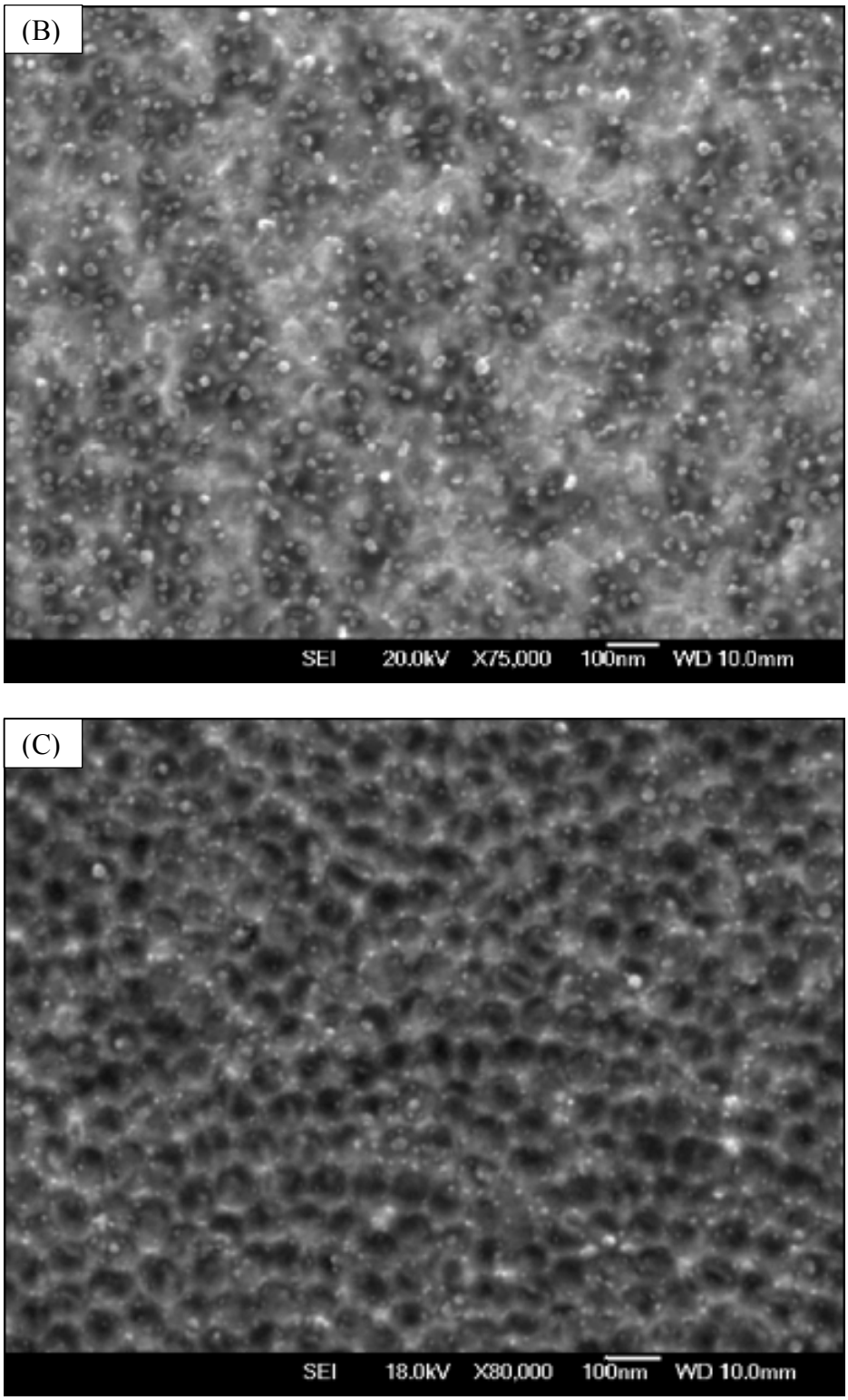

Fig. 4.30. SEM images of dimpled Al_2O_3 template with Co NPs ((A) and (B)) after reduction by protocol 2 (without CNT growth). The electrodeposition time for (A) is 50 ms and (B) is 100 ms. (C) is a blank dimpled Al_2O_3 substrate which was reduced in the CVD chamber with (A) and (B).

CNT growth was tested using Co-containing dimpled Al_2O_3 templates, prepared by Co electrodeposition for 100 ms, 50 ms, 20 ms and 10 ms. Fig. 4.31 shows that as the Co electrodeposition time decreases, the average diameters of CNTs decreases. For the sample deposited for 100 ms, a mixture of thick CNTs and CNFs grows during CVD. As the Co electrodeposition time decreases, the proportion of thin CNTs in the sample increases, although all samples show a range of CNT (or CNF) diameters. Thus, for these samples, the total amount of Co electrodeposited on the dimpled substrate appears to correlate with the duration of the electrodeposition and affects the aggregation of Co NPs during the reduction process. The shorter electrodeposition time results in formation of smaller Co NPs. As a consequence thinner CNTs are observed. On the other hand, low coverage of CNTs shows the poor uniformity of Co NP coverage.

The results for this series of samples do not match expectations based on the direct observation of Co-containing dimpled templates after reduction (Fig. 4.30 (A) and (B)). The images in Fig. 4.30 lead to the expectation that the sample with 50 ms of Co deposition would show a broader range of CNT diameters and overall larger diameters than the sample prepared with 100 ms of electrodeposition, however, the opposite trend in CNT diameters is observed. This could be due to incomplete aggregation of the deposited Co prior to CNT growth. Fig. 4.30 (B) shows the dimpled structure is less obvious than in Fig. 4.30 (A) which indicates CNFs or thick CNTs may be grown from the Co deposited for 100 ms and which was not subsequently aggregated into active catalyst particles.

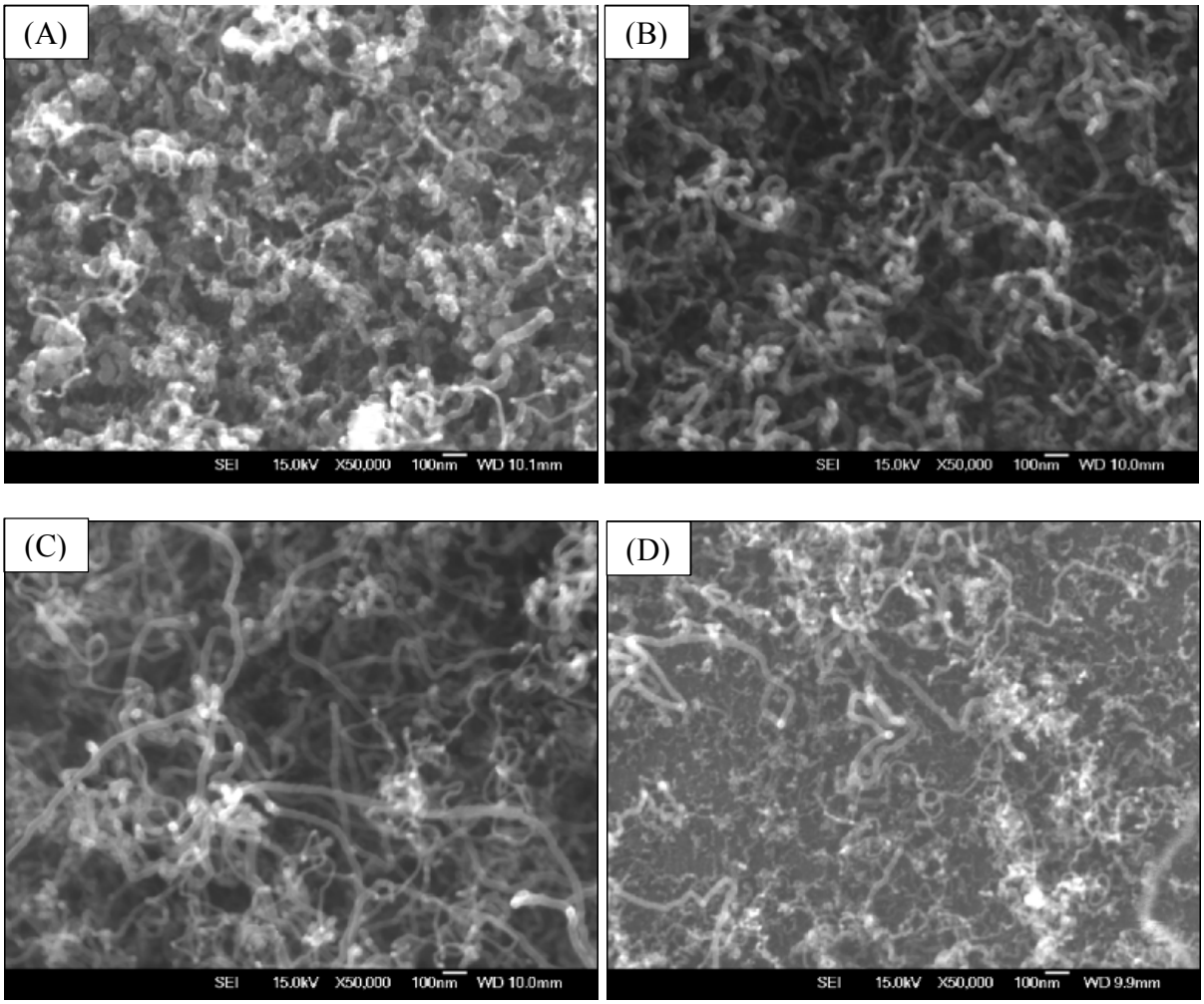

Fig. 4.31. SEM images of CNTs on dimpled Al_2O_3 substrates which underwent Co electrodeposition for (A) 100 ms, (B) 50 ms, (C) 20 ms and (D) 10 ms respectively. The CNTs were grown using CVD process protocol 2.

4.4 Conclusions

Since the coverage and uniformity of Co electrodeposition and a suitable reduction temperature for Co reduction are essential factors for growing dense CNTs, the optimisation of experimental procedures was divided into two parts in this work. For electrodeposition, the electrodeposition was split into several steps with a short deposition interval (1 × 100 ms) for each step with a long break (15 min) in between. This reduces the possibility of generation of $H_{2(g)}$ and allows any $H_{2(g)}$ which may be generated during the electrodeposition to diffuse out

of the pores at the same time allowing enough time to restore the concentration of Co^{2+} at the bottom of the pores. The pH of the Co^{2+} electrolyte solution was adjusted from 3.8 to 4.7 to decrease the effect of HER. $N_{2(g)}$ was purged to prevent the oxidative dissolution of the electrodeposited Co NPs during the electrodeposition and cleaning procedures. For the CVD process, the temperature of the reduction process was increased from 450 °C to 650 °C. The higher temperature (650 °C) ensures the deposited Co NPs were fully reduced to the metallic state without destruction of the PAA template. The coverage and the uniformity of Co NPs were significantly improved as evidenced by a dense coverage of CNTs.

In the later stages of this work, attempts were made to control the diameter of the CNTs by adjusting the size of Co NPs by controlling the electrodeposition time. A range of total electrodeposition times were studied from 50 ms to 100 ms × 20 . Although the results do not show the significant changes of CNT diameters when adjusting electrodeposition time in the range of 100 ms × 4 to 100 ms × 20, these experiments pinpointed a threshold of 100 ms for best uniformity of electrodeposition of Co NPs as evidenced by a narrow distribution of CNT diameters.. The electrodeposition time should be no more than 800 ms as the distribution of the CNT diameters becomes substantially wider at longer times.

The TEM study showed the presence of multi-walled (*ca.* 5 graphene layers per wall) CNTs and Co NPs encapsulated in carbon. The results of the Raman study also provide evidence of MWCNTs which were successfully grown in the final stages of this project on samples with short Co deposition times. In order to simulate the process of the reduction and aggregation of the Co NPs prior to CNT growth, the dimpled Al_2O_3 substrate was used so that direct observation using SEM would be possible. A very short electrodeposition time (down to 10 ms) was tested using this substrate and formation of very thin CNTs can be confirmed.

Although the subset of current results (electrodeposition times between 100 ms × 4 and 100 ms × 8) does not provide enough evidence to prove that the diameter of CNT can be controlled by adjusting the electrodeposition time. The reason for this could be the limited conductivity of barrier layer which results in a significant decrease of the actual voltage as measured by the auxiliary electrode (Fig. 4.24) throughout each consecutive 100 ms electrodeposition interval within these series potentially leading to significant decrease in efficiency of the electrodeposition. However, the CNT diameters change significantly when the electrodeposition time is 100 ms, with most CNTs being sub-30 nm in diameter in this case. Electrodeposition using such short intervals (around 100 ms) may lead to some control over CNT diameter; however, this would require further detailed study. Moreover, when electrodeposition time was 50 ms, very sparse and thin CNTs which apparently have the diameters smaller than 20 nm can be observed. Another factor which limited the study is the limitation of the available facilities. For example, a clear cross-section SEM image of a cut PAA template which is important for observing the electrodeposited Co or directly measuring the diameter of CNTs inside the pores could not be achieved using available facilities.

However, in this work, the coverage of electrodeposited Co and CNT growth have been significantly improved using PAA template for CNT growth. Potentially, the optimised experimental conditions can be applied on a through-hole PAA membrane attached to a conductive substrate (*e.g.* Si). This could overcome the limitation of electrodeposition and provide a precise size control of deposited metal.

4.5 References

1. Wackelgard, E., A study of the optical properties of nickel-pigmented anodic alumina in the infrared region. *J. Phys.: Condens. Matter* **1996,** *8* (27), 5125-5138.
2. Nielsch, K.; Muller, F.; Li, A. P.; Gosele, U., Uniform nickel deposition into ordered alumina pores by pulsed electrodeposition. *Adv. Mater.* **2000,** *12* (8), 582-586.
3. Jeong, S.-H.; Hwang, H.-Y.; Lee, K.-H.; Jeong, Y., Template-based carbon nanotubes and their application to a field emitter. *Appl. Phys. Lett.* **2001,** *78* (14), 2052-2054.
4. Lee, O. J.; Hwang, S. K.; Jeong, S. H.; Lee, P. S.; Lee, K. H., Synthesis of carbon nanotubes with identical dimensions using an anodic aluminum oxide template on a silicon wafer. *Synth. Met.* **2005,** *148* (3), 263-266.
5. Wada, K.; Hatano, T.; Uchida, K., Colored coatings on aluminium produced by varing the duration of AC electrolysis treatment I. thin coating. *J. Appl. Electrochem.* **1979,** *9* (4), 445-455.
6. Caboni, V., *Italian Patent* **1936,** *339* 232.
7. Sousa, C. T.; Apolinario, A.; Leitao, D. C.; Pereira, A. M.; Ventura, J.; Araujo, J. P., Precise control of the filling stages in branched nanopores. *J. Mater. Chem.* **2012,** *22* (7), 3110-3116.
8. Gerein, N. J.; Haber, J. A., Effect of ac electrodeposition conditions on the growth of high aspect ratio copper nanowires in porous aluminum oxide templates. *J. Phys. Chem. B* **2005,** *109* (37), 17372-17385.
9. Schuldin.S; Warner, T. B., Investigation of the kinetics of hydrogen and oxygen reactions on a platinium electrode in acid solution using pulse and decay techniques. *J. Electrochem. Soc.* **1965,** *112* (2P1), 212-218.
10. Lazic, M. S.; Simovic, K.; Miskovic-Stankovic, V. B.; Jovanic, P.; Kicevic, D., The influence of the deposition parameters on the porosity of thin alumina films on steel. *J. Serb. Chem. Soc.* **2004,** *69* (3), 239-249.
11. Gabe, D. R., The role of hydrogen in metal electrodeposition processes. *J. Appl. Electrochem.* **1997,** *27* (8), 908-915.
12. Shin, H. C.; Dong, J.; Liu, M. L., Nanoporous structures prepared by an electrochemical deposition process. *Adv. Mater.* **2003,** *15* (19), 1610-1614.
13. Sun, M.; Zangari, G.; Metzger, R. M., Cobalt island arrays with in-plane anisotropy electrodeposited in highly ordered alumite. *IEEE Trans. Magn.* **2000,** *36* (5), 3005-3008.
14. Sun, M.; Zangari, G.; Shamsuzzoha, M.; Metzger, R. M., Electrodeposition of highly uniform magnetic nanoparticle arrays in ordered alumite. *Appl. Phys. Lett.* **2001,** *78* (19), 2964-2966.
15. Ghaddar, A.; Gieraltowski, J.; Gloaguen, F., Effects of anodization and electrodeposition conditions on the growth of copper and cobalt nanostructures in aluminum oxide films. *J. Appl. Electrochem.* **2009,** *39* (5), 719-725.
16. Santos, J. S.; Matos, R.; Trivinho-Strixino, F.; Pereira, E. C., Effect of temperature on Co electrodeposition in the presence of boric acid. *Electrochim. Acta* **2007,** *53* (2), 644-649.
17. Santos, J. S.; Trivinho-Strixino, F.; Pereira, E. C., Investigation of Co(OH)2 formation during cobalt electrodeposition using a chemometric procedure. *Surf. Coat. Technol.* **2010,** *205* (7), 2585-2589.
18. Najafi, M.; Soltanian, S.; Danyali, H.; Hallaj, R.; Salimi, A.; Elahi, S. M.; Servati, P., Preparation of cobalt nanowires in porous aluminum oxide: Study of the effect of barrier layer. *J. Mater. Res.* **2012,** *27* (18), 2382-2390.

19. Jiang, S. P.; Chen, Y. Z.; You, J. K.; Chen, T. X.; Tseung, A. C. C., Reactive deposition of cobalt electrodes. *J. Electrochem. Soc.* **1990,** *137* (11), 3374-3380.
20. Jeong, S.-H.; Hwang, H.-Y.; Hwang, S.-K.; Lee, K.-H., Carbon nanotubes based on anodic aluminum oxide nano-template. *Carbon* **2004,** *42* (10), 2073-2080.
21. Xu, R., Preparation and characterisation of vertically aligned carbon nanotubes. *MSc thesis of University of Canterbury. Chemistry* **2010**.
22. Jeong, S. H.; Lee, O. J.; Lee, K. H.; Oh, S. H.; Park, C. G., Preparation of aligned carbon nanotubes with prescribed dimensions: template synthesis and sonication cutting approach. *Chem. Mater.* **2002,** *14* (4), 1859-1862.
23. Jeong, S. H.; Lee, O. J.; Lee, K. H.; Oh, S. H.; Park, C. G., Packing density control of aligned carbon nanotubes. *Chem. Mater.* **2002,** *14* (10), 4003-4005.
24. Jeong, S. H.; Lee, K. H., Field emission properties of low-density carbon nanotubes prepared on anodic aluminum-oxide template. *J. Korean Phys. Soc.* **2004,** *45* (2), L252-L255.
25. Kukovitsky, E. F.; L'Vov, S. G.; Sainov, N. A.; Shustov, V. A.; Chernozatonskii, L. A., Correlation between metal catalyst particle size and carbon nanotube growth. *Chem. Phys. Lett.* **2002,** *355* (5-6), 497-503.
26. Zaretskiy, S. N.; Hong, Y. K.; Ha, D. H.; Yoon, J. H.; Cheon, J.; Koo, J. Y., Growth of carbon nanotubes from Co nanoparticles and C2H2 by thermal chemical vapor deposition. *Chem. Phys. Lett.* **2003,** *372* (1-2), 300-305.
27. Huh, Y.; Green, M. L. H.; Kim, Y. H.; Lee, J. Y.; Lee, C. J., Control of carbon nanotube growth using cobalt nanoparticles as catalyst. *Appl. Surf. Sci.* **2005,** *249* (1–4), 145-150.
28. Lin, H.-Y.; Chen, Y.-W., The mechanism of reduction of cobalt by hydrogen. *Mater. Chem. Phys.* **2004,** *85* (1), 171-175.
29. Dehghan, R.; Hansen, T. W.; Wagner, J. B.; Holmen, A.; Rytter, E.; Borg, O.; Walmsley, J. C., In-situ reduction of promoted cobalt oxide supported on alumina by environmental transmission electron microscopy. *Catal. Lett.* **2011,** *141* (6), 754-761.
30. Borg, O.; Walmsley, J. C.; Dehghan, R.; Tanem, B. S.; Blekkan, E. A.; Eri, S.; Rytter, E.; Holmen, A., Electron microscopy study of gamma-Al_2O_3 supported cobalt fischer-tropsch synthesis catalysts. *Catal. Lett.* **2008,** *126* (3-4), 224-230.
31. Liu, B. H.; Ding, J.; Zhong, Z. Y.; Dong, Z. L.; White, T.; Lin, J. Y., Large-scale preparation of carbon-encapsulated cobalt nanoparticles by the catalytic method. *Chem. Phys. Lett.* **2002,** *358* (1-2), 96-102.
32. Matsushima, J. T.; Trivinho-Strixino, E.; Pereira, E. C., Investigation of cobalt deposition using the electrochemical quartz crystal microbalance. *Electrochim. Acta* **2006,** *51* (10), 1960-1966.
33. Li, J.; Moskovits, M.; Haslett, T. L., Nanoscale electroless metal deposition in aligned carbon nanotubes. *Chem. Mater.* **1998,** *10* (7), 1963-1967.
34. Belov, A. N.; Gavrilov, S. A.; Shevyakov, V. I.; Redichev, E. N., Pulsed electrodeposition of metals into porous anodic alumina. *Applied Physics a-Materials Science & Processing* **2011,** *102* (1), 219-223.
35. Knobloch, J., Cobalt nanoparticles: catalysts for the fabrication of carbon nanotubes. *UC Honours research report* **2009**.
36. Eklund, P. C.; Holden, J. M.; Jishi, R. A., Vibrational-modes of carbon nanotubes-spectroscopy and theory. *Carbon* **1995,** *33* (7), 959-972.
37. Bokobza, L.; Zhang, J., Raman spectroscopic characterization of multiwall carbon nanotubes and of composites. *Express Polym. Lett.* **2012,** *6* (7), 601-608.
38. Antunes, E. F.; Lobo, A. O.; Corat, E. J.; Trava-Airoldi, V. J., Influence of diameter in the Raman spectra of aligned multi-walled carbon nanotubes. *Carbon* **2007,** *45* (5), 913-921.

39. Rana, K.; Kucukayan-Dogu, G.; Bengu, E., Growth of vertically aligned carbon nanotubes over self-ordered nano-porous alumina films and their surface properties. *Appl. Surf. Sci.* **2012,** *258* (18), 7112-7117.
40. Su, Z. X.; Zhou, W. Z., Formation mechanism of porous anodic aluminium and titanium oxides. *Adv. Mater.* **2008,** *20* (19), 3663-3667.
41. Ron Jenkins, R. W. Gould., Quantitative x-ray spectrometry, second edition. *Marcel Dekker, New York,* **1995**.

Chapter 5. Growth of ZnO nanorods catalysed by Au nanocolloids using pulsed laser deposition

5.1. Introduction

5.1.1 Brief overview of ZnO fabrication methods.

ZnO is a wide gap semiconductor material and has a direct band gap (3.37 eV) giving the material many potential applications such as light emitting diodes, laser diodes and chemical sensors.[1] In recent years, ZnO nanorods and nanowires have attracted a lot of interest due to the high exciton binding energy (60 meV), piezoelectric properties, chemical stability and biocompatibility.[2] Such high exciton binding energy is very useful for developing various optoelectronic devices, such as, UV excitonic lasers, tuneable UV photodetectors and light emitting diodes.[2,3,4] Catalyst enabled growth of ZnO nanostructures which proceeds *via* a vapour-liquid-solid (VLS) mechanism gives the most promising results for synthesis of uniform arrays of high quality ZnO nanorods (Note, there is no formal distinction between nanorods and nanowires, however thinner structures are usually referred to as wires and thicker as rods. For the work carried out in this thesis, "nanowire" is used for structures with diameter < 25 nm. However, when discussing other authors' work, the term used by the authors will be used here).[3,4]

In the recent studies focused on synthesis of ZnO nanorods, PLD has been widely used due to the higher purity, crystallinity and other favourable material properties compared to ZnO made using other techniques.[5] For growing vertical and uniform ZnO nanorods or

nanowires, choosing a proper substrate and controlling the growth conditions are important.[6] Sapphire is considered the best substrate for epitaxial ZnO nanorod or nanowire growth because sapphire has a similar six-fold symmetric structure to that of ZnO.[6] More details relating to ZnO nanorod growth on a sapphire substrate are discussed in 5.1.6

5.1.2 Catalytic growth of ZnO nanorods and nanowires

As a variety of techniques for growing ZnO nanorods have been developed, using metal NPs as the catalyst for growth is the most popular method because it can be adapted to most of the techniques. However, some reports also demonstrate ZnO nanorod growth using a catalyst free PLD method.[7,8] Although the orientation and the length of the ZnO nanorods can be controlled by adjusting the PLD parameters, the control of the diameter of the ZnO nanorods is very limited when using a catalyst free PLD method.[7,8] Hence, the advantage of using metal NPs as the catalyst for ZnO nanostructure growth is obvious. The size of the metal NPs can be controlled by many strategies, for example, by de-wetting a thin metal film for which the thickness of the film is controllable, depositing metal nanoclusters with a desirable size from the gas phase or utilising pre-made metal nanocolloids which can be made with control over their size during the chemical synthesis process.

Recently, Au NPs have been widely used as the catalyst for ZnO nanorod or nanowire growth.[9,10] Apart from Au, there have also been reports on using Sn, Ni, Cu, Se, Pt and Ag as the catalyst.[11,12,13,14,15] In 2007, Zhang *et al.* used Au, Pt and Ag NPs as catalysts on Si substrates to grow ZnO nanorods by the CVTC (chemical vapour transport and condensation) technique.[15] They chose Au, Pt and Ag because these metals are catalytically active for ZnO nanorod growth but chemically inert. The sizes of metal NPs were controlled by annealing a

3 nm metal film at different temperatures (500, 600, 700 and 800 ºC) for 30 min. The ZnO nanorods were grown at 500 to 800 ºC for 1 h under a constant flow of $Ar_{(g)}$ with a trace amount (0.05 %) of $O_{2(g)}$ using the sample plus source material (ZnO/graphite powder (weight ratio: 1:1) or Zn powder). Graphite is used to reduce ZnO to Zn.[16] The authors compared the morphology of the ZnO grown on these catalysts (Fig. 5.1).[15]

Zhang *et al.'s* results show that the ZnO nanorods grown from Au NPs at 800 ºC were longer, thinner and have a narrower size distribution than those grown on Pt at 700 ºC and Ag at 500 ºC (Fig. 5.1).[15] Growth on Au NPs at 500 - 700 ºC was also examined and the ZnO nanorods grown at 800 ºC were found to have lower diameters than those grown at lower temperatures. (Fig. 5.1).[15]

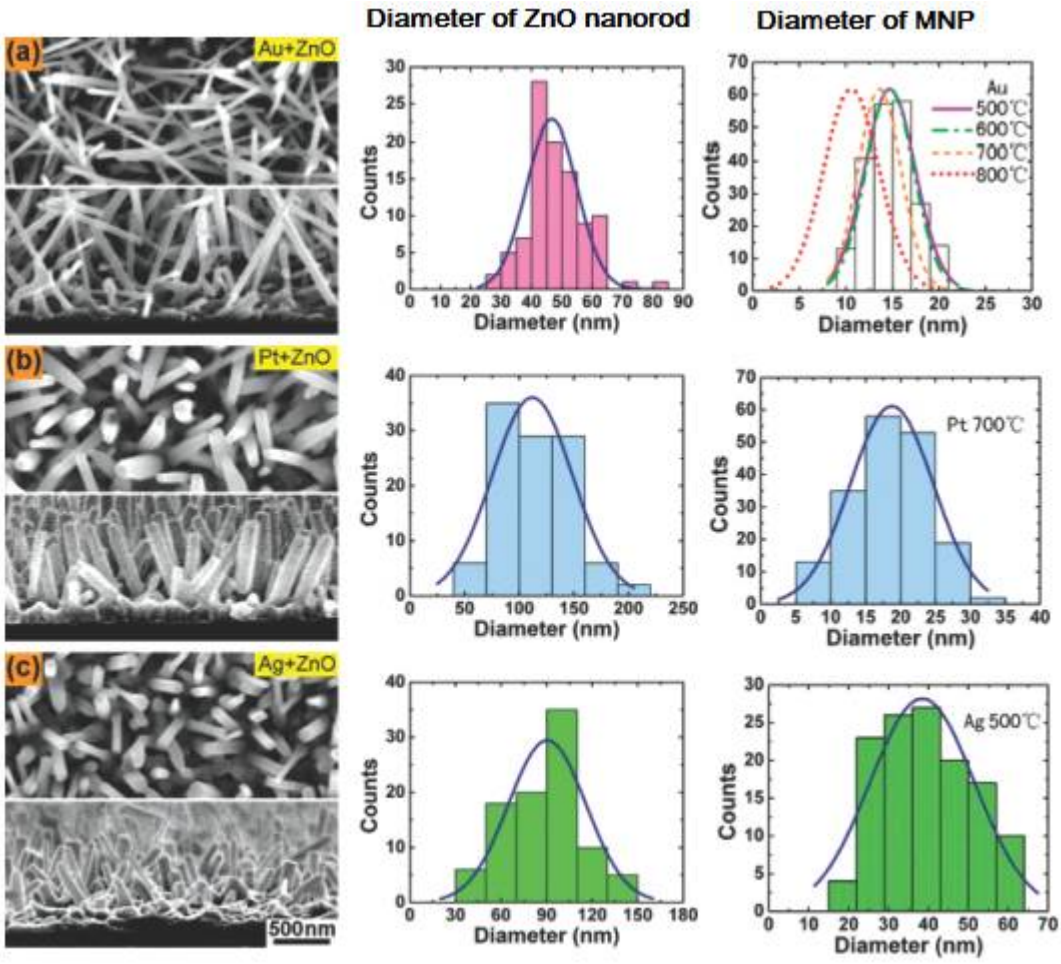

Fig. 5.1. Top and tilted views SEM images of ZnO nanorods grown from a ZnO/graphite source on (a) Au, (b) Pt and (c) Ag NPs and the growth temperatures were 800 ºC, 700 ºC and 500 ºC respectively. The

histograms of nanorod size distribution are shown in the middle line. The histograms of diameter distribution of the metal catalyst at different temperatures are shown on the right side. Figures reproduced from reference 15.

5.1.3 Different methods of preparing Au NP-modified substrates for controlling the diameter of ZnO nanorods

5.1.3.1 Control of the diameter of ZnO nanorods via adjusting the thickness of Au thin film

In 2001, Huang *et al.* reported a study of controlling the diameter of ZnO nanowires *via* controlling the thickness of Au film on a Si substrate.[17] The methodology was based on that of Holmes *et al.* who grew SiO_2 nanowires by the same approach.[18] The CVTC technique was utilised in both studies. Huang *et al.* examined the diameters of ZnO nanowires grown on two samples which were coated with Au film with thickness of 50 Å and 30 Å (Fig. 5.2).[17] Subsequently, ZnO nanowires were grown by heating the sample with ZnO/graphite powder (weight ratio: 1:1) to 900-925 ºC for 1-30 min under a constant flow of $Ar_{(g)}$.[17] According to the results, the diameter of ZnO nanowires ranged from 80-120 nm on the sample coated with 50 Å of Au and the diameter of ZnO nanowires ranged from 40-70 nm on the sample coated with 30 Å of Au.[17] Although the authors did not provide the details of the annealing conditions and the size of Au NPs after annealing, controlling the particle size *via* annealing a controlled thickness metal film is a well-known technique. Therefore, the authors claim that the diameter of ZnO nanowires can be controlled by adjusting the thickness of Au film.[17]

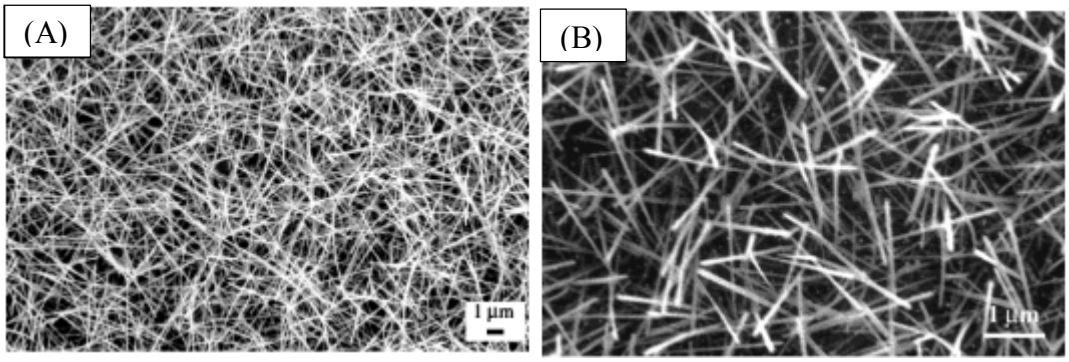

Fig. 5.2. SEM images of ZnO nanowires grown from ZnO/graphite powder at 900 - 925 ºC on the surface of Si substrate coated with (A) ~ 50 Å thick and (B) ~30 Å thick Au film. Figure reproduced from reference 17.

Another paper, reported by Wang *et al.* in 2004, described fabrication of patterned, aligned ZnO nanorods.[19] The authors utilised a monolayer of self-assembled polystyrene spheres with an average size of 895 nm on an A-plane sapphire substrate as the mask to allow sputtering of very small amounts of Au onto the substrate forming a pattern.[19] The Au was sputtered between the polystyrene spheres (Fig. 5.3 (A)), however, the authors did not report the thickness of the Au nanostructure. The polystyrene spheres were etched away after sputtering Au, followed by annealing for film break-down leading to formation of Au NPs which were used as a catalyst in the synthesis of ZnO nanorods using CVTC (source material: ZnO/graphite powder with a weight ratio of 1:1, growth temperature: 950 ºC and the growth time: 20-30 min) resulting in uniform patterns of vertically aligned ZnO nanorods (Fig. 5.3 (B)).[19] According to their results, the diameter of the ZnO nanorods was in the range of 50-150 nm.[19]

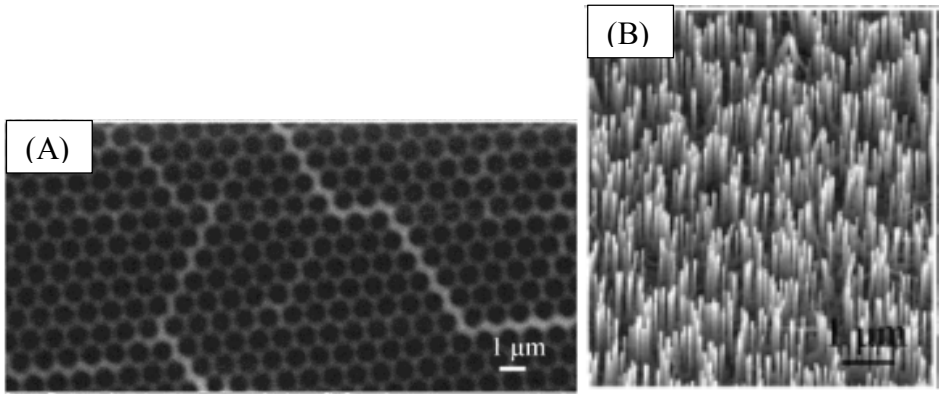

Fig. 5.3. SEM images of (A) Au pattern produced by sputtering onto a sapphire substrate using a monolayer of self-assembled polystyrene spheres as a mask, and (B) aligned ZnO nanorods grown via CVD using the annealed catalyst system shown in (A). Figure reproduced from reference 19.

A disadvantage of annealing a thin layer of Au or small amount of deposited Au is the problem of generating inhomogeneous sizes of Au NPs which leads to a wide range of diameters of ZnO nanorods.[20] Therefore, fabricating size-controlled Au nanoclusters or nanocolloids could be an alternative solution. One method to prepare such nanoclusters is to use an ultra-high vacuum (UHV) compatible magnetron sputtering system for sputtering metal nanoclusters on a substrate.[21] According to a study by Belić *et al*., the diameter of Ag-Au nanoclusters could be precisely controlled in the range of 3-10 nm and the coverage of nanoclusters on the substrate was in the range of 3-30 %.[21] However, this approach would seem unsuitable for ZnO nanorod growth because only a sparse coverage of nanorods could be achieved and aggregation of the nanoclusters is expected at the ZnO growth temperature. Aggregation of catalysts would generate a range of sizes and lead to inhomogeneous ZnO nanorod diameters. The effect of aggregation has been observed during CNT growth at Si substrates.[21,22]

5.1.3.2 Fabrication of a sub-monolayer of Au nanocolloids on a chemically modified substrate

A sub-monolayer of pre-formed Au colloids on a substrate could be a catalyst system for growing ZnO nanorods or nanowires. The synthesis of Au nanocolloids using sodium citrate to stabilise the Au NPs and first developed by Turkevitch *et al*.[23] This method has been refined by many researchers to give better size-control of Au nanocolloids.[24,25] Fig. 5.4 shows typical UV spectra of citrate-capped Au nanocolloids (13 nm diameter). The unaggregated Au nanocolloids (13 nm diameter) in the solution have an absorbance band at 520 nm. If the Au nanocolloids aggregate, a red-shifted band appears in the optical spectrum between 600-800 nm.[24,25]

Grabar *et al.* reported a method of coating a sub-monolayer of citrate-capped Au colloids onto a tether-modified substrate.[25] In the study by Keating *et al.*, this coating method was more clearly described (Scheme 5.1 (A)).[26] To prepare a tether-modified substrate, a substrate with hydroxyl/oxide groups on the surface (*e.g.* glass, quartz, SnO_2, Al_2O_3, *etc.*) is immersed in a solution containing a bi-functional organosilane with different terminal functional groups, that can bind to Au nanocolloids *via* electrostatic attraction. After preparation of the tether layer, the substrate is immersed in Au colloidal solution and Au nanocolloids self-assemble onto the surface as a sub-monolayer. (Scheme 5.1 (B)).[26] Keating *et al.* examined the correlation between the amount of Au nanocolloids on the surface and the immersion time in the Au colloidal solution. A glass substrate was modified with aminopropyltrimethoxy-silane (APTMS) and immersed into a ~17 nM Au colloidal solution for different times. The average size of Au nanocolloids was ~12 nm. The samples were then examined using UV-vis spectroscopy to obtain the absorbance data shown in Fig. 5.5 (A). In Fig. 5.5 (A), the points are the experimental data and the solid line was plotted from

theoretical values. The results show that the absorbance increases with immersion time to reach a constant value after 2500 s (Fig. 5.5 (A) insert). This suggests that the Au nanocolloids form a sub-monolayer on the substrate when the coating time is less than ~40 min, and reach the maximum packing when the immersion time is more than 41 min.

Keating *et al.* also discussed the correlation between the concentration of Au colloidal solution and the absorbance. Samples were prepared with various concentrations of Au colloidal solution by diluting the ~17 nM solution with H_2O. All samples were immersed in the solution overnight to ensure an equilibrium amount of Au nanocolloids were coated on the surface. As shown in Fig. 5.3 (B), the absorbance increases when the concentration of the Au colloidal solution increases, consistent with an equilibrium between concentration of Au nanocolloids on the surface and solution. To-date, there are no reports of use of this type of catalyst layer for ZnO nanorod growth.

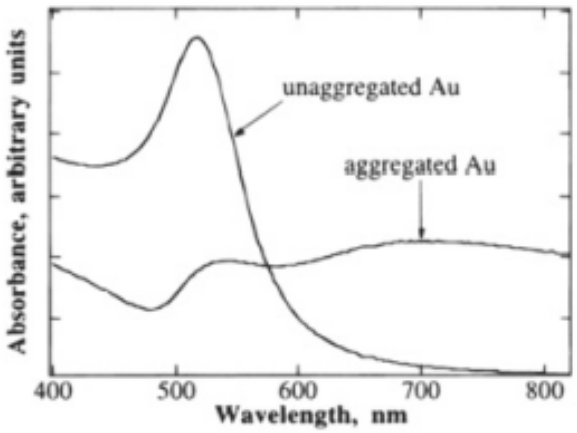

Fig. 5.4. Absorbance spectra comparing Au colloidal solution with unaggregated Au nanocolloids and aggregated Au nanocolloids. A typical λ_{max} at 520 nm indicates the unaggregated Au nanocolloids in the solution while aggregated Au nanocolloids have a second red-shifted absorbance centred at 700 nm. Reference adapted from 25.

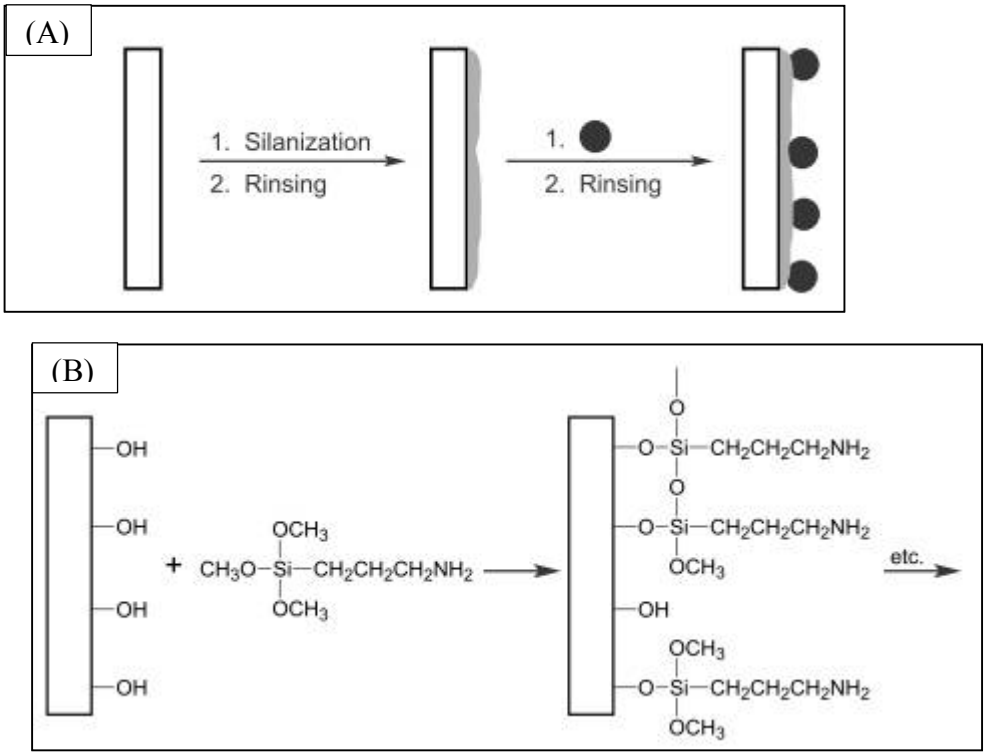

Scheme 5.1. (A) Fabrication of a monolayer of Au nanocolloids onto a glass substrate (B) covalent modification of substrate with aminopropyltrimethoxy-silane (APTMS) needed for preparation of the tether-coated substrate in (A). Figure reproduced from reference 26.

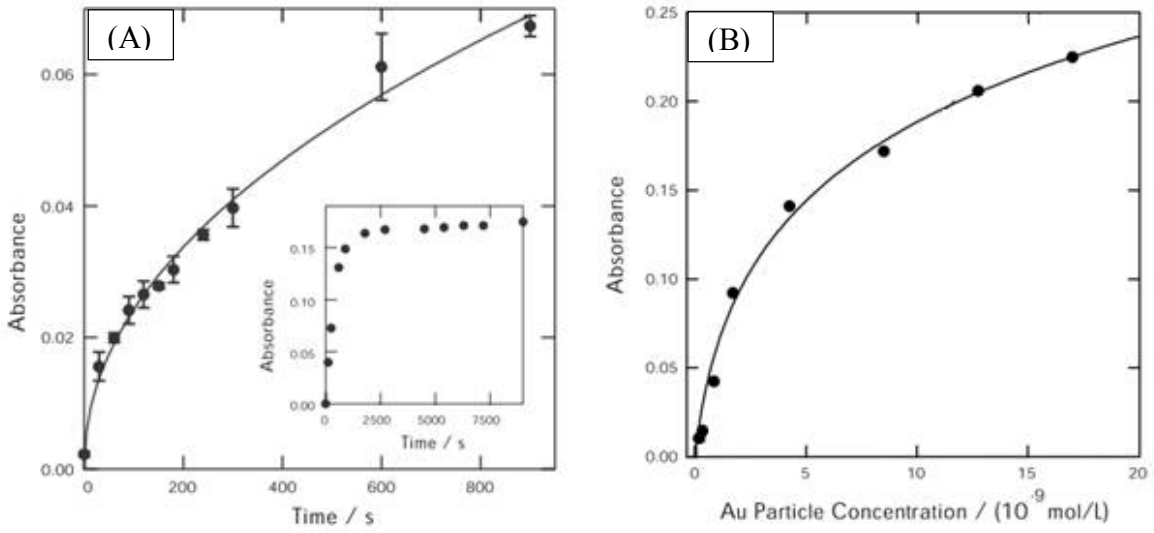

Fig. 5.5. (A) Absorbance vs time plot for an APTMS-modified glass slide after immersion in a 17 nM Au colloidal solution (inset: Absorbance vs time plot showing data points at longer times) and (B) absorbance at equilibrium versus colloid concentration. The diameter of the Au nanocolloids is around 12 nm. Figure reproduced from reference 26.

5.1.4. The development of the pulsed laser deposition ZnO growth method

Pulsed laser deposition (PLD) is a technique which uses high energy pulses of photons generated by a laser to ablate material from the surface of a target. During the ablation process, the vaporized material expands rapidly giving a laser-produced plasma plume containing neutral species, ions and electrons. (Fig. 5.6).[27] The plasma plume re-condenses onto the substrate which results in the growth of a film or a nanoscale structure on the substrate.[27] The parameters affecting the quality of deposition include the nature of the target, laser fluence and wavelength, background gas pressure and substrate temperature. The major disadvantage of PLD is that some particles of bigger size (also called droplets) resulting from an explosive spouting of a target can be directly deposited onto the substrate accompanying the deposition from the laser generated plasma plume. The scatter of the deposited droplets causes defects or uneven deposition.[28,29]

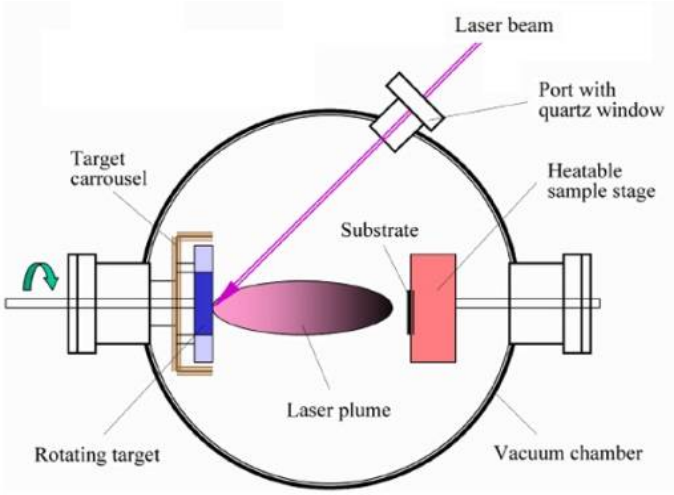

Fig. 5.6. Schematic view of a PLD system. Figure adopted from reference 27.

In 1994, Kinoshita *et al*. proposed the "eclipse method" for PLD by simply placing a shadow mask (10 mm × 10 mm) between the target material and substrate. The droplet problem is significantly overcome by use of the eclipse method (Fig. 5.7).[28] The shadow mask is like a shield to prevent the deposition of droplets and allows only the very small particles to diffuse to the substrate.[28] Due to the benefits of the eclipse method for uniform deposition, this method has been widely utilised and investigated.[30,31]

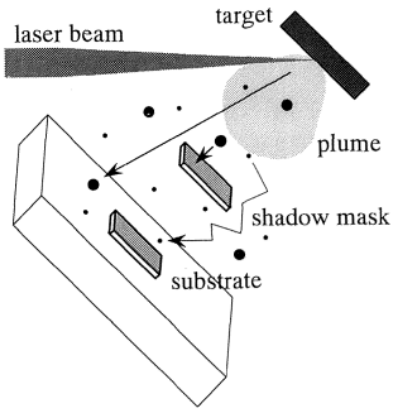

Fig. 5.7. Schematic view of eclipse PLD system. Figure adopted from reference 28.

The eclipse PLD method has been used to grow vertical metal oxide nanowires.[32,33] In a study by Marcus *et al.*, the morphologies of MgO nanowires which were located in the different areas of the substrate were investigated (under the shadow mask, outside the mask and at the interface between these two areas as shown in Fig. 5.8 (A)).[9] According to their results as shown in Fig. 5.8 (B)-(D), the MgO nanowires tend to grow in the area which is under the cover of the shadow mask (Fig. 5.8 (B)). The morphology of MgO deposited outside the cover of shadow mask resembles an island structure (Fig. 5.8 (D)) and an intermediate morphology can be observed in the area which is near the edge covered by the

shadow mask (Fig. 5.8 (C)). The following interpretations are based on another related research report of Marcus *et al.*[29] By using a fast framing camera, the authors obtained evidence that the droplets are stopped by the shadow mask. (Fig. 5.9).[29] After the laser generated plasma plume hits the shadow mask, the movement of the plume becomes fluid-like.[29,9] After this stage, most of components in the laser plasma plume are small and fine particles.[29,9] The growth of MgO nanowires under the shadow mask corresponds to the presence of the fluid-like plasma.[29,9] The small and fine particles can travel further than the bigger particles.[29,9] Hence, the morphology of MgO deposited on the substrate gradually changes across the area without the cover of the shadow mask and with the cover of the shadow mask.[9]

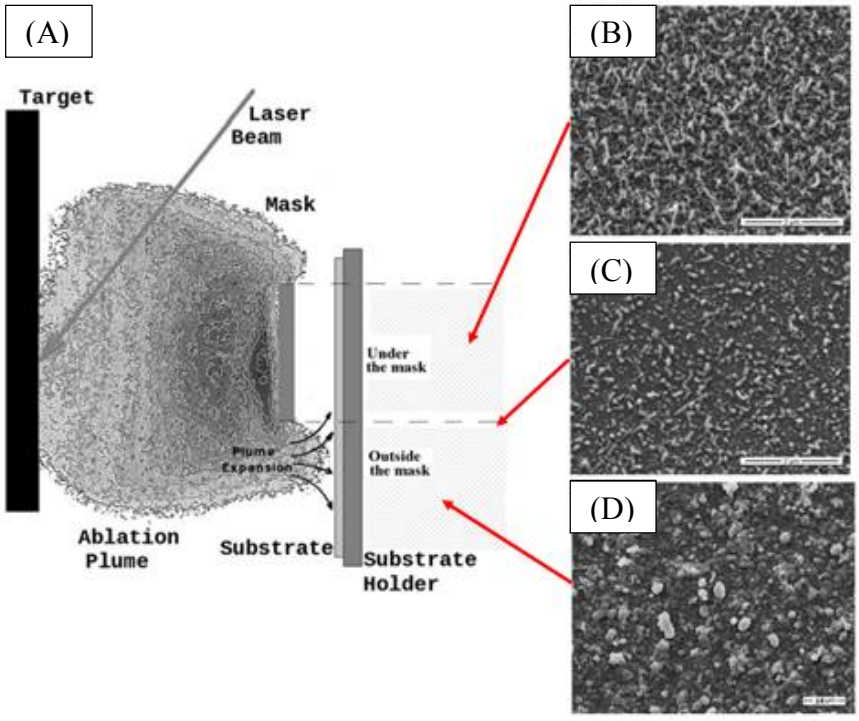

Fig. 5.8. (A) Schematic view of the laser plasma plume in an eclipse PLD system and three SEM images on the right side present the morphologies of MgO nanowires on three different areas of the MgO substrate: (B) under the shadow mask, (C) under the edge of the shadow mask and (D) outside the shadow mask. The EKSPLA Nd:YAG laser 4th harmonic 266 nm with the 25 mJ of laser power and 10 Hz of frequency was used to ablate the MgO target. Figure reproduced from reference 9.

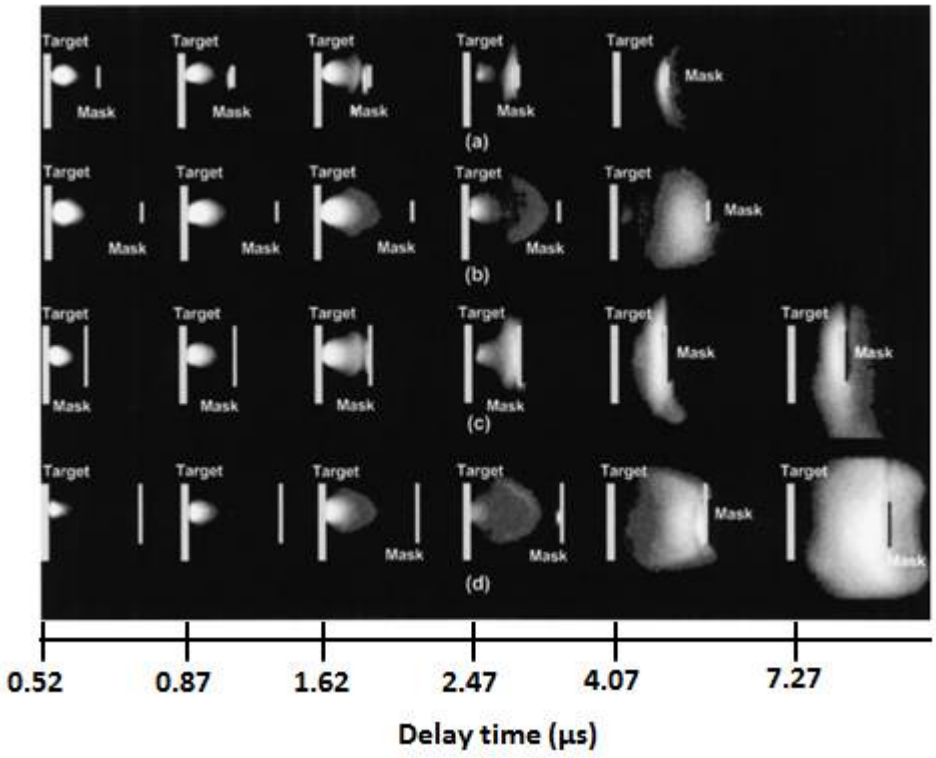

Fig. 5.9. Fast framing camera photographs of the luminous plume expansion in plane shadow mask configuration with different delay times; (a) and (b) use small size shadow mask with 0.5 cm diameter and target-mask distance are 1 and 2 cm respectively; (c) and (d) use large size shadow mask with 1.5 cm diameter and target-mask distance are 1 and 2 cm respectively. Figure reproduced from reference 29.

5.1.5. The factors affecting the morphology of ZnO nanorods during growth

As mentioned in section 5.1.2, the quality of deposition (uniformity of size and orientation) and morphology of ZnO nanorods can be affected by adjusting some PLD parameters such as laser fluence, background gas pressure and substrate temperature.[34,35,36] For catalytically grown ZnO nanorods using PLD, 2D nanosheets (which can appear cone-like in structure) are often obtained. Weigand *et al.* interpreted how the growth rates of the side facets affect the ZnO nanorod structure.[37] Fig. 5.10 (a) – (c) illustrates the nanorod growth at a fast growth rate in the ZnO [0001] direction through a VLS mechanism. Growth in the side facets is by a VS mechanism; when the VS growth rate on all facets is equal (Fig.

5.10 (b), a rod structure is formed. When the growth rates on the side facets are not equal, a nanosheet forms (Fig. 5.10 (e))[37] This phenomenon often occurs when the growth conditions allow for significant VS growth, for example, by increasing partial oxygen pressure when using a combination of gases (*i.e.* O_2/Ar).[38,39] In the study by Weigand *et al.*, Au NPs on C-plane sapphire substrates were used with two PLD growth conditions as shown in

Table 5.1.[37] According to their results, nanowires are preferably formed with 5 % $O_{2(g)}$ and 95 % $Ar_{(g)}$ in PLD.[37]

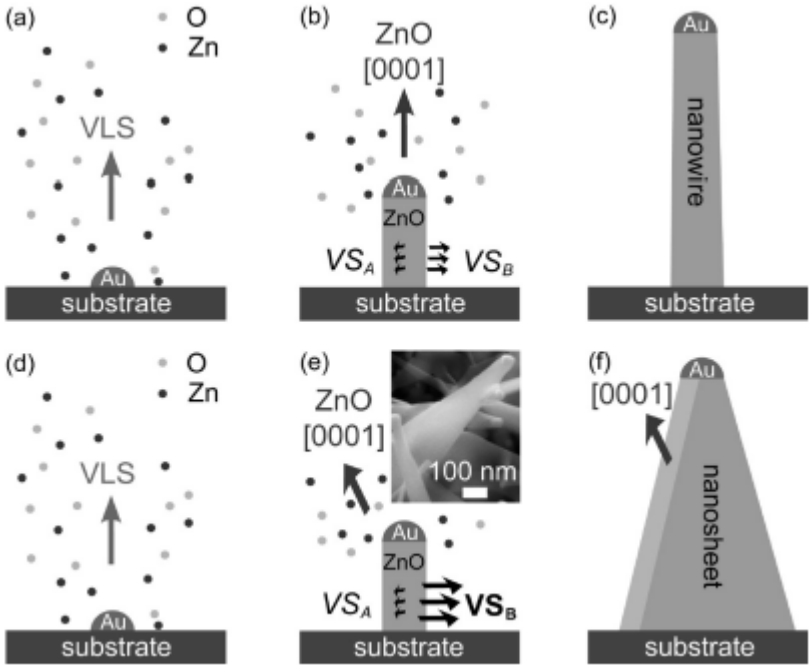

Fig. 5.10. Schematic illustration of the growth mechanism for a nanowire (a - c) and a nanosheet (d - f). In (b) the growth rate of facet A and B is shown to be equal (VS_A=VS_B); in (e) the growth rate on facet B » A (VS_B » VS_A). Figure adapted from reference 37.

Table 5.1. Growth conditions for Au NPs catalyst-assisted PLD samples. Table adapted from reference 37.

	parameter set 1	parameter set 2
temperature	800 °C	800 °C
gas composition	100% O_2	5% O_2–95% Ar
deposition time	60 min	60 min
total pressure	0.5 mbar	0.5 mbar
structures observed	nanosheets	nanowires

The repetition rate of laser pulses has recently been considered as an important factor for the crystallinity of thin film deposition.[40,41,42] However, the studies which relate to the effect of repetition rate on ZnO nanorod growth are very rare. In theory, a lower repetition rate of laser pulse at fixed pulse intensity results in a lower deposition rate and this allows more time for nucleation.[40,41,42] Guan *et al.* reported the relationship between the laser repetition rate and the island density on a substrate in the early stage of film deposition. The islands form by nucleating at the first landed atoms on a smooth surface.[40] According to Guan *et al.*, the island density increases with increase in laser repetition rate when the range of repetition rate is between 10-100 Hz (Fig. 5.11 (a)).[40] The size of the islands is also affected by the laser repetition rates.[40] A lower laser repetition rate gives fewer but larger island with better crystallinity than does a higher repetition rate.[40] This may suggest that during the formation of these islands, the growth on the side facets is more likely to occur at a lower repetition rate. For deposition of thin film, using a lower laser repetition rate is more preferable due to a better crystallinity.[40,41,42] However, a low repetition rate may negatively affect the growth of metal oxide nanowires as the growth on the side facets would be enhanced.

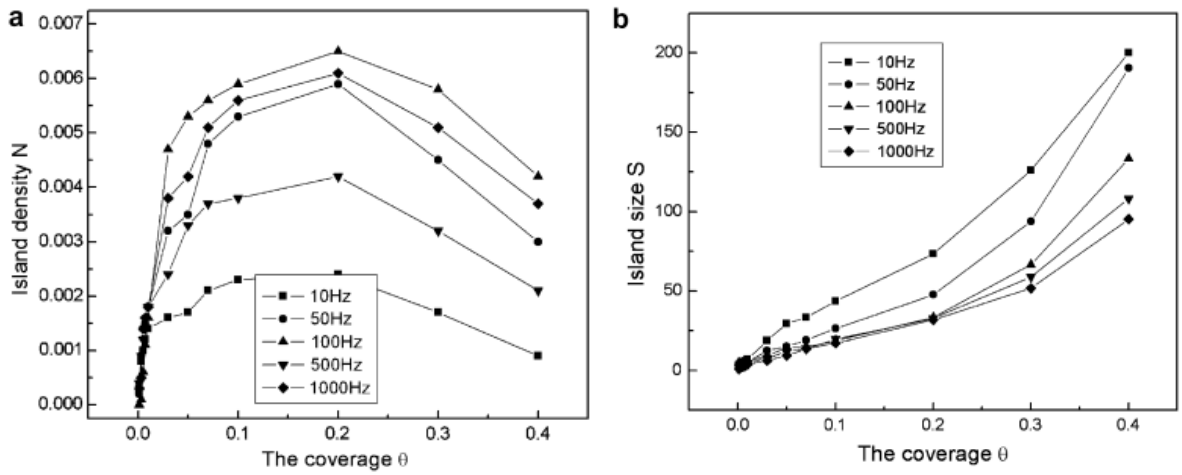

Fig. 5.11. (a) Island density and (b) island size versus coverage which is increased with the deposition time for the different laser repetition rates: 10 Hz, 50 Hz, 100 Hz, 500 Hz and 1000 Hz. Figure adapted from reference 40.

Guo *et al.* reported that the density of vertically aligned ZnO nanowires and the size of ZnO nanowires can be affected by many PLD parameters including the laser repetition rate.[43] In their study, ZnO nanowires were synthesised without metal catalyst and the nanoparticle assisted PLD (NAPLD) was utilised for growth.[8] In NAPLD, the ZnO nanowires were grown under a relatively high chamber pressure (260 Torr) with $A_{r(g)}$ as the background gas. Under such high pressure, the function of $Ar_{(g)}$ was to confine and cool the ablated species from the ZnO target. The condensation of the ablated species occurred and ZnO clusters formed nanoparticles before reaching the substrate. These condensed ablated species were subsequently deposited on a C-plane sapphire substrate and grew ZnO nanowires in the [0001] direction. In the absence of size control by a metal catalyst NP, the authors investigated many factors which can affect the size and density of the ZnO nanowires such as the distance between the target and substrate, the laser repetition rate and the laser energy. Although Guo *et al.*'s methodology is significantly different to that used in the present work, it is still informative to examine their results related to the effect of laser repetition rate on ZnO growth. The results obtained by Guo *et al.,* Fig. 5.12 (a)-(c), are shown in a series of histograms of the space between ZnO nanowires at different repetition rates. The space between nanowires indicates the density of the nanowires as a narrower space means a higher density. Fig. 5.12 (d) summarises the correlation between the average space between nanowires, density of nanowires and the laser repetition rate. Clearly, the density of the nanowires decreases with the decrease of the laser repetition rate. The authors also state that the size (tip diameter) of the ZnO nanowires became bigger as laser repetition rate decreased.

In general, increasing the laser repetition rate increases the amount of ablated species in the gas phase which results in the formation of higher density of ZnO nanowires. However, the reason for forming different morphologies at different laser repetition rates is unknown. Presumably, for ZnO nanorod growth under a high laser repetition rate, the growth rate of the

[0001] direction is faster than the growth rate of the side facets. As a result, the morphology of ZnO nanorods tends to be thin and long Fig. 5.10 (c). For the catalyst assisted growth of ZnO nanorods, the nucleation occurs on the catalyst particles (Fig. 5.10) and hence the effect of laser repetition rate may be different to that found by Guo *et al.*

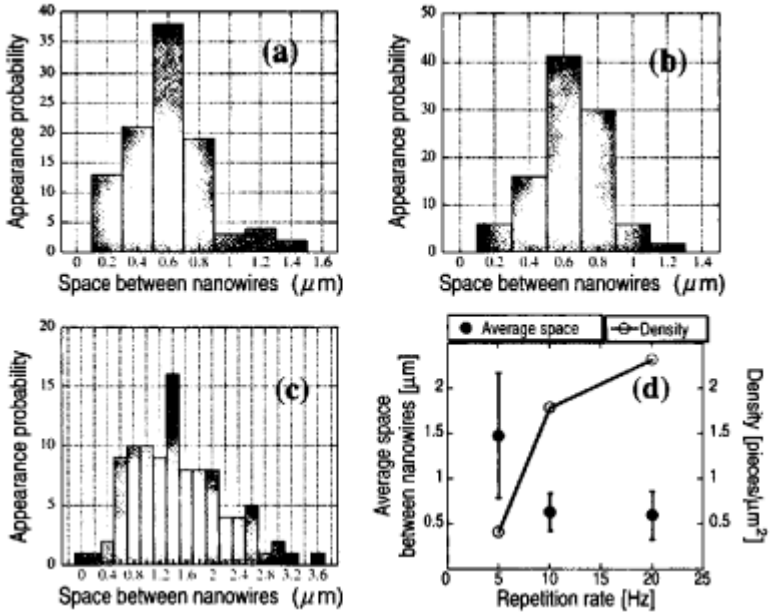

Fig. 5.12. Space probability histograms of ZnO nanowires grown at various laser repetition rates of (a) 20, (b) 10 and (c) 5 Hz; and (d) dependence of density and average space between nanowires on repetition rate. Figure adapted from reference 43.

5.1.6. Types of sapphire substrate surface facets

Sapphire substrates made by a single crystal Al_2O_3 growth method have been widely used for the epitaxial growth of ZnO nanostructures (*e.g.* thin films, nanorods and nanowires) due to similarities in the hexagonal crystal structures of sapphire and ZnO as well as the relative ready availability of highly crystalline substrates.[44,45,46] The four types of sapphire substrate which can be commercially purchased, A (1120), C (0001), R (1012) and M (1010), are defined by the crystal lattice/surface facet orientations as shown in Fig. 5.13.

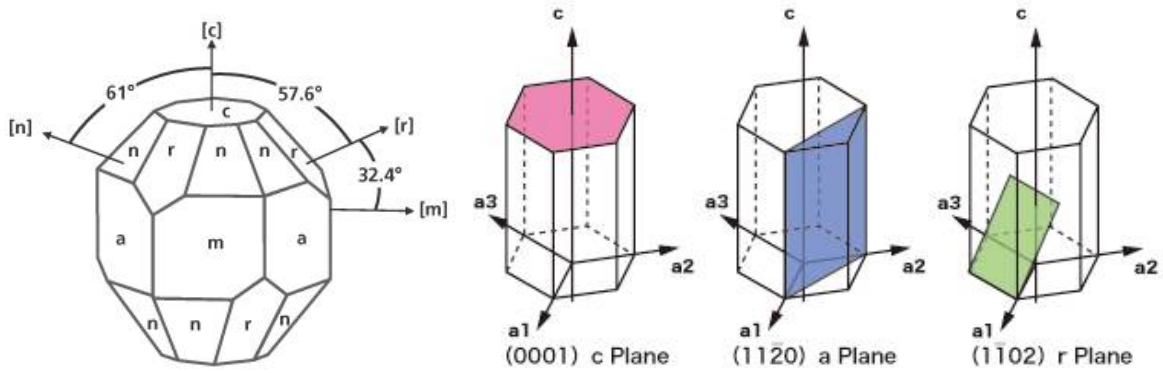

Fig. 5.13. Angular relations between the primary planes of the sapphire crystal. The C-plane is (0001), A-plane is (1120), R-plane is (1012) and M-Plane is (1010). Figures adopted from reference 47 and 48.

Kasuga *et al.* reported that the growth directions of ZnO nanostructures on the same type of sapphire substrate can be varied depending on the substrate temperature, vapour pressure and pretreatment.[49] The authors also summarised the growth directions of ZnO nanostructures on A, C and R-plane sapphire substrates (Table 5.2).[49] M-plane data are not included in Table 5.2 due to the limited research results that had been reported at that time. In fact, the M plane is significantly less popular than any other types of sapphire substrate due to the erratic ZnO growth direction.[50,51] For the purpose of growing vertically aligned and uniform ZnO nanorods or nanowires, A and C-plane sapphire substrates have been commonly used due to the preference of growth direction for ZnO (0001) which is along the direction perpendicular to the substrate surface.[6,46,52] Although the ZnO nanorods or nanowires sometimes grow on C-plane sapphire with an approximately 37º tilt angle relative to the surface, this can be avoided by adjusting parameters of the PLD process, such as gas composition and the pressure of oxygen.[37]

Table 5.2. ZnO –sapphire orientation relationship. Table adopted from reference 49.

Sapphire substrate		Epi-type	Planes ZnO	Directions ZnO//sapphire
R ($1\bar{1}02$)		R_1	($11\bar{2}0$)	[$\bar{1}100$]//[$11\bar{2}0$]
		R_2	($\bar{1}102$)	[$1\bar{1}00$]//[$\bar{1}2\bar{1}0$]
		R_3	(0001)	[$\bar{1}2\bar{1}0$]//[$11\bar{2}0$]
		R_4	($1\bar{2}16$)	[$\bar{1}010$]//[$\bar{3}302$]
A ($2\bar{1}\bar{1}0$)		A_1	(0001)	[$\bar{1}100$]//[$01\bar{1}0$]
		A_2 (= R_1)	($01\bar{1}\bar{1}$)	[$\bar{1}100$]//[$11\bar{2}0$]
C (0001)		C_1	(0001)	[$10\bar{1}0$]//[$11\bar{2}0$]
		C_2 (= R_2)	($11\bar{2}4$)	[$1\bar{1}00$]//[$\bar{1}2\bar{1}0$]

5.1.7. Aims for this chapter

The overall goal of work in this chapter is to grow vertically aligned ZnO nanorods of uniform diameters and density using pre-made size controlled Au NPs (nanocolloids) as catalysts. Most of work in this chapter is aimed at optimisation of the ZnO nanorods by tuning the catalyst fabrication strategy (preparation of Au nanocolloids immobilised on sapphire) and PLD conditions.

5.2. Experimental section

5.2.1 Synthesis of Au nanocolloids

All glassware used in the preparation of Au colloidal solutions was rinsed thoroughly in piranha solution which contains 4 parts of concentrated H_2SO_4 and 1 part of 30 wt% H_2O_2, washed with distilled water three times and finally rinsed with Milli-Q water. Warning: piranha solution is an aggressive oxidant. The glassware was dried in the oven before use. The Au colloid synthesis methods were previously reported by Grabar *et al.* which was based on the Turkevich method and are briefly described below.[23,25]

1. Au nanocolloids with the diameter of *ca*. 13 nm:

500 mL of 1 mM $HAuCl_4$ was brought to boil in a 1 L round-bottom flask with vigorous stirring on a magnetic stirring hot plate. 50 mL of 38.8 mM $Na_3C_6H_5O_7$ (trisodium citrate) was rapidly added into the $HAuCl_4$ solution and a burgundy colour developed after *ca*. 10 s. The solution was stirred and boiled continuously for 10 min. This solution was then removed from the hot plate and stirred while cooling to room temperature. The solution was transferred to a glass bottle wrapped with Al foil and stored in the dark. The concentration of Au nanocolloids in this colloidal solution is estimated to be ~ 17 nM. Fig. 5.14 shows the UV-vis absorption spectrum of the Au colloidal solution which indicates the diameter of the Au nanocolloids is around 13 nm.[26]

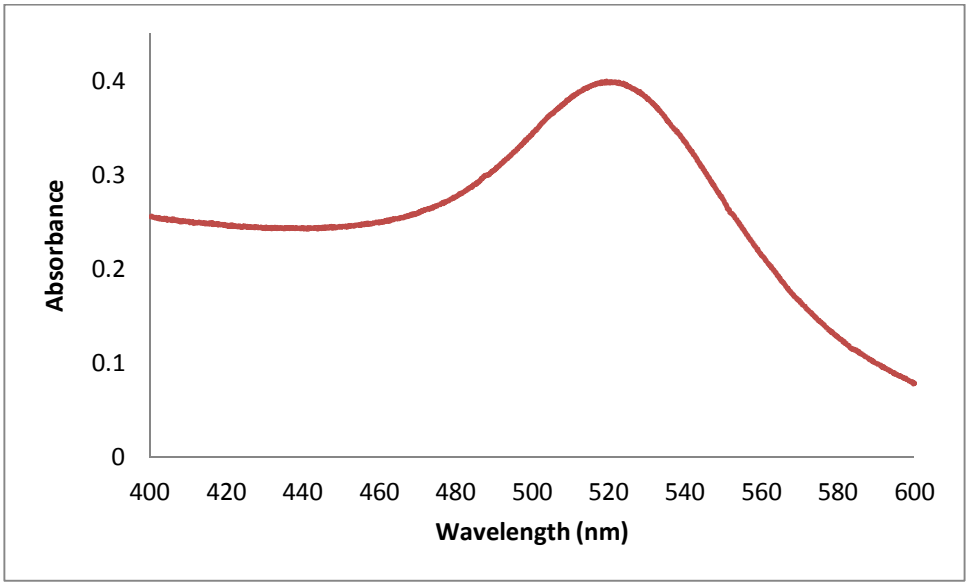

Fig. 5.14. UV-vis spectrum of *ca.* 3.4 nM Au colloidal solution containing *ca.* 13 nm particles.

2. Au nanoparticles with the diameters of *ca.* 3.5 nm:

This method was based on Martin *et al.*[53] The 50 mM $HAuCl_4$ solution was prepared by dissolving $HAuCl_4 \cdot 3H_2O$ in 50 mM HCl. The 1mL of 50 mM $HAuCl_4$ solution was mixed with 96 mL of Milli-Q water in round flask with vigorous string on a magnetic stirring plate. 3 mL of 50 mM $NaBH_4$ which was made by dissolving $NaBH_4$ in 50 mM NaOH was rapidly added into the diluted $HAuCl_4$ solution in the same round flask at room temperature. The concentration of the $HAuCl_4$ in this mixed solution is 0.5 mM. The mixture was kept stirring for 10 min after the burgundy colour was observed. According to the description by Martin *et al.,* the capping group of Au NPs is unclear. The BH_4^- is used to reduce Au^{3+} but the other anions including Cl^- and OH^- existing in the solution may also cap these "naked" Au NPs. The solution was collected in a glass bottle with Al foil wrapped and stored in the dark. The concentration of Au nanocolloids in this colloidal solution is estimated to be 0.38 μM.

5.2.2 Coating Au nanocolloids onto the sapphire or Si wafer substrate

Sapphire and Si wafers were used in this work as substrates for deposition of the catalytic layer. The substrate was cut into 5 mm × 5 mm pieces. Before any coating process, the substrates were degreased by sonicating in three solvents: trichloroethylene, acetone and methanol. The substrates were sonicated for 10 min in each solvent. The following variations in catalyst deposition approaches were tested:

1. Drop coating:

After degreasing, the sapphire or Si substrates were blow dried by $N_{2(g)}$ and placed on a piece of clean glass. The as-prepared 13 nm Au colloidal solution was dropped (approximately 1 μL) onto the substrates. The samples were oven-dried at 50-60 °C.

2. Direct dip coating:

After degreasing the substrates were blow dried by $N_{2(g)}$, and simply dipped into the Au colloidal solution for 5 min. The sample was quickly rinsed by immersing in Milli-Q water for 5 s and then blow dried with $N_{2(g)}$. As-prepared 13 and 3.5 nm Au colloidal solutions were used.

3. Sputter coating:

After degreasing the substrate, the sapphire substrates were blow dried by $N_{2(g)}$, and sputter coated with a sub-monolayer of Au NPs by using a turbo-pumped thermal evaporator (Emitech K975X Coater) for 10 s. The sputter coating was performed by Mike Flaws (Department of Mechanical Engineering, University of Canterbury).

4. Forming a sub-monolayer of Au nanocolloids by dip coating an APTMS modified substrate:

An alternative strategy involved immersing substrates into a solution containing 1 % (vol%) 3-aminopropyl-trimethixysilane (APTMS) in 100 mL of methanol (MeOH) for at least 10 min. A sample holder was used to support substrates vertically (up to 10 substrates including Si or C-plane sapphire substrates) when immersing in the APTMS/MeOH solution. After taking a substrate from the APTMS/MeOH solution, the samples were rinsed with MeOH and Milli-Q water, and finally blow dried with $N_{2(g)}$. Then the substrate was immersed into a vial containing 5 mL Au 13 nm colloidal solution or 3.5 nm Au colloidal solution for 5 min. A small PTFE sample holder was placed in the bottom of the vial in order to support the sample vertically during the dip coating. After dip coating, the sample was rinsed with Milli-Q water thoroughly and then blow dried. Only one sample was immersed in the Au colloidal solution at a time; other substrates remained in the APTMS/MeOH solution and were removed immediately prior to coating with Au colloid.

5.2.3 The parameters of PLD

All PLD experiments were performed by Max Lynam (Department of Electrical and Computer Engineering, University of Canterbury). The PLD apparatus is described in detail in Chapter 2. Section 2.3.2 shows the set-up of the PLD chamber. The excimer laser (Lamda physik, COMPex 205) with KrF radiation was used in this system (the wavelength is 248 nm). The repetition rate of the laser pulse was normally 10 Hz but in the later part of the study, 25 and 4 Hz were also examined. The incident energy focusing on a rotating ceramic ZnO target (ZnO 99.9% purity from Kurt J Lesker Company) was 100 mJ/pulse. The laser power is 1 W.

The laser fluence was controlled by using a focusing lens with f = 750 nm to produce a "spot" of 2.5 mm^2. The distance between the target and substrate with Au catalyst was 60 mm. A shadow mask (10 mm × 10 mm) was placed between the target and the substrate and its distance to the substrate was 20 mm.

The sample holder was coated with In52%-Sn48% and then heated to 140 °C. As the In52%-Sn48% started to melt, the samples were mounted on the top of molten alloy. After mounting the samples, the chamber was sealed, vacuum was applied and the substrate was heated.

In the early stage of this work, the chamber was purged with $O_{2(g)}$ after heating the substrate to 750 °C. While heating up the substrate, the chamber was pumped down to base pressure using a first roughing pump to 1 Torr and then a turbomolecular pump was used to reach a stable base pressure which was measured with an ion gauge (usually approximately 1 × 10^{-5} Torr but could vary between 5 × 10^{-6} Torr and 5 × 10^{-5}). Then, the valve on the fine pump was gradually closed until the pressure was stable for 5 min at 1 × 10^{-4} Torr. $O_{2(g)}$ was introduced into the chamber by slowly opening a needle valve. The pressure in the chamber would rise from 1 × 10^{-4} Torr to 5 × 10^{-2} Torr quickly. Once the pressure reached 5 × 10^{-2} Torr and was stable, the pulsed laser was started to induce the ZnO deposition.

In the later optimised procedure for the PLD process, the $O_{2(g)}$ purging was started when the substrate temperature reached 200 °C. The purge of $O_{2(g)}$ continued throughout the heating and PLD process until finishing the ZnO deposition. The pressure was carefully maintained at 5 × 10^{-2} Torr during the PLD process.

5.3. Results and discussion

5.3.1 Catalysis of ZnO nanorod growth by Au nanocolloids

The 13 nm Au nanocolloids were first tested to check the catalytic activity for ZnO nanorod growth. Hence, simple drop coating was applied to an A-plane sapphire substrate with only the centre part coated with Au nanocolloids. The sample was then used for deposition of ZnO by PLD. Fig. 5.15 (A) shows the substrate after deposition of ZnO. In region (i), no Au nanocolloids were present and there is no growth of nanorods. In region (ii), near the edge of the drop of Au nanocolloids, Fig. 5.15 (C) shows some very thin nanowires but also some chunky structures. In the centre of the drop of Au nanocolloids (region iii), a high density of ZnO nanorods is seen (Fig. 5.15 (D) with higher coverage than at the edge of the drop.

The images in Fig. 5.15 demonstrate that Au nanocolloids do catalyse the growth of ZnO nanorods however as clearly seen; the coverage of ZnO nanorods is not uniform. It is assumed that this is because drop coating does not give a uniform coating of Au nanocolloids and areas of high density lead to aggregation.

Based on the results described above, optimisation of the coating method aimed to form a sub-monolayer of Au nanocolloids in order to prevent the aggregation prior to the ZnO nanorod growth. However, prior to optimisation of the coating, the PLD process was optimised.

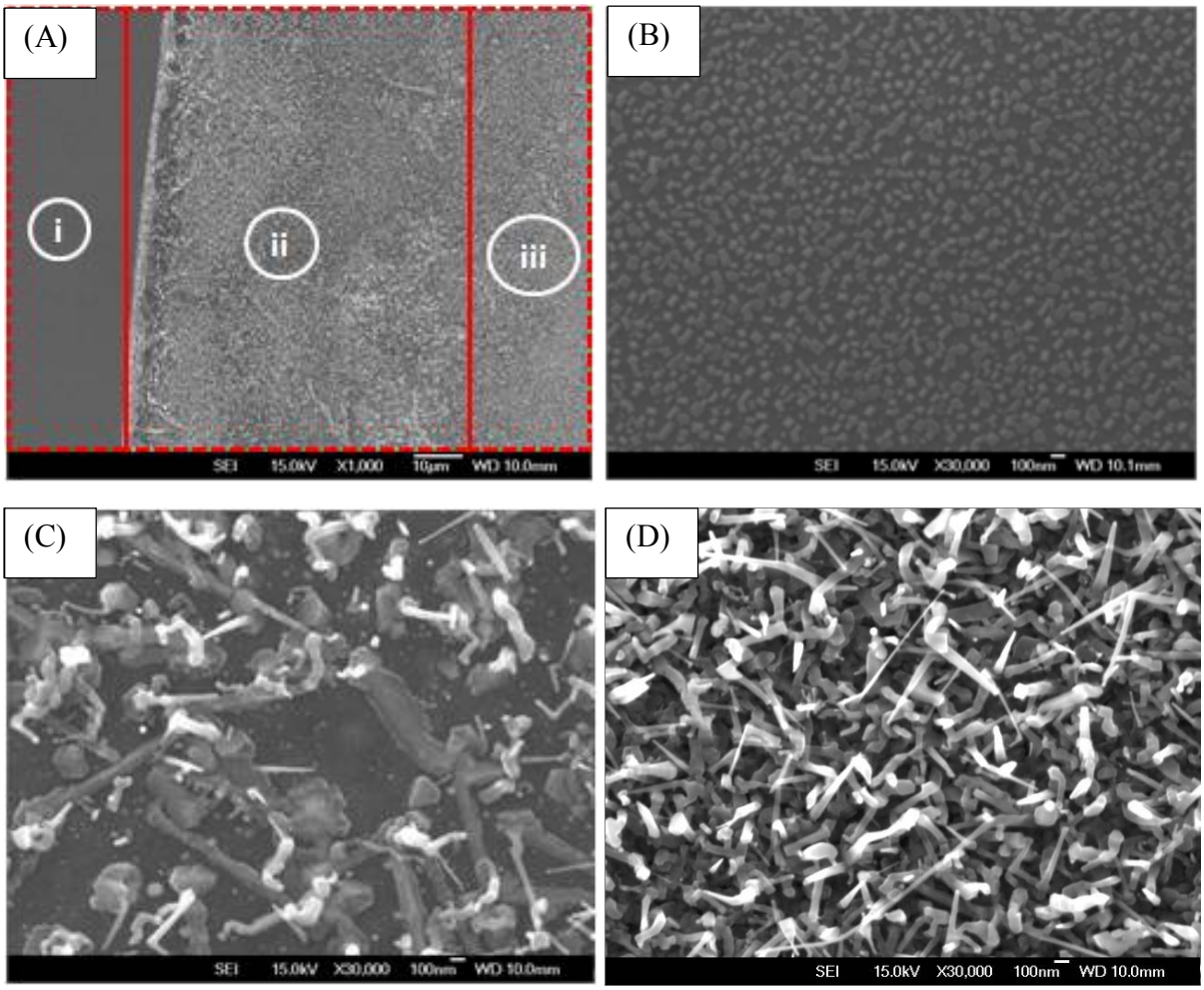

Fig. 5.15. Top view SEM images of ZnO nanorods grown using 13 nm Au nanocolloids on A-plane sapphire substrate (drop coating 17 nM Au colloidal solution onto the substrate). (A) is a low magnification image showing the regions with and without the presence of Au nanocolloids. (B)-(D) are obtained from the regions shown in (A): (B) is region (i) without Au nanocolloids, (C) is region (ii) which has sparse ZnO nanorods grown at the edge of the drop coating area and (D) is region (iii) which has dense ZnO nanorods grown in the centre of the drop coating area. The PLD process without shadow mask was applied on this sample.

5.3.2 Optimisation process

As mentioned in the Introduction, many factors can affect the growth of ZnO nanorods. Hence, the optimisation process in this work was divided into two stages as shown in Scheme 5.2. The optimised conditions are highlighted in red and each procedure will be discussed in the following sections.

The first stage aimed to improve the uniformity of deposition during the PLD process and to establish the basic experimental conditions such as selecting the type of sapphire substrate and the methods for coating Au catalyst. The uniformity of ZnO nanorods showed a significant improvement after the first stage. Hence, the second stage was aimed at improving the morphology of ZnO nanorods or nanowires and the orientation of growth.

First Stage:

Section: 5.3.3
Sapphire Type: A
Coating method: drop coating
PLD: without and **with shadow mask**

Section: 5.3.4
Coating method: drop coating
PLD: with E-plate
Sapphire Type: A, **C**, M and R

Section: 5.3.5
PLD: with E-plate
Sapphire Type: C
Coating method: drop coating, dip coating, sputter and **sub-monolayer coating on modified sapphire substrate**

Second Stage:

Section: 5.3.6
PLD: with E-plate
Sapphire Type: C
Coating method: sub-monolayer coating
Coating Times: 30, 15, 10, **5** and 1 **min**

Section: 5.3.7
PLD: with E-plate
Sapphire Type: C
Coating method: sub-monolayer coating
Coating Times: 5 min
PLD: change the sequence of purging $O_{2(g)}$ during PLD process.

Section: 5.3.8
PLD: with E-plate
Sapphire Type: C
Coating method: sub-monolayer coating
Coating Times: 5 min
PLD: Added process "heating under oxygen"
PLD: position check on sample holder.

Section: 5.3.9
PLD: with E-plate
Sapphire Type: C
Coating method: sub-monolayer coating
Coating Times: 5 min
Added process " heating under oxygen"
Position check
PLD: adjusting the repetition rate of laser pulse and examining the samples which were prepared using diluted Au colloidal solution.

Scheme 5.2. The optimising procedures for growing ZnO nanorods.

5.3.3 The Effect of using a shadow mask

In the first stage of this work, the sample was prepared by directly drop coating as-prepared 13 nm Au colloidal solution onto an A-plane sapphire substrate and then growing the ZnO nanorods in a PLD chamber without using a shadow mask. The SEM image Fig. 5.16 (A), taken from the centre of drop of Au nanocolloids shows that ZnO nanorods can be grown by this method. However the uniformity of ZnO nanorods was poor as varied morphologies and orientations can be observed. The ZnO nanorods appear "chunky" and the range of tip diameter is varied between 63-290 nm which may result from ZnO particles with various sizes directly depositing onto the substrate. As mentioned in 5.1.4, a shadow mask is used to prevent the deposition of larger particles on the substrate during the PLD process. The difference in morphology of ZnO nanorods grown without and with a shadow mask during the PLD process can be observed by comparing Fig. 5.16 (A) and (B). When using the shadow mask during the PLD process, sharper ZnO nanorods can be observed and the tip diameters of the ZnO nanorods is in the range between 17-57 nm which indicates that the shadow mask prevented deposition of large particles on the substrate (Fig. 5.16 (B)).

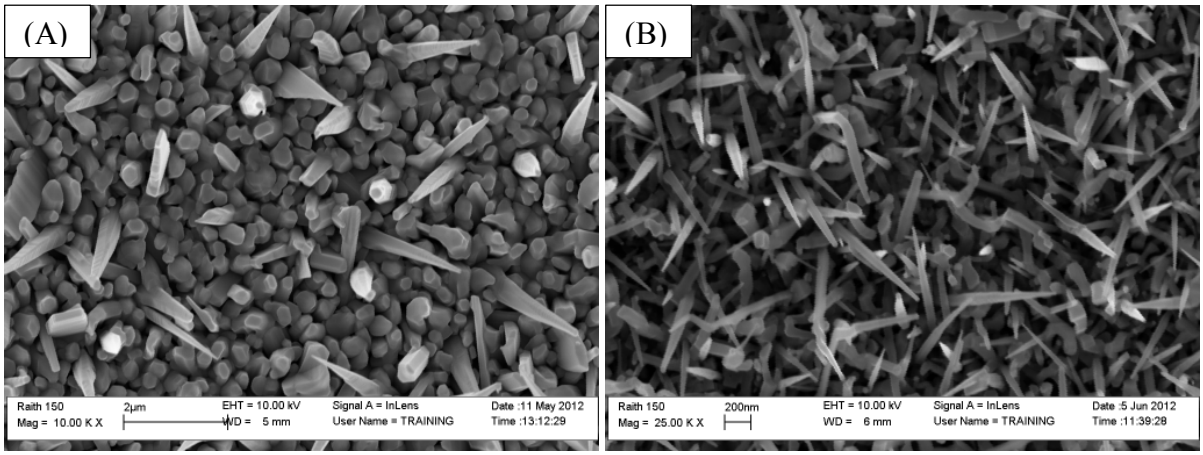

Fig. 5.16 Top view SEM images of ZnO nanorods grown using 13 nm Au nanocolloids on A-plane sapphire substrate (drop coating 17 nM Au colloidal solution onto the substrate). The PLD process was

(A) without the shadow mask and (B) with the shadow mask. SEM images were obtained by Max Lynam in the Department of Electrical and Computer Engineering, University of Canterbury.

5.3.4 Type of sapphire substrate

To examine the effect of the sapphire facet on ZnO nanorod growth, Au nanocolloids were drop coated onto sapphire substrates of various types: A, C, M and R. All other conditions remained constant during sample preparation and ZnO nanorod growth. The SEM images in Fig. 5.17, taken from the centre of the drop of Au nanocolloids show the ZnO nanorods grown on these four types of sapphire substrates. The morphology and orientations of the ZnO nanorods are clearly different across samples. ZnO nanorods grown on the M and R planes (Fig. 5.17 (A) and (B)) are thinner and longer than those grown on the A and C plane (Fig. 5.17 (C) and (D)). However, the orientations of the ZnO nanorods grown on the A, M and R-plane sapphire substrates are more disordered than the ZnO nanorods grown on the C-plane sapphire substrate. The ZnO nanorods grown on C-plane sapphire substrate are more vertical as more tips can be observed in the top view SEM images (Fig. 5.17 (D)). However, the range of the tip diameters is between 20-63 nm, much larger than the diameter of the Au nanocolloids (13 nm). This indicates that aggregation of the Au nanocolloids occurred during the elevated temperature of the PLD process. Nevertheless, C-plane sapphire is the best substrate for the growth conditions used in this work due to a better normal orientation for ZnO nanorods. The following experiments mainly used C-plane sapphire substrates.

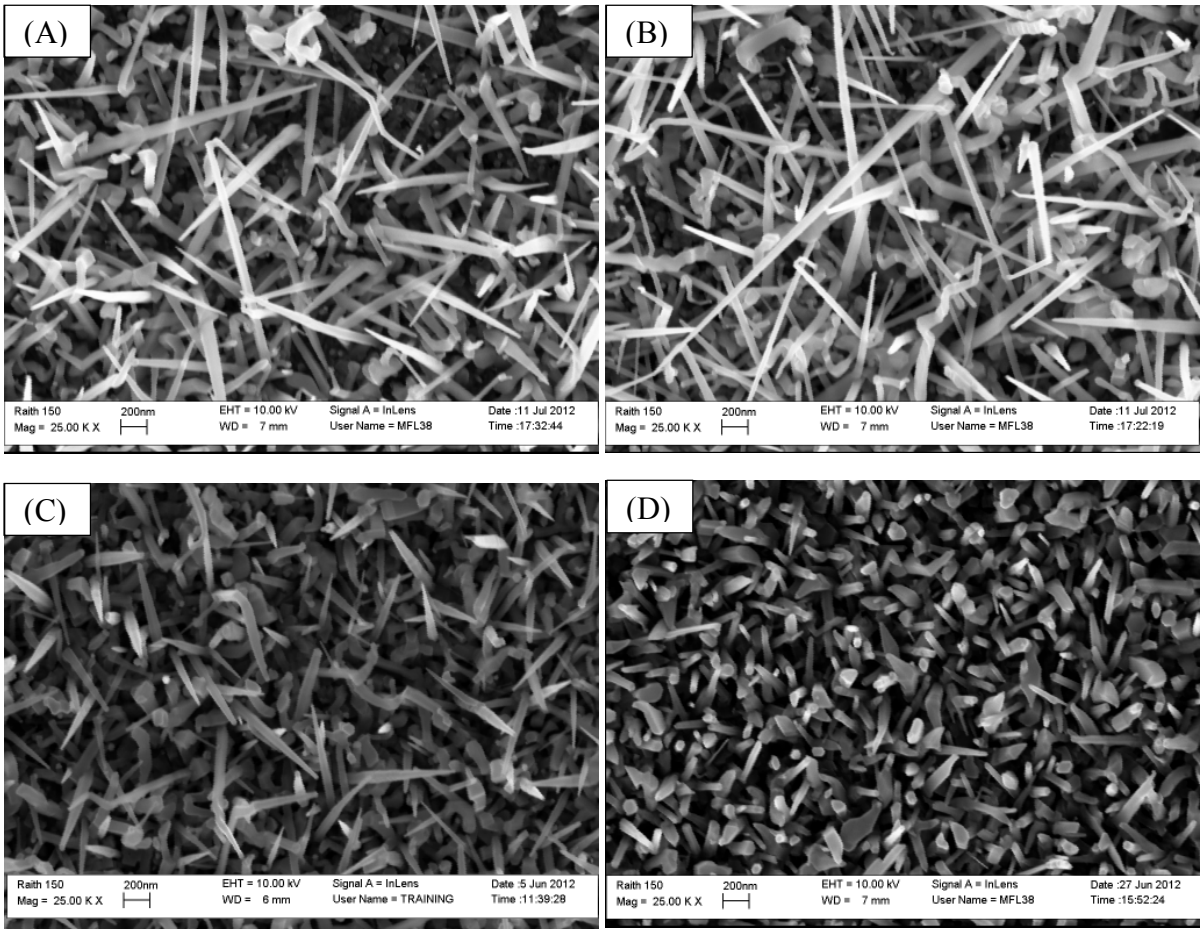

Fig. 5.17. Top view SEM images of ZnO nanorods grown using 13 nm Au nanocolloids on different types of sapphires (drop coating 17 nM Au colloidal solution onto the substrate): (A) M-plane, (B) R-plane, (C) A-plane and (D) C-plane. The PLD process was with the shadow mask. SEM images were obtained by Max Lynam in the Department of Electrical and Computer Engineering, University of Canterbury.

5.3.5 Coating methods for Au nanocolloids

Four methods for coating sapphire substrates with Au nanocolloids were tested in this work: drop coating, dip coating, sputter coating and dip coating using an APTMS modified substrate. Fig. 5.17. (D) shows the morphology of ZnO nanorods on a C-plane sapphire substrate which was drop coated with Au colloidal solution. As mentioned above, the diameter of ZnO nanorods is larger than that of the Au nanocolloids indicating that aggregation of the colloidal particles has been occurred.

In order to avoid the aggregation of Au nanocolloids on the substrate surface, the dip coating method was tested. After dip coating in 13 nm Au colloidal solution and the PLD process, sparse ZnO nanorods were observed. Fig. 5.18 shows that a single ZnO nanorod has grown in a 3.94 μm × 3.15 μm areas, suggesting that the coverage of Au nanocolloids is very low. The amorphous ZnO structure around this ZnO nanorod indicates that there are no Au nanocolloids and a lack of active catalytic sites.

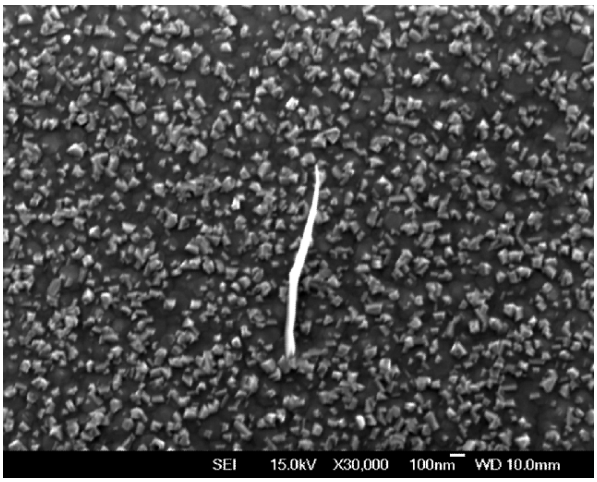

Fig. 5.18. SEM image of a single ZnO nanorod grown using 13 nm Au nanocolloids on C-plane sapphire substrate. Sample was directly dip coated in 17 nM Au colloidal solution for 5 min.

As an alternative approach, a sample was sputter coated with Au NPs using a thermal evaporator and a short deposition time of 10 s. It was expected that a very sparse coverage of Au NPs could be coated on the sapphire under these conditions. The Au NPs were too small to be observed in SEM and hence a TEM grid was sputtered with Au NPs by the same strategy and observed in TEM. The size of Au NPs is in the range of 3-5 nm (Fig. 5.19). After growing ZnO nanorods on the sapphire sample which was sputter coated with Au NPs, the morphology of ZnO nanorods is very different from the sample which was made by drop coating, From the comparison of the sample prepared by sputter coating (Fig. 5.20 (A)) and drop coating (Fig. 5.17 (D)), it is found that the orientation of ZnO nanorods is more uniform

than the samples which were made by drop coating and this phenomenon can be observed from the tilted angle SEM image (Fig. 5.20 (B)). Some very thin ZnO nanowires were obtained with approximately 5-10 nm diameters which indicate that less aggregation of Au NPs occurred during the PLD process on the sputter-coated sample than on the samples drop coated with catalyst (Fig. 5.17 (D)). This is a significant improvement for ZnO growth with respect to the diameter of ZnO nanorods and the orientation. However, the tip diameter of ZnO nanowire is still larger than the diameter of Au NPs indicating some aggregation has occurred. Furthermore, the Au NP deposition method was instrument intensive and hence an alternative coating method was developed in the following work.

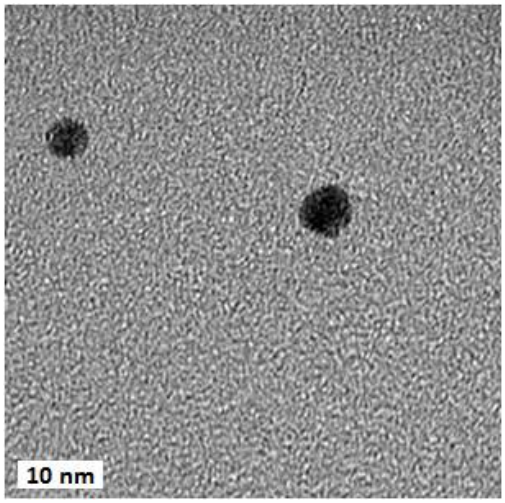

Fig. 5.19. TEM images of Au NPs sputtered for 10 s.

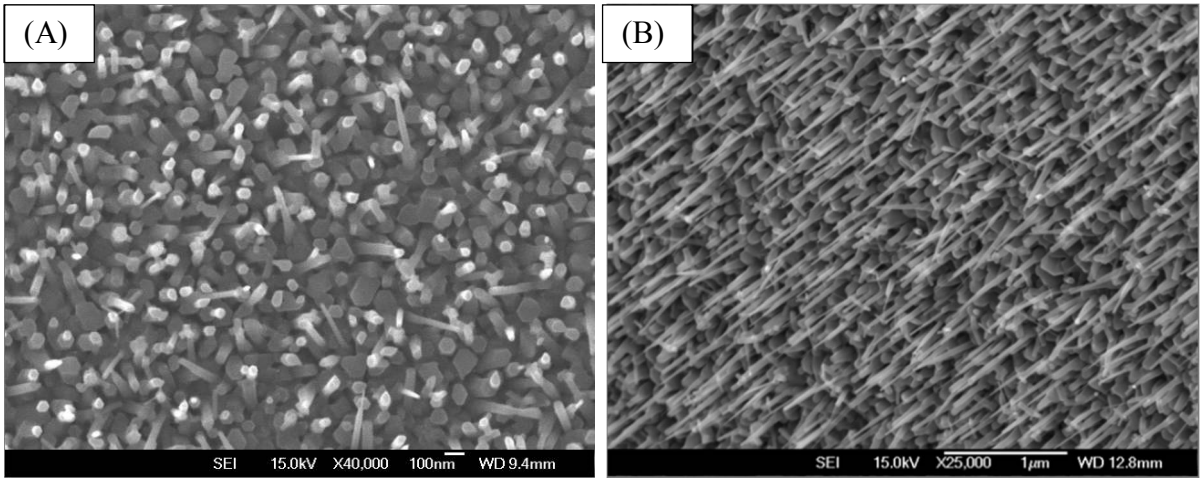

Fig. 5.20. SEM images of ZnO nanorods grown on a C-plane sapphire substrate sputter coated with Au NPs for 10 s (the diameter of Au NPs is in a range between 3 -5 nm). (A) top view, (B) a 40º tilted image of sample (A). SEM images were obtained by Max Lynam in the Department of Electrical and Computer Engineering, University of Canterbury.

Dip coating a APTMS modified substrate into a Au colloidal solution

As explained in the Introduction an APTMS layer can be used to promote assembly of a Au nanocolloid layer on a substrate. However, the method developed by Katherine *et al.* was based on a glass substrate and it was unknown whether a monolayer of Au nanocolloids would form on a sapphire substrate. After APTMS treatment of sapphire substrate and immersing in Au colloidal solution (13 nm diameter), it was difficult to observe the assembly of Au nanocolloids because sapphire is transparent and non-conductive. In order to examine the coverage and distribution of the Au nanocolloids, a Si substrate was used as the model substrate. Au nanocolloids could be easily observed on Si by SEM (Fig. 5.21 (A)). Although there are some spaces between the Au nanocolloids and some aggregation has occurred, the distribution of the Au nanocolloids is reasonably uniform. The subsequent growth of ZnO nanorods on the C-plane sapphire sample which was modified with APTMS and a sub-monolayer of Au nanocolloids showed better orientation (Fig. 5.21 (B)) than the samples prepared using drop coating (Fig. 5.17 (D) and dip coating (Fig. 5.18). From the SEM images of Fig. 5.21 (B), mainly the tips of ZnO nanorods can be observed and the tilted view SEM

image in Fig. 5.21 (C) indicates that the growth direction is vertical to the substrate. However, Fig. 5.22 shows that tip diameters of the ZnO nanorods are in a range between 35-68 nm which is larger than the diameter of Au nanocolloid (13 nm). This may result from the aggregation of Au nanocolloids during dip coating or during the PLD process. Despite the results of varied size of ZnO nanorods, the orientation of the ZnO nanorods is the best result of all coating methods. Therefore, the following optimisation work was based on this APTMS-assisted dip coating method. It was reasoned that the main effect of the APTMS layer was to control the assembly of a sub-monolayer of Au nanocolloids on the sapphire substrate. During heating in the presence of $O_{2(g)}$ in the PLD process, it is assumed that the APTMS would be decomposed leading a sub-monolayer of Au NPs on the substrate.

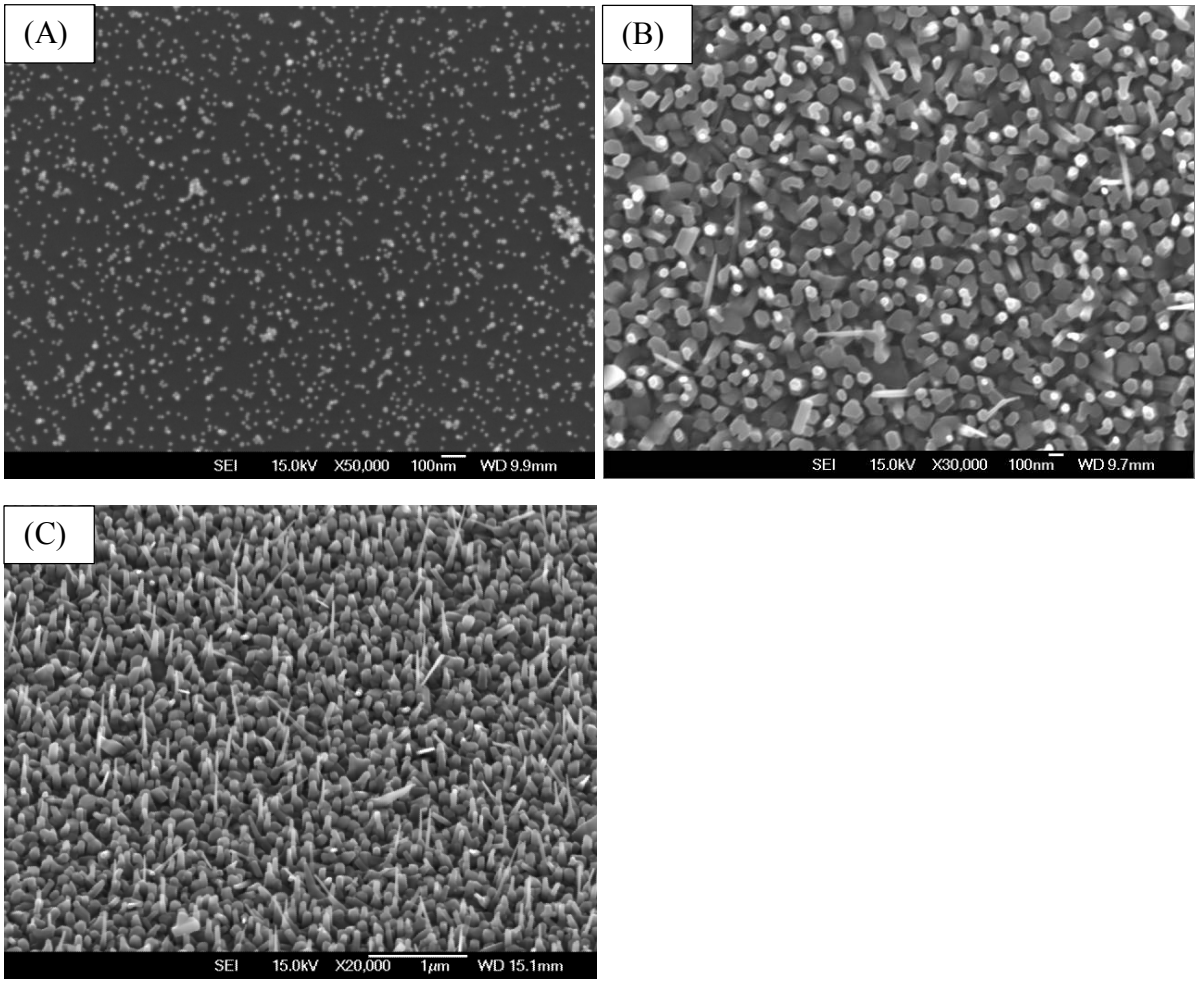

Fig. 5.21. Top view SEM images of (A) a sub-monolayer of 13 nm Au nanocolloids on a APTMS modified Si substrate and (B) ZnO nanorods grown on a C-plane sapphire substrate modified with APTMS and dip coated in 17 nM Au colloidal solution for 5 min (13 diameter Au nanocolloid). (C) 40° tilt view SEM

images of sample (B). In the PLD process for (B) and (C) the sample was heated to 750 ºC before purging with $O_{2(g)}$. The PLD process was with the shadow mask.

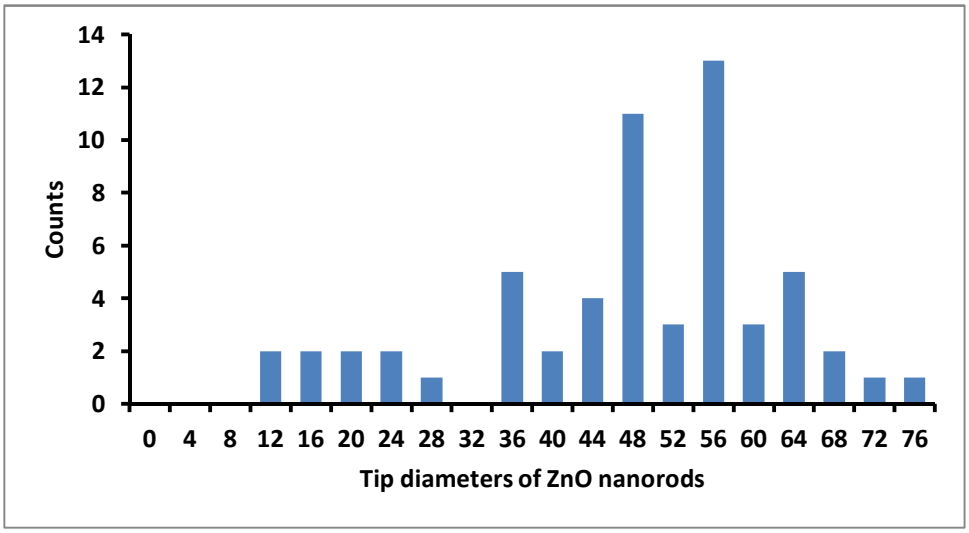

Fig. 5.22. The histogram of tip diameters for ZnO nanorods. Data is collected from Fig. 5.21 (C).

.

Use of smaller Au nanoclusters with the diameter of 3.5 nm was also tested using the same APTMS-assisted dip coating strategy. The TEM image shows the size of these Au nanoclusters (Fig. 5.23). Growth of ZnO nanorods from these Au nanoclusters was compared with that using sputtered Au NPs of similar size (Fig. 5.19). SEM images of ZnO nanorods grown on the sapphire/APTMS/3.5 nm Au nanoclusters indicate that aggregation of Au nanoclusters occurred prior to or during the PLD process (Fig. 5.24 (A) and (B)). The chunky morphology of ZnO nanorods reflects the effects of aggregation. Fig. 5.24 (C) shows the coverage of the Au nanocolloids (3.5 nm) on an APTMS modified Si substrate; diameters are in the range between 6-17 nm. Although these diameters show that some aggregation of the Au nanoclusters has occurred, the diameters of the ZnO nanorods in Fig. 5.24(A) and (B) are clearly much greater than those of the immobilised Au nanoclusters. It is possible that greater aggregation of Au nanocluster occurs on sapphire compared to Si or that aggregation occurs during heating in the PLD process. Regardless of the underlying reason, growth of ZnO nanorods on the 13 nm Au nanocolloids gave lower diameter nanorods, and hence the following experiments were focused on using the larger size Au nanocolloids.

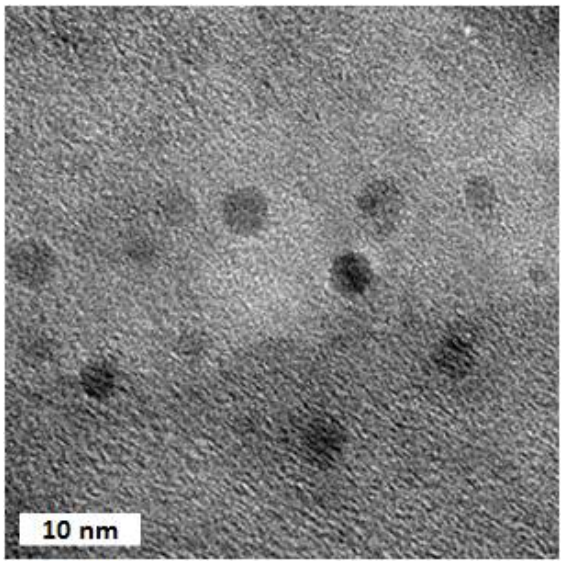

Fig. 5.23. TEM images of water based 3.5 nm Au nanocolloids.

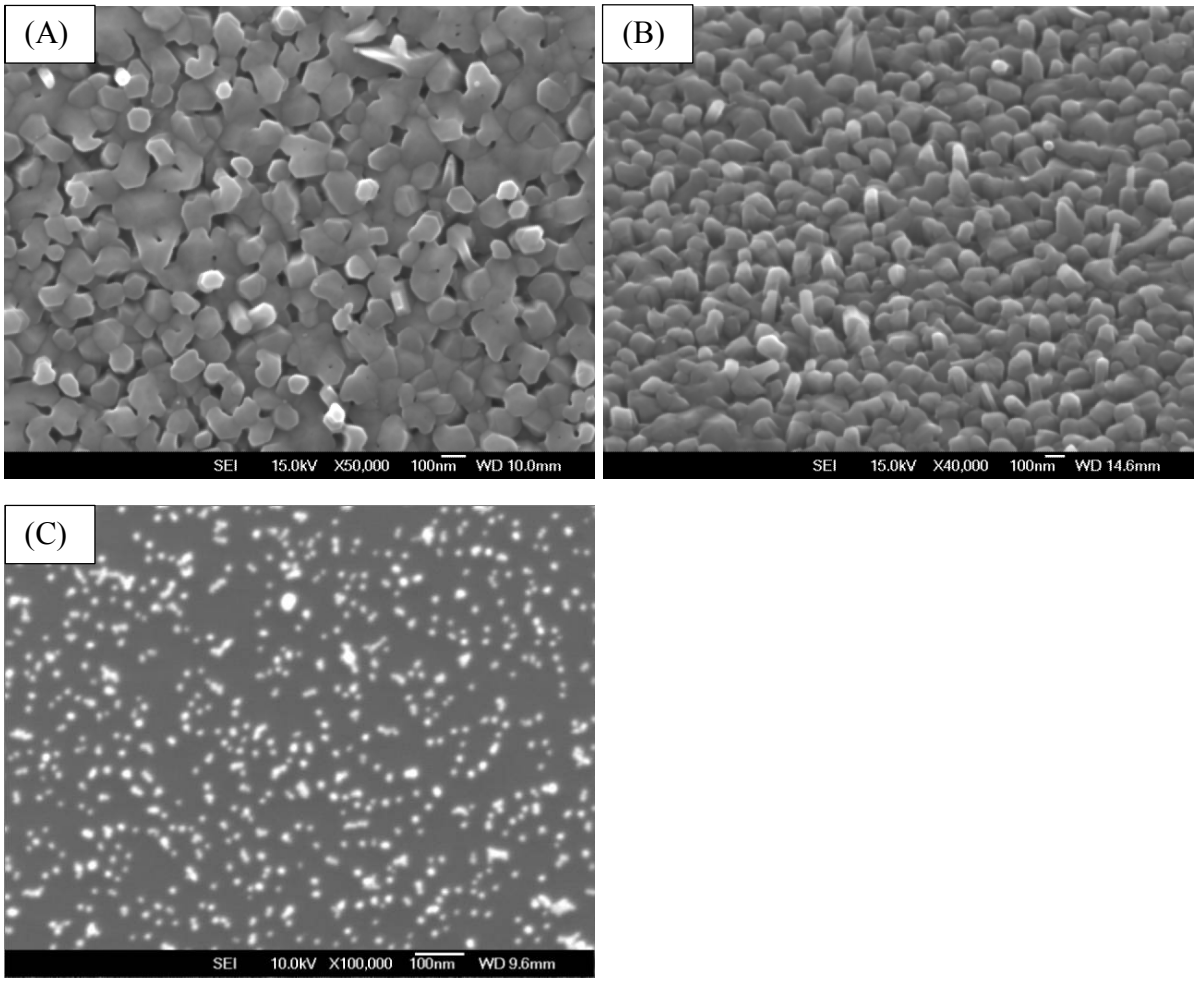

Fig. 5.24. (A) Top view and (B) 40° tilt view SEM images of ZnO nanorods on a C-plane sapphire substrate. The catalyst was Au nanocolloids (3.5 nm) coated on the substrate using APTMS as an adhesive and dip coating into a solution containing Au nanocolloids for 5 min. (C) top view SEM image of Au nanocolloids (diameter 3.5nm) coated on a Si substrate using the same strategy as (A) and (B).

5.3.6 Test of different coating times

As shown in the previous section, dip coating a sub-monolayer of Au nanocolloids onto the sapphire substrate with APTMS as a tether layer is achievable. The effect of dip coating duration in the 13 nm Au colloidal solution on the growth of ZnO nanorods was examined. Increasing the coating time is expected to increase the amount of Au nanocolloids on the substrate as mentioned in the Introduction 5.1.3.2 but this can also increase the possibility of aggregation of Au nanocolloids during the PLD process. Three coating times: 5, 15 and 30 min were examined in this work. A series of SEM images in Fig. 5.25 shows the different morphology between the samples which were dip coated for 5, 15 and 30 min and after ZnO nanorod growth. In the images, nanorod tips are seen as small dots with bright colour. The brightness difference between nanorods and the chunky structures can be distinguished by Image J software, hence, Image J was utilised to measure the coverage of these bright dots as the indicator of the amount of vertical ZnO nanorods. It should be noticed that some nanosheet structures (an example is shown in the circle of Fig. 5.25 (B)) were also taken into account when measured by Image J. A higher coverage of the bright dots could imply less aggregation of Au nanocolloids prior to or during the PLD process. When the dip coating time is 5 min, the coverage of these bright dots is 30 % (Fig. 5.25 (A)). When increasing the dip coating time to 15 min, the coverage decreases to 27 % (Fig. 5.25 (B)). In addition, the orientation of ZnO nanorods becomes worse and more inclined nanosheets can be observed (Fig. 5.25 (B)). When the dip coating time is 30 min, the coverage decreases to 7 % and mainly chunky structures can be observed (Fig. 5.25 (C)). As the result, 5 min coating time is the optimised condition.

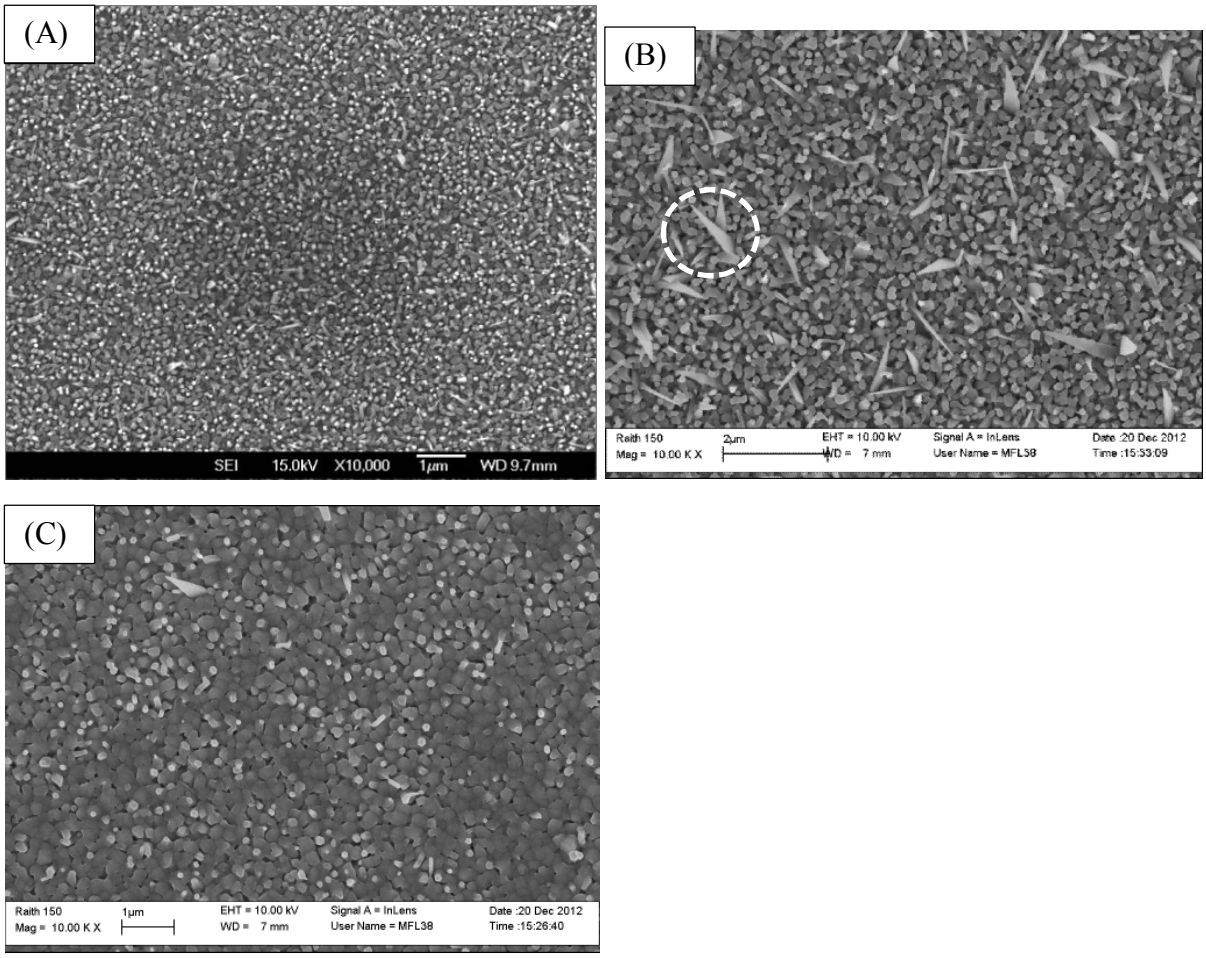

Fig. 5.25. The top view SEM images of ZnO nanorods grown on 13 nm Au nanocolloids which were dip coated by using the APTMS modified sapphire substrate with (A) 5 min, (B) 15 min and (C) 30 min of dip coating times. SEM images (B) and (C) were obtained by Max Lynam in the Department of Electrical and Computer Engineering University of Canterbury. The circle in (B) indicates a nanosheet.

During the initial experimental procedure of dip coating, the same vial of Au colloidal solution was often used for sequentially coating 3-5 samples. Only one sample could be placed in the dip coating solution at a time. In order to check that the coverage of the Au nanocolloids does not change due to solution re-use, two Si substrates were coated, one as the first sample and the one as last sample. Three sapphire samples were dip coated sequentially between these two Si samples. All the samples were dip coated in 5 mL of 17 nM Au colloidal solution for 5 min. Fig. 5.26 (A) and (B) show that the coverage of the two types of Si samples is very similar. The coverage of four samples of each type was determined giving an average value of 8.0 ± 0.5 % for the eight samples. Although these data show that no

changes in the Au colloidal solution occurred during repeat dip coating, in subsequent work after every 3 sapphire samples, an extra Si sample was also prepared as a reference sample. If the subsequent ZnO growth on the sapphire samples gave unexpected results, the Si sample was examined by SEM to check whether aggregation of Au nanocolloids had occurred. Fig. 5.27 shows the distribution of the diameters of Au nanocolloids on the sample which is shown in Fig. 5.26 (B).

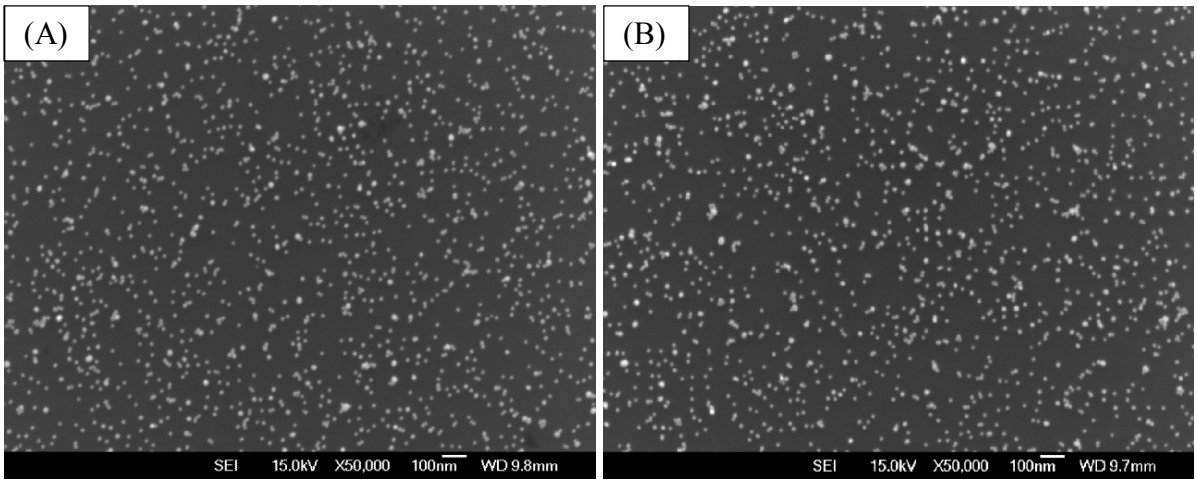

Fig. 5.26. SEM image of a sub-monolayer of 13 nm Au nanocolloids on an APTMS modified Si substrate: (A) was the first chip of experimental queue and (B) was the final chip of experimental queue. Samples were dip coated in a 17 nM Au nanocolloidal solution for 5 min.

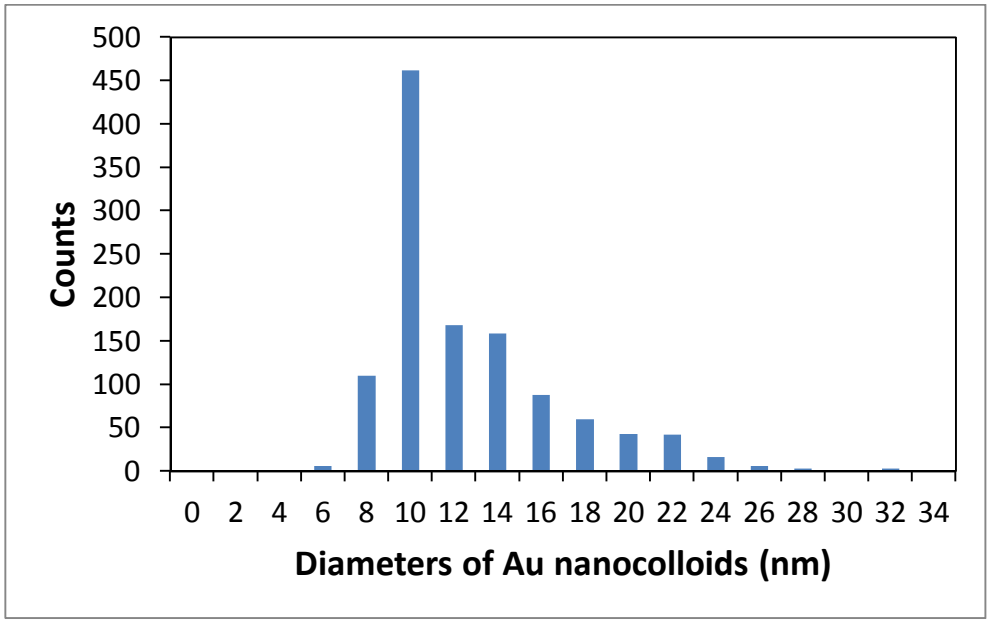

Fig. 5.27. The distributions of diameters of Au nanocolloids which were measured from SEM image Fig. 5.26 (B).

For the work described in the following sections, the optimised procedure for sample preparation was dip coating an APTMS modified C-plane sapphire substrate in 17 nM Au colloidal solution (13 nm Au nanocolloids) for 5 min. The Au colloidal solution was only used for 3 sapphire samples.

5.3.7 Changing the sequence of purging $O_{2(g)}$ during the PLD process

After optimising the coating method, the orientation of the ZnO nanorods showed improvement. However, the length and the tip diameters of nanorods were not uniform. From the tilted angle SEM image of Fig. 5.21 (C), some of the nanorods are very thin while most of the nanorod structures are chunky. The reason for forming the chunky ZnO nanorod structure is unclear. The aggregation of Au nanocolloids could occur during heating prior to the ZnO nanorod growth while the APTMS was decomposed. In the initial stage of this work, $O_{2(g)}$ was purged into the PLD chamber when the temperature of samples reached 750 °C. ZnO nanorod growth was started once the chamber pressure stabilised at 5×10^{-2} Torr. The time taken for pressure stabilisation varied from a few seconds to 30 min. Although the mechanism through which this variation could influence subsequent ZnO nanorod growth is not known, the PLD procedure was changed to remove the variable time of heating with $O_{2(g)}$ purging.

In order to observe the morphology of APTMS and Au nanocolloids prior to the growth of ZnO nanorods, an APTMS modified Si substrate with a sub-monolayer of 13 nm Au nanocolloids (prepared using the optimised coating conditions) was used and the sample was exposed to heating in the PLD system without growing ZnO nanorods. For this sample, $O_{2(g)}$ purging began after the sample reached 750 ºC. The SEM images of the resulting structure

(Fig. 5.28 (A) and (B)) show that Au nanocolloids have aggregated, presumably during or after decomposition of the APTMS layer. Another concern is that during the elevation of temperature between 200 to 750 ºC, the APTMS was decomposed without the presence of $O_{2(g)}$, hence some amorphous carbon might form and then mix with Au nanocolloids. The importance of mixing of these components during heating is unclear but it may be the reason for enhanced aggregation shown in Fig. 5.28 (A) and (B).

Another sample was prepared with the same coating conditions but with heating in the PLD system under different conditions. In the optimised PLD procedure, after mounting the samples onto the sample holder, the PLD chamber was sealed and vacuum was applied, $O_{2(g)}$ was continuously purged into the chamber. At this point, the temperature of the samples was around 200 °C. Subsequently, the PLD chamber was slowly heated to 750 °C with the vacuum system working and $O_{2(g)}$ purging. The comparison between Fig. 5.28 (A) and Fig. 5.28 (C) shows that the aggregation of Au nanocolloids has been effectively prevented by using this optimised PLD procedure (note: the unit of the scale bar shown on Fig. 5.28 (A) is 10 times larger than one shown on Fig. 5.28 (C)). A few big Au NPs can be observed which can be attributed to the uneven distribution of Au nanocolloids during the coating procedure. The distribution of the diameters of Au nanocolloids after this optimised PLD procedure (Fig. 5.29) shows that most diameters of Au nanocolloids range between 8-20 nm which is a similar to the sample before heating in the PLD (Fig. 5.27).

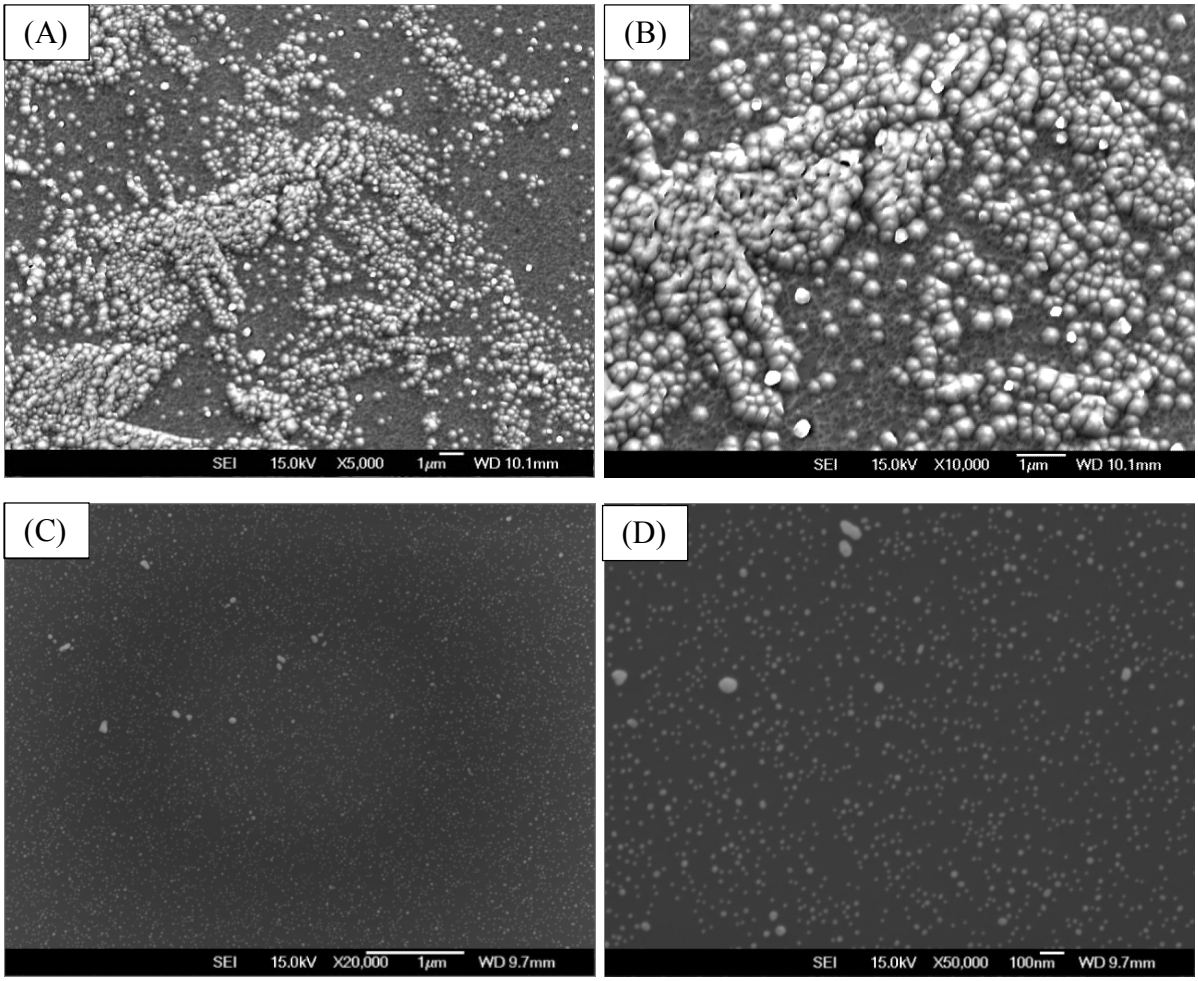

Fig. 5.28. SEM images of Si substrates modified with APTMS and dip coated in 17 nM Au nanocolloidal solution. These samples were subsequently treated to the heating and the procedures of $O_{2(g)}$ purging which were used in the PLD chamber prior to ZnO growth: (A) the sample was heated to 750 ºC and purged with $O_{2(g)}$; (B) a higher magnification image of (A); (C) the sample was heated to 200 ºC and purged with $O_{2(g)}$ until the temperature reached 750 ºC and (D) a higher magnification image of (C).

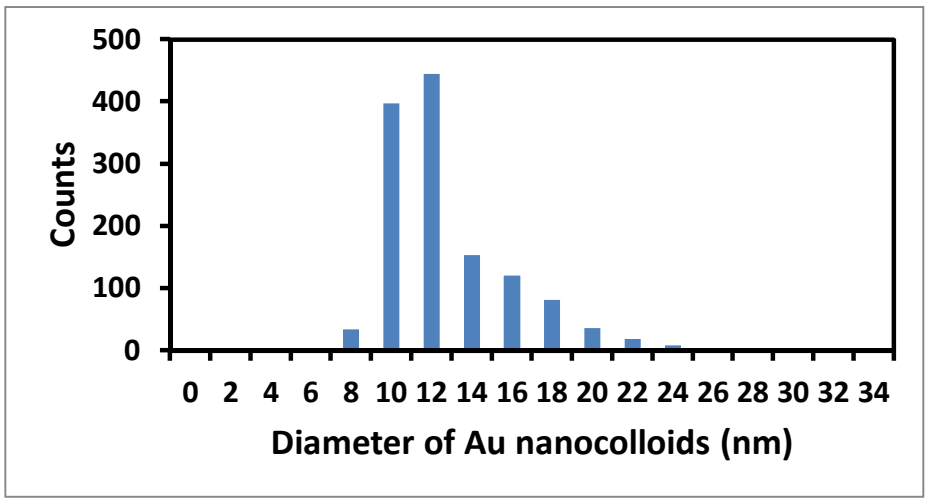

Fig. 5.29. The distribution of diameters of Au nanocolloids which were measured from SEM image Fig. 5.28 (C).

In order to observe the effect of the size of the Au nanocolloids on ZnO growth, an APTMS/sapphire substrate with a sub-monolayer of Au nanocolloids was examined by using the optimised PLD procedure and the subsequent ZnO nanorod growth. Fig. 5.30 shows the morphology of ZnO nanorods which are vertically oriented with longer and thinner features compared to the previous growth as shown in Fig. 5.21 (A). These differences between the nanorod growth before and after optimisation of the PLD procedure are consistent with the decreased aggregation of Au nanocolloids under the optimised PLD conditions, as shown in Fig. 5.21 (C).

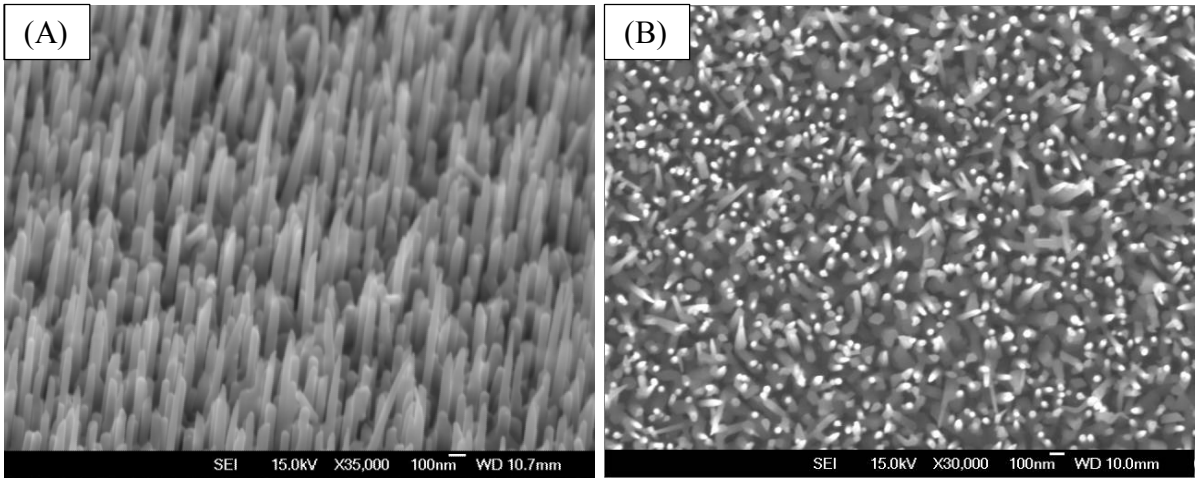

Fig. 5.30. (A) 40° tilt view and (B) top view SEM image of ZnO nanorods on a C-plane sapphire substrate modified with APTMS and dip coated in 17 nM Au colloidal solution. The PLD process was included heating under $O_{2(g)}$ from 200 ºC and was with the shadow mask.

5.3.8 Position check

When using the eclipse method in the PLD chamber for stopping the deposition of droplets, it is important to consider the effect of the positions where the samples are mounted on the sample holder with respect to the shadow mask. To test the influence of sample position on ZnO growth, three samples were mounted on the sample holder. Scheme 5.3

shows the relative positions of the shadow mask and the three samples. In order to compare the morphologies of ZnO nanorods in the positions which were covered and not covered by the shadow mask, ZnO structures grown at the six positions (P1-P6) as shown in Scheme 5.3 were examined by SEM.

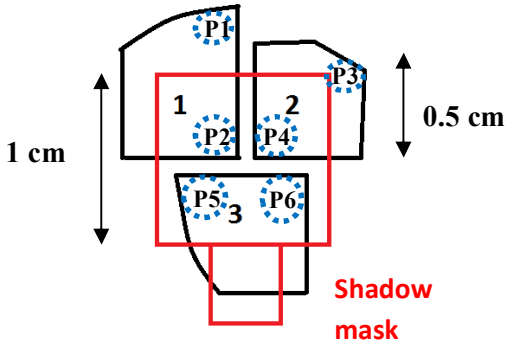

Scheme 5.3. The positions of samples and the shadow mask during PLD. The samples were labelled as 1, 2 and 3. The red square is the shadow mask which is 2 cm in front of samples. The circles with dashed lines are the positions examined by SEM and the SEM images are shown in Fig. 5.31.

The SEM images in Fig. 5.31 show the ZnO nanorods grown at these different positions. The ZnO nanorods at P1, P2, P3 and P4 positions have a similar thin uniform morphology (Fig. 5.31 (A)-(D)). Although P1 and P3 were not covered by the shadow mask, these positions may be in the area where mainly smaller particles are deposited. ZnO nanorods grown at P5 and P6 are relatively chunky and less uniform when compared to other positions. The reason for the growth of chunky nanorods at P5 and P6 is unclear because these positions are behind the shadow mask. Nevertheless, in later studies, all experiments were carried out by mounting two samples onto the area corresponding to the samples 1 and 2 to ensure the consistency of the growth conditions in the PLD chamber.

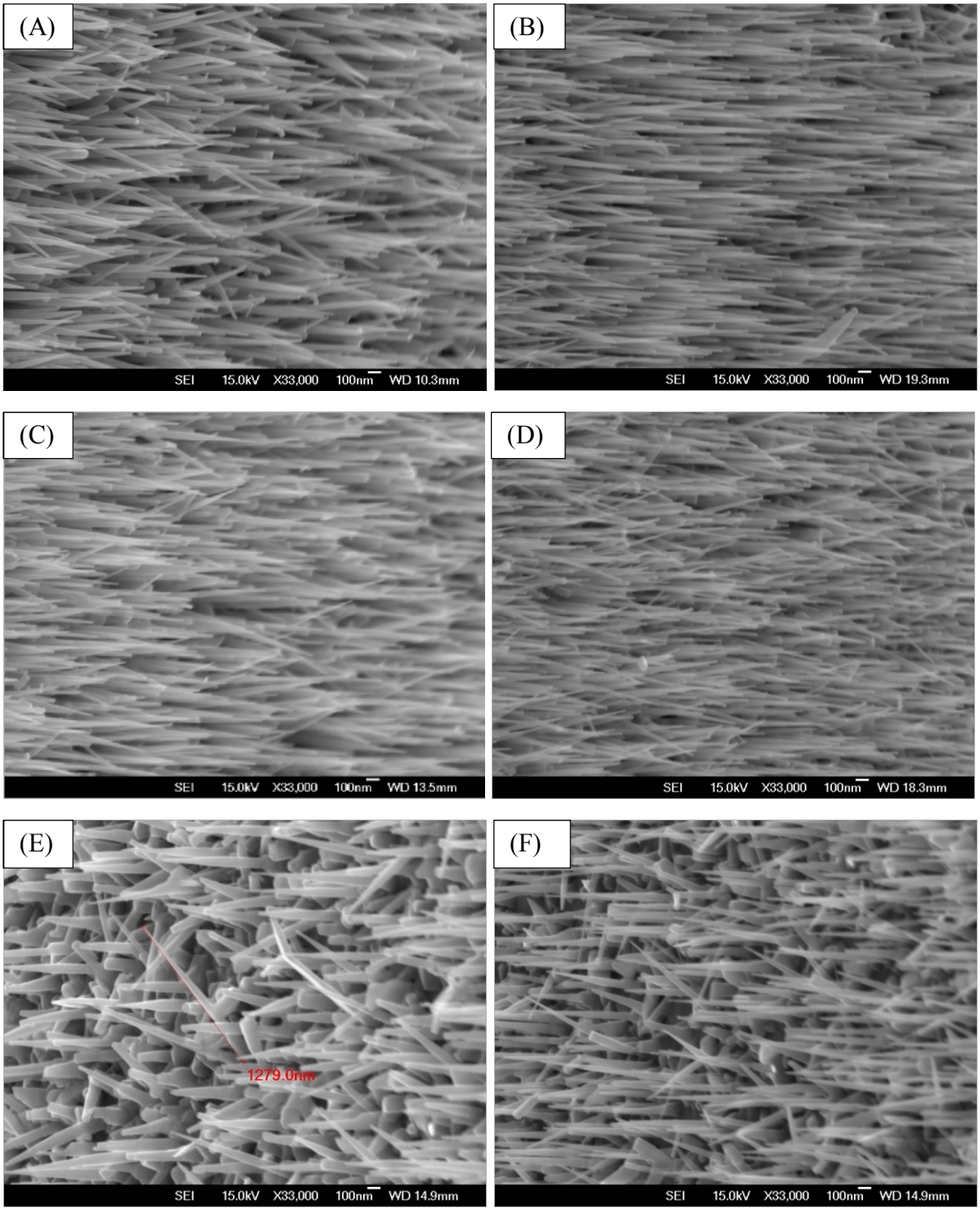

Fig. 5.31. 60° tilt view SEM images of ZnO nanorods at different positions of the samples, 1-3 as shown in Scheme 5.3. (A) position 1, (B) position 2, (C) position 3, (D) position 4, (E) position 5 and (F) position 6. The samples were prepared on C-plane sapphire substrates modified with APTMS and dip coating in 17 nM Au colloidal solution. The PLD process included heating under $O_{2(g)}$ from 200 ºC.

5.3.9 Effect of the frequency of laser pulse

According to the study by Weigand *et al.* the growth rate in the ZnO [0001] direction and the growth rates on the side facets can affect the morphology of the ZnO nanorods.[10] The study by Guo *et al.*, also observed that changing the laser repetition rate can change the density and the morphology of ZnO nanorods.[43] Hence, adjusting the repetition rate was examined in this work. Fig. 5.32 shows the results of ZnO nanorod growth using three different laser repetition rates. The original repetition rate used in this work described in previous sections was 10 Hz (Fig. 5.32 (B)). When decreasing the repetition rate to 4 Hz, the uniformity of ZnO nanorods was decreased as the lengths of nanorods become varied (Fig. 5.32 (A)). In addition, the density of ZnO nanorods decreases when compared with the sample grown using the 10 Hz repetition rate as gaps between nanorods can be observed easily (Fig. 5.32 (A) and (B)). However, the distributions of the tip diameters of ZnO nanorods for samples grown using 4 and 10 Hz are similar. When the repetition rate is increased to 25 Hz, the ZnO nanorods become thinner and they may be considered as nanowires (Fig. 5.32 (C)).The distribution of the tip diameters of ZnO nanowires is in a range between 12-24 nm which is close to the diameter of the Au nanocolloids. This indicates that the optimised laser repetition rate is 25 Hz.

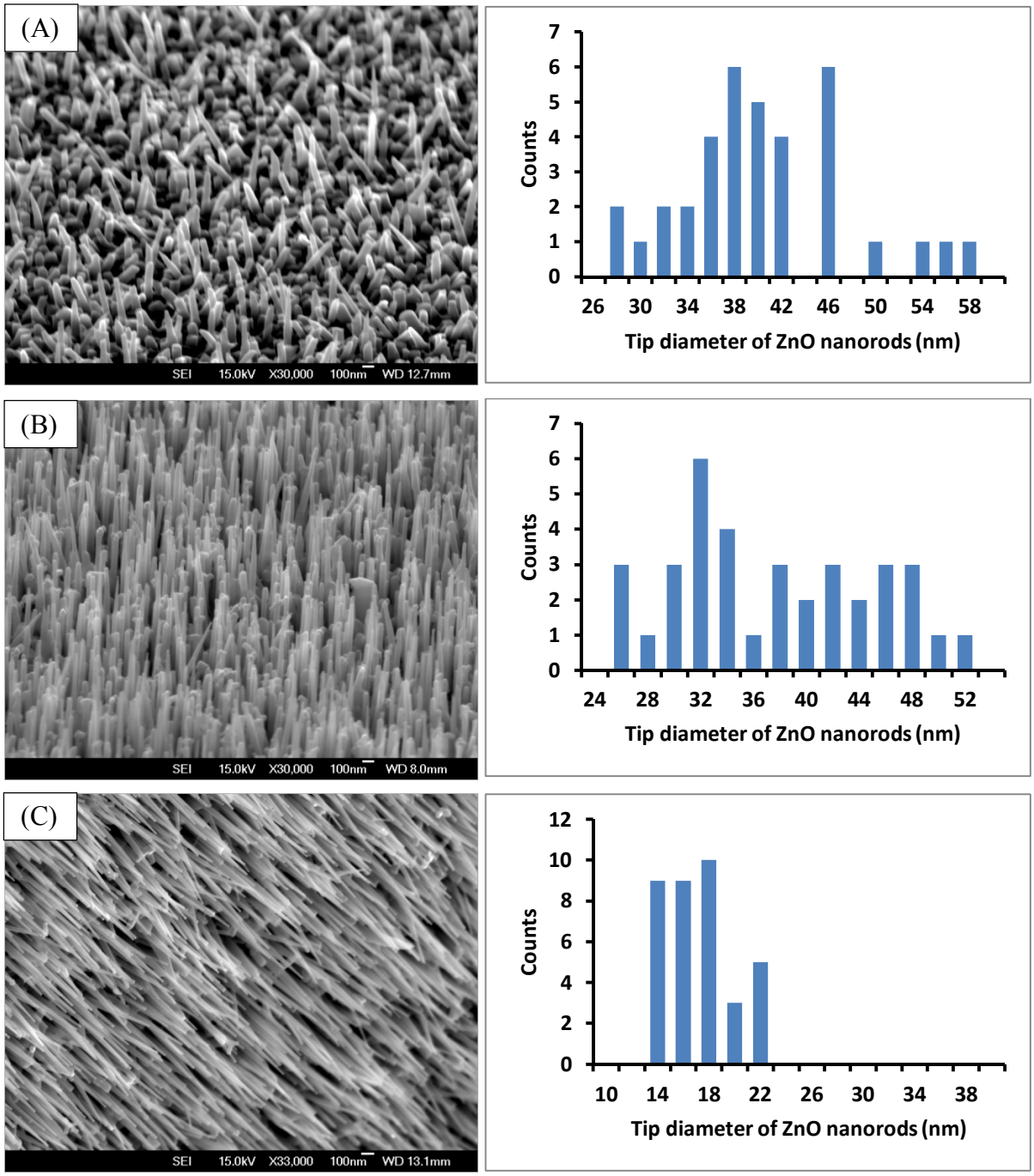

Fig. 5.32. 60° tilt view SEM images of ZnO nanorods grown with different laser repetition rates and corresponding histograms of tip diameters for ZnO nanorods: (A) 4 Hz, (B) 10 Hz and (C) 25 Hz. The samples were prepared on C-place sapphire substrates modified with APTMS and dip coating in 17 nM Au colloidal solution. The PLD process included heating under $O_{2(g)}$ from 200 °C and was with the shadow mask.

Further experiments were carried out to investigate why thinner ZnO nanowires grow when the laser repetition rate was increased. It was suspected that the aggregation of Au nanocolloids tends to occur at low repetition rate and hence the use of a more dilute Au

colloidal solution, which should decrease the tendency for aggregation, was investigated. The laser repetition rate was 10 Hz. Fig. 5.33 shows the comparison of ZnO nanorod growth on the samples prepared with 17 nM and 8.5 nM Au colloidal solutions. From the top view SEM images, the coverage of ZnO nanorods is assumed to represent the coverage of the Au nanocolloids on the samples. It is clear that a less dense coverage of ZnO structures is present on the sample that was prepared with 8.5 nM Au colloidal solution (Fig. 5.33 (B)). Some ZnO nanorods were inclined but some vertical ZnO nanorods can be observed. From the histograms of the ZnO nanowire diameters for this sample, Fig. 5.34(B) and that of the sample prepared with the same catalyst but with undiluted Au nanocolloids (Fig. 5.32 (B)), it is clear that less aggregation has occurred for dilute colloids. This gives indirect evidence that a decrease in aggregation may underlie the thinner nanostructures formed at high laser repetition rate.

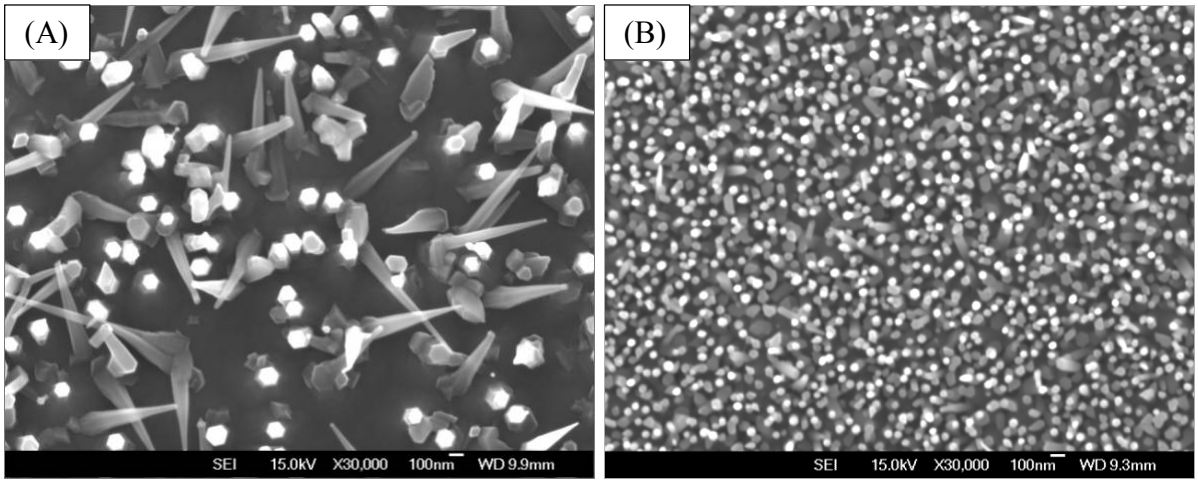

Fig. 5.33.Top view SEM images of ZnO nanorods grown on the samples prepared with different concentrations of Au colloidal solution: (A) 17 nM and (B) 8.5 nM. The samples were prepared on C-place sapphire substrates modified with APTMS and dip coating in Au colloidal solution. The PLD process included heating under $O_{2(g)}$ from 200 ºC and was with the shadow mask.

In order to examine this hypothesis, it was attempted to use samples which were prepared with 8.5 nM Au colloidal solution and to grow ZnO nanorods under different laser

repetition rates (4 Hz, 10 Hz and 25 Hz). From the tilted angle SEM images in Fig. 5.34, it is clear that the morphology of ZnO nanorods strongly depends on the repetition rate (Fig. 5.34). When using 4 Hz as the repetition rate, thick and short ZnO nanorods grow and the distribution of tip diameters are in a range between 60-92 nm (Fig. 5.34 (A)). When the laser repetition rate is increased to 10 Hz, the morphology of ZnO nanorods is cone-like and the distribution of tip diameters is in the range between 14-22 nm. When the laser repetition rate is increased to 25 Hz, the ZnO nanorods become much thinner than those using the lower laser repetition rates and structure is more like nanowire. The distribution of tip diameters is in a range between 12-20 nm (Fig. 5.34 (B) and (C)).

It is interesting to compare the morphology of ZnO nanorods grown with different coverage of Au nanocolloids but under the same conditions in PLD. By comparing Fig. 5.32 (A) and Fig. 5.34 (A) which show samples prepared with a 4 Hz laser repetition rate, the ZnO nanorods grown on the sample which was prepared with 17 nM Au colloidal solution are thinner and taller than those growth on the sample prepared with 8.5 nM Au colloidal solution. When a 10 Hz laser repetition rate was used for growing ZnO nanorods, the comparison between Fig. 5.32 (B) and Fig. 5.34 (B) shows the morphology of ZnO nanorods changes from a rod structure to a cone-like structure for the samples prepared by using 17 nM and 8.5 nM Au colloidal solutions respectively. It is possible that when fewer catalytic Au nanocolloids were present on the surface, the amount of materials available to grow from each particle is greater giving a thicker structure. On the other hand, there is no obvious difference between the samples which were prepared with 17 nM and 8.5 nM Au colloidal solution when using a 25 Hz laser repetition rate for growth (Fig. 5.35 (A) and (B)). Fig. 5.35 (A) and (B) show high magnification images of the samples prepared with the two Au colloidal solutions and a laser repetition rate of 25 Hz. The tip diameters indicated were measured from the tilt view SEM images. The top view images in Fig. 5.35 (C) and (D)

confirm that the coverage of both samples is very similar. At high laser repetition rate, the tip diameters of ZnO nanorods could represent the diameter of the Au nanocolloids as they are both in the range of 12-22 nm. Although it is not known why the laser repetition rate influences the ZnO growth, further experiments using Au colloids with other diameters would be necessary to confirm whether use of a high laser repetition rate allows growth of ZnO nanorods with diameters controlled by the size of the nanoparticle catalyst.

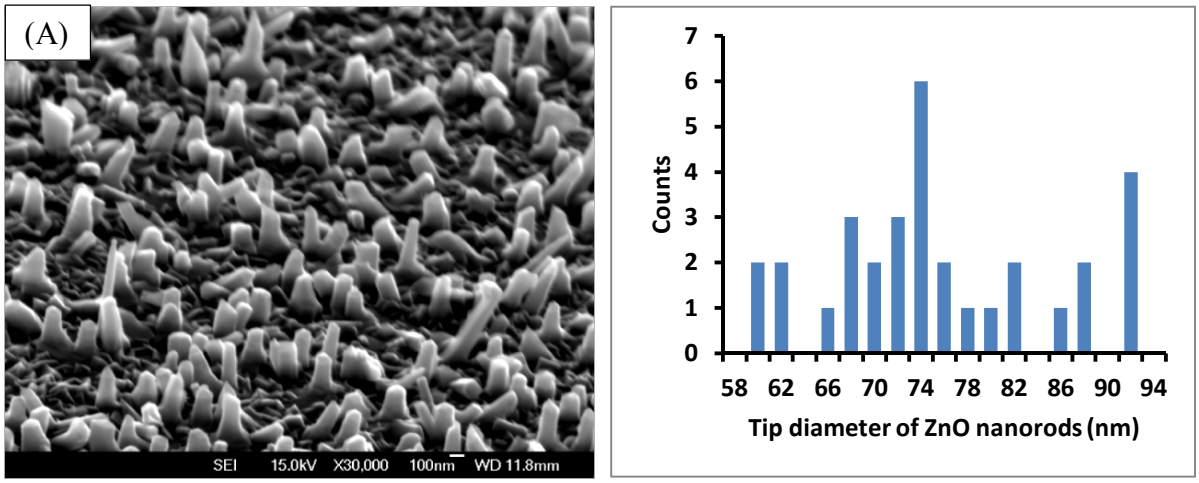

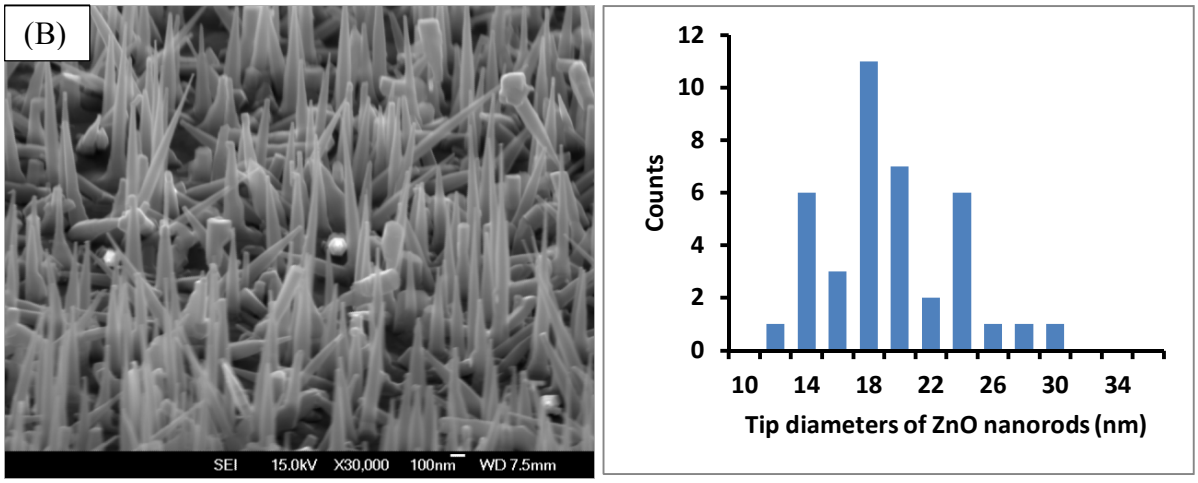

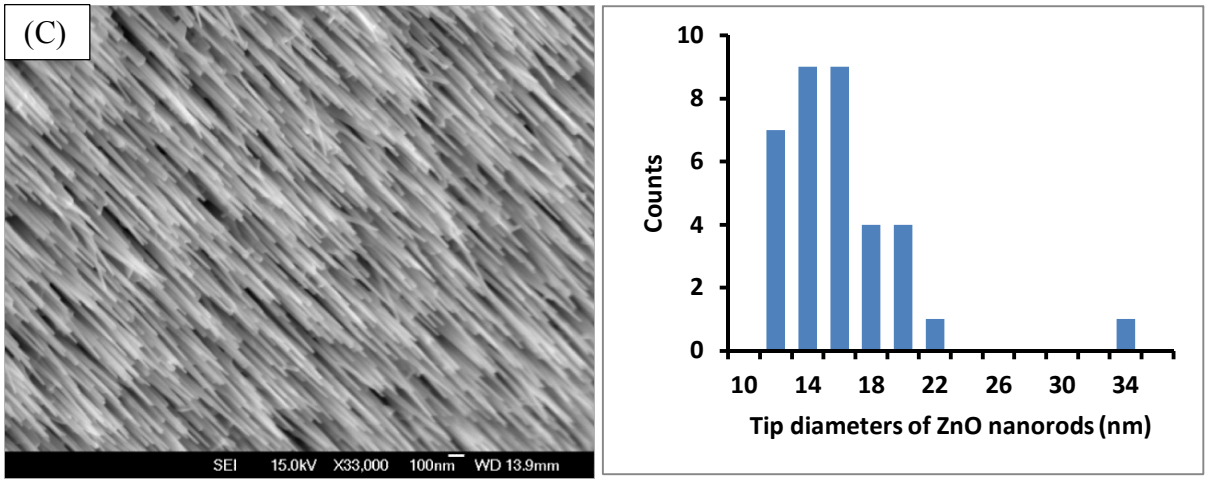

Fig. 5.34. 60° tilt view SEM images of ZnO nanorods grown with different repetition rates and corresponding histograms of tip diameters for ZnO nanorods: (A) 4 Hz, (B) 10 Hz and (C) 25 Hz. The samples were prepared on C-place sapphire substrates modified with APTMS and dip coating in 17 nM Au colloidal solution. The PLD process included heating under $O_{2(g)}$ from 200 °C and was with the shadow mask.

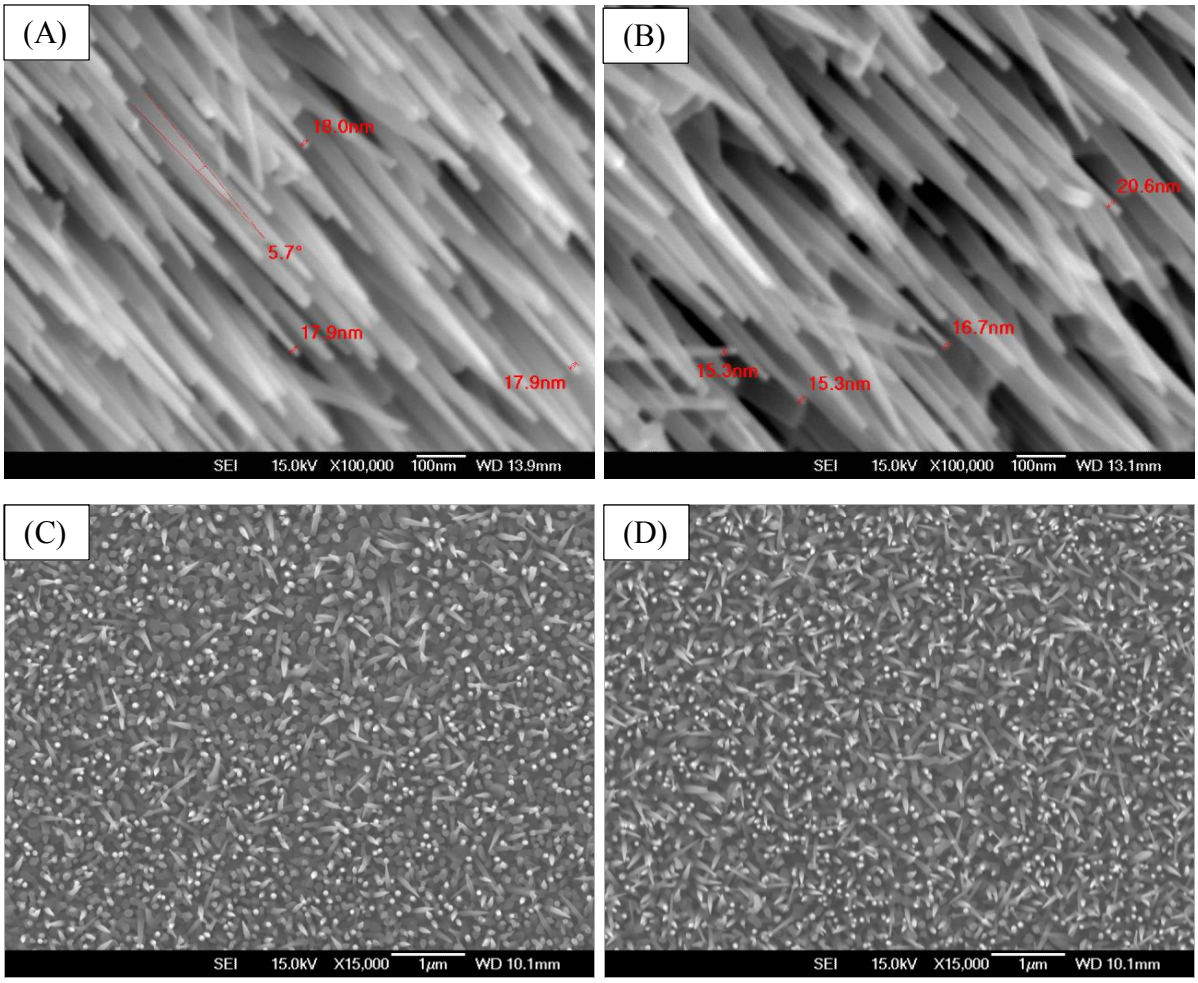

Fig. 5.35. SEM images of ZnO nanorods grown on the samples prepared with two different concentrations of Au colloidal solution. (A) 60° tilt view of sample using 8.5 nM Au colloidal solution, (B)

60° tilt view of sample using 17 nM Au colloidal solution, (C) top view of sample using 8.5 nM Au colloidal solution and (D)) top view of sample using 17 nM Au colloidal solution. The samples were prepared on C-place sapphire substrates modified with APTMS and dip coating in Au colloidal solution. The PLD process included heating under $O_{2(g)}$ from 200 ºC and was with the shadow mask..

5.4. Conclusion

In this series of studies, Au nanocolloids were used as the catalyst for ZnO nanorod or nanowire growth by PLD. In order to prevent the aggregation of the Au nanocolloids during the PLD process, sapphire substrate with a sub-monolayer of Au nanocolloids was applied. It is suggested that the presence of APTMS residues results in the disordered growth of the ZnO nanorods probably *via* the aggregation of Au nanocolloids on the surface. It appears that in order to completely remove the APTMS prior to the ZnO nanorod growth during PLD process, prolonged $O_{2(g)}$ purging during heating is required. Uniform ZnO nanorods were successfully synthesised with these optimised strategies.

The results of ZnO nanorod growth using different laser repetition rates suggests that using a high repetition rate (25 Hz) is beneficial for growing ZnO nanowires. The uniformity and the morphology of ZnO nanowires improved remarkably compared with those grown using 10 Hz. In addition, the concentration of Au colloidal solution does not seem to have significant effect on the morphology of ZnO nanowires, although this may need further study by observing the base structure of the ZnO nanowires and measuring their lengths. Nevertheless, 8.5 nM Au colloidal solution is still recommended for using in dip coating due to the lower possibility of aggregation during the PLD process.

The four types of sapphire substrate surface/facets (A, C, M and R) have been tested in the early stage of this work. According to the results, C-plane sapphire substrate provides

the best orientation growth for the Au nanocolloids used in this work. However, it is not known whether this substrate would give the best orientation of ZnO nanorods under the optimised conditions developed in the later part of work. This can be investigated in future work.

5.5. References

1. Wong, E. M.; Searson, P. C., ZnO quantum particle thin films fabricated by electrophoretic deposition. *Appl. Phys. Lett.* **1999,** *74* (20), 2939-2941.
2. Yi, G. C.; Wang, C. R.; Park, W. I., ZnO nanorods: synthesis, characterization and applications. *Semicond. Sci. Technol.* **2005,** *20* (4), S22-S34.
3. Wang, Z. L.; Song, J. H., Piezoelectric nanogenerators based on zinc oxide nanowire arrays. *Science* **2006,** *312* (5771), 242-246.
4. Sun, X. W.; Kwok, H. S., Optical properties of epitaxially grown zinc oxide films on sapphire by pulsed laser deposition. *J. Appl. Phys.* **1999,** *86* (1), 408-411.
5. Marcu, A.; Goyat, M.; Yanagida, T.; Kawai, T., ZnO nanowire mophology control in pulsed laser deposition. *J. Optoelectron. Adv. Mater.* **2009,** *11* (4), 421-424.
6. Yang, P. D.; Yan, H. Q.; Mao, S.; Russo, R.; Johnson, J.; Saykally, R.; Morris, N.; Pham, J.; He, R. R.; Choi, H. J., Controlled growth of ZnO nanowires and their optical properties. *Adv. Funct. Mater.* **2002,** *12* (5), 323-331.
7. Sun, Y.; Fuge, G. M.; Ashfold, M. N. R., Growth of aligned ZnO nanorod arrays by catalyst-free pulsed laser deposition methods. *Chem. Phys. Lett.* **2004,** *396* (1-3), 21-26.
8. Hartanto, A. B.; Ning, X.; Nakata, Y.; Okada, T., Growth mechanism of ZnO nanorods from nanoparticles formed in a laser ablation plume. *Applied Physics a-Materials Science & Processing* **2004,** *78* (3), 299-301.
9. Marcu, A.; Grigoriu, C.; Lungu, C. P.; Yanagida, T.; Kawai, T., Ablation particles parameters influences on VLS oxide nanowire growing. *Physica E-Low-Dimensional Systems & Nanostructures* **2012,** *44* (6), 1071-1073.
10. Weigand, C.; Tveit, J.; Ladam, C.; Holmestad, R.; Grepstad, J.; Weman, H., Epitaxial relationships of ZnO nanostructures grown by Au-assisted pulsed laser deposition on c- and a-plane sapphire. *J. Cryst. Growth* **2012,** *355* (1), 52-58.
11. Gao, P. X.; Ding, Y.; Wang, I. L., Crystallographic orientation-aligned ZnO nanorods grown by a tin catalyst. *Nano Lett.* **2003,** *3* (9), 1315-1320.
12. Li, S. Y.; Lee, C. Y.; Tseng, T. Y., Copper-catalyzed ZnO nanowires on silicon (100) grown by vapor-liquid-solid process. *J. Cryst. Growth* **2003,** *247* (3-4), 357-362.
13. Xu, C. X.; Sun, X. W., Field emission from zinc oxide nanopins. *Appl. Phys. Lett.* **2003,** *83* (18), 3806-3808.
14. Kong, Y. C.; Yu, D. P.; Zhang, B.; Fang, W.; Feng, S. Q., Ultraviolet-emitting ZnO nanowires synthesized by a physical vapor deposition approach. *Appl. Phys. Lett.* **2001,** *78* (4), 407-409.
15. Zhang, Z.; Wang, S. J.; Yu, T.; Wu, T., Controlling the growth mechanism of ZnO nanowires by selecting catalysts. *J. Phys. Chem. C* **2007,** *111* (47), 17500-17505.
16. Lv, H.; Sang, D. D.; Li, H. D.; Du, X. B.; Li, D. M.; Zou, G. T., Thermal evaporation synthesis and properties of ZnO nano/microstructures using carbon group elements as the reducing agents. *Nanoscale Res. Lett.* **2010,** *5* (3), 620-624.
17. Huang, M. H.; Wu, Y. Y.; Feick, H.; Tran, N.; Weber, E.; Yang, P. D., Catalytic growth of zinc oxide nanowires by vapor transport. *Adv. Mater.* **2001,** *13* (2), 113-116.
18. Holmes, J. D.; Johnston, K. P.; Doty, R. C.; Korgel, B. A., Control of thickness and orientation of solution-grown silicon nanowires. *Science* **2000,** *287* (5457), 1471-1473.
19. Wang, X. D.; Summers, C. J.; Wang, Z. L., Large-scale hexagonal-patterned growth of aligned ZnO nanorods for nano-optoelectronics and nanosensor arrays. *Nano Lett.* **2004,** *4* (3), 423-426.

20. Huang, M. H.; Mao, S.; Feick, H.; Yan, H. Q.; Wu, Y. Y.; Kind, H.; Weber, E.; Russo, R.; Yang, P. D., Room-temperature ultraviolet nanowire nanolasers. *Science* **2001,** *292* (5523), 1897-1899.
21. Belic, D.; Chantry, R. L.; Li, Z. Y.; Brown, S. A., Ag-Au nanoclusters: Structure and phase segregation. *Appl. Phys. Lett.* **2011,** *99* (17), 3.
22. Belic, D., Studies of Alloy Nanoclusters and Their Influence on Growth of Carbon Nanotubes. *PhD thesis of University of Canterbury. Chemistry* **2012**.
23. Turkevich, J.; Stevenson, P. C.; Hillier, J., A study of the nucleation and growth processes in the synthesis of colloidal gold. *Discussions of the Faraday Society* **1951,** *11* (0), 55-75.
24. Frens, G., Controlled nucleation for regulation of particle-size in monodisperse gold suspensions. *Nature-Physical Science* **1973,** *241* (105), 20-22.
25. Grabar, K. C.; Freeman, R. G.; Hommer, M. B.; Natan, M. J., Preparation and charaterization of Au colloid monolayers. *Anal. Chem.* **1995,** *67* (4), 735-743.
26. Keating, C. D.; Musick, M. D.; Keefe, M. H.; Natan, M. J., Kinetics and thermodynamics of Au colloid monolayer self-assembly - Undergraduate experiments in surface and nanomaterials chemistry. *J. Chem. Educ.* **1999,** *76* (7), 949-955.
27. An introduction to Pulsed Laser Deposition. [On line] http://www.andor.com/learning-academy/pulsed-laser-deposition-an-introduction-to-pulsed-laser-deposition.
28. Kinoshita, K.; Ishibashi, H.; Kobayashi, T., Improved surface smoothness of $YBa_2Cu_3O_y$ films and related multilayers by ArF excimer-laser deposition with shadow mask eclipse method. *Jpn. J. Appl. Phys. Part 2 - Lett.* **1994,** *33* (3B), L417-L420.
29. Marcu, A.; Grigoriu, C.; Jiang, W. H.; Yatsui, K., Pulsed laser deposition of YBCO thin films in a shadow mask configuration. *Thin Solid Films* **2000,** *360* (1-2), 166-172.
30. Tachiki, M.; Kobayashi, T., An improved laser ablation method using a shadow mask (eclipse method). *Electr. Eng. Jpn.* **2000,** *130* (1), 88-94.
31. Mendelsberg, R. J.; Kerler, M.; Durbin, S. M.; Reeves, R. J., Photoluminescence behavior of ZnO nanorods produced by eclipse PLD from a Zn metal target. *Superlattices Microstruct.* **2008,** *43* (5-6), 594-599.
32. Yanagida, T.; Nagashima, K.; Tanaka, H.; Kawai, T., Mechanism of critical catalyst size effect on MgO nanowire growth by pulsed laser deposition. *J. Appl. Phys.* **2008,** *104* (1), 3.
33. Morber, J. R.; Ding, Y.; Haluska, M. S.; Li, Y.; Liu, P.; Wang, Z. L.; Snyder, R. L., PLD-assisted VLS growth of aligned ferrite nanorods, nanowires, and nanobelts-synthesis, and properties. *J. Phys. Chem. B* **2006,** *110* (43), 21672-21679.
34. Wang, Z. Y.; Hu, L. Z.; Zhao, J.; Sun, J.; Wang, Z. J., Effect of the variation of temperature on the structural and optical properties of ZnO thin films prepared on Si (111) substrates using PLD. *Vacuum* **2005,** *78* (1), 53-57.
35. Kim, S. S.; Lee, B.-T., Effects of oxygen pressure on the growth of pulsed laser deposited ZnO films on Si (001). *Thin Solid Films* **2004,** *446* (2), 307-312.
36. Hasko, D.; Bruncko, J., AFM surface analysis of ZnO layers prepared by pulsed laser deposition at different oxygen pressures. *Vacuum* **2009,** *84* (1), 166-169.
37. Weigand, C. C.; Bergren, M. R.; Ladam, C.; Tveit, J.; Holmestad, R.; Vullum, P. E.; Walmsley, J. C.; Dahl, O.; Furtak, T. E.; Collins, R. T.; Grepstad, J.; Weman, H., Formation of ZnO Nanosheets Grown by Catalyst-Assisted Pulsed Laser Deposition. *Crystal Growth & Design* **2011,** *11* (12), 5298-5304.
38. Yan, H. Q.; He, R. R.; Pham, J.; Yang, P. D., Morphogenesis of one-dimensional ZnO nano- and microcrystals. *Adv. Mater.* **2003,** *15* (5), 402-+.

39. Nagashima, K.; Yanagida, T.; Oka, K.; Tanaka, H.; Kawai, T., Mechanism and control of sidewall growth and catalyst diffusion on oxide nanowire vapor-liquid-solid growth. *Appl. Phys. Lett.* **2008,** *93* (15), 3.
40. Guan, L.; Zhang, D. M.; Li, X.; Li, Z. H., Role of pulse repetition rate in film growth of pulsed laser deposition. *Nucl. Instrum. Methods Phys. Res. Sect. B-Beam Interact. Mater. Atoms* **2008,** *266* (1), 57-62.
41. Wang, Z. Y.; Sun, L. Y.; Hu, L. Z., Effect of laser repetition frequency on the structural and optical properties of ZnO thin films by PLD. *Vacuum* **2010,** *85* (3), 397-399.
42. Masin, M.; Kotrla, M., Influence of control and material parameters on island density in early stage of pulsed laser deposition. *Thin Solid Films* **2012,** *520* (15), 4965-4970.
43. Guo, R.; Nishimura, J.; Matsumoto, M.; Higashihata, M.; Nakamura, D.; Okada, T., Density-controlled growth of ZnO nanowires via nanoparticle-assisted pulsed-laser deposition and their optical properties. *Japanese Journal of Applied Physics* **2008,** *47* (1), 741-745.
44. Dalal, S. H.; Baptista, D. L.; Teo, K. B. K.; Lacerda, R. G.; Jefferson, D. A.; Milne, W. I., Controllable growth of vertically aligned zinc oxide nanowires using vapour deposition. *Nanotechnology* **2006,** *17* (19), 4811-4818.
45. Ohtomo, A.; Tsukazaki, A., Pulsed laser deposition of thin films and superlattices based on ZnO. *Semicond. Sci. Technol.* **2005,** *20* (4), S1-S12.
46. Baxter, J. B.; Aydil, E. S., Epitaxial growth of ZnO nanowires on a- and c-plane sapphire. *J. Cryst. Growth* **2005,** *274* (3-4), 407-411.
47. The sapphire crystal. [On line] http://baselabtools.com/resources/tutorials/sapphire-windows?
48. Single crystal sapphire growth and step sapphire waferes [On line] http://www.namiki.net/product/jewel/sapphire/.
49. Kasuga, M.; Mochizuki, M., Orientation relationships of zinc oxide on sapphire in heteroepitaxial chemical vapor deposition. *J. Cryst. Growth* **1981,** *59* (2), 185-194.
50. Moriyama, T.; Fujita, S., Growth behavior of nonpolar ZnO on M-plane and R-plane sapphire by metalorganic vapor phase epitaxy. *Japanese Journal of Applied Physics Part 1-Regular Papers Brief Communications & Review Papers* **2005,** *44* (11), 7919-7921.
51. Zuniga-Perez, J.; Rahm, A.; Czekalla, C.; Lenzner, J.; Lorenz, M.; Grundmann, M., Ordered growth of tilted ZnO nanowires: morphological, structural and optical characterization. *Nanotechnology* **2007,** *18* (19), 7.
52. Chen, H. G.; Li, Z. W.; Lian, H. D., Control of epitaxial growth orientation in ZnO nanorods on c-plane sapphire substrates. *Thin Solid Films* **2010,** *518* (19), 5520-5524.
53. Martin, M. N.; Basham, J. I.; Chando, P.; Eah, S. K., Charged gold nanoparticles in non-polar solvents: 10-min synthesis and 2D self-assembly. *Langmuir* **2010,** *26* (10), 7410-7417.

Chapter 6. Conclusions and Future Work

For controlled synthesis of CNTs and NWs using catalyst metal NPs and a VLS growth mechanism, preventing the sintering of metal NPs prior to growth is very important. In this thesis, two catalyst systems which can prevent the sintering of metal NPs have been demonstrated.

Optimization of a protocol for CNT growth using Co NPs electrodeposited within shallow PAA membrane was performed in an iterative fashion and involved three main stages. Firstly, different strategies have been tested during the optimisation of fabricating the shallow PAA membranes, which included annealing and electropolishing Al foil prior to the anodization process, optimising the procedure of anodization and trialling of a through-hole PAA membrane with a layer of Au coating on one side. The annealing and electropolishing Al foil caused a severe damage during the subsequent anodization process. The trialling of a through-hole PAA membrane with a layer of Au coating on one side was also not successful. The PAA membrane was too fragile as it was made using mild anodization. Ultimately, optimising the procedure of anodization was the best option for obtaining suitable membrane for electrodeposition of Co NPs.

During optimisation of PAA membrane, the fabrication method was changed from a 2-step anodization process to a 3-step anodization process and the anodization time of the 3rd step was shortened to 30 s. AFM was used to detect the uniformity of the dimpled surface after each step of the anodization process. The dimple structures were made by removing the porous Al_2O_3 structures formed during the 1st and the 2nd anodizations. Therefore, the first 2-step anodization process aimed to fabricate a uniform dimpled surface which allows a highly

uniform porous structure to be grown on this base during the final 3rd step anodization. In addition, the etching period was extended from 60 min to 65 min to make the pores wider without losing the integrity of the walls.

The PAA membranes made using an optimised approach provide the benefits, such as improved uniformity of electrodeposition and facilitated mass transfer for gases during CNT growth by CVD.

Secondly, optimisation of the Co electrodeposition procedure was performed. During all the optimisation steps care was taken to remove residual electrolyte from the PAA pores to ensure that observed CNT growth is due to electrodeposited Co catalyst. The generation of $H_{2(g)}$ bubbles during the electrodeposition often results in blockage of pores and negatively affects the uniformity of the electrodeposition. An innovative strategy was introduced in this thesis, which involves splitting of the electrodeposition into several steps with a short deposition interval (100 ms) for each step followed by a long rest period (15 min). For the same total deposition time, the coverage of CNTs was significantly increased when compared with samples which were directly electrodeposited without splitting the electrodeposition into several steps. Also, the pH of the electrolyte was adjusted from 3.8 to 4.7 to decrease the efficiency of hydrogen evolution reaction. In order to prevent the oxidative dissolution of deposited Co during the electrodeposition, $N_{2(g)}$ was purged during the electrodeposition. This procedure helps to maintain the quality of electrodeposition as reflected by a dense CNT growth.

Finally, the reduction temperature was increased in the optimised procedure to ensure that the deposited Co NPs which had been exposed to air were fully reduced to the metallic state *in situ* prior to the CNT growth *via* CVD process.

The above series of experiments helped to establish the optimised conditions for further studies using PAA templates for catalytic synthesis of nanostructures. In this work the diameter of CNTs smaller than the diameter of the PAA membrane pores was attained by using the optimised PAA membrane fabrication method in combination with a short Co electrodeposition time using the optimised electrodeposition method. Thus, the diameter of CNTs could be controlled by adjusting the electrodeposition time. However, more direct evidence to confirm this finding is required. Such evidence could be obtained, for example, by correlating the actual sizes of the deposited Co NPs with the diameters of CNTs. This experiment would require high resolution SEM and TEM images of a cross-section of a cut PAA template before and after CNT growth. Alternative electrodeposition strategies could involve a through-hole PAA membrane firmly attached to a layer of Au or other conductive metal. The better conductivity of such a working electrode (Au layer *cf.* Al_2O_3 barrier layer on Al) should allow better control of the Co particle size than does the optimised PAA template developed in this work. However, such an approach could also alter the catalytic behaviour of the Co NPs, as these would be interacting with Au and not the Al_2O_3 base. Clearly alloying, diffusion, adhesion *etc*., would all be different for Co NPs deposited on Au rather than Al_2O_3. Issues related to the mechanical and adhesive stability of the Au layer would also need to be considered.

For ZnO nanorod growth, Au nanocolloids were used as the catalyst and the fabrication of a catalyst system was developed in this work. Different methods of coating sapphire and silicon substrates with Au nanocolloids were tested: drop coating, dip coating, and forming a sub-monolayer of Au nanocolloids by dip coating an APTMS modified substrate. Experiments demonstrated that the best option is to use a sub-monolayer of Au nanocolloids on an APTMS modified C-plane sapphire substrate. However, it appeared that the APTMS may not be completely removed during the PLD process which could result in

the aggregation of Au nanocolloids. In order to solve this problem, an optimised procedure which involved prolonged exposure to $O_{2(g)}$ during heating up to the target ZnO growth temperature was introduced. Uniform ZnO nanorods were obtained after using this optimised procedure. Using a sub-monolayer of Au nanocolloids on an APTMS modified C-plane sapphire substrate for ordered ZnO nanorod growth is an innovative method as well as the optimised PLD procedures.

Other parameters of the PLD process could potentially affect ZnO nanorod growth using Au colloids as a catalyst. Experiments focused on the effects of different laser repetition rates showed that the morphology can change from nanorods to nanowire-like structures when the laser repetition rate is increased. At a high laser repetition rate (25 Hz), the tips of the ZnO nanowires were similar to the sizes of the Au nanocolloids. This indicates that the diameter of ZnO nanowire could be controlled *via* the size of Au nanocolloids using this strategy. Hence, the future work for this project will involve use of Au nanocolloids of different sizes under the optimised ZnO growth procedure reported here to observe effects of the catalyst size on the morphology of the ZnO nanorods or nanowires. Furthermore, although different types of sapphire substrates were trialled early in this work, the coating method had not been optimised yet at that stage. Therefore, further work should re-examine the effect of different substrates (*i.e.* Si or other types of sapphire substrates) using the optimized strategy for colloid deposition and ZnO growth reported here. Potentially, this ZnO nanorod array could be applied to the ultraviolet photodetectors and dye-sanitised solar cells.